OPTICAL ALIGNMENT WITH CGH PHASE REFERENCES

by

Eric Hathaway Frater

A Dissertation Submitted to the Faculty of the

DEPARTMENT OF OPTICAL SCIENCES

In Partial Fulfillment of the Requirements

For the Degree of

DOCTOR OF PHILOSOPHY

In the Graduate College

THE UNIVERSITY OF ARIZONA

2016

THE UNIVERSITY OF ARIZONA
GRADUATE COLLEGE

As members of the Dissertation Committee, we certify that we have read the dissertation prepared by Eric Hathaway Frater, titled Optical Alignment with CGH Phase References and recommend that it be accepted as fulfilling the dissertation requirement for the Degree of Doctor of Philosophy.

_____Date: 27 July 2016
James H. Burge

_____Date: 27 July 2016
Dae Wook Kim

_____Date: 27 July 2016
José M. Sasián

Final approval and acceptance of this dissertation is contingent upon the candidate's submission of the final copies of the dissertation to the Graduate College.

I hereby certify that I have read this dissertation prepared under my direction and recommend that it be accepted as fulfilling the dissertation requirement.

_____Date: 27 July 2016
Dissertation Director: James H. Burge

STATEMENT BY AUTHOR

This dissertation has been submitted in partial fulfillment of the requirements for an advanced degree at the University of Arizona and is deposited in the University Library to be made available to borrowers under rules of the Library.

Brief quotations from this dissertation are allowable without special permission, provided that an accurate acknowledgement of the source is made. Requests for permission for extended quotation from or reproduction of this manuscript in whole or in part may be granted by the head of the major department or the Dean of the Graduate College when in his or her judgment the proposed use of the material is in the interests of scholarship. In all other instances, however, permission must be obtained from the author.

SIGNED: Eric Hathaway Frater

ACKNOWLEDGEMENTS

I am grateful for the education I have received at the College of Optical Sciences.

The instructors who have shown me their genuine talent for teaching made a big impact on my understanding of optics. Among these instructors I would like to acknowledge the notable talent of John Greivenkamp, Scott Tyo, Tom Milster, Matt Dubin, Jim Burge, and José Sasián.

I would like to acknowledge the talented engineers and opticians who supported my efforts in the Large Optics Shop in the basement of Meinel Building:

Chang Jin Oh invested a great deal of trust in me to be a leader on the HET Wide Field Corrector alignment. This was an incredibly trying endeavor, but worth its length in lessons learned through experience.

Bryan Keener Smith is a true genius. My long period of work with him on HET was a real pleasure and I actively seek more opportunities to work with this man. Neglecting such opportunities is what troubles me most about leaving Tucson.

Todd Horne brought out my most practical side during the nine months I spent learning under his supervision. His broad skill set and demand for productivity have rubbed off on me.

Andrew Lowman and Matt Dubin were both very helpful and patient with me. Our collaborations taught me how to communicate effectively with my fellow engineers and work at a professional level.

Daniel Caywood, Norm Schenck, Vince Blair, Scott Benjamin, Bill Anderson, and Marco Favela were all willing to both help and teach me as I worked projects in the shop. Your expertise and kind personalities will be remembered.

The LOFT group as a whole has offered me tremendous support. Through our meetings, discussions, and collaborations I have been indoctrinated into optical engineering. Jim Burge, Dae Wook, Matt Dubin, Chunyu Zhao, Ping Zhou, Laura Coyle, Tianquan Su, Alex Maldonado, and Wenchuan Zhao have all been pillars of support to me during my time in this research group.

Finally, I thank Jim Burge for his mentorship and providing the project work opportunities I had hoped for. It was a pleasure to work with you.

DEDICATION

To my loving parents,

Julia & David Frater

To my grandparents,

Margaret Skinner

Angela & Allen Frater

To the memory of my grandfather,

Stuart Skinner

TABLE OF CONTENTS

ABSTRACT

The growing field of high-order aspheric and freeform optical fabrication has inspired the creation of optical surfaces and systems which are difficult to align. Advances in optical alignment technology are critical to fabricating and integrating aspheric components in advanced optical systems. This dissertation explores the field of optical alignment with a computer-generated hologram (CGH) used as a reference. A CGH is a diffractive optic which may be used to create a desired phase profile across a beam of light, project irradiance patterns, or serve as a mask for an incident beam. The alignment methods presented in this dissertation are concerned with the use of a CGH to create reference phase profiles, or "wavefronts", in a beam.

In one application a set of axisymmetric CGH references are co-aligned. Each CGH has also been aligned to an aspheric mirror so the co-alignment of the CGH references is also a co-alignment of the aspheric mirrors. Another application is concerned with aligning an interferometer to test an aspheric mirror surface. The interferometer measures a "null" interference pattern when its wavefront accommodates a known surface profile. In this alignment application the CGH creates wavefronts which accommodate a known set of small spherical reference features at the test surface. An interference null from all the "phase fiducial" reference features indicates an aligned projection of the CGH.

The CGH co-alignment method is implemented on a 4-mirror prime focus corrector known as the Hobby-Eberly Telescope Wide Field Corrector (HET WFC). It is shown that this method was very successful for centration alignment of some

mirrors, whereas mechanical stability was the hardware limitation for other degrees of freedom. The additional alignment methods used in this project are described in detail and the expected alignment of the HET WFC is reported.

The fabrication, characterization and application of spherical phase fiducials is demonstrated in a CGH-corrected Fizeau test prototype. It is shown that these reference features achieve < ±1.5μm transverse alignment precision. A pair of phase fiducials is also applied to constrain the clocking and magnification of a projected wavefront. Fabrication and coordinate measurement of the features present the dominant challenges in these demonstrations.

CHAPTER 1

INTRODUCTION

Optical alignment is vital to produce successful optical systems. It is most valuable in cases where high precision is valued over high production. In the most demanding cases the methods for alignment and testing commonly drive system performance. It is increasingly common to use large advanced aspheric surfaces in the astronomy and defense industries and these surfaces are particularly challenging to align. Additionally, the fabrication of these advanced surfaces is demanding from a testing perspective where precise optical alignment is also essential. The computer-generated hologram (CGH) is a class of diffractive optical elements which is highly valued for its versatility and applications in optical testing and alignment.

Axisymmetric optical systems require an alignment of each optical element in 5 degrees of freedom. Specifically, if the system is symmetric about the Z-axis a constraint is required for X, Y and Z translations and Rx and Ry rotations about X and Y, respectively. There is rarely a single diagnostic instrument for constraint of all these degrees of freedom for each of the system components. Commonly one of the elements is treated as a datum target to which all the other components are aligned and there are some degrees of freedom left to compensate first-order effects such as defocus and tilt. The other degrees of freedom may be constrained by an alignment plan which employs an alignment telescope, autocollimator, inside and outside micrometers, coordinate measuring machine, interferometer test, or other alignment

tools. The goal is to plan and execute a systematic solution where a series of measurements and adjustments accomplish an alignment to specified tolerances.

Some alignment tools are well-suited for measuring optical surfaces directly. An alignment telescope is useful to align a spherical surface center of curvature along a line of sight. These instruments may also be used to view an object- or image-space coordinate along the same line of sight and have a variety of applications in alignment[1]. An autocollimator is nothing more than a special type of autocollimating alignment telescope[2]. Despite the versatility of these apparatus they only work for elements that do not have a central obscuration. Annular mirrors cannot be aligned directly with an alignment telescope.

Optical surface contact measurements with micrometers or metering rods are also not as readily applied to annular mirrors because these mirrors lack a real vertex. The separation of these mirrors must be calculated from measuring off-axis points across the surfaces. A coordinate measuring machine and careful processing of the data is required to construct the system geometry if this approach is taken for aligning the spacing between the mirrors. Furthermore, the mirrors can only be measured this way *before* they are coated or there is a risk of damage to the optical coating.

Interferometric tests offer a very precise diagnosis of the transmitted wavefront through an optical system. Aberrations such as tilt and coma are commonly observed in these tests when the symmetry of a system has been broken due to a component misalignment[3]. It is possible to exploit an interferometer test for the sake of alignment, where the aberrations may be associated with a specific set of

misalignments. This is most readily done with a single surface under test because there are a sufficiently small number of degrees of freedom. This methodology breaks down in more complicated systems due to degeneracies where the misalignment of *different* degrees of freedom may influence the on-axis transmitted wavefront aberrations in the *same* way. It is necessary to complement these tests with other means of constraining the optics so that a small set of degrees of freedom are used to compensate the aberrations.

The use of separate alignment reference features is warranted in cases where the direct diagnosis of individual surfaces or alignment based on the system transmitted wavefront is not possible[4]. Reference features may be optical, mechanical or both. In either case the optic which is referenced must have a well-understood location relative to the alignment reference features[5]. These features are designed to be measured *in situ* during the component integration and system alignment. The goal is to offer a safe and precise measurement of a given component relative to the alignment datum. Computer-generated holograms offer the accuracy and versatility needed to create a suite of optical alignment references.

1.1 TAXONOMY OF CGH ALIGNMENT

A CGH may serve to produce a reference wavefront, project an irradiance pattern, or mask the beam in any desired pattern. These functions may be exploited in many different ways for optical alignment and testing. Many of these have already

been identified by Burge *et al.*[6]. This section will survey and define a taxonomy of the existing methods for optical alignment with a CGH.

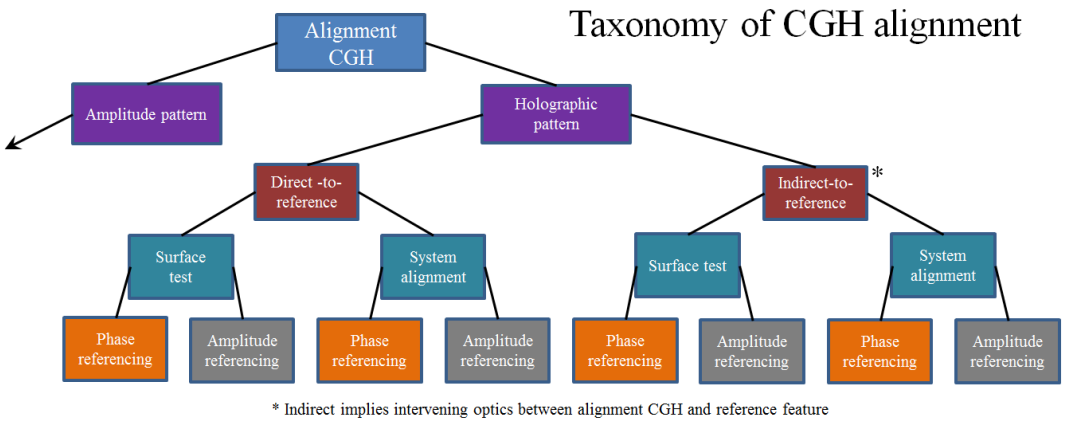

Figure 1.1: Diagram of the taxonomic structure for CGH alignment methods.

A taxonomic structure has been created which is shown in Figure 1.1. In order to designate a method within this taxonomy a set of labels has been applied to the structure. The labeling for the pattern type is “AmP” or “HoL” for amplitude pattern or holographic pattern. Labels “D” or “I” designate direct- or indirect-to-reference. The labels “SrF” and “SyS” are applied depending on whether a surface test or system is under alignment. A label of “A” or “P” is applied depending on whether the amplitude or phase of light, respectively, serves as the measured property for alignment. These distinctions which are drawn at different levels of the taxonomy are explained in order below. Table 1.1 and Table 1.2 provide lists of the existing methods for alignment with a CGH with taxonomic designations.

Table 1.1: Alignment of system to CGH and illumination

Types of CGH references	Types of alignment	Configurations	AmP, HoL	D, I	SrF, SyS	A, P
Focus projection	Alignment of PSD references to projection	Spot focused by CGH at PSD	HoL	(both)	(both)	A
		Spot pattern imaged onto PSD [7]	AmP	I	(both)	A
	Alignment of ball reference to projection	Ball reference remote from CGH [8]	HoL	D	SrF	P
		Ball reference connected to CGH [9]	HoL	D	SrF	P
	Coaxial optical element alignment	Multiple lens coaxial alignment [6]	HoL	I	SyS	P
		Multiple CGH coaxial alignment [5]	HoL	D	SyS	P
Crosshair projection	Alignment of optical substrate OD	Visual alignment[6]	HoL	D	SrF	A
	Alignment of PSD references to projection	Crosshair focused by CGH at PSD [6]	HoL	D	SrF	A
		Crosshair pattern imaged onto PSD	AmP	I	SrF	A
Wavefront reference	Alignment of wavefront to test surface.[6]	Interferometer surface test	HoL	(both)	SrF	P
	Alignment of wavefront to optical system[6]	Interferometer system test/alignment	HoL	(both)	SyS	P
	Null from alignment features [10]	Interferometer surface test	HoL	D	SrF	P
Amplitude pattern	Alignment along line of sight	Alignment telescope lens alignment [1]	AmP	I	(both)	P
	Mechanical datum alignment	Ball over reference pattern [11]	AmP	D	SrF	A

Table 1.2: Alignment of CGH to illumination

Types of CGH references	Types of alignment	Configurations	AmP, HoL	D, I	SrF, SyS	A, P
Wavefront reference	CGH alignment to spherical wavefront [12]	Interferometer test	HoL	D	SrF	P
	CGH alignment to aspherical wavefront [13]	Interferometer test	HoL	I	SrF	P
Amplitude pattern	Alignment along line of sight [1]	Alignment telescope imaging	AmP	D	(both)	A

A division has been made at the highest level based on whether the CGH is exploited for alignment as a simple photomask which solely influences the transmitted or reflected beam amplitude ("Amplitude pattern") or if the CGH alignment features are diffractive ("Holographic pattern"). Note that the structure of the taxonomy in Figure 1.1 also applies to "Amplitude pattern" CGH features. The division of alignment methods based on the type of CGH pattern is illustrated with the examples in Figure 1.2 and Figure 1.3. For a "*Spot focused by CGH at PSD*" the CGH has a set of holographic patterns which focus the beam at the position sensitive detectors (PSDs). The case with a "*Spot pattern imaged onto PSD*" uses a simple amplitude pattern to create small source points which are imaged by a projection lens near the test plate in a Fizeau interferometer. Using an amplitude pattern to mask a beam has limited applications and this section will focus on the more extensive field of methods which exploit the diffractive properties of a CGH.

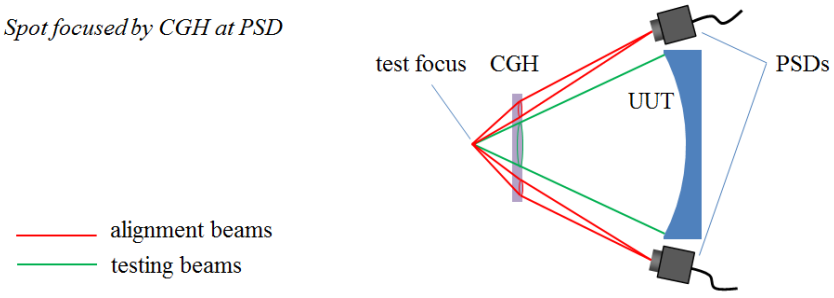

Figure 1.2: Alignment of PSD references to focus projections in a surface test. Designation: {HoL, D, SrF, A}.

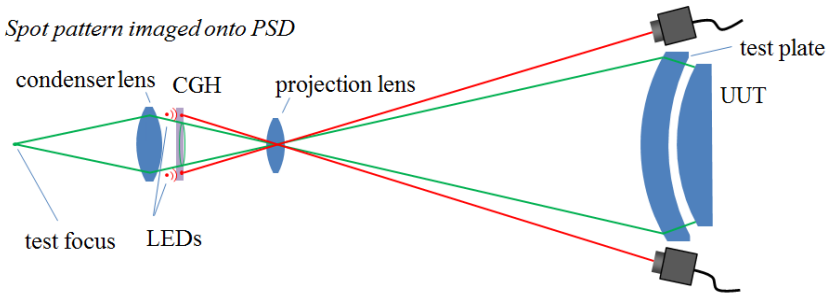

Figure 1.3: Alignment of position sensitive detector (PSD) references to focus projections in an interferometer system[7]. Designation: {AmP, I, SyS, A}

There is further division of the methods between a "Direct-to-reference" or "Indirect-to-reference" CGH alignment method. In general there is a reference which the light interacts with before a measurement is conducted. There is a notable difference between cases where the light propagates directly from the CGH to the reference ("Direct-to-reference") and where the light interacts with other testing or system optics before interaction with the reference ("Indirect-to-reference"). In some cases the CGH *is* the reference for alignment of the CGH to an illuminating wavefront[12, 13]. In this case there is a discrepancy between a "direct" illumination of the CGH from a spherical wave or "indirect" illumination through intermediary optics which distort the incident wavefront. Figure 1.4 and Figure 1.5 provide two examples which illustrate the discrimination between direct- or indirect-to-reference alignments. Figure 1.4 shows a direct-to reference alignment where an alignment beam from CGH #1 propagates directly to CGH #2 or CGH #3 to align these optics. There are no intermediary optics because the CGHs are exchanged and aligned individually. Figure 1.5 shows a similar co-axial alignment for lenses, but the lenses are left in place after lens 1 is aligned. Thus, the propagation of Wavefront 3 is

influenced by the position of lens 1 *and* lens 2. Wavefront 4 is influenced by *all* the lenses in the system under alignment. The presence of the intermediary optics defines the lens co-alignment as an indirect-to-reference alignment method.

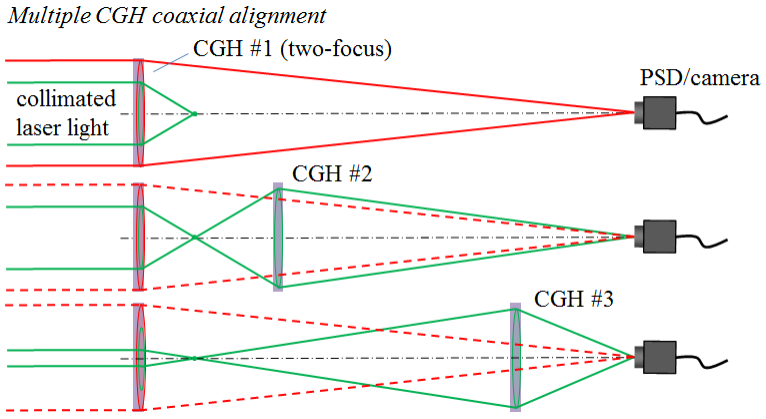

Figure 1.4: Coaxial CGH alignment from focus projections[5]. Designation: {HoL, D, SyS, P}.

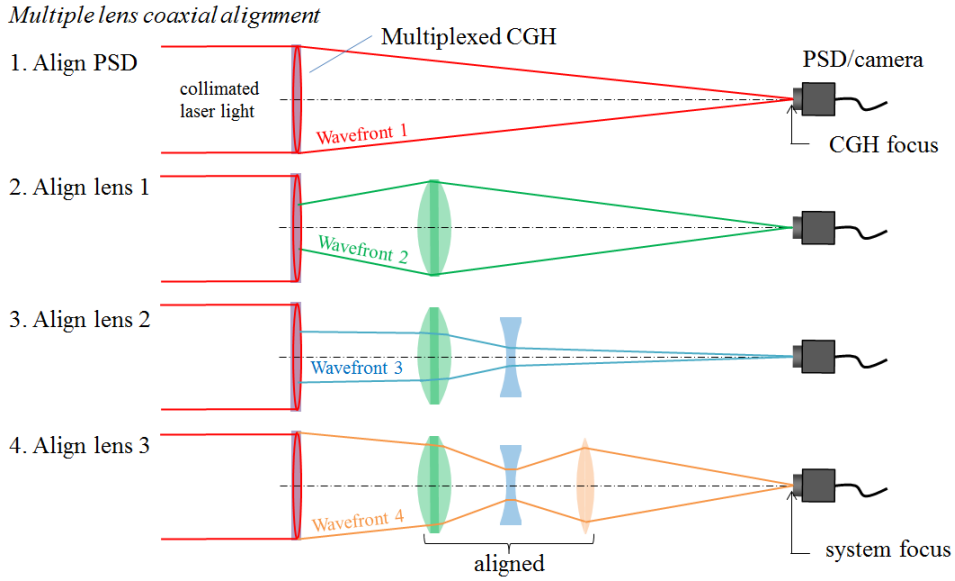

Figure 1.5: A reference CGH provides several wavefronts which are focused by 1, 2 and then 3 lenses at a reference location on a position sensitive detector (PSD) [6]. Designation: {HoL, I, SyS, P}.

The taxonomy has also been divided based on whether the alignment is concerned with a single optical surface or a system. In the case where there is only

one optical surface under measurement the method is categorized under “Surface test”. In such cases the only other optics are the CGH, other testing and alignment equipment, and any optical data under alignment to the surface. In other cases where there are two or more optical surfaces that must be aligned to comprise a stand-alone system the alignment method is categorized under “System alignment”. The discrimination between the taxonomic designations is given in Figure 1.6. There is an obvious difference in these example cases where the CGH produces a reference wavefront to accommodate either a single surface or a system made up of several surfaces.

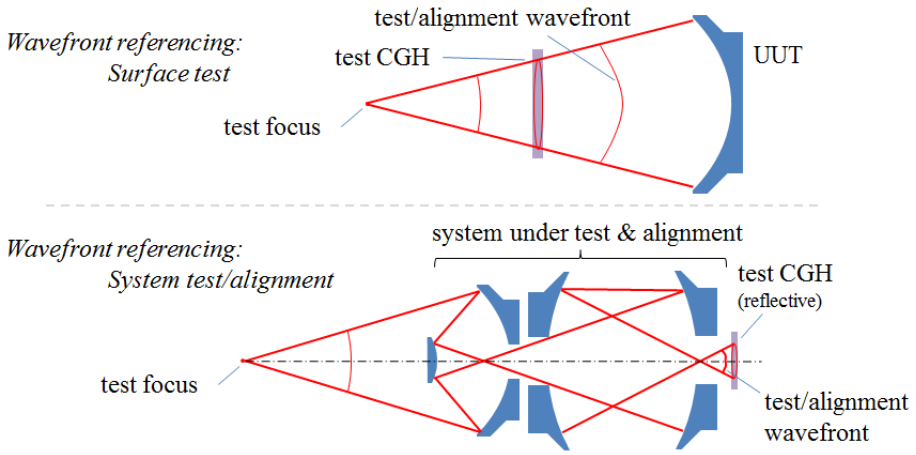

Figure 1.6: Alignment of optical tests based on aberrations from a test surface[6] (top) and a system of surfaces[4] (bottom). Designations: {HoL, D, SrF, P} (top) and {HoL, I, SyS, P} (bottom).

The final division is made between methods which are “Amplitude referencing” or “Phase referencing”. Amplitude signals may be measured as irradiance or radiance distributions and phase signals may be measured by interference or by geometric means. Amplitude referencing diagnoses include visual inspection of an illuminated target, irradiance measurement with a position sensitive detector (PSD), or imaging with an alignment telescope along a particular line of

sight. For phase referencing the typical methods of diagnosis are by interferometer measurement or comparison of the angle of a reflected or transmitted beam compared to a reference beam. The later method of phase referencing may be accomplished with an alignment telescope, PSD, or other custom alignment tools such as the "Ball Alignment Tool" used by Zehnder *et al.*[8]. Several examples of alignment hardware configurations which are amplitude and phase referencing are given in Figure 1.7 and Figure 1.8. In Figure 1.7 the CGH projects crosshair patterns at the periphery of the unit under test (UUT) which are observed visually and alternatively with PSDs. In Figure 1.8 the CGH projects a focus and under the condition of alignment with the

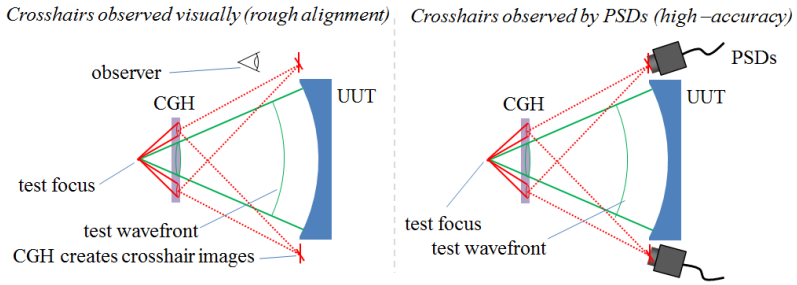

Figure 1.7: Visual and position sensitive detector (PSD) alignments of crosshair projections and test wavefront to UUT[6]. Designations: {HoL, D, SrF, A} (left and right).

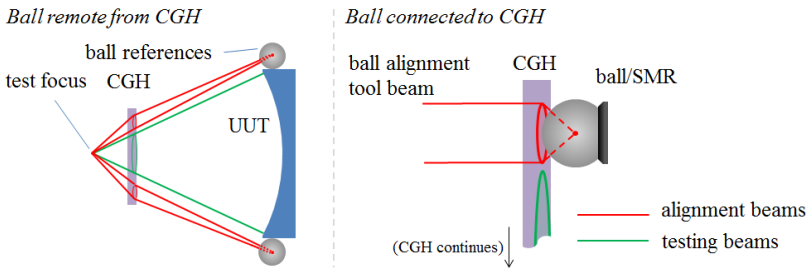

Figure 1.8: Alignment of ball references to focus projections[8, 9]. Designations: {HoL, D, SrF, P} (left and right).

center of a ball reference the light achieves auto-reflection back to the test focus. In these examples an interferometer is readily applied to measure the reflected phase distribution relative to a reference surface within the interferometer.

To further develop the concept of this taxonomic structure a more detailed description and comparison of several cases is given below. Consider an optical test where a Fizeau interferometer illuminates a null CGH with a spherical wavefront to conduct a null test on an off-axis parabola (OAP). If the CGH projects a set of crosshairs to the outer edge of the OAP which a technician measures relative to the edge of the mirror, then the CGH alignment is labeled {HoL, D, SrF, A}. This configuration is shown in Figure 1.7. If the alignment is made by compensating aberrations in the interferometer measurement of the OAP then the alignment is labeled {HoL, D, SrF, P}. The top diagram in Figure 1.6 illustrates this rather general example. Some level of alignment compensation is *always* done based on the surface measurement to remove tilt and possibly power aberrations.

Now consider a CGH-corrected Fizeau test where the CGH is projected to the test surface with a projection lens[7]. This configuration is shown in Figure 1.3. If the projection of the CGH is aligned based on projected image of a set of pinhole features that are outside the test aperture, then the alignment is labeled {AmP, I, SrF, A}. An alignment made to this surface test based on the aberrations in the test would be labeled {HoL, I, SrF, P}. These alignments are designated with "I" because the light leaving the CGH interacts with the projection lens and possibly the test plate before interacting with the reference feature. In these two cases the reference feature is a PSD outside the test aperture, or the unit under test (UUT). Each optic with which the light interacts adds further variables that influence the alignment diagnosis.

Another direct-test configuration which has a reflective alignment pattern on the test CGH is given in the top diagram of Figure 1.9. This configuration returns light directly to the interferometer by Littrow diffraction where a null is associated with the alignment of the CGH to the interferometer beam. In this case there are no intervening optics other than those of the interferometer itself and the method is labeled {HoL, D, SrF, P}. If there is an optic such as a fold sphere between the interferometer and the CGH alignment reference, as in the lower diagram of Figure 1.9, then the designation becomes {HoL, I, SrF, P}.

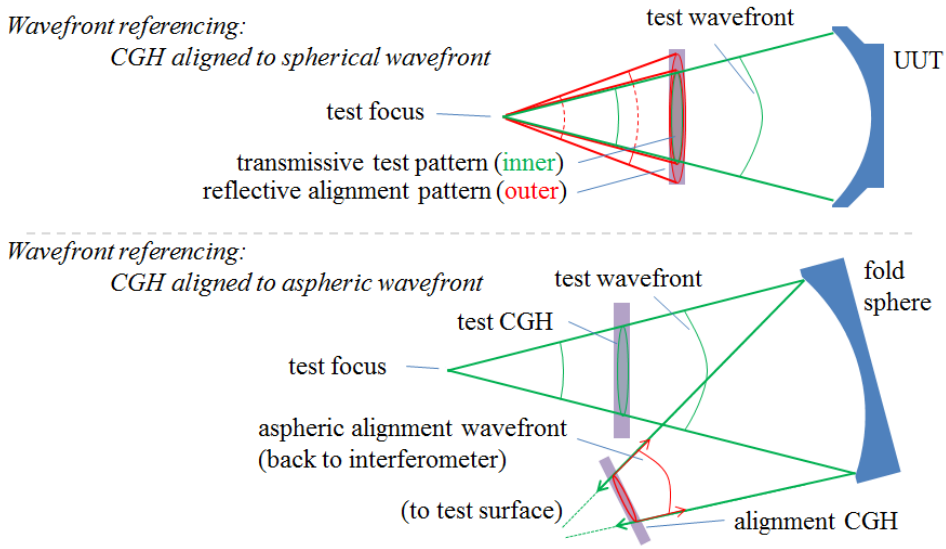

Figure 1.9: Alignment of a CGH by referencing a wavefront that is spherical[12] (top) to align a test CGH, or aspheric[13] (bottom) to align a CGH which locates the test wavefront after the fold sphere. Designations: {HoL, D, SrF, P} (top) and {HoL, I, SrF, P} (bottom).

Although it is not the focus of this research, the uses of an amplitude pattern as a reference on the CGH warrants a brief discussion. An amplitude pattern does not create a projection and the CGH must instead be imaged or otherwise complemented with other apparatus or system components to create a desired phase or amplitude

distribution elsewhere. An amplitude pattern on the CGH is commonly included as a means by which to register the holographic pattern(s) to external mechanical data as in Figure 1.10, or to locate the CGH with an alignment telescope as shown in Figure 1.11. It is also useful in some cases to generate datum point sources of light at known locations with pinholes in an otherwise chrome-coated area on the CGH. This method has radiometric inefficiency in generating diffraction-limited source points unless the illumination is deliberately coupled to the tiny apertures. Similar to the conceptual example in Figure 1.3, the Tokyo Atacama Observatory (TAO) secondary mirror test has pinholes illuminated by individual LEDs and imaged to detectors by the projection lens of the interferometer. This configuration is used to align the projection of the CGH with the Fizeau cavity. Although there are valuable ways to exploit amplitude patterns for optical alignment, this discussion will turn toward the more diverse field of using holographic alignment patterns on CGHs. Specifically, the practice of referencing the phase of alignment beams will be the field of alignment to which this research contributes.

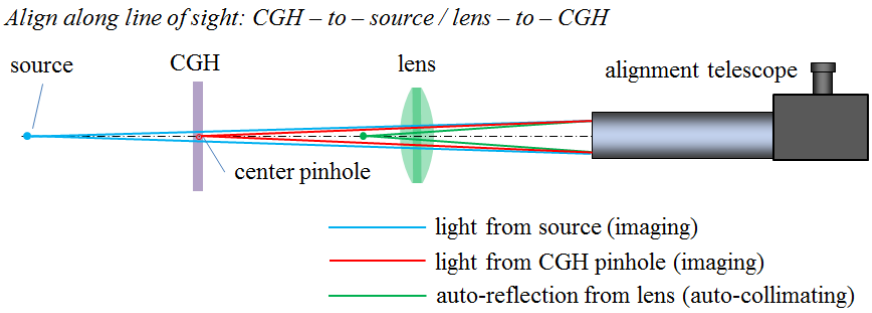

Figure 1.10: Amplitude pattern on CGH imaged by alignment telescope to align the CGH to a source point and a lens to the CGH. The alignment would be done sequentially (source, CGH, then lens) with the telescope alignment axis stationary[1]. Designation: {AmP, D, SyS, A}.

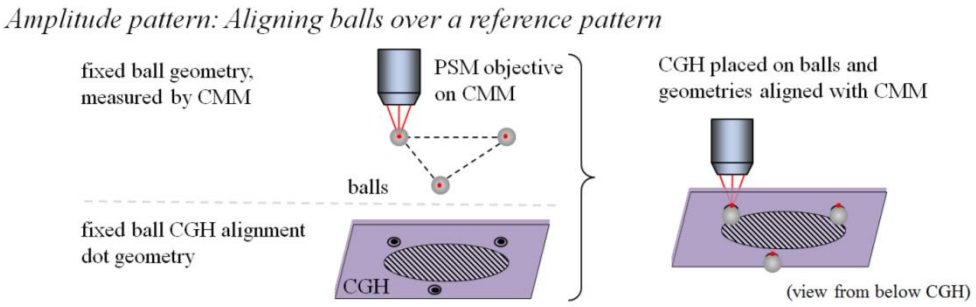

Figure 1.11: Amplitude pattern defines ideal locations for a set of balls. Balls may be used for a kinematic mount. Several CGH substrates may be mounted in fixtures with a common mounting interface on the CMM such that they may be co-aligned and exchanged in this mount within an optical system [11]. Designation: {AmP, D, SrF, A}.

1.2 PHASE-REFERENCING CGH ALIGNMENT TECHNIQUES

1.2.1 Introduction

The research presented in this dissertation is concerned with phase-referencing CGH alignment techniques. The phase-referencing alignment methods have already been separated from amplitude-referencing methods by taxonomic designation in Table 1.1 and Table 1.2. Referencing phase is readily achieved in interferometry where the measurement evaluates relative phase between beams. However, it is also common to reference phase with other optical alignment tools to gain high alignment sensitivities. Without an interferometer changes in tilt of a transmitted or reflected beam are readily measured as translation of an image in a simple camera or telescope. This section will review the use of the phase of a beam as feedback for optical alignment, discuss several important examples, and identify the impact of this dissertation on this area of CGH optical alignment.

1.2.2 Principle of phase-referencing

Referencing the phase of a beam for alignment always involves a reference beam to which an alignment beam is compared. In interferometry this is clear from the use of a reference and test beam in any typical surface or system measurement. When a camera is used there is an image coordinate associated with a reference phase distribution in the exit pupil. The comparison of the reference image coordinate with that of an alignment beam is also a comparison of phase. It is less typical for both beams to pass into a camera simultaneously, but the principle behind this measurement is identical to that of the alignment mode on a Zygo interferometer[14].

Consider the point source microscope (PSM)[11]. The PSM is an infinity-corrected microscope with an internal fiber-coupled laser source and CCD detector. The PSM is represented schematically and pictorially in Figure 1.12. Light from the laser is collimated by a condenser lens and comes to a focus at the best-focus object plane of the microscope objective. When light from the laser is retro-reflected it comes to a sharp focus on the CCD. Just like an interferometer you can force the condition of retro-reflection by placing a mirror at the focus in front of the microscope objective. This condition is often referred to as the “cat’s eye” retro-reflection. With cat’s eye retro-reflection the location of the focus at the CCD has a fixed position regardless of the mirror shape or orientation, to first-order approximation. The location of this focus represents the condition of retro-reflection and serves as a reference point for this alignment device.

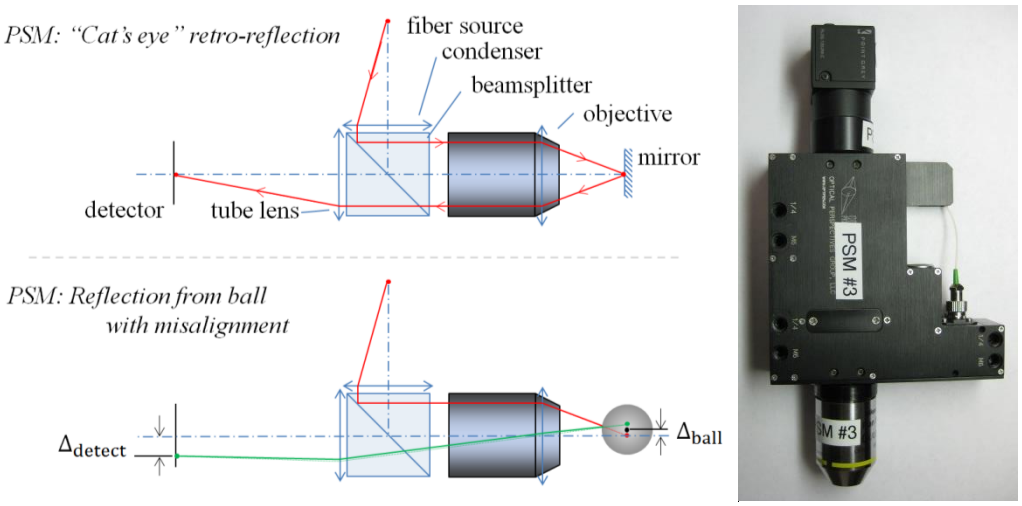

Figure 1.12: The point-source microscope (PSM). The condition of cat's-eye retro-reflection (upper left), reflection from focus near the center of a sphere (lower left), and a photograph of the device (right)[11].

Now consider the use of the PSM to align a sphere, specifically a Ø0.5" chromed steel ball as in the lower left diagram of Figure 1.12. The PSM achieves autoreflection when the focus in the object plane of microscope objective is coincident with the center of curvature of the ball. In this case the focus on the CCD is *also* coincident with the reference location. A misalignment of the focus from the center of curvature is evident from a translation or defocus of the spot at the CCD. The signal of the CCD is analogous to a spot diagram in an optical model with the origin set by the reference signal and from which we can derive the relative phase across the incoming beam. Note that depth of focus is dependent on the f-number of the beam in object-space, $(f/\#)$, where,

$$\pm 2.44\lambda(f/\#)^2 = \text{DOF range}, \tag{1.1}$$

and by the Rayleigh criterion the transverse spot resolution is,

$$1.22\lambda(f/\#) = \text{transverse resolution}. \tag{1.2}$$

Typical f-number values are not ≤ 0.5 so generally the transverse resolution is less than the DOF range. Small defocus errors do not disturb the ability to evaluate the centroid of the spot on the CCD. Additionally, Rayleigh transverse resolution criterion assumes imaging two points. However, measuring movement of a single spot by its centroid location on a PSD may be done at a higher precision. Thus, autoreflection alignment instruments such as the PSM are typically used for measuring the orientation or centration of flat or curved optical surfaces.

To align several surfaces with distinct center of curvature locations the autoreflecting instrument must change the conjugate focus position to achieve autoreflection from the other surfaces. This is done by either moving the entire instrument and its focal point or moving the objective lens to focus the light at a different conjugate[1, 11]. In either case the motion must be controlled such that the conjugate positions before and after the motion are known within the desired alignment uncertainty. Some of the measurements contributing to this research have a PSM mounted on a CMM so that the translation of the instrument is measured in 3D [11]. The typical application of an autoreflecting alignment telescope involves focusing the instrument at the center of curvature of different surfaces in sequence to co-align the surfaces of a lens system[1]. In either case the mechanical precision of the motion is correlated with the precision of the relative alignments.

The instrument motion and its corresponding error can be eliminated if the foci for the reference and alignment beams are on a common plane. There are two interesting examples of such a situation which we will explore in this section, both of which exploit CGH technology. Instead of using an autocollimating instrument these

methods have an external and fixed source of illumination, a reference CGH, and a set of optics under alignment[5, 6]. The beams are observed as a set of foci which may be observed with a camera or visual instrument across a common conjugate plane.

Burge *et al.* propose the use of a multiplexed CGH for lens alignment[6]. A schematic of this alignment scheme is provided in Figure 1.5. There is a reference CGH which produces several wavefronts, a set of intermediary optics under alignment and a PSD which observes the transmitted beams. One pattern on the CGH provides a reference focus at the PSD which depends on the orientation of the input beam and location of the CGH and PSD. When the first lens is inserted at an axial location the reference beam is blurred and a second pattern on the CGH generates a wavefront which focuses on the PSD. The lens is translated to move the focus so it matches where the reference focus was on the PSD. The second and third lenses are then inserted and a similar procedure is followed so that they focus light from their respective reference CGH patterns onto the PSD at the reference focus location. In this way the centration of a set of lenses may be constrained by phase-referencing with a simple camera and a reference CGH.

Coyle *et al.* modified this method to create an alignment scheme for large mirrors with CGH center references [5]. This method was introduced above and shown in conceptual form in Figure 1.4. In their method there are one or more CGHs under alignment relative to a reference “CGH A”. Each CGH is in fact a reference for the position of a large mirror to which the CGH has already been aligned. In this way alignment of the CGHs also aligns the mirrors. A first-order layout for the alignment

scheme is shown in Figure 1.13. CGH A is illuminated with an autocollimator so that the illuminating beam can be aligned normal to the planar CGH substrate. Each CGH substrate serves as a tilt alignment reference, so one part of the alignment is making sure the autocollimator beam is normal to each reference. This is done by interchanging the CGHs to measure their tilts individually while adjusting each mirror.

Once the mirror tilts are aligned the decenter scheme is exercised, where the multiplexed CGH A produces two reference foci: one near CGH A and one at a distant plane where it serves as a reference spot viewed by a video microscope. The other CGHs under alignment have a single pattern which focuses an alignment beam from the near spot of CGH A at the object plane of the video microscope. Similar to the lens alignment method proposed by Burge[6], the alignment beam focus translates in the object plane of the video microscope as a function of the centration alignment of CGH B. CGH B is positioned such that the alignment beam focus is coincident with the location of the reference focus. As stated by Coyle, the focus deviation ε from a decenter Δs of CGH B is,

$$\varepsilon = \Delta s(1 - m_B)\,, \tag{1.3}$$

where m_B is the transverse magnification between the near spot from CGH A and the object plane of the microscope[5].

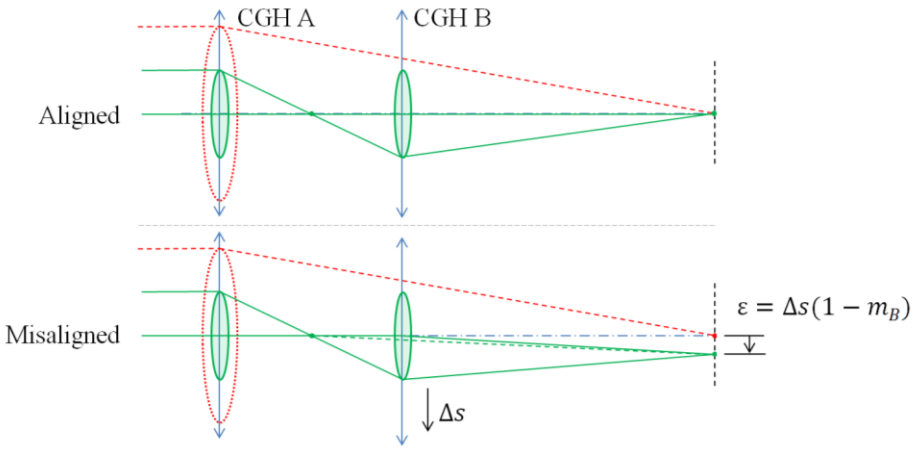

Figure 1.13: Decenter alignment error of CGH B becomes a focus translation at the detector [5].

The multiple CGH alignment demonstrated by Coyle was implemented to align the Hobby-Eberly Telescope Wide Field Corrector (HET WFC)[15]. The expected uncertainty contributions from the CGH alignment scheme to centration alignment in the HET WFC are $< 3\mu m$ for all the mirrors. This performance expectation highlights the strength of phase-referencing in alignment. A centration alignment of the mirrors by imaging patterns at each mirror or by coordinate measurement would have a much higher random uncertainty. A detailed presentation of the HET WFC alignment design implementation is given in Chapter 4.

Another important area of optical alignment is the alignment of surface and system tests. Misaligned optical testing equipment can easily result in the fabrication of inaccurate optical surfaces, acceptance of misaligned systems, or conflicting results between diagnostics which should be consistent. In many cases a CGH alignment involves relatively few optics. The interferometer, test CGH and optic under test may be the only optics involved. In such cases it is common to use an alignment pattern on

the CGH to align it to the interferometer and move the optic under test to find the position which eliminates tilt and coma aberrations[6]. There are other cases which preclude a simple alignment and benefit from other specialized methods of alignment[4].

No less than 7 different CGH null tests were also used to achieve and verify the HET WFC system alignment. Each test is an example of a CGH used for alignment by producing a reference wavefront. These phase-referencing alignment configurations will be presented in Chapter 4 to show how the HET alignment was accomplished by a combination of CGH alignment methods.

Another possibility exists for alignment of an optic under test to the test wavefront. A reference wavefront may be produced through sub-apertures on the test CGH to accommodate a set of alignment features *at the test optic*. Such features will be referred to as "phase fiducials" because they are positioned in registered locations across the test optic and exploited for alignment by phase-referencing. These features may be polished into the surface or attached, but their shape is distinct from the test optic. A demonstration of these kinds of alignment features has been made by Scheiding *et al.*[10]. This demonstration had a set of four features diamond-turned at the periphery of a diamond-turned test optic. In this dissertation the phase fiducials are fabricated and demonstrated as very shallow polished spherical pockets *within* the clear aperture of a *glass* calibration optic. Figure 1.14 shows a picture of a phase fiducial made on an optical flat. When the CGH wavefront projection is appropriately aligned to the calibration optic a null can be achieved from the surface under test *and*

the phase fiducials. The condition where interference from *all* the optical surfaces is devoid of alignment-dependent aberration indicates alignment of the CGH wavefront.

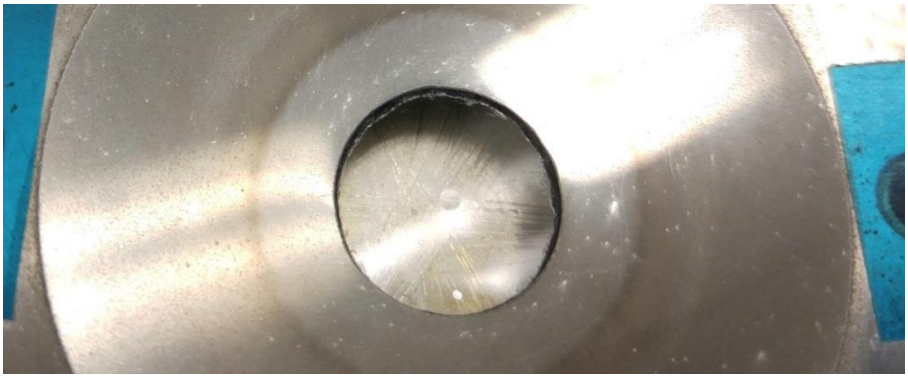

Figure 1.14: Phase fiducial on an optical flat surrounded by fabrication guide ring. Radius = 80 mm, CC and Ø = 2 mm

The phase fiducials are added to provide a higher alignment sensitivity than the test optic would and improve the accuracy of alignment for the optical test system. With an extremely slow phase fiducial like the one pictured in Figure 1.14 it is still possible to achieve a high alignment sensitivity, specifically 13μm/wave at 632.8nm. With an interferometer OPD measurement precision of $\pm\lambda/10$ this translates to ±1.3μm alignment precision.

1.3 DISSERTATION OVERVIEW

Several alignment methods are presented in this dissertation through a presentation of their applications, design and analysis, and experimental demonstration. The applications include two contracted projects: the HET WFC and the TAO secondary mirror. The prescriptions for the HET WFC and the

interferometer test of the TAO secondary mirror are provided in Chapter 2. A set of three interferometer tests designed as case studies for simulation and analysis are also described in Chapter 2. The parametric design and performance prediction for CGH co-alignment is given in Chapter 3. The design and analysis of phase fiducial alignments is also given in Chapter 3. Chapter 4 provides a substantial description of the HET WFC alignment implementation methods and results. Chapter 5 shows how a set of phase fiducials were made and demonstrates their performance in a bench test interferometer. Chapter 6 notes the important conclusions that have been drawn from this body of research.

CHAPTER 2

APPLICATIONS

A discussion of optical alignment is not complete without clearly described applications for the methodologies. The alignment methods presented by design and analysis in Chapter 3 are applied to the systems defined in this chapter. The Hobby Eberly Telescope Wide Field Corrector (HET WFC)[4], a surface test for the Tokyo Atacama Observatory secondary mirror (TAO SM)[16], and a set of contrived test configurations are described thoroughly below for reference in the discussion of alignment designs and demonstrations.

2.1 HET WIDE FIELD CORRECTOR

The Hobby Eberly Telescope Wide Field Corrector (HET WFC) is a 4-mirror prime focus corrector[4]. The corrector is shown pictorially in Figure 2.1. The Hobby Eberly Telescope has an 11-m segmented primary mirror which a highly aberrated prime-focus. The WFC is an upgrade to HET which will expand the field of view to a 22 arcmin FFOV with 80% encircled energy within 0.45 arcsec for a 5 arcmin of field and 0.8 arcsec at 11 arcmin of field[4]. Each mirror is aspheric and two of the mirrors are high-order aspheres. The optical design and alignment requirements of this system will be described in the sub-sections that follow. It is shown that the alignment of this system requires advanced methods and the methodology behind the alignment plan will be introduced.

Figure 2.1: HET WFC in assembly and testing mount with interferometer mounted in tower above system.

2.1.1 System design

The as-built surface specifications for the HET WFC mirrors are given in Table 2.1. The positions of the mirrors and other surfaces in the HET system design are given relative to the paraxial focus of the primary mirror in Table 2.2. An optical layout of the system is also provided in Figure 2.2. The radii of curvature, aspheric terms and Z-positions are all given under a self-consistent sign convention. Within this sign convention the Z-sag of a mirror surface is given by,

$$Z(r) = \frac{r^2/R}{1+\sqrt{1-(K+1)\frac{r^2}{R^2}}} + \alpha_3 r^6 + \alpha_4 r^8 + \alpha_5 r^{10}, \qquad (2.1)$$

where r is the transverse radial coordinate with units of mm, R and K are the radius of curvature and conic constant given in Table 2.1, and α_3, α_4, and α_5 are the high-order aspheric terms with inverse distance units also given in Table 2.1. All of the mirrors have a central hole. M4 is the only convex mirror, and it is also much smaller

than the 1-m class M2, M3 and M5 mirrors. M3 has the most severe aspheric departure of any of the mirrors with a 1.2 mm P-V aspheric surface departure. M5 is extraordinarily fast with F/0.4 paraxial f-number. These data are useful to understand the scale and level of aspheric departure associated with the system under alignment. Additionally, these as-built values represent the best measurements of the individual surfaces with which the alignment and system test data are concerned. A more complete description of the system design, specifications and performance may be found in the proceedings paper by Burge *et al.* and other related publications[4].

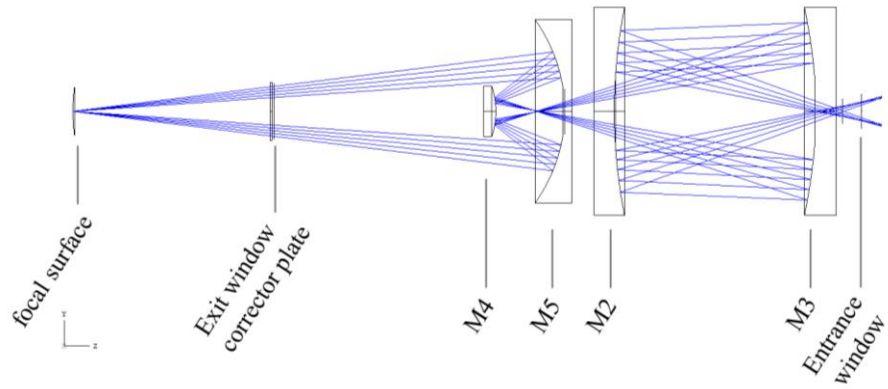

Figure 2.2: Optical layout of the HET WFC tracing from the center of its field of view.

Table 2.1: HET WFC as-built mirror surface prescriptions.

	M2	**M3**	**M4**	**M5**
Diameter (mm)	1020.32	1020.37	247.9	900.18
Radius of curvature R (mm)	2620.719	-2032.675	-376.604	-742.343
Conic Constant K	0.6628	-7.7137	-2.09847	-0.2672
α_3 (mm^{-5})	-	8.2493E-17	-	-1.5875E-19
α_4 (mm^{-7})	-	-8.4345E-23	-	-6.4401E-26
α_5 (mm^{-9})	-	3.8661E-29	-	-
CA OD (mm)	960	980	244	880
CA ID (mm)	326	325	30	260

Table 2.2: HET WFC final design surface positions.

Surface	**Z (mm)**
Primary Mirror vertex	13081.960
Paraxial focus	0.000
Entrance window, S1	285.048
Entrance window, S2	283.048
M2 vertex	-925.759
M3 vertex	61.466
M4 vertex	-1505.881
M5 vertex	-1168.496
Exit pupil	-2591.152
Exit window/corrector plate, S1	-2601.152
Exit window/corrector plate, S2	-2611.152
Focal surface	-3575.522

2.1.2 Alignment requirements

Alignment errors dominate the error budget for the HET WFC system. The error contribution from alignment is given relative to the other error contribution by Burge *et al.*[4]. The error tree from this publication is given in Figure 2.3 to show the significant portion of the budget allocated to alignment errors. Table 2.3 shows the alignment tolerances associated with the simulated error contributions. The largest tolerances refer to axial spacing and allow only 100μm error between the M2-M3 and M2-M5 mirror pairs. The tightest tolerances are those concerned with the centration and axial spacing of M4 relative to M5. These tolerances allow only a 20μm error per axis of translation. The alignment precision and accuracy required to meet these tolerances is state of the art and represents the threshold of what is currently possible. The next section will define the alignment system required for this alignment to

provide the appropriate background for a presentation its implementation on the HET WFC.

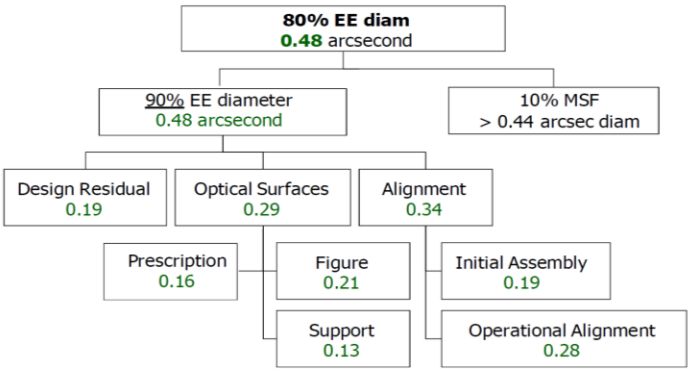

Figure 2.3: Error contributions to the HET WFC 80% encircled energy (EE) requirement evaluated at 5.4 arcmin of field. There is a dominant contribution from alignment errors. [4, Figure 4]

Table 2.3: Alignment tolerances for the HET WFC mirrors [4].

Degree of Freedom	**Tolerance**	**Unit**
M2 to M3 axial	100	µm
M2 to M5 axial	100	µm
M4 to M5 axial	20	µm
M2 decenter (x or y)	50	µm
M3 decenter (x or y)	50	µm
M4 decenter (x or y)	20	µm
M4 M5 decenter (x or y)	50	µm
M2 tilt (x or y)	49	µrad
M3 tilt (x or y)	49	µrad
M4 tilt (x or y)	81	µrad
M4 M5 tilt (x or y)	56	µrad

2.1.3 Alignment methodology

The alignment methodology associated with the WFC alignment tolerances was designed and analyzed by Coyle *et al.*[5, 17]. The method relies on a set of CGH references which are aligned to each mirror within “center reference fixtures”. Figure

2.4 provides a conceptual layout of the center reference fixtures installed in each mirror. The method accomplishes an alignment of the mirror surfaces by co-alignment of their CGH references. The co-alignment of the CGHs follows the scheme described in Chapter 1. One of the mirrors, M4 in this case, carries a CGH which generates two foci. This CGH defines an alignment axis. The other CGH references must be centered on this axis to achieve a co-alignment in centration. The illuminating beam is *also* an autocollimator, so the CGH substrates can serve as tilt references. The references are exchanged and a co-alignment is achieved for tilt and centration.

The first section of Chapter 3 will provide a first-order parametric description of the HET WFC alignment system. The CGH separations within the assembled WFC will be applied to the parametric model in order to predict the performance of this method. It will be shown that the method is suitable to meet the WFC alignment tolerances under a set of important assumptions. Chapter 4 will show the results of implementing the alignment and address the breakdown of some of the assumptions which are important to the alignment.

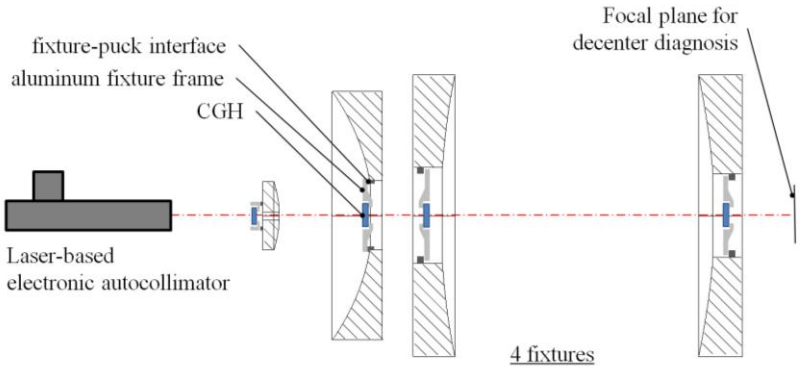

Figure 2.4: Conceptual layout of the CGH center reference fixtures within the 4 mirrors of the WFC.

2.2 TAO SECONDARY MIRROR TEST

The Tokyo Atacama Observatory secondary mirror (TAO SM) is a 0.9m convex hyperboloid[16]. A test was devised to measure this mirror within 6 sub-apertures evenly spaced along an inner circle and 12 sub-apertures evenly spaced along an outer circle. a map of the measured regions across the secondary mirror aperture is given in Figure 2.5 and a photograph of the interferometer test is given in Figure 2.6. The interferometer is a CGH-corrected Fizeau interferometer which has both a spherical reference surface and a CGH which accommodates the plane-symmetric aspheric sub-apertures. This section will describe the design of the interferometer, its sensitivity to CGH projection misalignment, and the current projection alignment methodology. Chapter 3 and Chapter 5 will present an alternative approach for aligning this type of interferometer which will be compared to the alignment method described in this chapter.

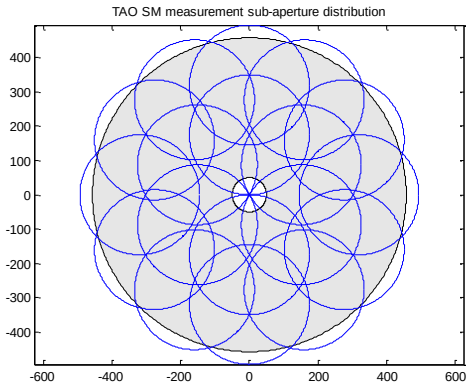

Figure 2.5: Measured sub-aperture distribution across the TAO SM clear aperture. Lateral units are mm.

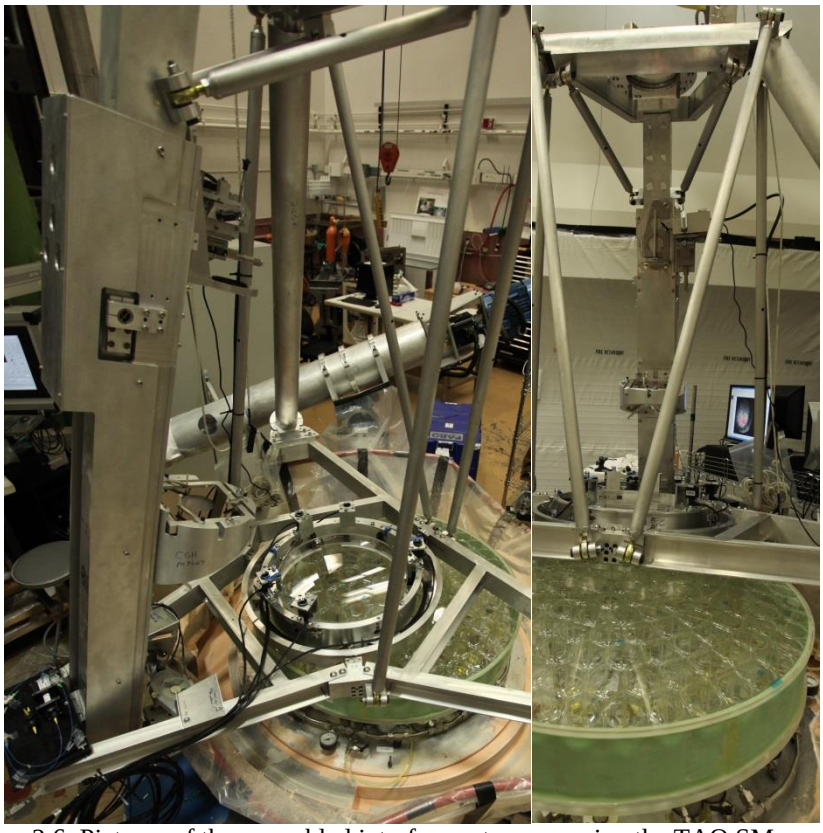

Figure 2.6: Pictures of the assembled interferometer measuring the TAO SM.

2.2.1 Surface test design

The TAO SM interferometer is a CGH-corrected Fizeau interferometer. The Fizeau cavity is composed of a spherical reference surface and a plane-symmetric sub-aperture of the mirror under test. The interferometer also has a CGH which is conjugate to the test surface and which provides correction for the plane-symmetric aspheric departure in the Fizeau cavity. The design of such an interferometer is described for its application in testing mirror segments by Burge *et al.*[7]. The TAO SM interferometer is shown in unfolded conceptual form in Figure 2.7. A labeled diagram of the actual system layout is given in Figure 2.8.

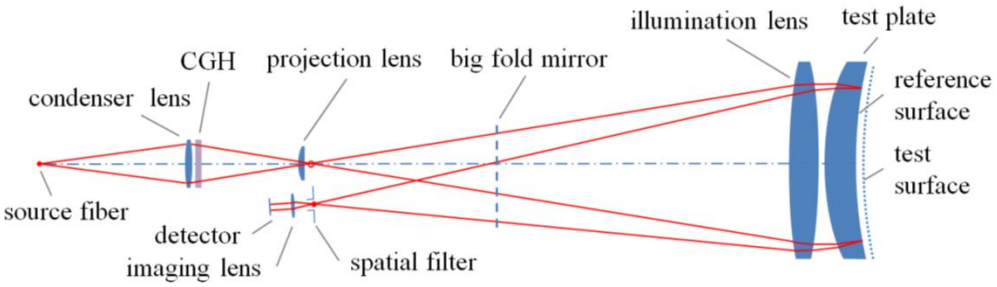

Figure 2.7: Conceptual layout of the TAO SM interferometer

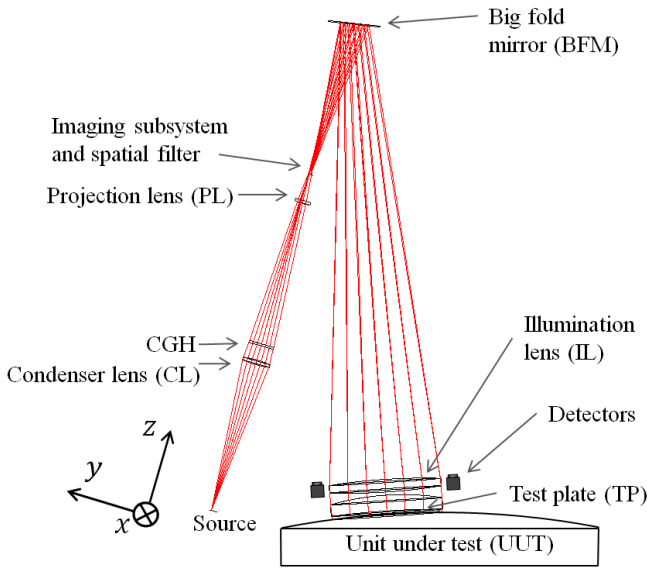

Figure 2.8: Layout from final TAO SM design with folded optical path. The imaging subsystem is located out-of-plane (+X in object/source coordinates) and outside the incident beam, similar to the conceptual layout. This diagram illustrates testing an inner sub-aperture.

The optical element materials, as-built curvatures, thicknesses and clear aperture diameters are given in Table 2.4. The nominal specifications for the TAO SM, also referred to as the UUT, are given in Table 2.6. The air gaps between the optical elements in the interferometer test are given in Table 2.5. These air gaps were derived directly from the thicknesses between surfaces in the optical model. The coordinates which define where a sub-aperture is on the UUT are defined in Figure 2.9, and the coordinates of the sub-apertures under test are given in Table 2.7. Table

2.8 lists values for the source fibers' wavelength, and coordinates, the spatial filter location, definition of the stop surface, and orientation of the optics integral to the Fizeau cavity.

Table 2.4: TAO SM interferometer element prescriptions.

Interferometer element	**R1 (mm)**	**R2 (mm)**	**ct (mm)**	**CA OD (mm)**	**Substrate Material**
synthetic extended source (SES) plates	∞	∞	25.4	64	BK7
condenser lens (CL)	300.605	-300.453	15.044	92	n_d = 1.517110 V_d = 64.14
CGH	∞	∞	6.392	80.7	Fused Silica
projection lens (PL)	174.52	∞	9.988	49.5	Fused Silica
big fold mirror (BFM)	∞	-	38	168	Fused Quartz (mirror)
illumination lens (IL)	1915.7	-1919.3	40.273	360	Fused Silica
test plate (TP)	832.93	2712.87	49.759	360	Fused Silica
spatial filter	-	-	-	2.4	-

Table 2.5: Air gaps between optical elements in the TAO SM interferometer.

Surfaces	*Air gap (mm)*
source-SES	292.000
SES -CL front	266.663
CL back - CGH front	46.892
CGH back - PL front	464.000
PL back - IL front	2034.943
IL back - TP front	10.000
TP back - UUT	10.000
IL front - spatial filter	1950.000

Table 2.6: TAO SM (UUT) specifications.

R (mm)	2657
Conic constant K	-1.58331
CA ID (mm)	100
CA OD (mm)	896

Table 2.7: Sub-aperture testing locations and diameters.

sub-aperture diameters (mm)	350
inner DecY (mm)	-175.019
inner vertex sag (mm)	-5.149
inner Rx (deg)	+3.7635
outer DecY (mm)	-320.075
outer vertex sag (mm)	-17.931
outer Rx (deg)	+6.8388

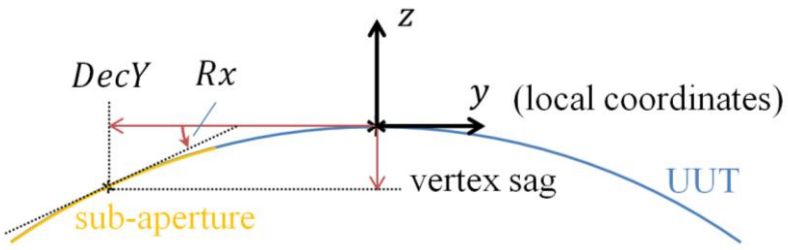

Figure 2.9: Definition of sub-aperture test location coordinates relative to UUT vertex. Sub-aperture locations given in terms of the UUT surface local coordinates.

Table 2.8: Definitions of various parameters of the TAO SM interferometer design. The tilts are imposed and reversed with coordinate breaks before and after the corresponding group of optics. All values of X, Y, Rx and Ry are relative to local surface coordinates

Design Parameter	*Value*
test wavelength	632.8 nm
source coordinates (test beam)	-8.25 mm(X), +6 mm(Y)
source coordinates (reference beam)	-11.75 mm(X), +6 mm(Y)
spatial filter off-axis distance	+50 mm(X)
stop surface	TP back (second pass)
stop diameter	350 mm
IL, TP & UUT , tilt about front of IL	+0.0776 deg(Rx), +0.7516 deg(Ry)
UUT, tilt about sub-aperture center	-0.1934 deg(Rx), -0.0459 deg(Ry)

There are several interesting aspects to the design of this interferometer which are notable. There are two fiber-coupled sources of light which output opposite-handed circular polarizations. Both fibers are coupled to a common HeNe laser source operating at 632.8nm. The sources are separated spatially and both are off-axis. The interference of light from one source reflected from the reference surface with light from the other source reflected from the test surface is measured with a 4-D sensor[18]. A 4-D sensor provides instantaneous 4-step phase shifting between beams of opposite-handed polarization with an array of linear polarizers across CCD pixels.

The CGH is also very interesting. It is multiplexed by superposition of two phase-etched patterns. The first pattern provides the appropriate aberration correction to focus the reference beam sharply at the spatial filter. The second pattern provides additional aberration correction to focus the test beam sharply at the spatial filter for a given sub-aperture surface figure on the TAO SM. The pattern which corrects aberration in the reference beam is called the "common" pattern because the interferometer is meant to use the +1-order of diffraction from this pattern in *both* beams. The other pattern is called the "measurement" pattern because it depends on the surface under measurement. The reference beam is used in the 0^{th}-order and the test beam in the +1-order of the measurement pattern.

Each pattern also has a tilt term added so that the diffracted orders are spatially separated at the spatial filter. In particular, the tilt terms are *crossed* so that diffracted orders from the common pattern are spatially separated in a direction orthogonal from the diffracted orders produced by the measurement pattern. Thus, each source creates a grid of diffracted orders which must be appropriately aligned to

the spatial filter after reflection from the correct surface in the Fizeau cavity. Figure 2.10 shows a footprint diagram of light from the two sources reflected from both surfaces in the Fizeau cavity. The tilt of the illumination lens and test plate is adjusted together to direct the desired diffracted beam from the reference surface to center of the spatial filter. Similarly, the UUT is tilted relative to the test plate to direct the desired diffracted beam from the test surface source location through the spatial filter.

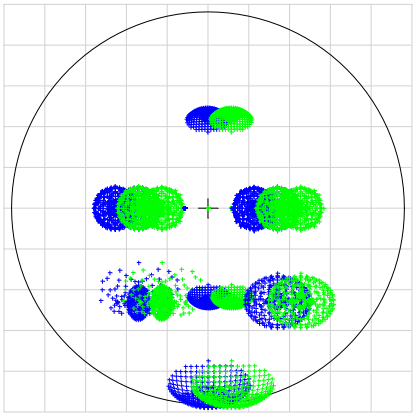

Figure 2.10: Ray footprints from nearest diffracted orders to center of spatial filter with TAO SM interferometer aligned to an inner sub-aperture of the TAO SM. The rays are colored differently for the two sources. Full scale: 54 mm

The synthetic extended source uses two spinning wedges after the source fibers to move both sources' effective locations. The wedges spin at different speeds and have different wedge angles to move the sources in *two* rings at different speeds and with different angular deviations. This synthetic extended source was analyzed and presented as a practical implementation by Morel and shown to be effective at reducing coherent noise in an interferometer test[19].

The TAO SM interferometer measurements are stitched together to find the full-aperture surface departure map for the TAO secondary mirror. The performance

of the interferometer has negligible design residual due to the precise exploitation of CGH design with high-order phase surfaces. This condition of nearly perfect performance is subject to significant degradation due to optical element figure and refractive index errors, coherent artifacts, and alignment errors. The optical elements were designed with spherical and relatively slow surfaces to help achieve appropriately small uncertainty of their as-built prescriptions. All of the lenses are nearly common-path with the exception of the projection lens and the reference surface. Both of these optics were independently tested with interferometer tests to verify their accuracy in transmission and reflection, respectively. This leaves alignment as the remaining major concern to address.

2.2.2 Sensitivity to projection misalignment

Each optical element in the TAO SM design was perturbed in every degree of freedom to find the alignment sensitivities of the design. A set of compensators were also used to make realistic compensations to predict the performance of the real system after assembly in the presence of each misalignment. The most major offender in the alignment error budget is related to the alignment of the projection of the CGH to the test surface. The CGH accommodates aspheric departure in the Fizeau cavity at a given sub-aperture, but it is remote from the Fizeau cavity. Thus, a projection lens is used to bring the CGH phase influence into alignment with the test surface. The projection of the CGH is most sensitive to misalignment of the projection lens and big fold mirror relative to the CGH and test plate cell.

Aberrations induced by the projection lens in the interfering beams have to be compensated or they create measurement errors. The projection must also have the appropriate magnification and alignment in clocking and transverse location. A misalignment of the projection with the test surface generates measurement errors that scale with the slope of the aspheric departure. The big fold mirror is adjusted to align the transverse location of the projection and it is also translated to set the optical path length to achieve the correct magnification. Thus, a tilt of the beams caused by the projection lens can be compensated to first-order with the fold mirror, but higher order aberrations persist. The alignment accuracy of the big fold mirror is limited primarily by the ability to determine where the projection *is* relative to the test surface.

The astigmatism, coma and spherical aberration errors from the dominant projection alignment tolerances within the inner and outer sub-apertures of the test are given in Table 2.9 and Table 2.10. The CGH projection alignment tolerances represent two degrees of translation and one degree of rotation about the center of the test aperture relative to the test surface sub-aperture. The resulting aberrations are interesting because they can cause low-order errors in the full aperture stitched departure map. It is clear that with these tolerances the alignment of the projection in Y is critical to keep Z6 and Z8 coefficients sufficiently low. Axial misalignment of the projection lens ("CGH-PL *Z*") is the largest contributor to spherical aberration coefficient Z11 which is part of the motivation to keep a tight tolerance on this degree of freedom.

Table 2.9: Aberrations in the inner test of the TAO SM due to CGH projection alignment errors.

Inner test aperture			OPD Zernike Standard terms (noll ordering)				
Alignment	Tolerance	Units	Z5(nm)	Z6(nm)	Z7(nm)	Z8(nm)	Z11(nm)
PL DecX	0.100	mm	2.9	0.1	0.1	1.0	0.0
PL DecY	0.100	mm	0.0	0.0	0.1	0.0	0.3
CGH-PL Z	0.025	mm	0.0	1.7	1.1	0.0	0.5
CGH projection Dec X	0.150	mm	26.6	0.2	0.0	6.6	0.0
CGH projection Dec Y	0.150	mm	0.2	27.2	7.1	0.2	0.2
CGH projection Rz	0.0098	deg	5.4	0.0	0.0	1.5	0.0
		RSS	27.3	27.3	7.1	6.8	0.6

Table 2.10: Aberrations in the outer test of the TAO SM due to CGH projection alignment errors.

Outer test aperture			OPD Zernike Standard terms (noll ordering)				
Alignment	Tolerance	Units	Z5 (nm)	Z6(nm)	Z7(nm)	Z8(nm)	Z11(nm)
PL DecX	0.100	mm	10.3	0.3	0.2	1.4	0.0
PL DecY	0.100	mm	0.0	0.0	0.4	0.0	0.3
CGH-PL Z	0.025	mm	0.0	4.6	1.6	0.0	0.1
CGH projection Dec X	0.150	mm	46.3	0.0	0.0	6.8	0.0
CGH projection Dec Y	0.150	mm	0.2	48.5	8.1	0.4	0.4
CGH projection Rz	0.0098	deg	17.6	0.0	0.0	2.7	0.0
		RSS	50.6	48.8	8.3	7.5	0.5

2.2.3 Alignment methodology

There are many steps involved in the complete alignment of the TAO SM interferometer, but this discussion will focus on the alignment of the CGH projection. Note that the projection lens must be aligned well to the CGH because the different diffracted beams pass through the projection lens (PL) at distinct locations making it *not* common-path. A footprint diagram which shows how the reference and test beams occupy the test aperture are given in Figure 2.11. This alignment was done to the given tolerances with an alignment telescope and coordinate measuring devices as

a sub-system alignment. The alignment of the projection *at* the test surface involves the use of several CGH alignment features, external illumination, and a set of detectors outside the test aperture. The steps taken to make this alignment will be described in this section.

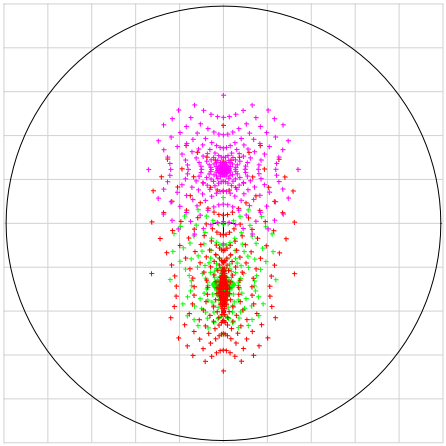

Figure 2.11: Ray footprint diagram at the projection lens showing the reference beam (pink), inner sub-aperture test beam (green), and outer sub-aperture test beam (red). Aperture diameter is 49.5 mm.

The projection alignment is done between subsystems of the interferometer. The alignment of the CGH projection is first performed relative to the reference surface. The CGH was made with a set of small circular apertures in the chrome mask outside the phase-etched test pattern. Within the optical model it is determined how light from an LED behind each small aperture is expected through an aligned projection lens and where the centroid of each spot should be near the test plate cell. There are CCD detectors connected to the test plate cell which holds the illumination lens and test plate. The spots from the apertures on the CGH illuminate these detectors so the detectors can provide information about the location of the CGH

projection. Figure 2.12 provides a conceptual image of the CGH projection alignment to the test plate cell. The detectors' pixels must be registered relative to the test plate cell axis of symmetry and reference surface height with a coordinate measuring machine in order to serve, collectively, as the datum for alignment of the CGH projection. The test plate cell is shown on the CMM in Figure 2.13 where the test plate (TP) and illumination lens (IL) are being registered to the detectors and to a set of nested 0.5" balls which serve as mechanical data for a laser tracker.

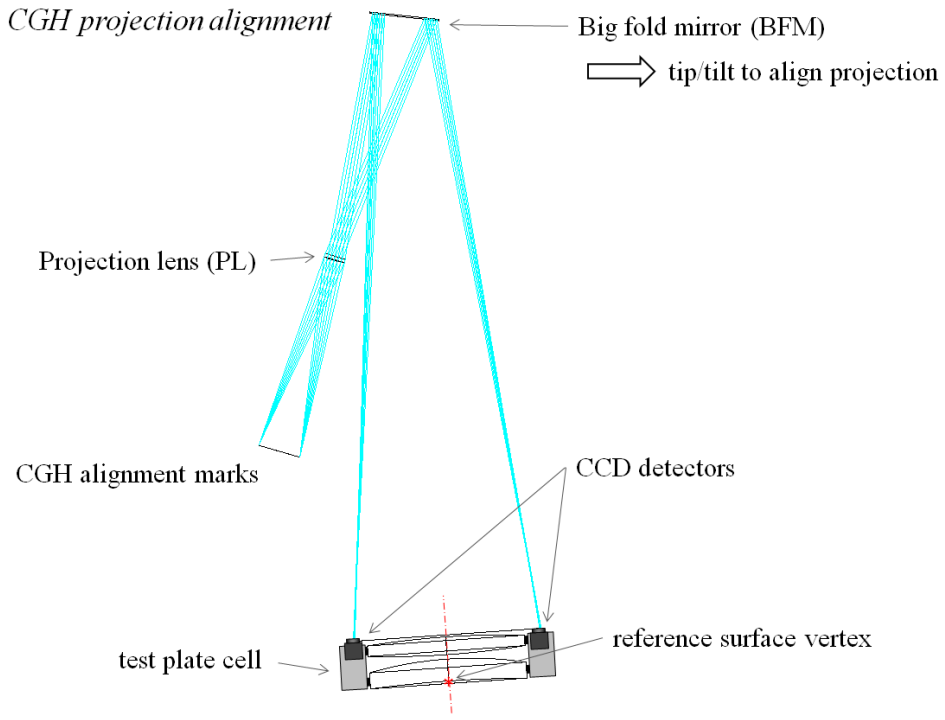

Figure 2.12: Conceptual diagram of the alignment of the CGH projection. Small holes in a chrome mask on the CGH are illuminated and imaged to datum detector pixel coordinates at the test plate cell. The detector pixels are registered to the test plate axis of symmetry and reference surface vertex.

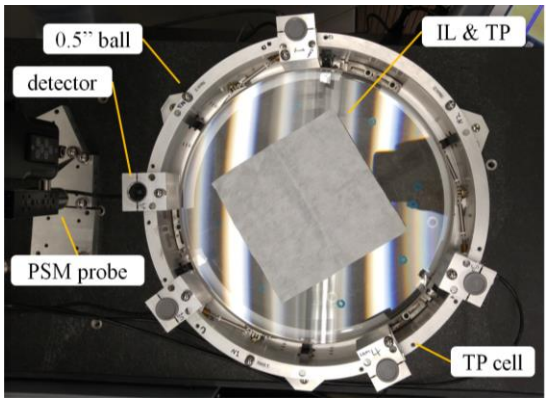

Figure 2.13: Registration of the detector pixels and 0.5" nested balls to the illumination lens (IL) and test plate (TP) with a point source microscope (PSM) on a CMM arm.

The centroid locations of the projected spots from the CGH were found within a common coordinate frame. These measured spot coordinates were compared to calculated spot coordinates. The alignment was performed to match the measured spot locations with the ideal locations in the local coordinates of the test surface. This alignment involved locating the UUT and test plate cell with a laser tracker so that the measured spot centroids could be related to the UUT local coordinates. Neglecting the alignment residual, the best-fit between the measured spot pattern and the calculated pattern is given in Table 2.11. Note that the RMS values for translation are 0.049 mm (X) and 0.041 (Y), so we can estimate that the transverse radius of the 95% confidence region for locating the projection is at least 0.09 mm. This captures random errors from measuring the relative locations of all the detectors' pixels as well as random errors from projecting and measuring the centroids. Irregularity of the illumination between the small apertures is very possible because each aperture has an independent LED source, but the error contributions from the detector acquisition are expected to be small. There is a 181 mm separation in height between the

detectors and the test surface, so there is also an extrapolation from the measurement location to the test surface. This fact is mentioned to point out that this is not a particularly direct diagnosis of the CGH projection at the test surface. The measurement scheme involves a complicated set of coordinate measurements and transformations to derive the projection alignment at the test surface.

Table 2.11: Discrepancies between measured spot centroid locations and expected centroid locations caused by irregularity of the measured pattern. Acknowledgement to Matt Dubin for alignment and measurement of this data.

	ε_X(mm)	ε_Y(mm)	ε_Z(mm)
CAM 1	-0.064	0.051	-0.189
CAM 2	0.004	0.036	0.269
CAM 3	-0.039	-0.015	0.102
CAM 4	0.021	-0.065	-0.265
CAM 5	0.078	-0.007	0.083
RMS	0.049	0.041	0.198

There are other alignment considerations which make the full treatment of this instrument quite subtle, but the particular issue of making a reliable measurement of the CGH projection relative to a mechanical datum is extremely important. The methodology used in the TAO SM alignment has been shown to be extrinsic, where the detection of alignment occurs on independent detectors which neglect any interaction with the optics in the test plate cell. In Chapter 3 this application will be used as a case study to show how a recently demonstrated alignment method may be useful for alignment of this type of interferometer.

2.3 DIRECT-TEST CGH-CORRECTED SURFACE TESTS

A set of three CGH-corrected surface tests were designed to use as simulated case studies in Chapter 3 of this dissertation. These designs are referred to as "direct-tests" in which the light propagates directly from the test CGH to the surface under test. In each case a commercial Fizeau interferometer illuminates the CGH with a collimated beam through a transmission flat. The cases vary by interferometer beam diameter, test surface diameter and test surface radius, but all of the test surfaces are F/3 paraboloids.

2.3.1 Surface test designs

The surface test designs fit two typical commercial interferometer beam diameters: 6" and 4" beams. There is additional space on each CGH substrate outside of the test pattern clear aperture and within the maximum extent of the beam which may be used for creating alignment patterns. The parameters defining each model and the corresponding optical layouts are given in Table 2.12 – Table 2.14 and Figure 2.14 – Figure 2.16. All of the models are axisymmetric. The CGH is designed to achieve nearly perfect retro-reflection from the paraboloid surfaces. The test surface is not intended to represent a meaningful application but rather serves as a place holder in an optical test with the given aspect ratio. The alignment methods applied to these tests are also applicable in more interesting tests of off-axis and free-form optics.

Table 2.12: Design parameters for the Model #1 axisymmetric test of a 4" convex F/3 paraboloid.

Model #1 parameter	
test wavelength	632.8 nm
CGH test pattern OD	108 mm
CGH substrate thickness	6.35 mm
CGH substrate material	Fused silica
CGH-UUT separation	10.345 mm
UUT radius	304.8 mm,CX
UUT conic constant	-1
UUT CA OD	101.6 mm

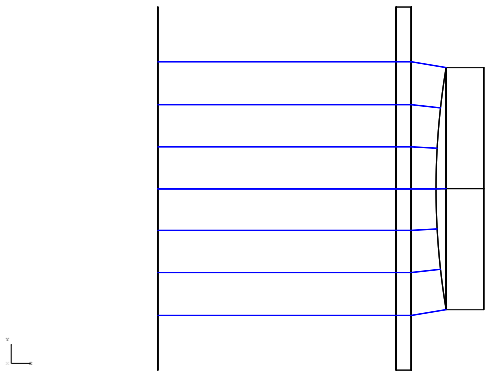

Figure 2.14: Optical layout of Model #1 direct-test.

Table 2.13: Design parameters for the Model #2 axisymmetric test of a 4" concave F/3 paraboloid.

Model #2 parameter	
test wavelength	632.8 nm
CGH test pattern OD	85 mm
CGH substrate thickness	6.35 mm
CGH substrate material	Fused silica
CGH-UUT separation	56 mm
UUT radius	-304.8 mm,CC
UUT conic constant	-1
UUT CA OD	101.6 mm

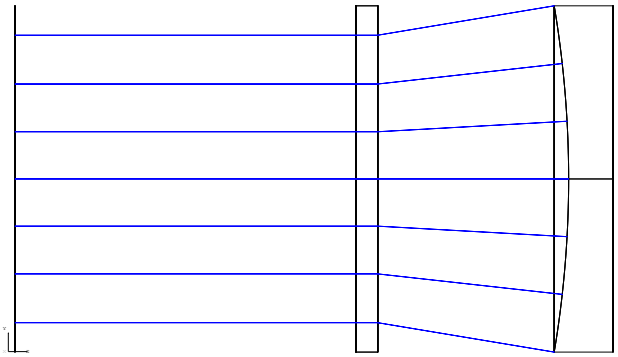

Figure 2.15: Optical layout of Model #2 direct-test.

Table 2.14: Design parameters for the Model #3 axisymmetric test of a 7.5" concave F/3 paraboloid.

Model #2 parameter	
test wavelength	632.8 nm
CGH test pattern OD	85 mm
CGH substrate thickness	6.35 mm
CGH substrate material	Fused silica
CGH-UUT separation	326.3 mm
UUT radius	-571.5 mm,CC
UUT conic constant	-1
UUT CA OD	190.5 mm

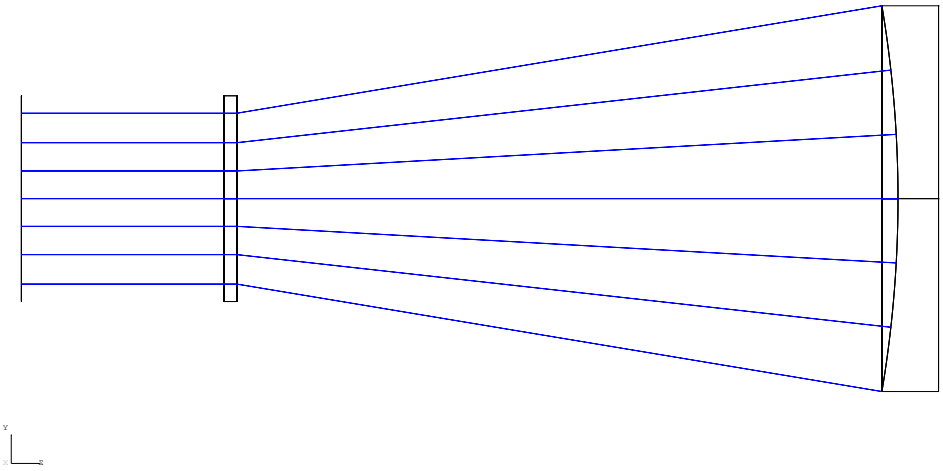

Figure 2.16: Optical layout of Model #3 direct-test.

2.3.2 Alignment methodology

In tests such as these it is common to align the test surface by wavefront reference to the test beam. Alignment-dependent aberrations like tilt and coma are often compensated by aligning the test surface to get the lowest possible RMS optical path difference from these aberrations. This approach neglects any registration of the test beam phase reference to an independently measureable optical or mechanical datum. This dissertation will present an approach for conducting these tests with alignment features on the UUT. It will be shown in Chapter 3 that these features are useful to obtain a measurement of the test beam with high-precision from a datum which is independent of the test surface.

CHAPTER 3

DESIGN AND ANALYSIS OF PHASE-REFERENCING SYSTEM ALIGNMENTS

In this chapter a CGH co-alignment and phase fiducial interferometer test alignments are analyzed parametrically. The performance metrics for each alignment technique are defined in terms of design parameters and constraints. Generally the constraints are particular to the application. The applications described in Chapter 2 provide case studies for each type of alignment. Each of the case studies is evaluated with the parametric expressions and in each case the limitations and constraints are demonstrated.

3.1 CGH CO-ALIGNMENT

3.1.1 Introduction

The co-alignment of CGHs is an interesting way to use CGHs as an alignment datum *and* as phase reference features. In this parametric description of a CGH co-alignment, originally presented by Coyle *et al.*, each CGH is a reference for the alignment of a mirror to which it is attached[5]. The co-alignment method is effective for the alignment of tilt and centration of each CGH and its corresponding mirror. Tilt is measured with an autocollimator and reflection of the 0-order from the CGHs. Centration is measured by observing beam focus deviations with a camera. This technique exploits kinematic interfaces so that the CGH references may be mounted and removed with a repeatable registration to the mirrors under alignment.

The tilt alignment does not exploit the CGH pattern design. The CGH is also nominally a plane parallel plate, so an autocollimator can readily measure the angle of each CGH substrate from the 0-order reflected beam. This is effectively a flat phase reference, but only in a rather trivial sense. However, the use of a CGH *does* allow the creation of a diffractive lens and a flat tilt reference at the same surface with a consistent registration to a mirror. This design freedom represents one of the valuable aspects of CGHs in optical alignment.

The centration alignment scheme for CGH co-alignment use a multi-focal spatially multiplexed datum CGH reference (CGH A) and one or more other CGH references (CGH B, CGH C, etc.) which are aligned to the datum CGH. There are two configurations of this alignment scheme for each CGH under alignment to the datum: CGH A focus at the image plane and CGH A + CGH B focus at the image plane. All of the CGH patterns are Fresnel zone plates (FZPs).

3.1.2 First-order model

A diagram of the first-order CGH co-alignment model is given in Figure 3.1:

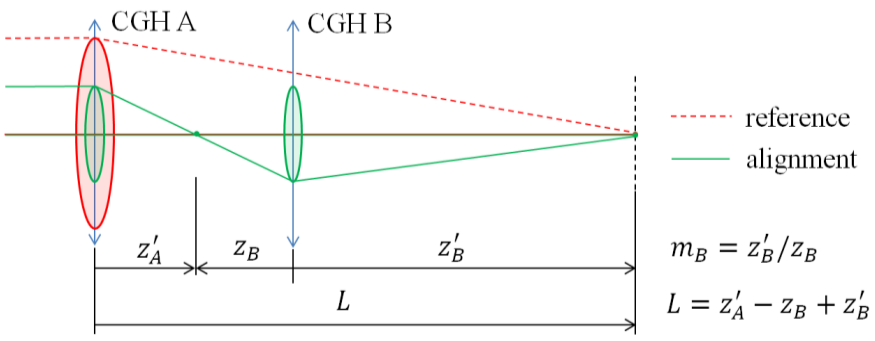

Figure 3.1: First order model of the CGH co-alignment system[5].

In the reference configuration CGH A acts as a thin lens with focal length *L* to focus the collimated illumination at the image plane. In the alignment configuration CGH A has focal length z_A' to focus the beam creating an intermediate image in front of CGH B. These two foci define the alignment axis which is dependent on the location of CGH A and the angle of the illuminating beam. CGH B is designed with the appropriate focal length to image the spot at the image plane a distance *L* from CGH A. The imaging conjugates are labeled in the diagram. The transverse magnification factor between the foci through CGH B is called m_B. This factor is given in the diagram for reference in the analysis. In both configurations the illuminating beam is focused at a common plane, but the transverse spot location for the alignment configuration is dependent on the position of CGH B. The reference spot location is recorded prior to alignment of CGH B to make alignment and reference foci coincident. The next subsection will analyze the sensitivity of this model to misalignments through a series of perturbed cases.

3.1.3 Sensitivity and dynamic range

Figure 3.2 provides a diagram of the foci from CGH A. The axis defined by the foci is rotated about the center of CGH A as a function of the angle of the collimated illuminating beam. The transverse deviations of the near and far foci caused by changes in beam angle are given by,

$$\Delta_{far} = L * \tan(\Delta\theta), \tag{3.1}$$

where $\Delta\theta$ is the beam deviation angle and,

$$\Delta_{near} = z'_A * \tan(\Delta\theta), \tag{3.2}$$

where z'_A is the distance from CGH A to the near focus.

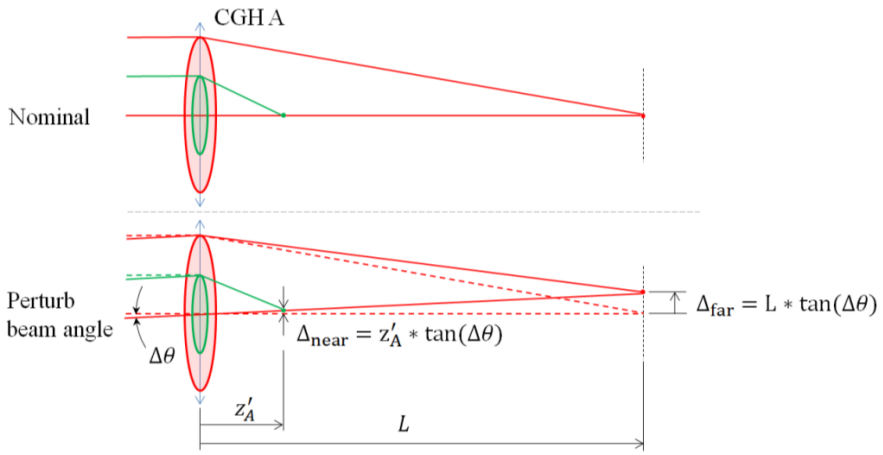

Figure 3.2: CGH A focus at the image plane providing reference point for alignment. Misalignment of collimated illuminating beam angle causes deviations in the near and far reference foci from inner and outer CGH zones.

The alignment configuration is shown with CGH B on and off the datum alignment axis from CGH A in Figure 3.3. When CGH B is centered on the datum axis produced by illuminating CGH A the focus from CGH B is coincident with the far focus from CGH A. If CGH B is perturbed by a transverse distance Δ_B the focus from CGH B moves at the image plane with sensitivity (Δ'_B/Δ_B) and dynamic range $\Delta_{B,Max}$ given by,

$$\frac{\Delta'_B}{\Delta_B} = (1 - m_B), \tag{3.3}$$

and,

$$\Delta_{B,Max} = \frac{\Delta'_{B,Max}}{(1-m_B)}. \tag{3.4}$$

It is clear from these expressions that with $m_B < 0$ the sensitivity to CGH B centration alignment increases with $|m_B|$ while the dynamic range decreases. For a fixed total system length L and fixed CGH A near focal length z'_A, the alignment sensitivity will degrade as $|z_B|$ increases. The dynamic range is also function of $\Delta'_{B,Max}$, the half field of view across the image plane. Typically there is a tradeoff between the resolution and field of view for a camera, so high spot shear sensitivity or fine imaging resolution will compromise the dynamic range in this scheme.

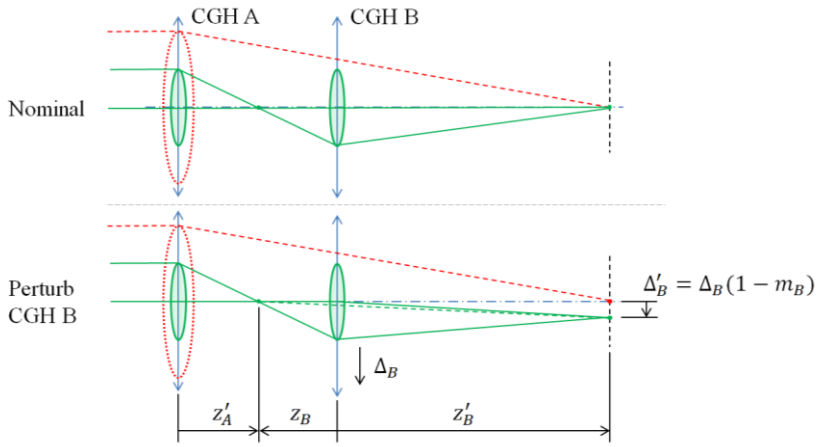

Figure 3.3: CGH A + CGH B focus at the image plane providing centration alignment feedback for CGH B[5]. Misalignment of CGH B from the line between the CGH A reference foci causes a deviation in the alignment focus from the location of the far focus of CGH A.

Note that it is highly relevant what is chosen to be the datum. It has been mentioned that the CGH substrates are tilt references. There is an attraction to the idea of making the illumination normal to CGH A so that CGH A may be the datum which defines the orientation of the centration alignment axis. This by default makes the tilt and centration errors of CGH A equal to zero. However, when finite accuracy and repeatability and precision of beam alignment conspire to perturb the beam angle relative to CGH A this ideal condition is disturbed. When the beam angle deviates the

datum axis intersects CGH B at a different point which is measured as a centration deviation of CGH B. Figure 3.4 provides a clear illustration and set of expressions which are helpful to understand this behavior. In particular, the apparent transverse deviation of CGH B due to a beam angle deviation,

$$\Delta_B = -(z'_A - z_B) * \tan(\Delta\theta), \tag{3.5}$$

increases with respect to the distance from CGH A to CGH B. This expression is useful to understand how a random variation in beam angle translates to random variation in the measurement of CGH B centration.

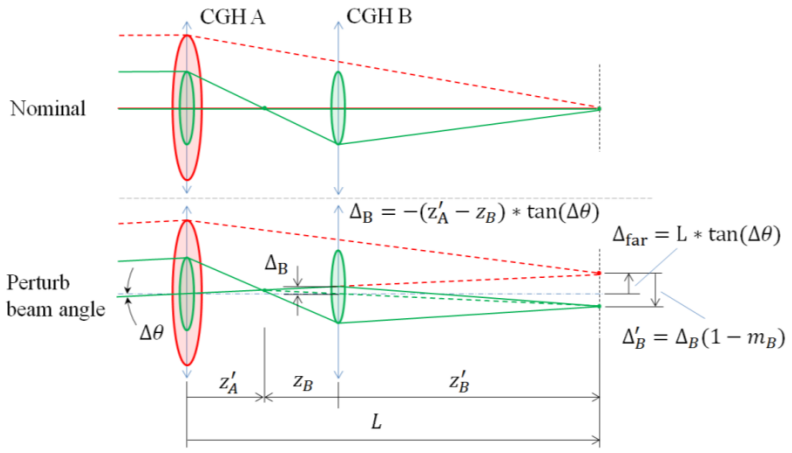

Figure 3.4: CGH A + CGH B focus at the image plane. Misalignment of collimated illuminating beam angle changes the datum axis angle and causes a transverse deviation of the axis relative to the center of CGH B.

Holding CGH A as the datum for tilt and centration may also be impractical from a tolerance standpoint. In a multiple mirror alignment there will be finite stability and resolution of adjustment for each mirror. There may exist a case where the mirrors are in a state of alignment consistent with tolerances, but a datum axis normal to CGH A may project too far from a particular CGH B to claim that CGH B is aligned within its centration tolerance. Making adjustments takes time and effort,

especially in large optical assemblies, and could even perturb an acceptable system in an *unfavorable* manner. Allowing the datum axis to deviate in angle slightly from the surface normal of CGH A can eliminate the appearance of a misaligned system in some cases and save significant time and effort. The HET alignment implementation in Chapter 4 will provide an example of how careful alignment data processing is key to successfully meeting tolerances in a demanding application of this technique.

3.1.4 HET Wide Field Corrector co-alignment design

Optical layouts of the 4 configurations of the HET Wide Field Corrector CGH co-alignment are shown in Figure 3.5. The M4 CGH was designed with nominal first-order parameters,

$$L = 2149.6 \text{ mm}, \quad z_A' = 150 \text{ mm}. \tag{3.6}$$

Although z_A' is fixed the length L to the best-focus for the as-built CGH pairs varies by configuration. The first-order parameters for the CGH pair configurations are given in Table 3.1. The CGH substrates are 6.35 mm thick plane parallel plates made of fused silica. These substrates are treated as reduced thicknesses to calculate the first-order parameters from the optical models. The test wavelength is 635 nm and the estimated refractive index of fused silica at this wavelength is 1.4566. The diameters of the CGH patterns are given in Table 3.2.

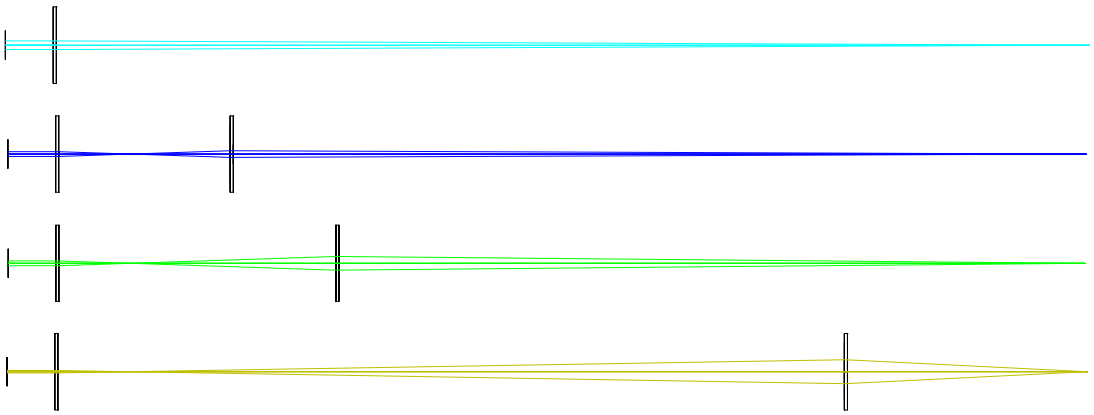

Figure 3.5: Configurations of the HET Wide Field Corrector CGH co-alignment design. From top to bottom: M4 far spot, M4-M4 pair, M4-M2 pair, and M4-M3 pair.

Table 3.1: First-order parameters of the CGH pair configurations of the HET Wide Field Corrector CGH co-alignment.

CGH pair	z_B	z_B'	m_B	$1 - m_B$
M4-M5	-207.12	1940.763	-9.37	10.37
M4-M2	-441.541	1436.611	-3.25	4.25
M4-M3	-1499.686	503.507	-0.34	1.34

Table 3.2: CGH pattern clear apertures in the HET Wide Field corrector CGH co-alignment

CGH pattern	CA OD (mm)	CA ID (mm)
M4 far spot	18	10
M4 near spot	10	0
M5	20	0
M2	35	0
M3	50	0

With these as-built first-order parameters of the CGH co-alignment it is straightforward to apply the parametric sensitivity expression given above in Equation (3.3) to each case. Using the optical model a transverse perturbation of 0.01 mm was applied to each of the M5, M2 and M3 CGHs under alignment. The predicted and simulated results are given for comparison in Table 3.3. The close agreement of the first-order calculations with the ray trace simulations supports the

use of the convenient first-order model to design and characterize this alignment scheme.

Table 3.3: Results from simulating a ±0.01 mm transverse misalignment of CGH B in the three CGH pair configurations. The resulting spot centroid displacements are compared to the first-order predictions.

	Spot centroid displacement (mm)	
CGH pair	Simulation	First-order
M4-M5	±0.10365	±0.10370
M4-M2	±0.04251	±0.04254
M4-M3	±0.01368	±0.01336

The error contributions to this centration alignment scheme were carefully analyzed and a demonstration performed by Coyle *et al.*[5]. It is reasonable to expect the random alignment errors due to the precision of the spot measurement to depend on the sensitivity to misalignment. Note that the alignment sensitivity scales with the factor $(1 - m_B)$. The demonstration presented by Coyle showed that with $(1 - m_B) = 1.37$ the as-aligned centration of CGH B had a 1σ uncertainty of $1.40\mu m$. Scaling this result by the alignment sensitivities yields the expected random errors given in Table 3.4. The same autocollimator and a microscope of identical sensitivity were used for measuring the CGH angles and projected spots in the lab demonstration and in the actual implementation. Therefore, these errors are fully expected in the HET WFC alignment.

Table 3.4: Expected alignment random errors of CGH B for the three CGH reference pairs in the HET WFC alignment.

CGH pair	$(1 - m_B)$	2σ Tilt Uncertainty [μrad]	2σ Centration Uncertainty [μm]
M4-M5	9.99	5.66	0.38
M4-M2	4.56	5.66	0.84
M4-M3	1.33	5.66	2.88

3.2 INTRODUCTION TO PHASE FIDUCIALS

3.2.1 Definition

A “phase fiducial” refers to a feature created on a parent optic under test and whose curvature is distinct from that of parent optic. Phase fiducials are a special type of aspheric departure which have a specific aberration signature to identify a given misalignment mode. Figure 3.6 shows a conceptual cross-sectional profile of a spherical phase fiducial surface departure map and a spherical optical surface with phase fiducials. These features are meant to be measured with a CGH-corrected interferometer test.

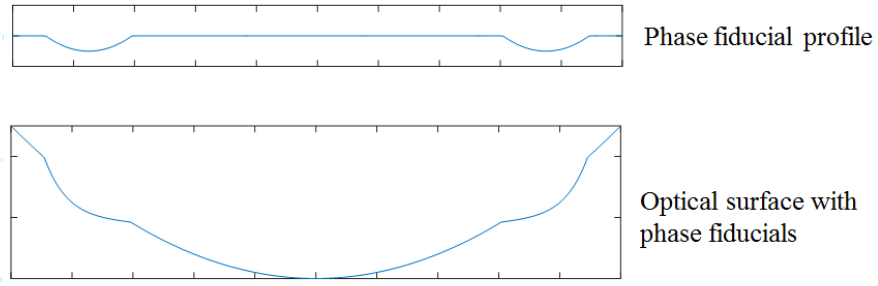

Figure 3.6: Conceptual cross-sectional profile of the fiducial surface departure from the parent optic (top) and a cross-section of the test optic with fiducials.

3.2.2 Applications in optical surface testing

There are two classes of interferometer test configuration that are especially well-suited toward exploiting phase fiducials for optical alignment. An indirect-test involves some optic or set of optics between the CGH and the phase fiducials. A direct-test has no intervening optics and the CGH-corrected wavefront propagates directly to the phase fiducials.

3.2.2.1 Indirect-test

The indirect-test configuration is generally used when the illumination and CGH are not sufficient to provide wavefront correction for a null test. Highly aspheric optics and convex optics motivate the use of additional null corrector elements or a reference surface near the optic under test. For example, a fold sphere may be used in combination with a CGH to test a large off-axis parabola[13]. In this application the fold sphere provides a folded beam path with an influence on the test wavefront to cancel spherical and other aberrations in the null test. The use of the fold sphere reduces the feature density on the CGH which may be much smaller than the optic under test. It is also possible to project the CGH test wavefront to a surface under test with a projection lens. Such a test may be used to conduct a CGH-corrected Fizeau test of a mirror segment or sub-aperture of a convex optic[7]. In this application it is highly important to align the projection of the CGH to the reference optic and optic under test. A large contribution of error in such a test comes from shear between the aspheric test surface and the aspheric wavefront departure induced by the CGH.

The parametric design and analysis of phase fiducials used in an indirect-test configuration will consider the CGH-corrected Fizeau interferometer application. This case has the interesting property of conjugate pupils at the CGH and optic under test. The field of other possible indirect-test configurations is too broad to treat as a parametric design space. However, it will be shown that the sensitivity of the fiducial features does not depend on the particular intervening optics.

3.2.2.2 Direct-test

The direct-test configuration represents many conventional interferometer tests. A null test preferentially has a minimum number of optical surfaces and it is common to test optical surfaces using only a CGH as a null corrector[20]. In such cases the illuminating beam from an interferometer is diffracted by the CGH such that the outgoing wavefront accommodates the phase influence of a surface or system under test in double-pass.

The parametric design and analysis of phase-fiducials used in a direct-test configuration will consider a test where the reference beam is internal to the interferometer, the test beam fills the aperture of a test CGH, and the optic under test is a mirror surface. The phase fiducials are designed as both spherical sub-aperture surfaces within the aperture of the mirror and as Ø0.5" ball references at the periphery of the mirror aperture. The analysis of these approaches shows the design trade of using the two kinds of references as a function of the test geometry.

3.3 PHASE FIDUCIAL DESIGN AND PERFORMANCE ANALYSIS

3.3.1 Indirect-test

This sub-section will present a first-order model of the CGH-corrected Fizeau interferometer and use the parameters of the model to define the possible sensitivity and dynamic range of a given phase fiducial design. A conceptual illustration of this class of interferometer is shown in Figure 3.7. The constraints set on the design of the

fiducials will be defined. Finally, the parametric design is applied to the TAO secondary mirror test application to demonstrate the design space for this proposed implementation and show its agreement with a ray-trace analysis.

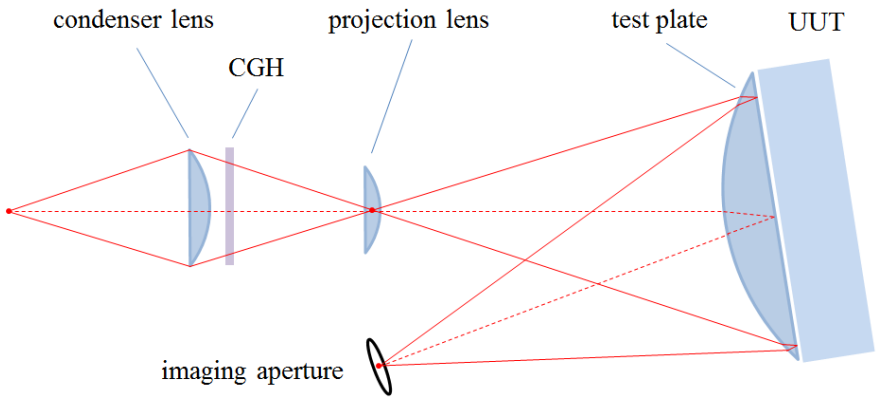

Figure 3.7: Conceptual diagram of the CGH-corrected Fizeau interferometer.

3.3.1.1 First-order model

The CGH-corrected Fizeau interferometer uses a CGH in single-pass to accommodate the aspheric departure of a UUT relative to a spherical reference. The design and use of this type of interferometer is discussed extensively by Burge *et al.* [7]. The basic layout involves a coherent point source, condenser lens, CGH, projection lens, test plate (reference optic), unit under test (test optic), and a telecentric camera with an aperture at its front focal plane. The reference and test beams are focused at the imaging aperture and the telecentric camera both collimates each beam in image space and images the UUT surface.

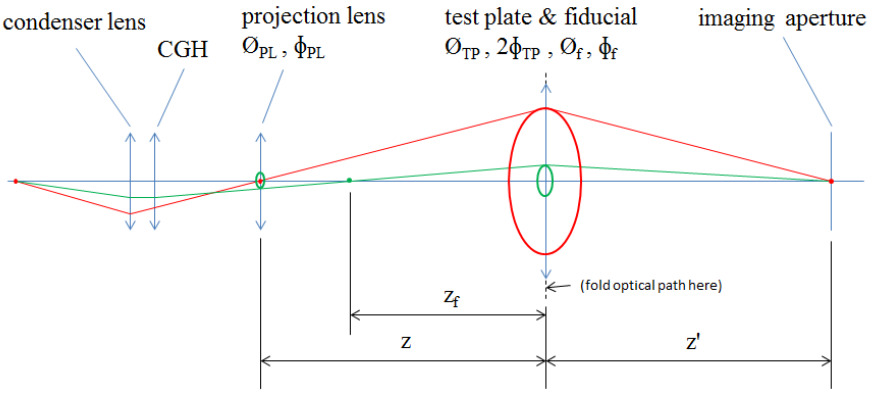

Figure 3.8: First-order axisymmetric and unfolded model of a CGH-corrected Fizeau interferometer. Relevant parameters of the system are listed next to the related elements. The marginal ray of the reference beam is traced in red and the marginal ray of the test beam reflected from the fiducial is traced in green.

A first-order model of this instrument is presented diagrammatically in Figure 3.8. There is only one field point and marginal rays are traced for the reference beam (red) and a test beam which interacts with a phase fiducial on the UUT (green). The diagram shows the interferometer in its most simple form: unfolded and axisymmetric, neglecting any tilted or decentered elements. The first-order model also places the focus of the intermediate focus of the reference beam exactly at the projection lens and has the test plate relay this image of the source to the imaging aperture at 1:1 magnification. Thus,

$$-\frac{1}{z} = \frac{1}{z'} = \phi_{TP}, \tag{3.7}$$

where ϕ_{TP} is the effective optical power. This effective power is given by

$$2\phi_{TP} = 2\phi_{transmit} + \phi_{reflect}, \tag{3.8}$$

where $\phi_{transmit}$ is the optical power of the front surface of the test plate and $\phi_{reflect}$ is the optical power of the internal reflection with the reference surface. The condition

of unity magnification makes light reflect exactly normal to the reference surface on the back of the test plate. This is preferred because it avoids adding power to the test beam which transmits through the reference surface. In reality the test plate is tilted to return light to an off-axis imaging system, but to first-order this only serves to steer the folded reference beam.

With a spherical optic under test in this axisymmetric model the test beam would also reflect normal to the UUT. When a phase fiducial is added this condition is violated. The change in curvature to the UUT makes the condition of unity magnification of the source image impossible. The image distance z' must remain fixed for the light to have a null interference with the reference beam, but

$$2\phi_{TP} + \phi_f = \frac{1}{z'} - \frac{1}{z_f}, \tag{3.9}$$

so for $\phi_f \neq 0$,

$$z_f \neq z. \tag{3.10}$$

The transverse magnification of the source image by the fiducial is given by

$$m_f = \frac{z'}{z_f}, \tag{3.11}$$

so this magnification varies depending on the shape and corresponding optical power of the fiducial. To understand the significance of this, consider Figure 3.9. This figure illustrates what will happen to the reference beam and test beam from the fiducial in the presence of a transverse misalignment of the test plate and fiducial. Both of the beams deviate in angle, but the discrepancy in magnification of the source image

causes a difference in angle between the beams entering the imaging aperture. The interference pattern will show tilt aberration as the signature of this misalignment. The discrepancy in angle and alignment sensitivity increases linearly as a function of $m_f - 1$.

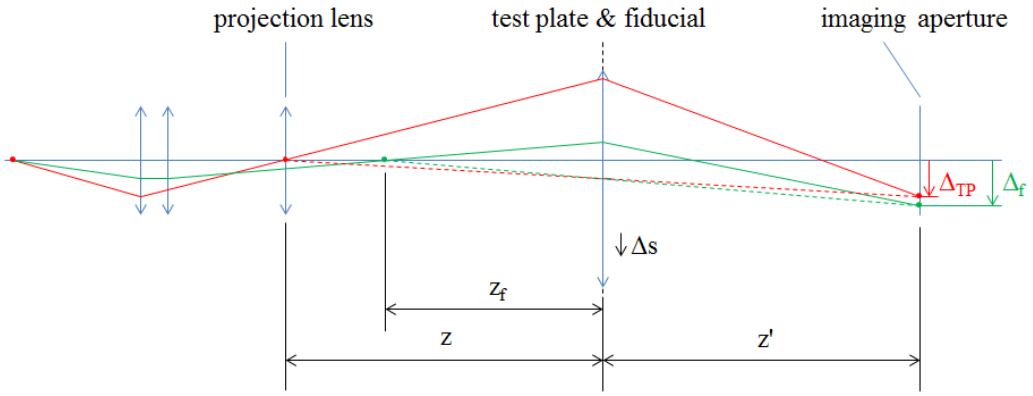

Figure 3.9: First-order model of the CGH-corrected Fizeau interferometer with the test plate and fiducial decentered by Δs. Note that the deviation of the focus Δf from the fiducial is greater than the light from the rest of the test plate due to the curvature and optical power departure implied by the fiducial.

Another interesting property is the expansion of the beam within the aperture of the projection lens as a function of ϕ_f. The slope of the marginal ray is linear with both ϕ_f and $\emptyset_f$. It is useful to consider the nominal marginal ray path to the fiducial in the backwards direction. By paraxial raytrace we can find the marginal ray height at the projection lens as a function of the fiducial optical power and size and test plate power. The paraxial angle of light leaving the fiducial and test plate is given by

$$u' = u - y\phi = 0 - \left(\frac{\emptyset_f}{2}\right)(\phi_{TP} + \phi_f). \tag{3.12}$$

The distance from the test plate to the projection lens is the focal length is $1/\phi_{TP}$, so the ray height at the projection lens is

$$y_{PL} = y + u't = \frac{\emptyset_f}{2}\left(1 - \frac{(\phi_{TP} + \phi_f)}{\phi_{TP}}\right) = -\frac{\emptyset_f \phi_f}{2\phi_{TP}} \tag{3.13}$$

From this expression we can derive three limits. In one limit $\phi_f = 0$ and there is no fiducial, in which case $y_{PL} = 0$ as expected. The other limits are $y_{PL} = \pm(\emptyset_{PL}/2)$, in which the beam fills the projection lens aperture. In these limits

$$\emptyset_f \phi_f = \pm \phi_{TP} \emptyset_{PL}. \tag{3.14}$$

This expression is useful for setting bounds on the design of a phase fiducial within a test with a given test plate and projection lens.

These results demonstrate how the parameters of this model relate to the behavior of light in the reference and phase fiducial beams within the interferometer. The discussion will now turn to a treatment of the OPD measured as a function of the fiducial shape and alignment. The relevant performance metrics are sensitivity and dynamic range.

3.3.1.2 Sensitivity and dynamic range

The alignment this method is concerned with is transverse alignment of the parent optic. In the case where the parent optic is not flat this transverse alignment is treated as a *roll* of the parent optic in a sense where a given fiducial translates nearly parallel to a plane tangent to the parent optic at its location. Additionally the variable

defining the curvature of a fiducial C_f is curvature *departure* relative to the curvature of the parent optic. The curvature departure is given by

$$C_f = \frac{1}{R_f} - \frac{1}{R_{UUT}}, \tag{3.15}$$

where R_F is the absolute radius of the fiducial surface and R_{UUT} is the radius of the test optic or "unit under test". This curvature departure is related to the first order parameter ϕ_f like

$$\phi_f = 2C_f. \tag{3.16}$$

This follows from the paraxial expression for optical power where light is reflected from a spherical surface.

In the previous sub-section an argument was made for sensitivity scaling linearly with $m_f - 1$. This factor is related to the fiducial and test plate parameters by

$$m_f = \frac{z'}{z_f} = \frac{\phi_{TP} + \phi_f}{\phi_{TP}} \quad \rightarrow \quad m_f - 1 = \frac{\phi_f}{\phi_{TP}} = \frac{2C_f}{\phi_{TP}}. \tag{3.17}$$

This expression demonstrates that the sensitivity to alignment is proportional to C_f. If the measurement process only observed the spots at the imaging aperture then C_f would be the most relevant parameter and $\emptyset_f$ would only serve to change the spot size. Let us now consider the sensitivity of the OPD measured across the fiducial to evaluate the sensitivity of tilt in the interferogram more directly.

Consider a small spherical surface departure at the fiducial of the form,

$$\Delta z_f = \frac{C_f}{2}(x^2 + y^2), \tag{3.18}$$

where x and y are transverse coordinates relative to the center of the fiducial. In reflection this will induce

$$OPD_f \approx C_f(x^2 + y^2), \tag{3.19}$$

relative to the reference beam of the interferometer. With a CGH influencing the OPD as well we have two contributions to the OPD between the reference and test beams at the fiducial. When the two are complimentary we have

$$\delta OPD_f = OPD_f - OPD_{CGH} = 0, \tag{3.20}$$

and there is a null interference at the fiducial. However, in the general case where there is some shear between the complimentary wavefront from the CGH and the fiducial,

$$\delta OPD_f = 2C_f(x * \Delta x + y * \Delta y) . \tag{3.21}$$

Note that this is purely tilt. Thus, shear of the wavefront relative to the fiducial produces a slope in the OPD measured by the interferometer. This result is valid as a paraxial approximation where the shallow fiducials are treated as parabolic. If higher order terms are included in the formula for surface departure different aberrations may be introduced, but the dependence of *tilt* in the measured OPD still has this dependence. From this result we find that the sensitivity of alignment is

$$\frac{PV\ (\delta OPD_f)}{\sqrt{\Delta x^2 + \Delta y^2}} = 2\emptyset_f C_f, \tag{3.22}$$

where the OPD slope has been multiplied by the diameter of the fiducial to find the peak-to-valley OPD contribution from a misalignment. Another interesting portrayal of the sensitivity is the shear of the fiducial associated with 1 wave of tilt,

$$\frac{\text{fiducial shear}}{\text{wave, OPD}} = \frac{\lambda}{2\left(C_f \emptyset_f\right)}. \tag{3.23}$$

This factor can be easily scaled by the interferometer measurement precision to understand what performance to expect for an alignment.

The dynamic range is also of high importance as this is a common limitation in interferometry. In temporal phase-shifting interferometry there is a limit to how dense fringes can be and still have sufficient sampling to evaluate the phase. Using the Hariharan algorithm as an example, there are 4 distinct shifted acquisitions of the fringe pattern and a fifth acquisition which is ideal identical to the first[21]. Thus, a given point on a fringe will translate to 4 distinct positions and must be measured at each. When the fringe pattern becomes so dense that there are only 4 pixels across one cycle of the fringe pattern the sampling frequency is

$$f_{samp} = 2f_{nyquist}, \tag{3.24}$$

and below this sampling frequency there are variations in contrast between acquisitions that start to cause errors in the phase evaluation. Also, pixels with a width equal to the sampling pitch wash-out the fringes at $2f_{nyquist}$[22, p.550]. The

limit of sampling tilt fringes at $2f_{nyquist}$ will be considered as the practical limit for temporal phase-shifting interferometry in this derivation of expected dynamic range.

The sampling frequency within a given sub-aperture is most likely limited by the number of samples across the imaging detector and the size of the UUT. Under this assumption the sampling frequency at the fiducial is

$$f_{samp} = \frac{N_{samp}}{\emptyset_{UUT}}, \tag{3.25}$$

where N_{samp} is the number of samples across the UUT, limited by the shirt axis of the detector, and $\emptyset_{UUT}$ is the diameter of the UUT. The slope of the OPD from a misalignment of the fiducial is given in waves by

$$\text{slope}\left(\delta OPD_f\right) = \sqrt{\Delta x^2 + \Delta y^2} \cdot \frac{2C_f}{\lambda}, [\text{waves/mm}]. \tag{3.26}$$

The maximum measureable slope is limited by the corresponding fringe density and the sampling frequency where,

$$\text{slope}\left(\delta OPD_f\right)_{MAX} = \pm \frac{\frac{1}{4}\text{ waves}}{(1/f_{samp})} = \pm \frac{f_{samp}}{4}, [\text{waves/mm}]. \tag{3.27}$$

Thus, the maximum shear of the fiducial that is measureable under the current assumptions is given by

$$MAX\left(\sqrt{\Delta x^2 + \Delta y^2}\right) = \pm \frac{\lambda f_{samp}}{8C_f}. \tag{3.28}$$

This is the dynamic range for detecting a misalignment of the fiducial under the assumption that the minimum sampling frequency for tilt fringes is twice the Nyquist frequency.

Notice that there is an inherent tradeoff between sensitivity and dynamic range for a phase fiducial of a given size and with a given sampling frequency, where

$$\text{Sensitivity} \propto C_f, \quad \text{and} \quad \text{Dynamic range} \propto 1/C_f.$$

This inverse relationship is represented in Figure 3.10 with a graph of sensitivity and dynamic range for a $\emptyset_f = 5.25\text{mm}$ fiducial in the TAO SM test application.

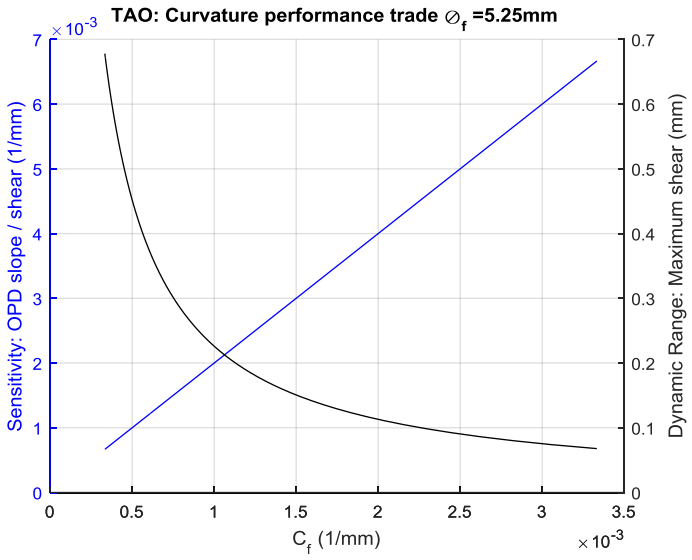

Figure 3.10: Plot of the sensitivity (blue) and dynamic range (black) of a $\emptyset_f = 5.25\text{mm}$ fiducial in the TAO SM test application.

3.3.1.3 Design constraints

The primary design constraints are fiducial size and maximum slope. For a given curvature these quantities are coupled, but the size of the fiducial is also

constrained by the maximum acceptable obscuration within the test aperture and the minimum number of samples across the fiducial. For a minimum number of samples N_{min} the corresponding constraint is,

$$\emptyset_f \geq \frac{N_{min}}{f_{samp}} = \frac{N_{min}}{N_{samp}} \emptyset_{UUT}. \tag{3.29}$$

A practical limit on maximum fiducial size would keep the fiducial diameter less than 10% of the UUT diameter. Under these constraints the diameter of the fiducial is limited by the inequality,

$$\frac{N_{min}}{N_{samp}} \emptyset_{UUT} \leq \emptyset_f \leq 0.1\, \emptyset_{UUT}. \tag{3.30}$$

The first-order model exposed one limitation on the fiducial design, which is the beam footprint at the projection lens. The first-order analysis showed that in the two limits where the projection lens aperture is filled by the illuminating beam to the fiducial the optical power and fiducial diameter are given by,

$$\emptyset_f \phi_f = \pm \phi_{TP} \emptyset_{PL}, \tag{3.31}$$

where $\phi_f = 2C_f$, and $1/\phi_{TP} = -z$ is the distance from the projection lens to the test plate. Recasting this expression in a more directly relevant way,

$$-\frac{\emptyset_{PL}}{|z|} \leq 2\emptyset_f C_f \leq \frac{\emptyset_{PL}}{|z|}. \tag{3.32}$$

In a realistic system there is often a tilt term in the CGH wavefront design to separate diffracted orders. If this "tilt carrier" displaces the beam to the fiducial by a radial offset d_{tilt} from the center of the projection lens, as illustrated in Figure 3.11, then

the beam diameter must be smaller to avoid clipping at the edge of the projection lens. The constraint on beam diameter at the projection lens becomes,

$$\emptyset_{beam} \leq \emptyset_{PL} - 2d_{tilt}. \tag{3.33}$$

Therefore, in the presence of this tilt of the beam we have,

$$-\frac{\emptyset_{PL} - 2d_{tilt}}{2|z|} \leq \emptyset_f C_f \leq \frac{\emptyset_{PL} - 2d_{tilt}}{2|z|}. \tag{3.34}$$

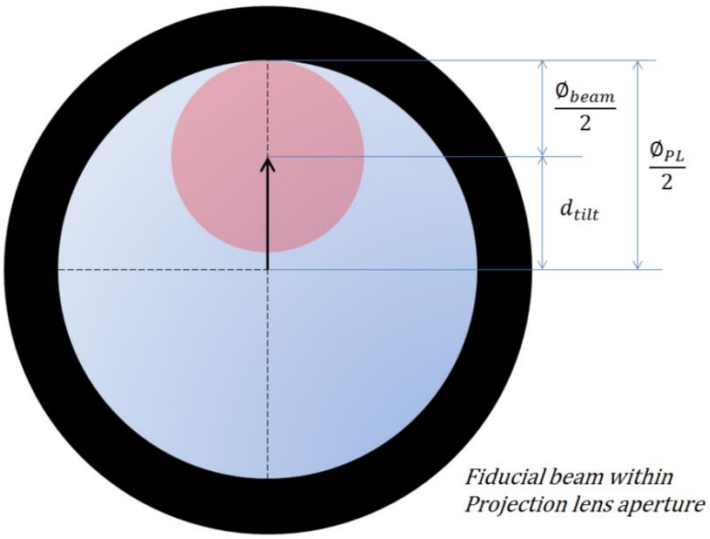

Figure 3.11: Illustration of the influence on effective clear aperture for the fiducial beam at the projection lens as a function of the tilt carrier induced beam displacement.

The last major constraint on phase fiducial design for a CGH-corrected Fizeau interferometer is that the CGH must be able to create the required wavefront to accommodate the fiducial. The projection lens induces aberrations that are increasingly severe as the beam diameter increases. Taking the perspective of a backwards raytrace, the projection lens must image the fiducial onto the CGH without

any ray-crossings. If rays that are coincident with different surface slopes on the fiducial intersect at the CGH there is no way to design a phase influence at the CGH to accommodate the corresponding areas on the fiducial. This limit is highly dependent on the projection lens design and the constraint on phase fiducial design set by projection aberrations will be evaluated in the TAO secondary mirror test case study.

3.3.1.4 TAO phase fiducial design space

The TAO secondary mirror test interferometer has first-order parameters given in Table 3.5. These will be used to evaluate the constraints and performance of phase fiducials designed for the alignment of this test. An optical model will also be used to confirm the accuracy of the calculations made with these parameter values.

Table 3.5: First-order model parameters for the TAO secondary mirror test.

Parameter	Value	Units
λ	632.8	nm
N_{samp}	1000	-
$\emptyset_{TP}$	350	mm
ϕ_{TP}	1/1995	mm^{-1}
$\emptyset_{PL}$	49.5	mm
ϕ_{PL}	1/375	mm^{-1}
d_{tilt}	8.2	mm
$\emptyset_{CGH}$	80.46	mm

Based on the parameters of this test and setting $N_{min} = 11$, the constraints on concave fiducial shape are,

$$3.85\text{mm} \leq \emptyset_f \leq 35\text{mm}. \tag{3.35}$$

and,

$$\emptyset_f C_f \leq 0.0083. \tag{3.36}$$

From the limit set on $\emptyset_f C_f$ it can immediately be evaluated that regardless of the choice of fiducial diameter the maximum sensitivity is

$$\frac{\text{fiducial shear}}{\text{wave, OPD}} = \frac{\lambda}{2\left(C_f \emptyset_f\right)} = 0.038\text{mm}. \tag{3.37}$$

If the interferometer can measure peak-to-valley OPD tilt with $\sigma_{OPD} \leq \lambda/10$ random uncertainty, then the random uncertainty for shear of the fiducial is:

$$\sigma_{shear} \leq 0.0038\text{mm}. \tag{3.38}$$

The first-order parameters and constraints for the TAO test correspond to a finite design space for phase fiducials. This design space has been mapped out with a set of curves of constant sensitivity in Figure 3.12. There are constraints on this design space due to minimum and maximum fiducial diameters, the sign of curvature departure, and cases where aberrations projecting from the CGH to the fiducial exceed what is possible to compensate with a single pattern on the CGH. The concept of reverse raytracing has already been mentioned as a tool used in design to check where rays intersect the testing optics from the imaging aperture up to the CGH. This method is useful to check for ray crossings before the CGH in a null configuration and also to check for vignetting at the projection lens. By contrast, a forward raytrace is useful to verify the performance of a fiducial design for a perturbed alignment.

The minimum fiducial diameter was set by a chosen minimum number of samples across the image of the fiducials where,

$$N_{min} = 11 \quad \rightarrow \quad \emptyset_{f,min} = 3.85\text{mm} \approx 4\text{mm}. \tag{3.39}$$

The plot in Figure 3.12 has the minimum diameter threshold set at 4 mm and shows design cases up to a maximum diameter at 25 mm. Naturally, the maximum diameter is mostly a matter of how much of the clear aperture is sacrificed for the sake of alignment. The curve with $\emptyset_f C_f = 0.0083$ corresponds to the upper limit of attainable sensitivity with the projection lens diameter, but higher sensitivity cases were also generated with the parametric and raytrace models where the projection lens was allowed to increase in diameter with the same plano-convex lens prescription. These extra cases were included to show the trend in aberration thresholds at each sensitivity.

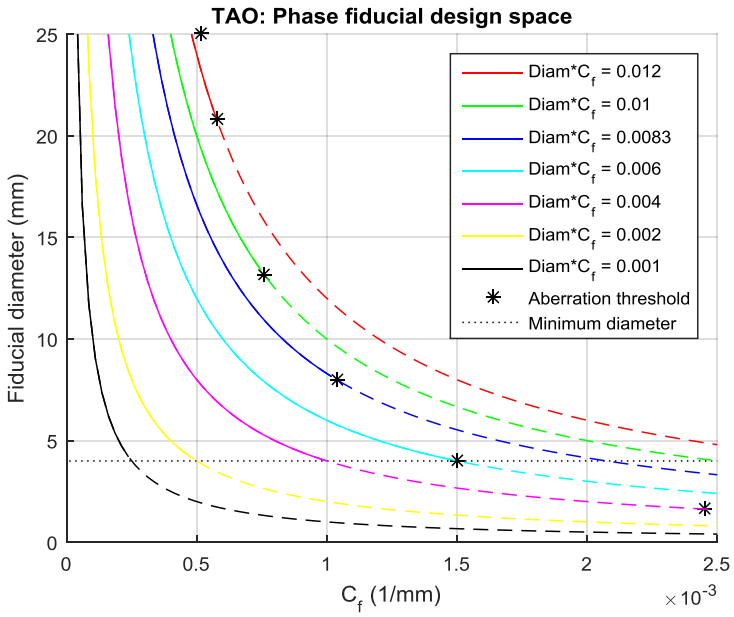

Figure 3.12: Curves of constant sensitivity representing fiducial diameter vs. fiducial curvature departure. The dotted violate design constraints.

The constraint on sensitivity was predicted by the first-order equations to be $\emptyset_f C_f \leq 0.0083$. This was simulated in the raytrace model of the optical test and

Figure 3.13 provides a plot of the ray intersections with the projection lens aperture from a uniform rectangular sampling grid across the stop. It is clear from the figure that the ray at the lower edge of the beam is very near the boundary of the projection lens clear aperture and that there is no opportunity to increase the sensitivity of the phase fiducial. In addition to this constraint, when the fiducial diameter is 8 mm the beam footprint at the CGH is given by Figure 3.14. In this plot of ray intersections the rays at the lower edge of the beam begin to overlap. An overlap or crossing of rays that are conjugate to distinct locations across the fiducial makes it impossible to compensate the OPD each of these rays experiences in reflection. This case approaches the limit of the design space for this sensitivity, where a larger diameter and lower curvature at the *same* sensitivity reduces this overlap of the rays. Figure 3.15 provides an example of another fiducial design at the same sensitivity with a diameter of 25mm to show how the distribution of rays across the CGH becomes much more evenly distributed with a larger fiducial.

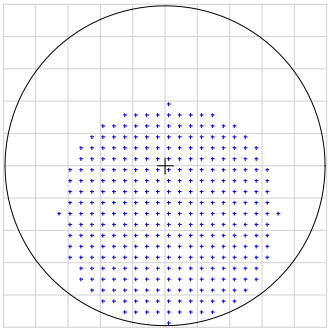

Figure 3.13: Ray intersections at the *projection lens* with $\emptyset_f C_f = 0.0083$ and $\emptyset_f = 8\text{mm}$ in the optical model of the TAO secondary mirror test. This represents the limit of the projection lens aperture diameter on phase fiducial sensitivity. 50.0mm full-scale.

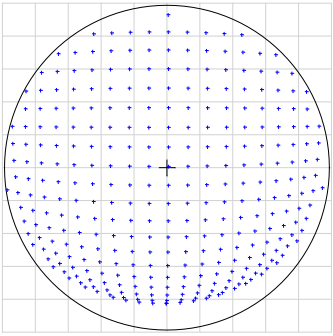

Figure 3.14: Ray intersections at the CGH with $\emptyset_f C_f = 0.0083$ and $\emptyset_f = 8$mm in the optical model of the TAO secondary mirror test. This represents the limit of the aberration which a CGH pattern can compensate. 1.62mm full-scale.

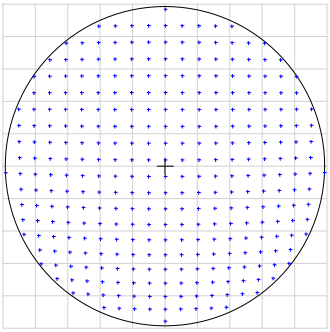

Figure 3.15: Ray intersections at the CGH with $\emptyset_f C_f = 0.0083$ and $\emptyset_f = 25$mm in the optical model of the TAO secondary mirror test. The increased diameter reduces high-order projection aberrations. 5.60mm full-scale.

The first-order model also predicts the OPD measured as a result of rolling the UUT about its center of curvature. The shear refers to the translation of the fiducial tangent to the UUT. Thus, shear is a function of the UUT roll like,

$$\text{shear} = \mathrm{R_{UUT}} \cdot \tan(\theta_{ROLL}), \tag{3.40}$$

where θ_{ROLL} is the roll angle of the UUT. The forward raytrace model of the optical test was configured to roll the calibration sphere UUT and 3 fiducial configurations such that the UUT did not tilt its reflected test beam. In this configuration θ_{ROLL} was

chosen to provide a certain shear of the fiducials and the peak-to-valley OPD from wavefront tilt was evaluated. The first-order model evaluations of the OPD from tilt and the values generated by fitting the OPD to Zernike Standard terms in Zemax are given in Table 3.6. Note that the maximum discrepancy between these values is only 0.8%. This represents a good agreement between the parametric design performance prediction and the simulated performance of the fiducial sensitivity.

Table 3.6: Results for peak-to-valley tilt in OPD within in the TAO secondary mirror test interferometer for three different phase fiducial designs. First-order parametric model calculations are compared to the ray trace model simulation results.

Fiducial parameters			**Ray trace**		**First-order**
$\emptyset_f C_f$	$\emptyset_f$ $[\mathbf{mm}]$	C_f $[\mathbf{1/mm}]$	**PV, OPD (Δx) [waves]**	**PV, OPD (Δy) [waves]**	**PV, OPD (Δx or Δy) [waves]**
0.004	8	0.0005	$\pm$0.998	$\pm$0.996	$\pm$1
0.008	8	0.0010	$\pm$1.994	$\pm$1.992	$\pm$2
0.004	16	0.0005	$\pm$1.994	$\pm$1.992	$\pm$2

3.3.2 Direct-test

This sub-section will present a first-order model of a CGH-corrected interferometer surface test with parameters set to define the possible sensitivity and dynamic range of a given phase fiducial design. The constraints set on the design of the fiducials will also be defined. Finally, the parametric design is applied to a set of case study simulations to demonstrate the agreement of the parametric model with a ray-trace.

A conceptual schematic of the direct-test configuration under consideration is given in Figure 3.16. Note that this is an example in which the illuminating test beam is collimated through a transmission flat, but in general this beam may also be

spherical and produced by a transmission sphere on a Fizeau interferometer or diverger lens on a long unequal-path interferometer (LUPI).

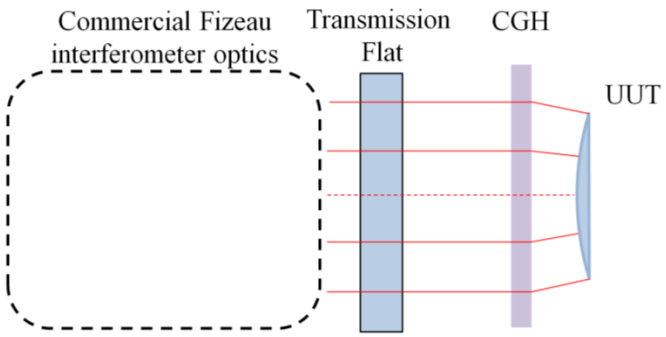

Figure 3.16: Conceptual layout of one example of the direct-test configuration with a Fizeau interferometer and transmission sphere and convex UUT.

3.3.2.1 First-order model

The direct test may be performed on a UUT which is concave, convex or nominally flat. Figure 3.17 and Figure 3.18 show first-order diagrams of the ray paths for a convex and concave UUT, respectively. These figures also show the ray paths associated with a null at a fiducial on the surface of the UUT. These diagrams have distances and parameters of the tests given with a sign convention such that a radius or distance to the right is positive and to the left is negative. The UUT is treated as a sphere in these first-order models and the nominal model is constructed to achieve retro-reflection from the UUT and fiducial. In order to achieve this condition the CGH may be treated as a thin lens with appropriate optical power to focus the illuminating wavefront at the center of curvature of the UUT and fiducial sub-aperture.

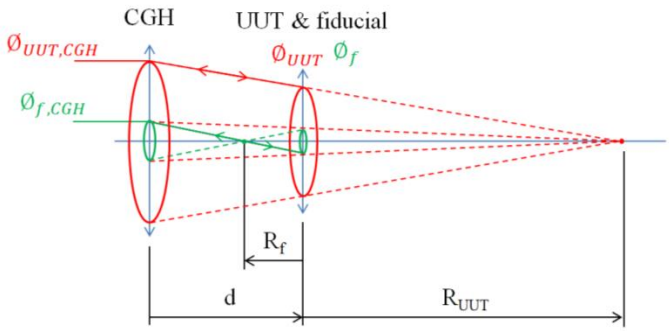

Figure 3.17: Layout of the first-order model for a direct-test of a convex UUT ($R_{UUT} > 0$) and fiducial at the center of the optic.

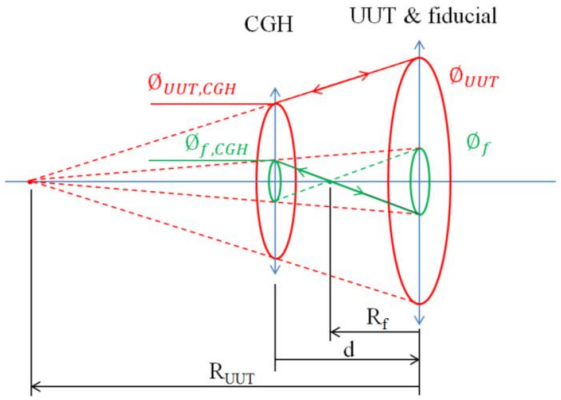

Figure 3.18: Layout of the first-order model for a direct-test of a concave UUT ($R_{UUT} < 0$) and fiducial at the center of the optic.

3.3.2.2 Designing for matched obscuration fiducials

In order to match the obscuration of the fiducial at the CGH and at the UUT a condition must be satisfied which is illustrated in Figure 3.19. There is a correct choice for the radius of the fiducial R_f depending on the distance from the CGH to the UUT and the radius of the UUT R_{UUT}. To find the expression for R_f to satisfied matched obscurations by the fiducial we first trace the red ray to the edge of the fiducial and solve for the ray height,

$$y = \frac{\emptyset_f}{2} = \frac{\emptyset_{f,CGH}}{2} - d\frac{\emptyset_{f,CGH}}{2(d + R_{UUT})}. \tag{3.41}$$

This relationship may be recast to find the ratio,

$$\frac{\emptyset_f}{\emptyset_{f,CGH}} = 1 - \frac{d}{d + R_{UUT}}. \tag{3.42}$$

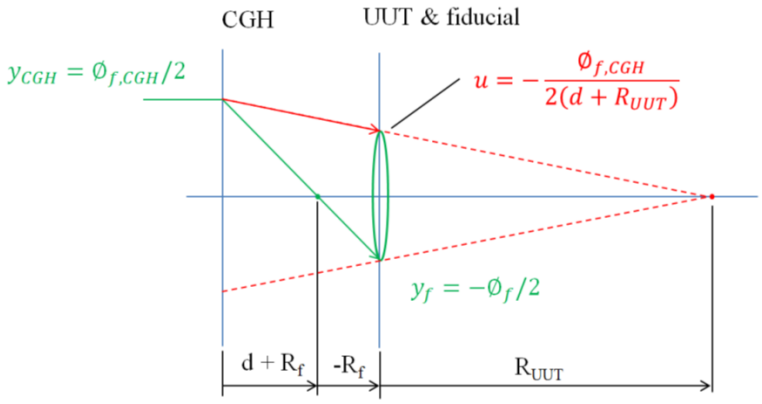

Figure 3.19: Diagram of the condition for matched obscuration of the test beam by the fiducial at the CGH and UUT within the first-order model of the direct-test.

Now consider the green ray which is retro-reflected by the lower edge of the fiducial. There are similar triangles created in the diagram by the ray crossing the optical axis between the CGH and the fiducial. Thus, it is straightforward to derive that,

$$\frac{\emptyset_f}{\emptyset_{f,CGH}} = -\frac{R_f}{d + R_f}, \tag{3.43}$$

and by substitution we can write,

$$-\frac{R_f}{d + R_f} = 1 - \frac{d}{d + R_{UUT}}. \tag{3.44}$$

Solving this equation for R_f yields,

$$R_f = -\frac{d}{\left(\frac{d}{R_{UUT}}\right) + 2}. \tag{3.45}$$

This expression defines the correct choice, to first-order, for the fiducial radius to achieve a matched obscuration of the fiducial at the CGH and UUT. Note that regardless of R_{UUT} the radius $R_f < 0$, so matched obscuration fiducials are *always* concave.

3.3.2.3 Designing for ball-references

There may be motivation to violate the condition of matched obscuration in certain cases. In particular, the direct-test configuration is much more versatile and allows the use of very high curvature reference features without the aberration limitation presented in the case of the indirect-test CGH-corrected Fizeau interferometer. One high-curvature feature of interest is a ball reference. Ball references may be positioned just outside the clear aperture of the UUT with the CGH designed to focus a portion of the beam at the center of curvature of each ball. Such a case is shown in Figure 3.20. In this case the ball references replace the fiducials which were on the UUT surface, but the references remain stationary relative to the UUT and are integral to the optic in this sense. Ball references may be considered with the same analysis to check sensitivity and dynamic range as phase fiducials provided that reflection from their surfaces occurs along an extrapolation of the UUT surface.

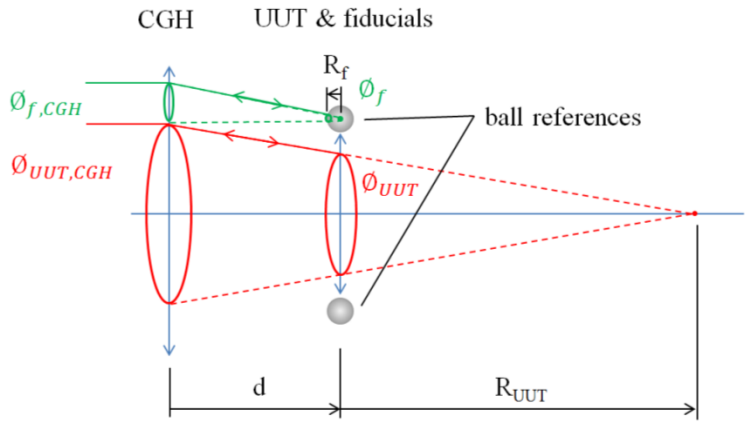

Figure 3.20: Layout of the first-order model for a direct-test of a convex UUT ($R_{UUT} > 0$) and ball reference outside the edge of the UUT.

It is impossible to choose a ball radius or *any* convex radius which matches the obscuration at the CGH and the UUT. Thus, it is very inefficient to place a ball reference within the UUT testing aperture as this will create a much larger obscuration of the test surface for the same sensitivity as a phase fiducial. This will be shown with a case study that compares the designs and performance of a phase fiducial and ball reference at equivalent magnitude of curvature.

3.3.2.4 Sensitivity and dynamic range

The sensitivity of OPD to misalignments of a fiducial is identical to the sensitivity derived for the CGH-corrected Fizeau interferometer. Provided that the test is a interferometer mirror surface test the analysis of the sensitivity according to the shape of the fiducial is,

$$\frac{\text{fiducial shear}}{\text{wave, OPD}} = \frac{\lambda}{2\left(C_f \emptyset_f\right)}, \tag{3.46}$$

where as in the direct test the parameter C_f is curvature departure of the reference feature relative to the UUT,

$$C_f = \frac{1}{R_f} - \frac{1}{R_{UUT}}. \tag{3.47}$$

The dynamic range of the alignment may be limited by the sampling frequency at the UUT, as in the indirect-test. For all cases in the direct-test the dynamic range is given by

$$MAX(\text{fiducial shear}) = \pm \frac{\lambda f_{samp,f}}{8C_f}, \tag{3.48}$$

where $f_{samp,f}$ is the spatial frequency of sampling at the fiducial surface and λ is the testing wavelength. However, it is notable that $f_{samp,f}$ is only equal to the sampling frequency in the test beam, f_{samp}, if the matched obscuration condition is met. The use of ball references presents a counter example where the sampling frequency for measuring OPD across the alignment feature will tend to increase with a larger portion of the illuminating beam incident on a small portion of the ball.

A reevaluation of the sampling spatial frequency is warranted for the direct-test alignment features. Let $f_{samp,CGH}$ be the sampling frequency across the interferometer beam at the CGH. This spatial frequency is constant to first-order and does not depend on anything other than interferometer illumination and detection. This sampling frequency is scaled by the size of the beam footprint on the CGH

relative to the footprint on the phase fiducial. The relationship between sampling at the CGH and sampling at the fiducial surface, $f_{samp,f}$, is given by,

$$f_{samp,f} = f_{samp,CGH} * \frac{\emptyset_{f,CGH}}{\emptyset_f}. \tag{3.49}$$

This should be compared to the sampling frequency across the UUT, f_{samp}, given by,

$$f_{samp} = f_{samp,CGH} * \frac{\emptyset_{CGH}}{\emptyset_{UUT}}. \tag{3.50}$$

In the case of matched obscuration we set constraints to ensure that,

$$\frac{\emptyset_{f,CGH}}{\emptyset_f} = \frac{\emptyset_{CGH}}{\emptyset_{UUT}}, \tag{3.51}$$

which is easily applied to these sampling equations to find that,

$$f_{samp,f} = f_{samp}, \tag{3.52}$$

under the constraint of matched obscurations.

For a ball reference it is useful to refer to Figure 3.21 to calculate the change in sampling frequency. From tracing the green marginal ray to the ball reference surface it is straightforward to find the beam footprint on the ball given by,

$$\frac{\emptyset_f}{2} = \frac{\emptyset_{f,CGH}}{2} - d * \frac{\emptyset_{f,CGH}}{2(d + R_f)} = \frac{\emptyset_{f,CGH}}{2} * \frac{R_f}{d + R_f}. \tag{3.53}$$

Based on this relationship the ratio of the beam footprints is given by,

$$\frac{\emptyset_{f,CGH}}{\emptyset_f} = \frac{d + R_f}{R_f}, \tag{3.54}$$

and the sampling frequency at the ball surface is given by,

$$f_{samp,f} = f_{samp,CGH} * \frac{d + R_f}{R_f}. \tag{3.55}$$

Similarly, the sampling at the UUT is given in terms of the UUT radius by

$$f_{samp} = f_{samp,CGH} * \frac{d + R_{UUT}}{R_{UUT}}. \tag{3.56}$$

A comparison of the sampling frequencies shows that for a ball reference,

$$f_{samp,f} = f_{samp} * \frac{d + R_f}{d + R_{UUT}} * \frac{R_{UUT}}{R_f}. \tag{3.57}$$

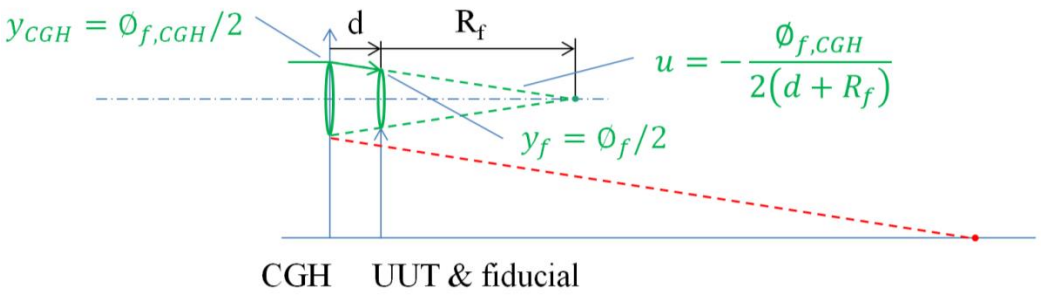

Figure 3.21: Diagram for calculation of the beam footprint on a convex phase reference surface from a direct-test.

The dynamic range may also be limited by beam "walk-off" in the case of a direct-test where the beam experiences a double-pass through the CGH sub-aperture. In the direct-test the symmetry of incoming and reflected light makes the fiducial or ball act as a 1:1 magnification relay for real or imaginary foci. The curvature departure C_f determines the deviation of the chief ray angle of the reflected beam as a function of shear resulting from roll about the UUT center of curvature. The shear of

the reflected beam footprint at the CGH is dependent on this angle and the separation d between the CGH and the fiducial. The diagram in Figure 3.22 shows the relevant geometry to determine the beam deviation for a fiducial of a given curvature. In the example shown the UUT is a flat and $C_f = 1/R_f$ for simplicity, but using curvature departure and treating the shear as tangent to the spherical UUT surface may be addressed with the same parametric results.

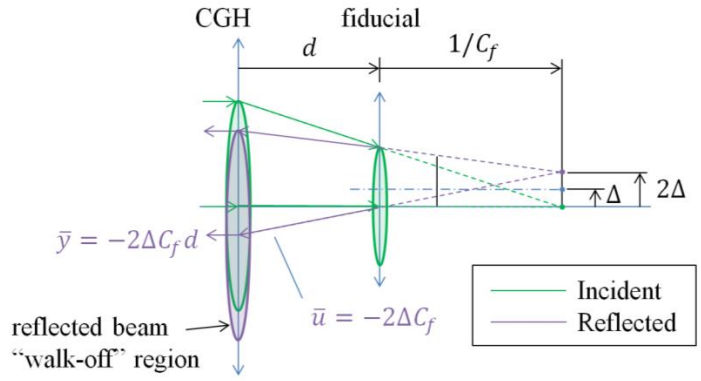

Figure 3.22: Diagram illustrating reflected beam "walk-off" for a shear Δ of the fiducial surface with a curvature departure C_f. The reflected chief ray angle and height are given in terms of the test parameters.

The diagram shows a trace of the marginal and chef ray toward a virtual focus, a fiducial surface decentered by Δ, and the reflected marginal and chief rays which appear to come from another virtual focus that is a distance 2Δ off-axis. The marginal ray trace demonstrates that the beam footprint stays the same size at the CGH and the chief ray trace demonstrates the deviation of the beam footprint due to a shear misalignment of the fiducial feature,

$$\bar{y} = -2\Delta C_f d. \tag{3.58}$$

The illustration in Figure 3.22 shows a case where the fiducial is convex, but this is immaterial as the parameters are general to all possible design forms. For a concave fiducial with $C_f < 0$ the sign of the chief ray deviation sensitivity changes and there are *real* foci between the CGH and the fiducial.

To connect the beam walk-off with dynamic range a tolerance for walk-off must be set. A reasonable but adaptable requirement is,

$$\bar{y} \leq \frac{\emptyset_{f,CGH}}{4}, \tag{3.59}$$

which sets a demand for loss of samples across any given dimension of the measurement not to exceed a factor of 0.25. Under this constraint we can set the dynamic range in a case where the walk-off is the limiting factor as,

$$MAX(\text{fiducial shear}) = \pm\frac{\emptyset_{f,CGH}}{8C_f d}, \tag{3.60}$$

and for a sampling-limited case, as shown before,

$$MAX(\text{fiducial shear}) = \pm\frac{\lambda f_{samp,f}}{8C_f}. \tag{3.61}$$

The walk-off effect is entirely dependent on the test geometry and *not* on the wavelength or sampling. However, the sampling factor is also dependent on the test geometry like,

$$f_{samp,f} = f_{samp,CGH} * \frac{d + R_f}{R_f}. \tag{3.62}$$

This makes it clear that there is an inverse relationship between the two conditions for dynamic range limitation with respect to d. For a ball reference design this is particularly clear because all parameters other than d may be kept constant across several design forms. For matched obscuration fiducials C_f and R_f are coupled with R_{UUT} and d which makes the relationship more subtle.

To explore the relationship between these criteria for dynamic range, consider a 4" flat test where,

$$R_{UUT} = \infty \quad \rightarrow \quad C_f = 1/R_f. \tag{3.63}$$

Additionally, let $N_{samp} = 1000$ and $\emptyset_{beam} = 6"\,(152.4\text{mm})$ which implies sampling at,

$$f_{samp,CGH} = 6.56\text{mm}^{-1}, \tag{3.64}$$

and let the test wavelength be,

$$\lambda = 632.8\text{nm}. \tag{3.65}$$

Under these constraints consider two types of phase reference design with a 0.5" ball outside the flat or a fiducial on the flat.

For the ball reference let,

$$\emptyset_{f,CGH} = 25.4\text{mm} \quad \text{and} \quad R_f = 6.35\text{mm}.$$

For the fiducial on the flat let,

$$\emptyset_{f,CGH} = 10\text{mm} \quad \text{and} \quad R_f = \frac{d}{2}.$$

With all the relevant parameters defined, the dynamic range constraints are simulated for these two cases using the parametric expressions. The results are plotted in Figure 3.23 and Figure 3.24. From Figure 3.23 it is clear that there is a point of maximum dynamic range for a ball reference in this test where the two constraints are equivalent before crossing. This crossing occurs at,

$$d = 195\text{mm}, \ \text{Dynamic range} = \pm 0.1\text{mm}.$$

The fiducial has a much larger maximum dynamic range, but the equivalency of the constraints occurs at such a low curvature that the trade-off for sensitivity is much too severe to be practical. In either case there is a trade-off where sensitivity is reduced for a larger distance d, but for the ball reference it is not advantageous to increase d beyond the point of equivalent constraints, and the use of the ball fails for a large enough distance d where diffraction dominates the beam at the ball surface.

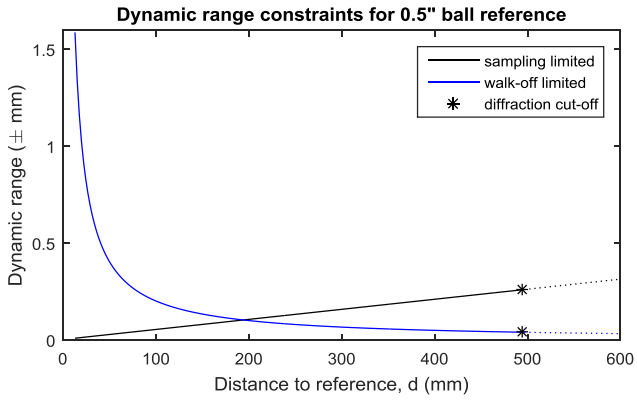

Figure 3.23: Plot of the dynamic range constraints for detecting shear in the case of a 0.5" ball reference. There is a point of equality of these constraints that represents the maximum possible dynamic range. There is also a maximum distance, d, before the beam is too slow and diffraction dominates at the point of reflection.

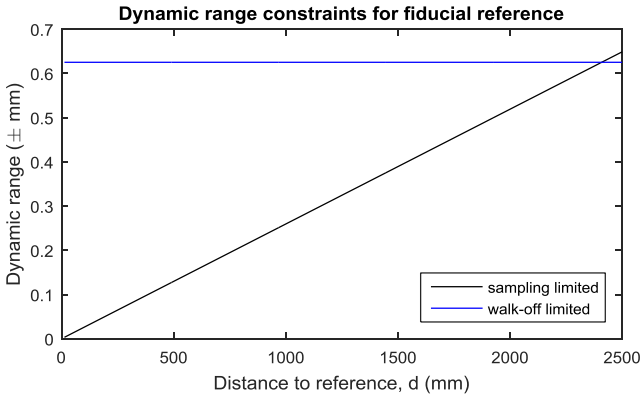

Figure 3.24: Plot of the dynamic range constraints for detecting shear in the case of a matched obscuration phase fiducial on the flat. There is a point of equality of these constraints that represents the maximum possible dynamic range. This occurs at a point where the curvature is too low to provide a useful sensitivity.

The evaluation of geometric beam footprint at the ball (illustrated in Figure 3.21) is also relevant to another design constraint for ball references. It is important to keep the ball surface sufficiently far from the virtual focus at its center of curvature to avoid reflecting the light where diffraction dominates the phase distribution. There is a factor z_R given in units of distance known as the Rayleigh range. The factor may be

applied to predict the radius of curvature of a Gaussian beam of a given wavelength and numerical aperture[23]. This factor is given by,

$$z_R \approx \frac{\lambda}{\pi\,\mathrm{NA}^2}. \tag{3.66}$$

To illustrate how this factor applies to a focused Gaussian beam, consider Figure 3.25 where the normalized diffracted beam footprint is plotted against a geometric beam footprint. The Gaussian beam converges to a minimum beam waist w_0 rather than an infinitesimal focus.

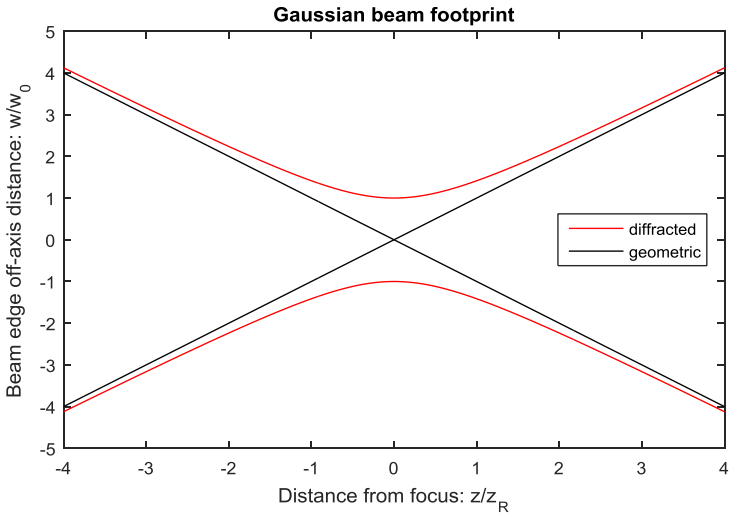

Figure 3.25: Comparison between the diffracted Gaussian beam footprint and a geometric focusing beam.

The radius of curvature of the wavefront of a Gaussian beam a distance z from the geometric focus is given by[23],

$$R(z) = z\left[1 + \left(\frac{z_R}{z}\right)^2\right]. \tag{3.67}$$

In the limit where $z = 0$ the wavefront is flat. It is also clear in this expression that the term $(z_R/z)^2$ represents the discrepancy between the actual radius of the

wavefront and the geometric prediction. Thus, if we have a reflection a distance z from a real or virtual focus it is important that this term is sufficiently small so that the geometric ray trace design is valid. As an arbitrary factor to use in this discussion, assume that it is suitable to reflect light from a phase fiducial where the wavefront radius discrepancy is $\leq 10\%$. This corresponds to the requirement,

$$\left(\frac{z_R}{z}\right)^2 \leq 0.1, \tag{3.68}$$

which may be evaluated to derive the design requirement,

$$|z| \geq 3.13 z_R. \tag{3.69}$$

The relationship between the diffracted Gaussian beam wavefront radius and the radius of a geometric spherical wave are plotted against each other in Figure 3.26.

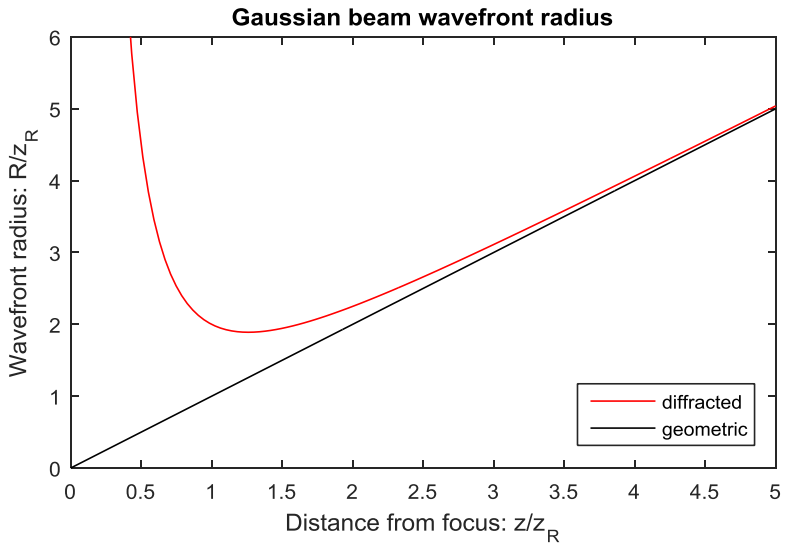

Figure 3.26: Comparison of Gaussian beam wavefront radius to the radius of a geometric spherical wave.

A common size for balls used in coordinate measurement is 0.5 inch diameter. If this type of ball is used as a reference then the offset of the reflective surface from geometric focus is,

$$|z| = R_f = 6.35\text{mm}, \tag{3.70}$$

and the requirement becomes,

$$6.35\text{mm} \geq 3.13 z_R = 3.13 \frac{\lambda}{\pi \text{NA}^2}. \tag{3.71}$$

Solving this for NA with test wavelength $\lambda = 632.8\text{nm}$ yields, approximately,

$$\text{NA} \geq 0.01 \text{ for } z \geq 3.13 z_R. \tag{3.72}$$

This limit occurs at small marginal ray angles where the paraxial ray and u may be equated to NA to cast NA in terms of the test parameters to find,

$$\text{NA} = \frac{\emptyset_{f,CGH}}{2\left(d + R_f\right)}. \tag{3.73}$$

The tolerance on wavefront error may be adjusted by the designer and the parameters adjusted as required for different test geometries and wavelengths to make sure the wavefront radius is suitable for a given design.

3.3.2.5 Design space

The choice of designs of a matched obscuration fiducial or an external ball reference will be evaluated by the parametric model and by ray trace for the three direct-test configurations given in Chapter 2. These test geometries will set up a

discussion of the design trade between using a high-curvature ball reference or a slower matched-obscuration phase fiducial. Further, the cases also represent some limiting conditions within the design space of these phase references for alignment of a direct test.

The parameters of fiducial reference and ball reference designs for these models are given in Table 3.7. In the table there are several parameters with subscripts that have not been presented with the following indicated correspondence to the parametric expressions:

$$d_f, d_{ball} \rightarrow d$$

$$\emptyset_{ball},\ \emptyset_{ball,CGH} \rightarrow \emptyset_f,\ \emptyset_{f,CGH}$$

$$R_{ball} \rightarrow R_f$$

The fiducial designs achieve the condition of matched obscuration and consistently have a diameter on the UUT,

$$\emptyset_f = 0.04\ \emptyset_{UUT}. \tag{3.74}$$

The ball references are designed to consume a reasonably small portion of the CGH to show practical applications of these alignment references.

Table 3.8 and Table 3.9 give the performance specifications for fiducial and ball phase references, respectively, used in the three models. The optical layouts are shown in Figure 3.27 - Figure 3.29. Model #2 and Model #3 maintain constant parameters $\emptyset_{ball,CGH}$ and $\emptyset_{UUT,CGH}$ to show how the performance of the ball

references degrades when the distance d becomes very long. Model #1 and Model #2 demonstrates cases where the ball references perform quite well, with superior dynamic range to the fiducials with both performing at nearly identical sensitivities in both cases. Model #3 demonstrates the expected breakdown in the performance of the ball references when d becomes sufficiently large. In Model #3 the fiducials still have a nearly identical sensitivity as ball references, but 8 times the dynamic range. The dynamic range decreases for the large path to the ball due to reflected beam walk-off. In Model #3 the numerical aperture of the beam to the ball is also 0.01, which is the lower limit of NA based on the proposed criteria based on Gaussian beam propagation theory.

Table 3.7: Summary of the parameters of the phase reference designs for the three case study direct tests

	Model #1	**Model #2**	**Model #3**	
N_{samp}	1000	1000	1000	-
$f_{samp,CGH}$	7.42	10.25	10.2	samp/mm,CGH
$\emptyset_{UUT}$	101.6	101.6	190.5	mm
$\emptyset_{UUT,CGH}$	106.46	84.34	84.38	mm
R_{UUT}	304.8	-304.8	-571.5	mm
d_f	13.4	51.8	324.2	mm
R_f	-6.35	-29.3	-228.3	mm
$\emptyset_f$	3.78	4.04	7.58	mm
$\emptyset_{f,CGH}$	4.4	3.4	3.19	mm
d_{ball}	14.93	52.96	322.6	mm
R_{ball}	6.35	6.35	6.35	mm
$\emptyset_{ball}$	4.04	0.706	0.128	mm
$\emptyset_{ball,CGH}$	14.2	6.6	6.6	mm

Table 3.8: Sensitivity and dynamic range performance specifications for fiducial references in direct-test case studies.

Model #	Fiducial Shear Sensitivity [mm/wave,OPD]	Dynamic range [mm, @UUT]	Dynamic range limitation
1	-0.00052	0.0042	sampling
2	-0.00254	0.0221	sampling
3	-0.01587	0.1297	sampling

Table 3.9: Sensitivity and dynamic range performance specifications for balll references in direct-test case studies.

Model #	Ball Shear Sensitivity [mm/wave,OPD]	Dynamic range [mm, @UUT]	Dynamic range limitation
1	0.00051	0.0134	sampling
2	0.00279	0.0472	sampling
3	0.01552	0.0161	beam walk-off

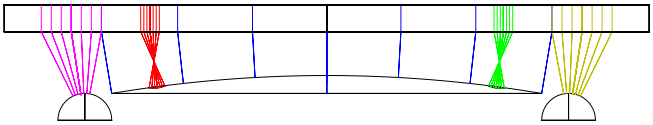

Figure 3.27: Layout of Model #1, "Convex 4" f/3 paraboloid test with 6" CGH"

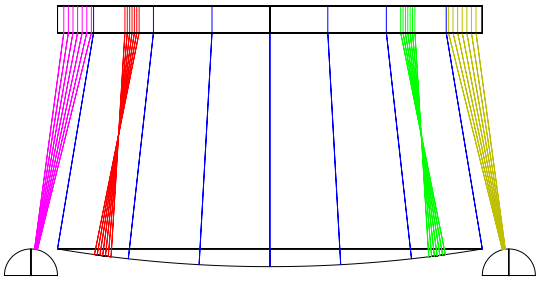

Figure 3.28: Layout of Model #2, “Concave 4" f/3 paraboloid test with 4" beam”

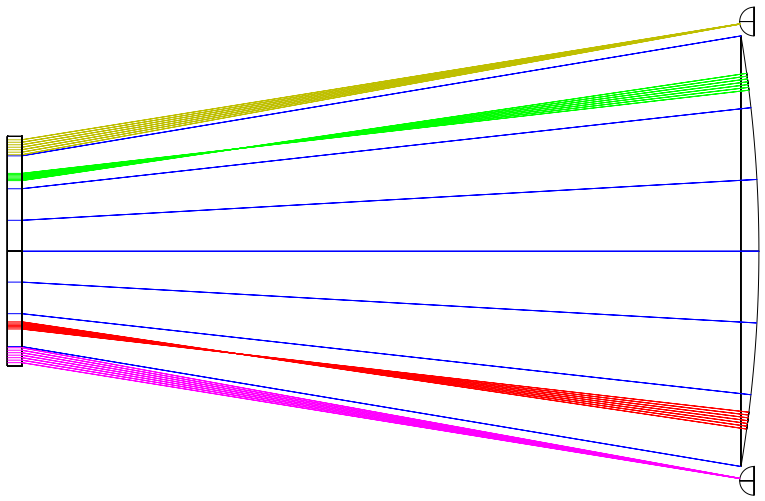

Figure 3.29: Layout of Model #2, “Concave 7.5" f/3 paraboloid test with 4" beam”

The Zemax ray trace models were also used to confirm that the sensitivity calculations from the parametric model are valid. The phase reference features and UUT were perturbed by rolling all the surfaces about the base center of curvature of the UUT. The tilt induced in the reflected beams was evaluated in terms of Zernike Standard coefficients Z2 and Z3 in Zemax. The stop was set at the CGH sub-aperture which accommodates each phase reference. Table 3.10 lists the results of the ray trace evaluations of the expected tilt from a given shear of each phase reference as well as parametric evaluations of the expected tilts. The agreement is quite strong with relative error of the parametric calculations within the bounds,

$$-0.76\% \leq \frac{\varepsilon_{OPD_f}}{OPD_f} \leq 0.60\%, \tag{3.75}$$

and,

$$-1.76\% \leq \frac{\varepsilon_{OPD_{ball}}}{OPD_{ball}} \leq 1.12\%. \tag{3.76}$$

The parametric model is quite reliable and valuable for designing these alignment references for a given optical test.

Table 3.10: Results for peak-to-valley OPD in the direct-test for a fiducial on the surface and for An external ball reference. First-order parametric model calculations are compared to the ray trace model simulation results.

Configuration		**Fiducial parameters**			**Ray trace**		**First-order**
Model #	**Reference type**	$\emptyset_f C_f$	$\emptyset_f$ [mm]	C_f [1/mm]	**PV, OPD (Δx) [waves]**	**PV, OPD (Δy) [waves]**	**PV, OPD (Δx or Δy) [waves]**
1	fiducial	-0.608	3.78	-0.1608	±1.006	±1.059	±1
1	ball	0.623	4.04	0.1542	±1.011	±1.069	±1
2	fiducial	-0.125	4.04	-0.0308	±0.992	±0.996	±1
2	ball	0.113	0.706	0.1608	±0.988	±0.989	±1
3	fiducial	-0.020	7.58	-0.0026	±0.993	±0.993	±1
3	ball	0.020	0.128	0.1592	±0.123	±0.123	±0.125

3.3.3 Error contributions to phase fiducial alignments

There are several major contributions to the error expected from an alignment with phase fiducials: OPD measurement accuracy, fiducial surface aberrations, and accuracy of measuring fiducial locations. The OPD measurement accuracy depends on the accuracy of the interferometer. This is decoupled from the design and tolerances on the phase fiducials. The fiducials will in general have some residual aberrations that are not compensated by the CGH which arise from fabrication or testing errors. The most influential aberrations are power, or radius error, and coma. The fiducial locations are also important when there is a set of fiducials that are compensated by the CGH, or if the locations must be known relative to a set of mechanical data. The relative locations of the fiducials and their locations relative to

the mechanical data are measureable with a PSM and CMM. The aberrations and location measurement error contributions depend on the accuracy of testing fiducial surface figure and fiducial surface location provided the CGH is designed to as-built optical specifications.

Residual power aberration causes a variation in the OPD tilt as a function of the measured region. Consider the formula for Zernike standard power aberration:

$$\mathrm{OPD}(\rho,\theta) = \mathrm{Z4} * \sqrt{3} * (2\rho^2 - 1). \tag{3.77}$$

If the coordinate system is translated in x by a fraction Δ of the radial distance across which $\rho = 1$, then within the shifted frame OPD has the form,

$$OPD(\rho',\theta') = \mathrm{Z4} * \sqrt{3} * (2\rho'^2 + 4\Delta\rho'\cos\theta'), \tag{3.78}$$

subtracting contributions to piston. The basis translation parameter Δ is illustrated in Figure 3.30. The result given in Equation (3.78) leads to the conclusion that the peak-to-valley OPD tilt error contribution from power depends on the Zernike standard power coefficient Z4 and the fractional shift of the discrete Zernike basis Δ like,

$$\varepsilon(PV - OPD_{tilt}) = \mathrm{Z4} * 8\sqrt{3} * \Delta. \tag{3.79}$$

There is a hard constraint on Δ based on the number of pixels across the measured region on the fiducial. Without interpolation, the basis for processing may only be assigned to a precision of ±1 pixel. If the basis has a radial extent of N pixels then,

$$|\Delta| \geq 1/N. \tag{3.80}$$

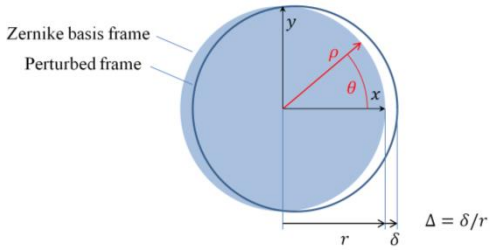

Figure 3.30: Illustration of the normalized lateral Zernike basis shift Δ.

Coma aberration in given Zernike basis becomes a combination of tilt and coma within a basis with a different radius. If the locations of the fiducials are determined by an optical response across an aperture distinct from that measured during alignment there is a tilt error due to residual coma in the fiducial surface. Consider two Zernike basis frames distinguished by a radial shift coefficient, as shown in Figure 3.31. The even Zernike standard coma coefficient is given by,

$$\mathrm{OPD}(\rho,\theta) = \mathrm{Z8} * 2\sqrt{2} * (3\rho^3 - 2\rho)\cos\theta. \tag{3.81}$$

With a radial shift of the normalized reference frame by the factor "a" the functional form of the same OPD is given in the perturbed coordinate frame by,

$$\mathrm{OPD}(\rho',\theta') = \mathrm{Z8} * 2\sqrt{2}\mathrm{a}^3\left(3\rho'^3 - 2\rho' + 2\left(1 - \tfrac{1}{\mathrm{a}^2}\right)\rho'\right)\cos\theta'. \tag{3.82}$$

There is a similar relationship between the orthogonal coma coefficient Z7 and tilt in the orthogonal orientation:

$$\mathrm{OPD}(\rho',\theta') = \mathrm{Z7} * 2\sqrt{2}\mathrm{a}^3\left(3\rho'^3 - 2\rho' + 2\left(1 - \tfrac{1}{\mathrm{a}^2}\right)\rho'\right)\sin\theta'. \tag{3.83}$$

These results leads to the conclusion that the peak-to-valley OPD tilt error magnitude from coma depends on the Zernike standard coma coefficients Z7 and Z8 and the radial shift of the discrete Zernike basis as,

$$\varepsilon(PV - OPD_{tilt}) = \sqrt{(\mathrm{Z8})^2 + (\mathrm{Z7})^2} * 8\sqrt{2} * (\mathrm{a}^3 - \mathrm{a}). \tag{3.84}$$

Similar to the basis translation, the radial shift can only be controlled to ±1 pixel. If the measured region has a radial extent of $N \pm 1$ pixels then,

$$\mathrm{a} = 1 \pm 1/N. \tag{3.85}$$

In practice the pixel resolution is not the dominant concern. The use of an auto-reflection optical probe to locate the fiducials may introduce a larger error. Such a probe may reflect light from a larger region than the interferometer which creates an inconsistency between the measurement of fiducial location and the measurement of fiducial alignment.

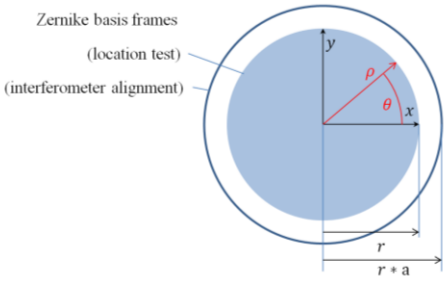

Figure 3.31: Illustration of the radial basis shift coefficient a.

In cases where the phase fiducials are distinct from mechanical data it may be required that the fiducials be located relative to a set of datum targets. The use of ball references which are also easily measured mechanical data avoids this issue, but the use of ball references is very restrictive. To diagnose the positions of one fiducial

vertex relative to a set of external data 7 measurements are required: 1 of the fiducial center of curvature (CoC), 3 of the mechanical data, and 3 on the surface of the parent optic. These are most readily made with an optical probe such as the PSM which uses auto-reflection to locate spherical optics and mechanical data. An axis is projected from the CoC of the fiducial to the CoC of the parent optic. The intersection of this axis with the optical surfaces defines the fiducial vertex. The calculation of this location is subject to error in the fiducial CoC measurement and error in the projection angle. The projection angle error is labeled ε_θ and the corresponding transverse fiducial vertex location error is,

$$\varepsilon_x = R_f \tan(\varepsilon_\theta). \tag{3.86}$$

The projection angle error is proportional to surface height errors ε_Z of the three measurements across the parent optic and inversely proportional to the separation between the surface measurements. Figure 3.32 shows a conceptual example of this where a fiducial on a flat is under test.

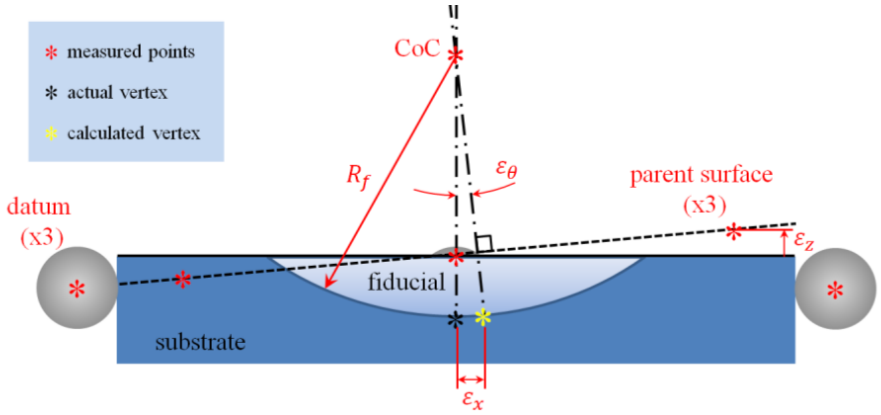

Figure 3.32: Conceptual example of measuring a fiducial vertex relative to mechanical data by projecting from the fiducial center of curvature (CoC) along the local surface normal of the parent optic.

This measurement scheme is limited primarily by detection of the parent optic surface slope. The much larger and low-curvature parent must be measured at discrete points if the same probe is to be used for all the measurements. It has been shown in Chapter 1 that typical auto-reflection instruments are inherently better at locating points in the transverse plane. This fundamental limitation makes the diagnosis of the fiducial CoC much more precise than diagnosis of the parent optic surface slope. This issue can be mitigated to some extent by averaging results from more than 3 measurements on the parent surface and using the fastest beam possible in the optical probe. However, this is not a limitation for locating the *relative* positions of a *set* of phase fiducials. The relative CoC locations can be found with much higher precision and used for reference in the design of the CGH.

The error sources for a phase fiducial alignment are outlined in Table 3.11. The errors discussed above influence either the measurement of the *relative* location of the projection to the fiducials or the diagnosis of the *absolute* projection location within an external reference frame. All of the errors are relative errors except for the projection angle error that results from locating the vertices of the features relative to separate mechanical data. In practice this is important because the fiducials must have known locations relative to the parent optic for this approach to be useful. The lower relative error for diagnosis of the fiducials *is* useful for design of a CGH though, because the design can be constrained to accommodate the measured *pattern*. The sources of error are independent and the total expected errors can be evaluated by root-sum-square.

Table 3.11: Summary of error contributions to a phase fiducial alignment. Errors given in waves of peak-to-valley tilt are related to alignment error by the alignment sensitivity of the phase fiducials.

Error contribution	Error Sources	Relative error	Absolute error
OPD acquisition	Measurement	~0.05 waves	~0.05 waves
Power	Fabrication & Measurement	Eq. (3.79)	Eq. (3.79)
Coma	Fabrication & Test	Eq. (3.84)	Eq. (3.84)
CoC measurements	Fabrication & Test	(CMM)	(CMM)
Projection to vertices	Fabrication & Test	-	Eq.(3.86)

For the TAO SM test application the error contributions for a fiducial with

$$R_f = 1.585\text{mm} \quad \text{and} \quad \emptyset_f C_f = 0.0083,$$

may be made to satisfy the error budget given in terms of projection shear in TABLE. These estimated values assume a 0.35m baseline across which to diagnose the parent optic surface with a laser tracker with ~0.005mm accuracy. The center of curvature locations are also assumed to be diagnosed with PSM focus locations measured by the same laser tracker. Contributions to coma and power have been mitigated in this budget. The expected 33μm absolute alignment error for such a fiducial is much smaller than the current 0.150 mm alignment tolerance and offers opportunities to achieve higher accuracy measurements with reduced systematic aberration error.

Table 3.12: Expected errors for the alignment of the TAO SM test CGH projection relative to phase fiducial(s) and in absolute position relative to external mechanical data at the test optic.

Error contribution (TAO SM)	Error Sources		Alignment error (μm)	
			Relative	Absolute
OPD acquisition	Measurement		2	2
Fiducial CoC relative locations (est.)	Fabrication & Test		5	5
Fiducial vertex absolute location (est.)	Fabrication & Test		-	32
		RSS	5.3	33

CHAPTER 4

HET WIDE FIELD CORRECTOR ALIGNMENT

This chapter presents the path we followed to align the HET Wide Field Corrector. The original CGH reference alignment scheme has been described in Chapter 3. The alignment of the CGH references and additional laser tracker references for the HET WFC alignment is documented in this chapter. The explanation of these alignment results are extensively drawn from the SPIE proceedings paper written collaboratively by Chang Jin Oh and Eric Frater[15].

An issue with drift in the reference positions is also presented. The assumptions we worked with are made clear to set the conditions under which we executed a revised alignment plan. The revised alignment is presented and the risk of correlated alignment errors made clear so that the precision and limitations of the methods are clear. The various types of CGH-based alignment used in this plan shall be identified to show where each fits within the taxonomy set out in Chapter 1. Finally, the expected as-aligned status at time of delivery shall be presented to show the successful result of the alignment.

4.1 CENTER REFERENCE FIXTURES

Each mirror in the wide field corrector has alignment references which are referred to as center reference fixtures. Representative examples of these fixtures are shown in Figure 4.1. The fixture is kinematically mounted to three V-blocks about the geometrical axis of each mirror. The center reference fixtures all have a CGH

mounted at their center. This CGH is used as a reference for the decenter and tilt alignments. There are also three sphere mounted retroreflector (SMR) nests bonded to the fixtures for M2, M3, and M5. The SMR nests provide a reference for the axial location of each mirror vertex. The vertex of M4 is referenced to a single SMR on a separate fixture, also shown in Figure 4.1, which uses the backplane of the mirror as the datum for vertex location.

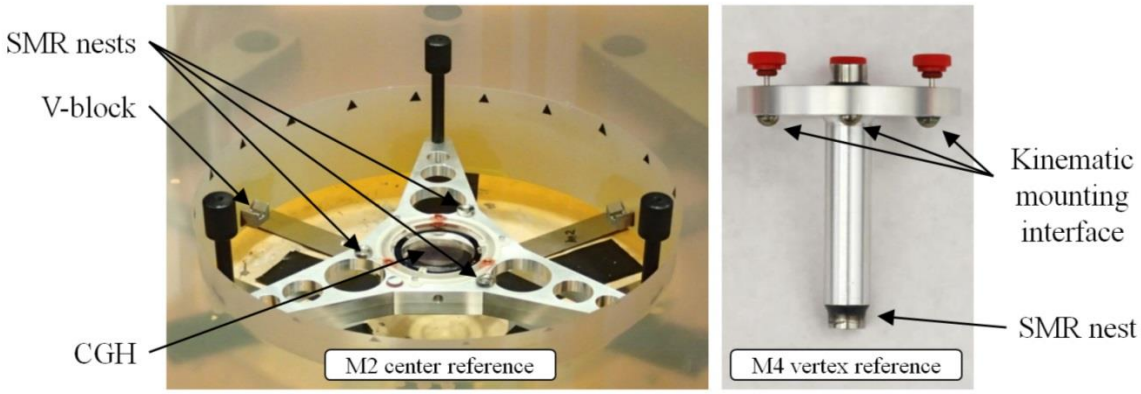

Figure 4.1: Examples of a center reference fixtures. The SMR nests mount laser tracker retroreflector targets for coordinate measurement of the mirror position. The CGH is used for precision tilt and decenter alignment.

The following subsections will show how the CGH and SMR nests are aligned and/or registered to the optical axis and vertex of each mirror. There is a laser tracker measurement which measures the height of the optical surface relative to the SMR nests on a given center reference fixture. This measurement locates the vertex height for reference during the mirror spacing alignment. In order to provide a reference for mirror tilt and centration the axis of symmetry of each CGH reference must coincide with the mirror it is mounted to. To align the CGH references to the mirrors we used

4 different setups similar to the one shown in Figure 4.2 and followed the steps given below:

Step 1: Align decenter and tilt of the optical axis of the mirror relative to the axis of rotation of the air-bearing by evaluation of modulations in coma and tilt induced by misalignments.
Step 2: Install the center reference fixture, with the CGH installed, and the point source microscope (PSM).
Step 3: Align the optical axis of the CGH relative to the axis of rotation in decenter by evaluation of the CGH center mark coordinates on rotation.
Step 4: Align the optical axis of the CGH relative to the axis of rotation in tilt by evaluation of the CGH angle on rotation with the point source microscope in the autocollimator mode.

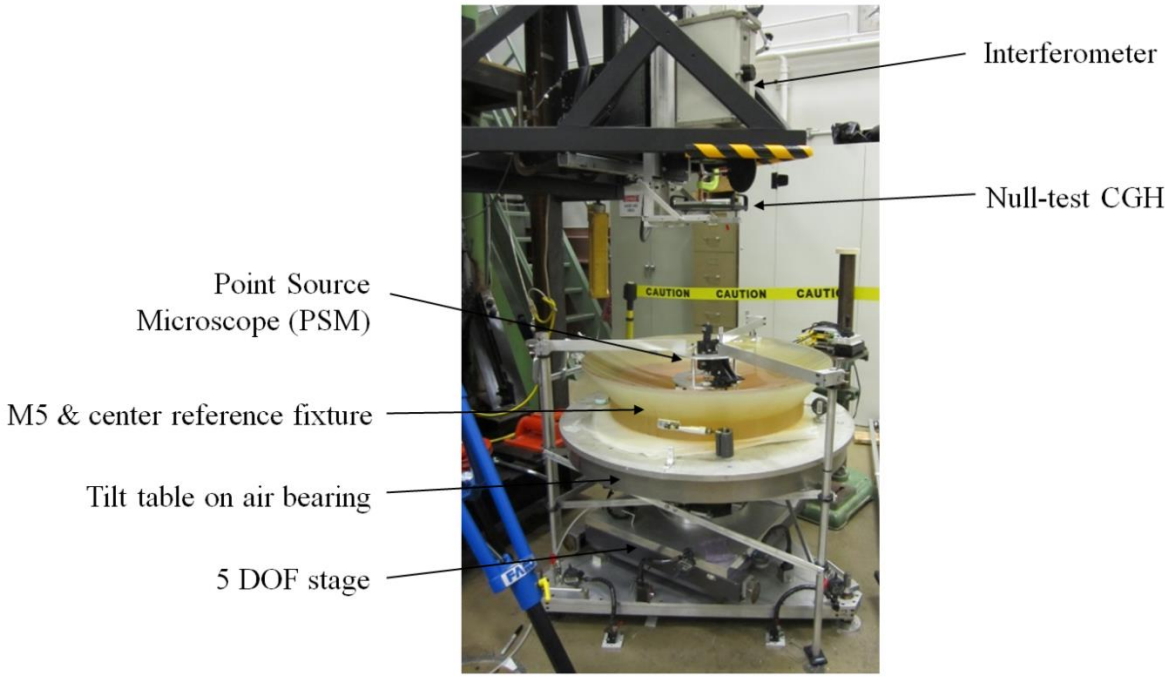

Figure 4.2: Surface testing and alignment setup for alignment of the M5 CGH reference in a center reference fixture.

4.1.1 Mirror to bearing alignment

In order to clearly explain the concepts presented in this section, a set of labels for the relevant aberration coefficients is used. The notation for the aberration

coefficients is summarized in Table 4.1. The labels for misalignments of the mirror or CGH are explained in Table 4.2.

Table 4.1: Zernike fringe aberration coefficient

Zernike Coefficient	Wavefront fit polynomial
Z_2	$\rho\cos\theta$
Z_3	$\rho\sin\theta$
Z_7	$(3\rho^3 - 2\rho)\cos\theta$
Z_8	$(3\rho^3 - 2\rho)\sin\theta$

Table 4.2: Zernike fringe aberration coefficient

Misalignment Label	Description of Mirror/CGH Position
Rx	Sloped along y-axis, tilted about x-axis
Ry	Sloped along x-axis, tilted about y-axis
Δ_x	Decentered along x-axis
Δ_y	Decentered along y-axis

Each aspheric mirror in the WFC has an associated null CGH test which is used to test the aspheric surface of the mirror. The null test for each mirror was simulated in Zemax in order to find the sensitivities of tilt and third-order coma Zernike coefficients to misalignments of the mirror. Simulated misalignments were introduced at the vertex of each mirror and sensitivities of the Zernike coefficients were evaluated for decenter and tilt independently. The net Zernike coefficients from a decenter, Δ_x, and tilt, Ry are described in Equation (4.1) and Equation (4.2).

$$\begin{bmatrix} Z_2 \\ Z_7 \end{bmatrix} = \begin{bmatrix} \emptyset_{11} & \emptyset_{12} \\ \emptyset_{21} & \emptyset_{22} \end{bmatrix} \cdot \begin{bmatrix} \Delta_x \\ \mathrm{Ry} \end{bmatrix} \tag{4.1}$$

where the sensitivities are defined as,

$$\emptyset_{11} = Z_{2\Delta}/\Delta_x,\ \emptyset_{12} = Z_{2\theta}/\mathrm{Ry}, \quad \text{(a)} \tag{4.2}$$

$$\emptyset_{21} = Z_{7\Delta}/\Delta_x, \text{ and } \emptyset_{22} = Z_{7\theta}/\mathrm{Ry}. \quad \text{(b)}$$

The net Zernike coefficients from a decenter, Δ_y, and tilt, Rx are described in Equation (4.3) and Equation (4.4).

$$\begin{bmatrix} Z_3 \\ Z_8 \end{bmatrix} = \begin{bmatrix} \emptyset_{11} & \emptyset_{12} \\ \emptyset_{21} & \emptyset_{22} \end{bmatrix} \cdot \begin{bmatrix} \Delta_y \\ Rx \end{bmatrix} \quad (4.3)$$

where the sensitivity is defined as,

$$\emptyset_{11} = Z_{3\Delta}/\Delta_y, \emptyset_{12} = Z_{3\theta}/Rx, \quad \text{(a)} \quad (4.4)$$

$$\emptyset_{21} = Z_{8\Delta}/\Delta_y \text{ and } \emptyset_{22} = Z_{8\theta}/Rx. \text{ (b)}$$

Note that due to the axisymmetric geometry the form of these equations and magnitudes of the sensitivities are identical for x and y oriented aberrations and misalignments as shown in the example data for M5 in Table 4.3.

Table 4.3: Tilt and coma sensitivity calculation from known perturbation in the M5 null test.

M5 Perturbation	**Z_2 (μm)**	**Z_7 (μm)**
Δ_x= 0.05 mm	-87.4668	8.7967
Ry= .001 degree	23.23439	-2.0650
	Z_3 (μm)	**Z_8 (μm)**
Δ_y= 0.05 mm	-87.4668	8.7967
Rx= .001 degree	23.2344	-2.0650

Mirror misalignments are evaluated with from the inverse of Equation (4.1) and Equation (4.3) given by,

$$\begin{bmatrix} \Delta_x \\ Ry \end{bmatrix} = \begin{bmatrix} \emptyset_{11} & \emptyset_{12} \\ \emptyset_{21} & \emptyset_{21} \end{bmatrix}^{-1} \cdot \begin{bmatrix} Z_2 \\ Z_7 \end{bmatrix} \quad (4.5)$$

and,

$$\begin{bmatrix} \Delta_y \\ Rx \end{bmatrix} = \begin{bmatrix} \emptyset_{11} & \emptyset_{12} \\ \emptyset_{21} & \emptyset_{21} \end{bmatrix}^{-1} \cdot \begin{bmatrix} Z_3 \\ Z_8 \end{bmatrix}, \quad (4.6)$$

where the sensitivities for Equations (4.5) and (4.6) come from Equations (4.2) and (4.4), respectively. The calculation of decenter and tilt based on measured Zernike

coefficients can be used to find the absolute misalignment of the mirror within the null-test and quantify how the alignment of the mirror changes as it is rotated about an axis. The tilt and third order coma Zernike coefficients are sinusoidal with rotation angle and when the mirror optical axis is aligned with the air bearing axis the amplitude of modulation in the Zernike coefficients approaches zero.

Figure 4.3 shows data from aligning M5 to the rotation axis of the air bearing. Data are collected every 45 degrees on rotation. The alignment of M5 to the bearing axis will be used as a representative example of the mirror alignment procedure. The average value of the Zernike coefficients represents a static misalignment of the rotation axis relative to the null-test CGH optical axis. The static misalignment is minimized to reduce measurement errors and the mirror axis is aligned to the air bearing axis by minimizing the modulation of the Zernike coefficients on rotation.

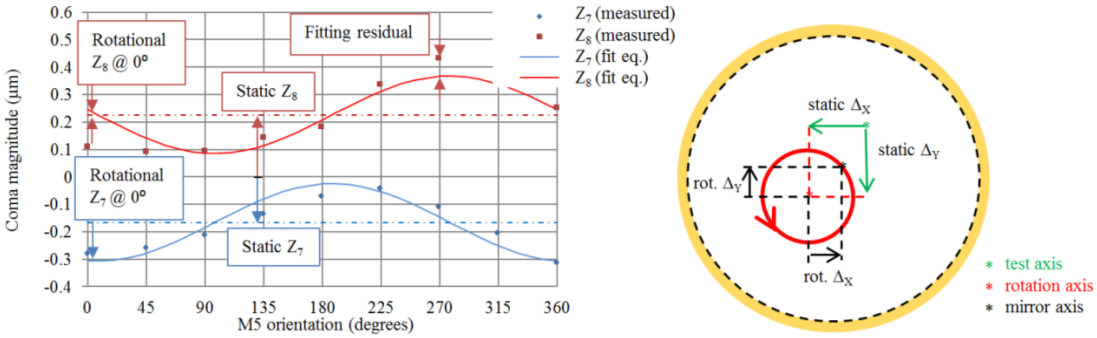

Figure 4.3: Example of coma data from the M5 null test with parameters relevant to the mirror alignment labeled on the plot (left) and geometric relationship of calculated axis locations (right).

The resulting dataset for each Zernike coefficient as a function of rotation angle was given by a least-squares fit of the measurements to a sine-wave. The relative phase of the fit-functions for *x* and *y* coefficients of each aberration was set at

90 degrees and the modulation amplitudes were set equal. The amplitudes were set equal because *x* and *y* components of the same aberration must vary with the same amplitude in rotation. The 90 degree relative phase follows directly from the expectation that rotational components of *x* and *y* components of the same aberration exchange magnitudes when the optic is rotated by 90 degrees.

The sine-wave least-squares fits determine the static aberration magnitudes and orientations, rotational modulation amplitudes of the aberrations, and the orientations of the rotational components of the aberrations. The static component of all Zernike coefficients was subtracted from each fit-function in order to isolate the mirror's misalignment from the bearing axis. The mirror's position was always evaluated and adjusted at the nominal orientation. The values of the isolated rotational components of the Zernike coefficients at the nominal orientation were entered in Equations (4.5) and (4.6) to determine the magnitude and direction of decenter and tilt of the mirror relative to the bearing. Decenter was always adjusted with two digital indicators against the OD of the mirror along the *x* and *y* axes. These indicators provided position feedback while adjusting mirror position to reduce the decenter between the mirror's optical axis and the bearing axis. Tilt was generally adjusted using the interference fringes as feedback, but the tilt of the mirror optical axis relative to the bearing was always measured during alignment of the alignment-CGH to properly quantify the resultant alignments.

Ideally the curve-fit is representative of the mirror to bearing alignment without any mechanical instability. If the mirror deviates slightly from its ideally sinusoidal changes in position and tilt during the measurement the aberrations associated with

the small deviation become residual values in the curve-fit. As the mirror approaches a level of rotational alignment that is comparable to the stability of the optical test the motion errors become dominant in the aberration data. Repeated averaged measurements at each mirror orientation ensure that the random interferometer errors are negligible in comparison to the aberration fitting residuals. Thus, the fitting residuals for aberration coefficients Z_2, Z_3, Z_7, and Z_8 at a particular orientation of the optic are correlated errors. For a given orientation the residual value of each coefficient is propagated into a mirror *x* direction residual using Equation (4.5), and similarly for y using Equation (4.6). Performing this calculation at each rotation angle generates a set of mirror position fitting residuals that are used in an RMS calculation of mirror position standard deviation for each degree of freedom. In order to claim 95% confidence in the alignment results the standard deviations of the mirror decenter and tilt are multiplied by two. The measured mirror alignments are given in Table 4.4.

Table 4.4: Mirror alignment errors relative to the air-bearing axis for each CGH alignment. Uncertainties given for a 2σ confidence interval.

	Mirror decenter magnitude (μm)	**Mirror tilt magnitude** (μrad)
M2, CGH1	18.5 ± 17.2	5.7 ± 5.6
M2, CGH2	13.6 ± 15.3	2.6 ± 7.2
M3, CGH1	3.7 ± 6.0	1.4 ± 2.1
M3, CGH2	3.5 ± 6.1	1.2 ± 2.2
M4, CGH1	2.4 ± 3.2	6.2 ± 12.7
M4, CGH2	2.5 ± 2.6	7.2 ± 9.7
M5, CGH1	4.1 ± 2.8	4.9 ± 3.0
M5, CGH2	4.2 ± 2.8	5.1 ± 2.9

4.1.2 CGH reference alignment

Runout of the CGH center mark and changes in CGH tilt angle were observed on rotation of the mirror and minimized such that the CGH optical axis was coincident with the bearing axis. The center reference fixtures provide adjustment of the CGH position in all degrees of freedom, as shown in Figure 4.4. Each fixture has three steel ball-point fine threaded actuators that provide axial support near the edge of the CGH. A plastic retainer ring with three leaf-springs puts a light preload on the CGH above the axial support contacts. There are also three radial contacts separated by 120º. One contact is a passive nylon ball and spring contact. This nylon ball contact puts a preload on the CGH to hold it against two fine threaded actuators which are identical to the axial constraints. The fine threaded actuators were either picomotors or #8-100 thumb screws. With feedback from the PSM either type of actuator permits adjustment resolutions of ~1μm for decenter and ~5μrad for tilt angle. The stability of the air-bearing allowed alignment of the CGH to the bearing axis with a precision of <2 μm in centration and <5 μrad in tilt.

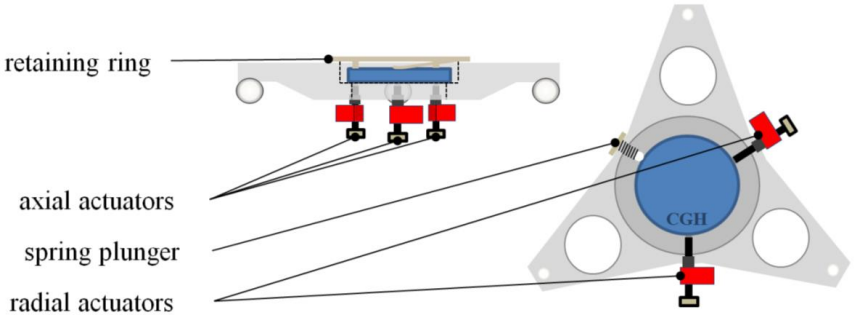

Figure 4.4: Geometry of actuators for CGH alignment.

The decenter and tilt of the CGH were monitored with a point source microscope (PSM) which may be used for imaging or autocollimation. In order to monitor the decenter of the CGH the PSM illuminated the surface of the CGH with a quasi-monochromatic LED and imaged a 40µm outside diameter center mark, shown in the top images of Figure 4.5. To monitor the CGH tilt the microscope objective was removed from the PSM and a fiber laser was used as the point source for autocollimation as in the bottom images of Figure 4.5.

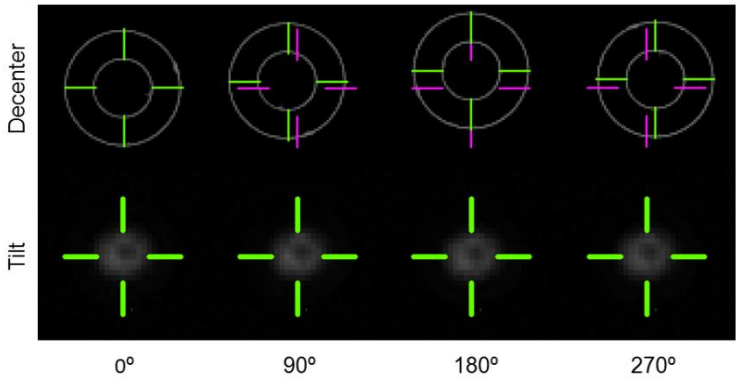

Figure 4.5: PSM diagnosis of the M5 CGH2 alignment after bond curing. 5.7µm residual decenter, 5µrad residual tilt.

Each CGH was bonded to the center-referencing fixture with RTV566 following the alignment procedure described above. To reduce the influence of bond contraction on the alignments the CGHs were prepared with three bond-pads to fill part of the gap from the CGH OD to the fixture ID. All of the CGHs were bonded to their fixtures with the fixtures still mounted to the mirrors. After removing the constraints each CGH was measured again to quantify its decenter and tilt relative to the mirror axis after the bond had cured. The CGH reference alignment results, which include both

measured alignment errors and uncertainties associated with the alignment diagnostics, are given in Table 4.5.

Table 4.5: CGH alignments relative to the mirrors' optical axes.

	CGH decenter magnitude (μm)	**CGH tilt magnitude** (μrad)
M2, CGH1	13.9 ± 24.1	10.8 ± 9.5
M2, CGH2	15.7 ± 23	5.2 ± 9.6
M3, CGH1	0.6 ± 6.0	35.9 ± 2.9
M3, CGH2	0.3 ± 6.1	21.6 ± 3.4
M4, CGH1	1.1 ± 4.5	7.6 ± 15.2
M4, CGH2	4.5 ± 4.5	8.3 ± 16.8
M5, CGH1	1.4 ± 3.8	3.6 ± 5.7
M5, CGH2	6.6 ± 4.1	5.4 ± 3.8

The parametric model and simulation for the HET WFC centration alignment presented in Chapter 3 makes it clear that the CGH alignment method offers precision and accuracy which is superior to the alignment of the CGHs to the mirrors. Thus, the accuracy of the CGH reference alignments is what drives the alignment errors and *not* the alignment scheme itself. Interestingly, the CGH centration alignments to the mirrors were performed with *amplitude* referencing to serve the *phase* referencing co-alignment scheme. The PSM used for the tilt alignment is also a fairly imprecise autocollimator due to its short focal length 100mm lens. However, the primary limitation for each of the CGH alignments was uncertainty in the alignment of the mirror to the bearing axis. The aberration alignment sensitivities are the highest for M5 and lowest for M2 and correspondingly the centration alignment uncertainties are much lower for M5 than for M2. Both of the mirrors were aligned to the same interferometer on the same air bearing with different transmission spheres and null CGHs.

4.1.3 Vertex registration of M2, M3, M5

In order to measure the spacing between the mirrors during the system alignment there must be a reference for the vertex locations. The center reference fixtures for M2, M3 and M5 have three SMR nests so that a laser tracker can measure the reference fixture position that is registered to the vertex of the mirrors by defining the spatial relationship between the calculated mirror vertex location and the SMR nest locations.

Each mirror is aspheric and has an optical axis which passes through a center bore. There is no physical vertex for any of the mirrors in the WFC. After the as-built mirror surface parameters have been determined the mirror surface is measured with the laser tracker by holding an SMR against the optical surface in a fixture that contacts the ID of the mirror and defines a consistent radial offset to the SMR center. A set of about 20 points were measured at the ID of each mirror, followed by a set of measurements on SMRs mounted in the center reference fixtures. The measurements made in contact with the optic define a circular geometry about the mechanical axis of the mirror. The geometry of the measurements is illustrated in Figure 4.6.

Given the measured mirror parameters, the virtual surface subtended by the measurement points can be modeled as equivalent to the mirror surface with its radius of curvature reduced by the radius of the SMR. The measured surface slope is easily determined by differentiating the sag equation and substituting the reduced radius for the mirror radius. Equations (4.7) and (4.8) give the mathematical form of the mirror surface sag and measured surface slope, respectively.

$$z(r) = \frac{r^2}{R + \sqrt{R^2 - (K+1)r^2}} + a_3 r^6 + a_4 r^8 + a_5 r^{10} \tag{4.7}$$

$$z'(r) = \frac{r}{\sqrt{R'^2 - (K+1)}} + 6a_3 r^5 + 8a_4 r^7 + 10a_5 r^9 \tag{4.8}$$

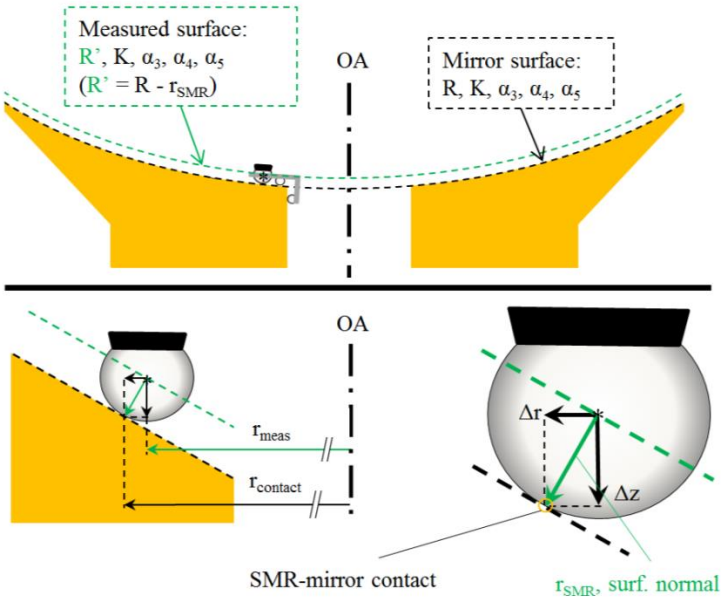

Figure 4.6: Cross-sectional view of the SMR in contact with the mirror. The surface subtended by the center of the SMR is shown in green and the mirror surface is in black.

The circular geometry constructed through the measured points has radius r_{meas} and the slope of the measured surface at r_{meas} is used to project the appropriate radial and axial distances Δr and Δz from the measurements to the actual point of contact with the mirror surface. These offsets are applied as a change in radius and an axial location of the fit-circle to create an average region of circular contact on the optical surface.

After the circular contact of the SMR against the mirror is determined the mirror surface sag equation is used to determine the z-offset of the vertex relative to

the measured points. This offset is referred to as z_{vertex}. The expressions for Δr, Δz, $r_{contact}$, and z_{vertex} are given below:

$$\Delta z = r_{SMR}\cos\left(tan^{-1}\left(z'(r_{meas})\right)\right) \quad \text{(a)}$$

$$\Delta r = r_{SMR}\sin\left(\tan^{-1}\left(z'(r_{meas})\right)\right) \quad \text{(b)} \qquad (4.9)$$

$$r_{contact} = r_{meas} + \Delta r \quad \text{(c)}$$

$$z_{vertex} = -\Delta z - z(r_{contact}) \quad \text{(d)}$$

Figure 4.7 shows the actual set up for the vertex registration of M2. This configuration allowed the laser tracker to be easily and stably positioned relative to the mirror and along its optical axis. In this geometry the encoder errors in the laser tracker should be symmetric and approximately equivalent between any two adjacent points.

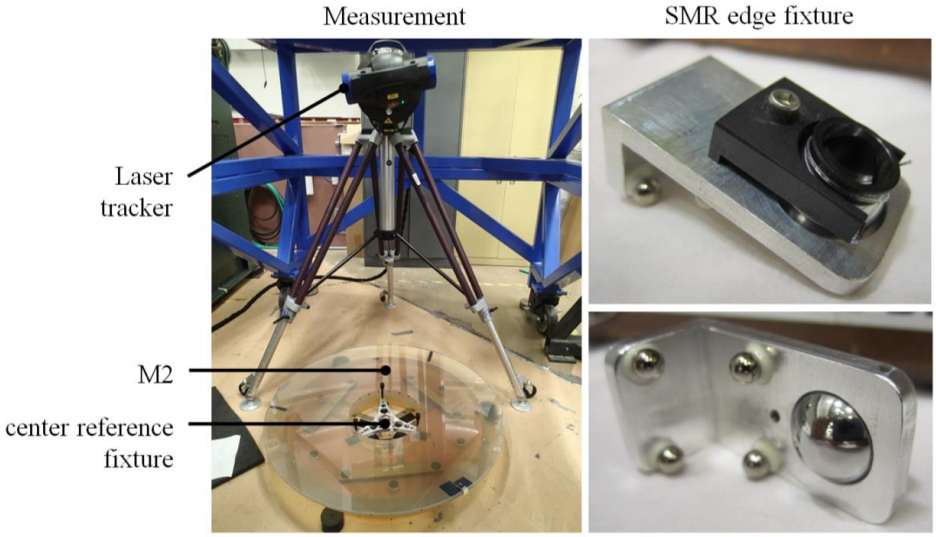

Figure 4.7: Laser tracker measurement setup for the M2 vertex registration. A similar configuration was also used for the M3 and M5 vertex registrations.

Table 4.6 presents the coordinates of the vertex of each mirror within a coordinate system that is established based on three SMR nests. This coordinate system is shown visually in Figure 4.8 using the M5 fixture as an example. The coordinate system is established by constructing a z-axis normal to a plane coincident with the three mounted SMR centers of curvature and coincident with the centroid of the three SMR center locations. The x-axis is coincident with one particular SMR center location on each fixture. The coordinate system is established based on the locations of the SMR centers so that during the system assembly the vertex location can be constructed within the measurement set.

The uncertainty of these coordinates includes the laser tracker measurement repeatability in measuring the mounted SMRs and determining the radius and height of the circle of measurements about the ID of the mirror. The uncertainty of the calculated vertex z-coordinate as a function of mirror surface parameter uncertainties was much smaller than the tracker uncertainties, so the glass-contact and fixture-mounted SMR measurement uncertainties dominated the vertex registration uncertainty. The independent components of the uncertainties for the M5 measurement are given in Table 4.7 to show how the 2σ uncertainties of the individual measurements result in the observed z-coordinate 2σ uncertainty. The uncertainty shown in Table 4.7 is the estimated 2σ uncertainty based on the results of several independent trials of the same vertex measurement and calculation.

Table 4.6: Registered vertex coordinates for each mirror within the coordinate system of the SMRs.

Mirror	X (mm)	Y (mm)	Z (mm)
M2	-0.134 ± 0.009	-0.045 ± 0.014	30.326 ± 0.007
M3	0.743 ± 0.003	-0.693 ± 0.006	55.109 ± 0.008
M5	0.069 ± 0.003	-0.018 ± 0.009	-26.998 ± 0.004

Table 4.7: Error contributions from dataset 1 of 6 from the M5 vertex measurement.

M5 vertex-height error source	error magnitude	$2\sigma_Z$ (mm)
Mirror Radius (mm)	0.04	0.00070
Mirror Conic	0.0001	0.00001
C-fit radius (mm)	0.0032	0.0012
C-fit z-coord. (mm)	0.0036	0.0036
	RSS	**0.0039**

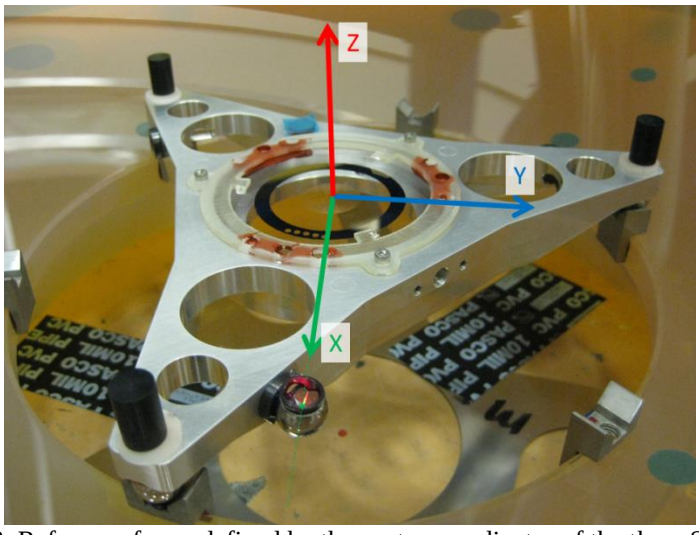

Figure 4.8: Reference frame defined by the center coordinates of the three SMRs on the M5 center reference fixture. Reference frame for the M2 and M3 fixtures was defined similarly.

4.1.4 Vertex registration of M4

The M4 vertex was registered to a single SMR on a vertex reference fixture. This was done by conducting two separate measurements. After polishing M4 its center was cored-out leaving the center core undamaged. The maximum thickness of this core was measured normal to its backplane to determine the normal distance from the polished M4 backplane to the mirror vertex. This measurement was performed by setting the planar surface of the core onto a flat and measuring both the curved

surface of the core and the surface of the flat. The measurements were performed with a point source microscope attached to a coordinate measuring machine (CMM) arm, where surface points were collected by the CMM encoders as the microscope reached a cat's eye retro-reflecting condition. Figure 4.9 shows the core measurement setup. The points collected on the curved surface of the core were used to construct a sphere and a plane was constructed from the points measured on the surface of the flat. The maximum normal distance from the flat to the curved core surface was determined by subtracting the normal distance from the plane to the sphere's center from the radius of the sphere.

The second measurement determined the normal distance from the center of the mounted SMR to the backplane of M4. In order to determine this distance the backplane of M4 was set on top of 3 chrome steel balls on the CMM with its vertex fixture fastened to the V-blocks, as shown in Figure 4.10. The CMM was used again with a point source microscope in order to measure the center of curvature location and radius of each ball contacting the M4 backplane and of the SMR mounted in the fixture. This measurement was performed 4 times and both M4 and its fixture were re-mounted each time the measurement was conducted.

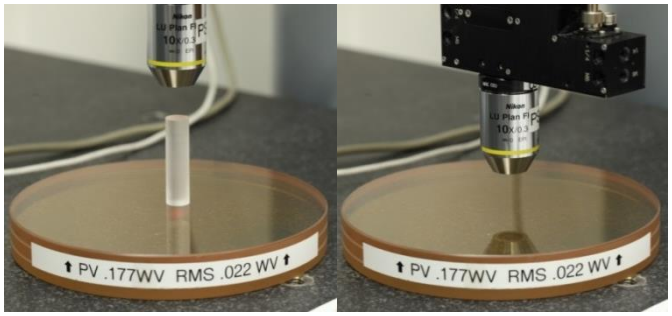

Figure 4.9: PSM on a CMM arm measuring the curved surface of the M4 core (left), and measuring the flat underneath the core (right).

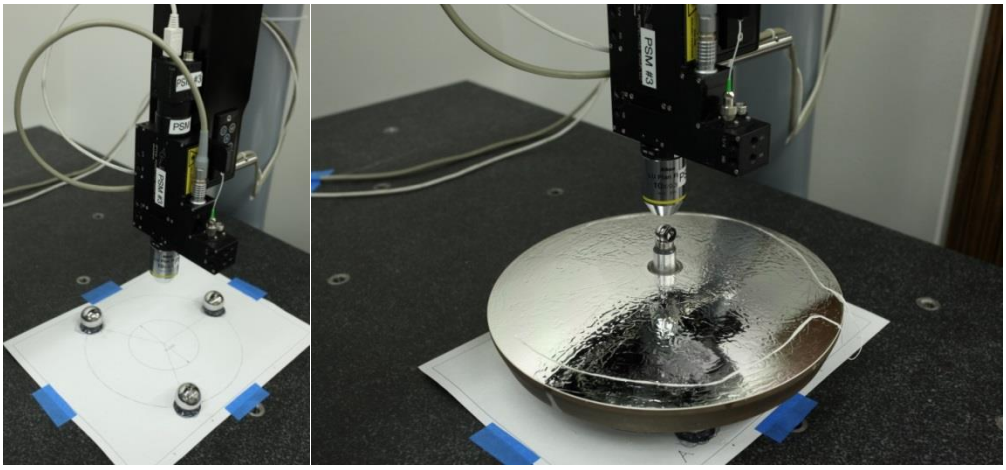

Figure 4.10: PSM on a CMM arm measuring the radii and center positions of the M4 support which is three steel balls (left) and the center of an SMR mounted in the M4 vertex reference fixture (right).

After conducting the measurements the data was processed in Spatial Analyzer. The data sets were transformed to match each other to best-fit, where the locations of the three balls contacting the backplane were aligned to each other at center of curvature. A total of 14 measurements were collected, per ball, to determine their radii. A reference frame was constructed such that the *xy* plane was coincident with the mirror backplane by ensuring that the center of curvature of each ball had a *z*-offset from the plane equal to its measured radius. The *z*-coordinates of the measured SMR locations in this reference frame were used to determine the expected offset of the SMR from the M4 backplane along its surface normal. The SMR location was registered to the vertex location by calculating the difference between the core thickness and the SMR offset from the M4 backplane. The measured quantities and their individual uncertainties are summarized in Table 4.8 to show how the final result was found.

Table 4.8: Uncertainties contributing to the M4 vertex reference fixture registration uncertainty.

Quantity	*Value (mm)*	*Uncertainty, 2σ*
Core surface radius	359.9213	0.00057
Core center of curvature to backplane	316.1135	0.00053
Ball A radius	12.703	0.0014
Ball B radius	12.304	0.0010
Ball C radius	12.699	0.0010
SMR center height from backplane	70.0568	0.0064
SMR to vertex, normal distance	**26.2490**	**0.0066**

4.1.5 Expected alignment performance

The HET WFC alignment performance is expected to depend on the reference accuracy and the accuracy of the alignment diagnosis. The expected reference accuracies are given above in terms of residual error and uncertainty in Table 4.5 and Table 4.6. Table 4.9 documents the worst-case combinations of the reference errors in relation to the HET WFC alignment tolerances. In all of the centration and tilt alignments the reference errors are much larger than the corresponding expected random diagnostic errors given in Table 3.4 in Chapter 3. For the axial alignments an additional estimated ±10μm random uncertainty should be considered for laser-tracker diagnosis of the SMR reference heights *in situ*. The adjustment accuracy and stability of the mirrors is the other major alignment error source. The contributions to centration alignment from other effects are analyzed by Coyle[5], but were ultimately either mitigated or deemed negligible in this implementation. These reference errors are expected to be consistent with a successful implementation for the alignment of the HET WFC.

Table 4.9: Worst-case combinations of CGH and SMR reference errors in relation to the alignment tolerances. All of the degrees of freedom have sufficiently low reference errors.

Degree of Freedom	Tolerance	Maximum reference error (2σ)	Unit
M2 to M3 axial	100	10.6	µm
M2 to M5 axial	100	8.1	µm
M4 to M5 axial	20	7.7	µm
M2 decenter (radial)	71	38.4	µm
M3 decenter (radial)	71	8.2	µm
M4 decenter (radial)	28	7.6	µm
M4 M5 decenter (radial)	71	5.2	µm
M2 tilt (magnitude)	69	17.4	µrad
M3 tilt (magnitude)	69	26.6	µrad
M4 tilt (magnitude)	114	24.6	µrad
M4 M5 tilt (magnitude)	79	9.2	µrad

4.2 INITIAL ALIGNMENT

4.2.1 Laser tracker alignment

A reference frame was established based on the locations of three hemispherical kinematic mounting interfaces on the corrector's frame to meet the system requirement for the location of the optical axis of the WFC in the telescope. This reference frame is illustrated in Figure 4.11. Within this reference coordinate frame the mirrors have prescribed nominal *z*- coordinates that are derived from the system prescription in Table 2.2. The CGH in each mounted center reference fixture must be aligned such that it is centered on and normal to the *z*-axis.

Although the laser tracker only serves as a final alignment reference for mirror spacing it is very useful for initial mirror alignment. The three SMR locations on the center reference fixtures for M2, M3, and M5 were registered to the centroid and plane of their reference CGHs using the PSM mounted on a CMM arm, as shown in

Figure 4.12. This registration allows the set of mounted SMR locations for each fixture to be used as a reasonably accurate reference from which to define mirror tilt and centration. After this registration is performed the mirror's reference locations are diagnosed within the reference frame of the corrector to determine how the mirror must be moved to achieve its nominal alignment. With the guidance of the laser tracker the Wide Field Corrector is aligned to the specification of initial alignment as in Table 4.10.

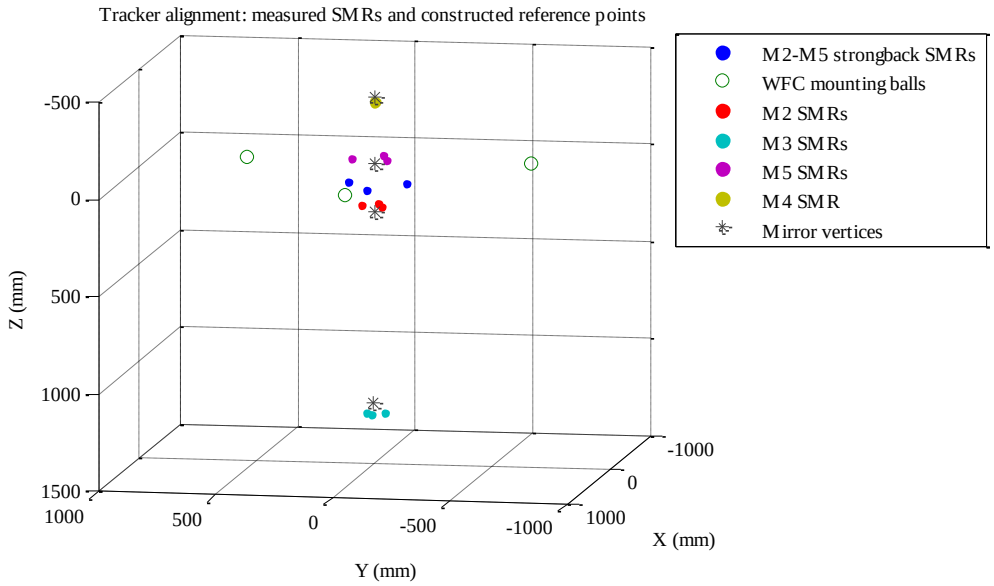

Figure 4.11: Reference frame for the WFC system alignment.

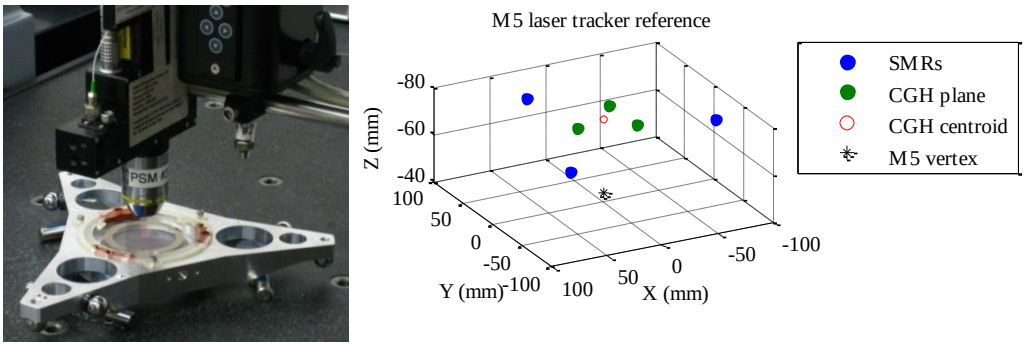

Figure 4.12: M5 center reference fixture in measurement setup under the PSM on a CMM (left) and measured points of SMR centers, points on the plane of the CGH, location of the CGH centroid, and registered vertex location (right).

Table 4.10: Initial expected mirror alignment errors using the center reference fixtures with the laser tracker guidance

	M2	M3	M4	M5
Tilt, X (µrad)	-23	-5	N/A	13
Tilt, Y (µrad)	23	-24	N/A	-4
Decenter, X (µm)	6	-15	13	26
Decenter, Y (µm)	9	16	-1	-38
Axial position error, Z (µm)	-69	-9	-8	4

4.2.2 CGH alignment

Following the laser tracker alignment of the mirrors were measured in tilt and centration relative to M4 using the proposed CGH alignment scheme. The conceptual layout for this setup was given in Figure 2.4 of Chapter 2. The autocollimator is shown on its calibration mount in Figure 4.13. This autocollimator is the same as the one which achieved 2σ tilt measurement uncertainties of ±5.66µrad in the demonstration by Coyle[5]. The autocollimator has a 300mm achromatic doublet objective lens with an adjustable iris diaphragm aperture. The adjustable aperture allows adjustment of the beam size to illuminate the inner and outer zones of the M4 reference CGH or just the inner zone. Figure 4.13 also shows the fringes which were used to collimate the autocollimator beam. The alignment autocollimator is mounted directly above M4 and all the other WFC mirrors in a separate hexapod structure as shown in Figure 4.14. From this position it illuminates the M4 reference and other reference CGHs through the M4 center hole. Below the WFC and mounted to the M3 strong back there is a video microscope, as shown in Figure 4.15. This microscope is infinity-corrected with a 100mm tube lens and a Point Grey Flea2 monochrome FL2G-13S2M-C CCD detector, both of which are common to the PSM used in the demonstration of this alignment. The microscope objective was exchanged between

4X and 10X Olympus RMS-thread objectives to vary the field of view and sensitivity as needed to diagnose the centration alignments.

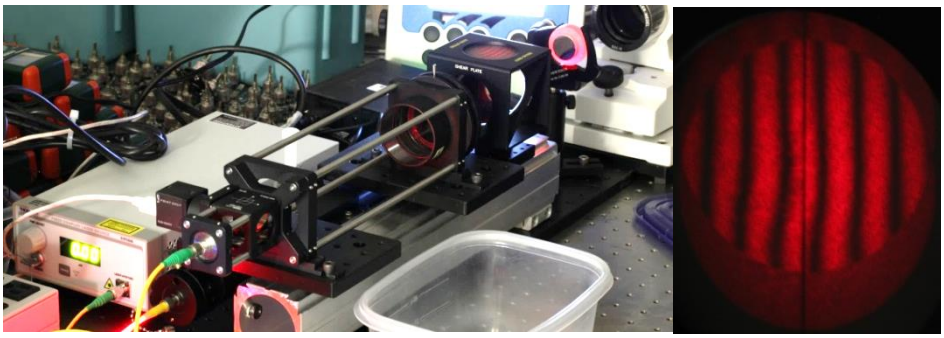

Figure 4.13: CGH center reference tilt and centration alignment autocollimator (left) and the shear plate interferometer beam measurement (right).

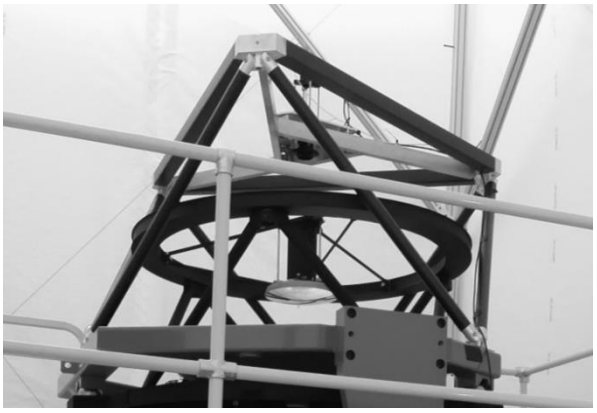

Figure 4.14: Alignment autocollimator mounted in hexapod structure above the M4 head ring and hexapod holding M4.

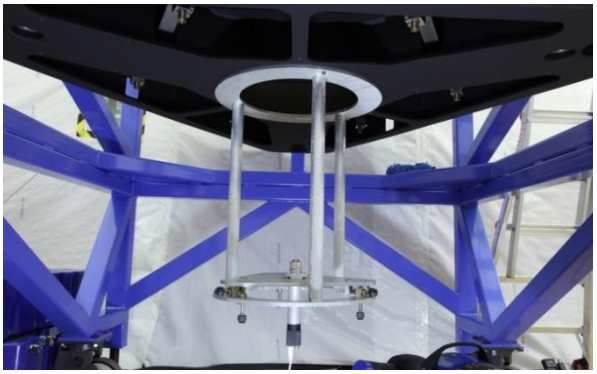

Figure 4.15: Video microscope on fixture at the M3 strong-back interface for measuring the centration alignment spots.

The tilt and centration alignments were carried out several months after the alignment verification of each of the CGH references. A set of images showing the spot image data in each configuration of the centration check is given in Figure 4.16. It has already been claimed that the primary limiting factor in this implementation is the accuracy of the CGH reference alignments. To check the stability of the references the tilt and centration alignments measurements were made with one reference for a given mirror under alignment before exchanging this for the other redundant reference. The expectation was that the decenter measurement results should be consistent between these redundant references to the accuracy of the PSM measurements at the time the CGHs were aligned. Note that the location of the mirror relative to the bearing during this alignment is not relevant to the *consistency* of the CGH alignments. The consistency between the centration diagnoses for the mirrors is given in Table 4.11.

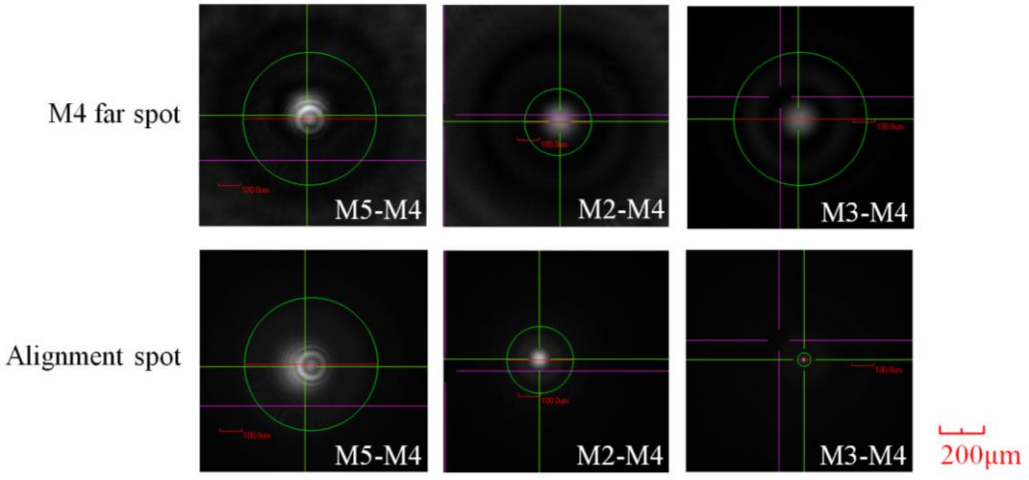

Figure 4.16: Video microscope images of the spots produced by the CGH alignment configurations. The top row are produced by the M4 CGH reference directly and the bottom row are produced by the M4 CGH and a second mirror reference. All images have the same object-space scale given at right.

Table 4.11: Consistency of CGH references in tilt and centration at first diagnosis, 09/11/2013.

Mirror	Tilt consistency	Centration consistency
M4	24 ± 6	7.5 ± 1
M5	72 ± 6	36.2 ± 0.4
M2	80 ± 6	1.0 ± 0.4
M3	192 ± 6	0.5 ± 1

The data in Table 4.11 represent a significant problem. The RTV566 used to bond the CGH references to the aluminum frame was not dimensionally stable over a period of several months. The tilt consistencies are all greater than expected and for M5, M2 and M3 the discrepancies are larger than the tilt alignment tolerances. The centration consistency for the M5 references is also outside of the allowable alignment tolerance for M5 decenter relative to M4. After making these measurements the project took on significant risk by continuing under a set of assumptions. Table 4.12 outlines which degrees of freedom were considered to be without a legitimate alignment reference and which degrees of freedom were assumed to be constrained by the references. The assumption that M4 retained legitimate references for tilt and centration was based on the relatively small discrepancies between its redundant CGH references. The same can be said for the other references which were assumed to be legitimate. Constraint of the other degrees of freedom was done through a set of subsystem interferometer tests in a revised alignment plan.

Table 4.12: Outline of assumptions on which alignment references are valid in HET WFC alignment, where ”Y” represents yes and “N” represents no with reference to their validity.

Mirror	Tilt Reference	Centration Reference	Axial Reference
M4	Y	Y	Y
M5	N	N	Y
M2	N	Y	Y
M3	N	Y	Y

4.2.3 Revised alignment plan

In the presence of misaligned references the decision was made to align the HET WFC with the references which were assumed to still be accurate and two subsystem null tests. The subsystem null tests are referred to as the M2-M3 subsystem test and the M4-M5 subsystem test. Each of these tests are axisymmetric and the interferometer focus position and CGH position are measureable by laser tracker and with the alignment autocollimator. Figure 4.17 and Figure 4.18 show labeled layouts of each of the subsystem tests to identify where the components are, which are aligned by reference measurements and which mirror degrees of freedom (DOF) are used to compensate aberrations in the test.

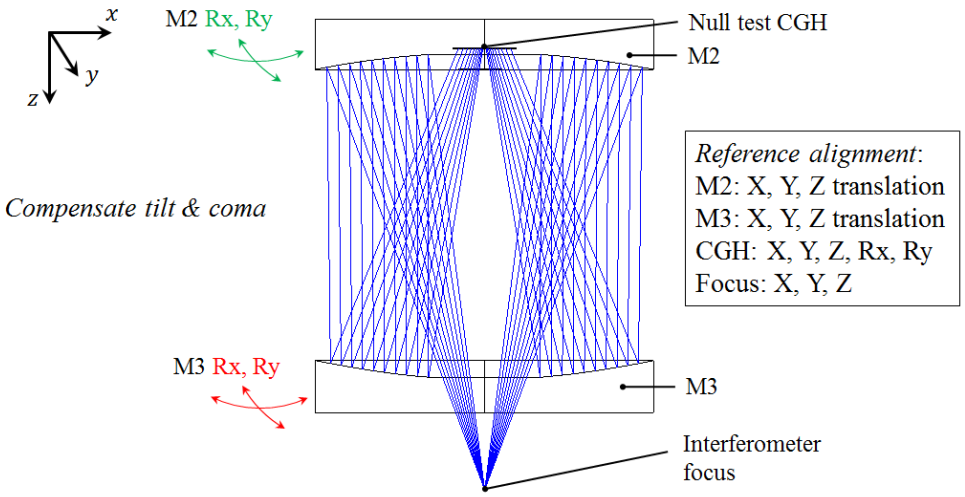

Figure 4.17: Layout of the M2-M3 subsystem null test. The tilt of M2 and tilt of M3 were adjusted to compensate tilt and coma in the test wavefront with other optical components aligned by other methods.

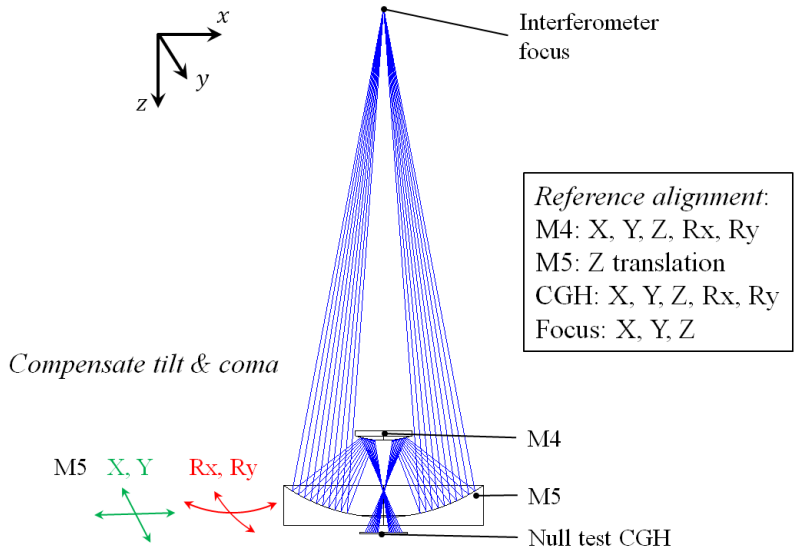

Figure 4.18: Layout of the M4-M5 subsystem null test. The translation and tilt of M5 were adjusted to compensate tilt and coma in the test wavefront with other optical components aligned by other methods.

Figure 4.19 provides an example of how the mirror alignments are calculated from aberrations in the M2-M3 test. Each misalignment has an aberration sensitivity "fingerprint" represented by the columns of matrix "A" in the forward linear equation. The distinction between the ratios between tilt and coma from a tilt of M2 versus a tilt in M3 allows the *inverse* calculation to derive the misalignments with a reasonably small degeneracy. If the alignment sensitivities were identical for these two mirrors this method would be ineffective at identifying between a misalignment in M2 and a misalignment in M3. The calculation of decenter versus tilt of M5 in the M4-M5 test follows an identical approach with different sensitivities applied in matrix "A".

Forward equation (M2-M3 pair)

Sensitivities (wv/deg)						Alignments (deg)			Coefficients (wv)	
Z2	**23575.6**	0	**-23156.8**	0		M2 Ry	**0.000756**		Z2	**56.694**
Z3	0	**-23597.6**	0	**23157.2**		M2 Rx	**-0.00032**		Z3	**17.697**
Z8	**14.698**	0	**71.794**	0		M3 Ry	**-0.00168**		Z8	**-0.111**
Z7	**0**	**-14.725**	0	**-71.797**	*	M3 Rx	**0.000441**	=	Z7	**-0.027**
Z16	**-1.562**	0	**-5.002**	0					Z16	**-0.016**
Z17	0	**1.562**	0	**5.003**					Z17	**-0.008**
Z30	**0.962**	0	**-0.731**	0					Z30	**0.013**
Z29	0	**-0.962**	0	**0.731**					Z29	**0.003**
	A						B			C

Inverse equation: $B = [A^T A]^{-1} A^T C$

Figure 4.19: Example of the least-squares inverse calculation method used to derive the expected alignment of M2 and M3 tip/tilt from Zernike standard annular tilt, primary coma, and higher order coma coefficients.

The subsystem tests were *not* used as verification of the system alignment. The risk of misalignment within a subsystem or between the subsystems was addressed with two independent tests. A second M4-M5 subsystem test was carried out by the University of Texas to check the transmitted wavefront through this

subsystem from a grid of source locations. A full system double-pass CGH-corrected null test was also performed to confirm that the on-axis transmitted wavefront aberration coefficients were within the expected range for an aligned system.

4.3 SUBSYSTEM ALIGNMENTS

This section will describe the designs of the M2-M3 and M4-M5 subsystem tests, provide documentation of the experimental setups, and give alignment results for each test. The alignment of the mirrors and test optics with optical and mechanical references will be described and the results of alignment of the mirrors based on the test aberrations will also be given.

4.3.1 M2-M3 subsystem test

The M2-M3 test is composed of 4 optical surfaces with a 4D Phasecam 6000 focusing light and measuring light from the focus surface. The axial positons of these surfaces are given relative to the paraxial focus of the HET in Table 4.13.

Table 4.13: Axial positions of the M2-M3 test surfaces. Paraxial focus of HET is used as the reference location, consistent with the WFC prescription given in Chapter 3.

Surface	Z (mm)
M2-M3 test focus	394.682
M2 vertex	-925.759
M3 vertex	61.466
M2-M3 test CGH	-937.156

The alignment of the test optics was performed with a laser tracker and the alignment autocollimator. The interferometer focus only requires translation alignment. An SMR was placed on an XYZ stage and aligned to the target focus

position. The XYZ stage with an SMR nest on the end of a rod is shown mounted to the M3 strong-back in Figure 4.20. The interferometer was positioned with a separate mount to focus at the center of the SMR. This alignment of the interferometer focus was diagnosed by observing a null from the interferometer to indicate retro-reflection from the ball surface.

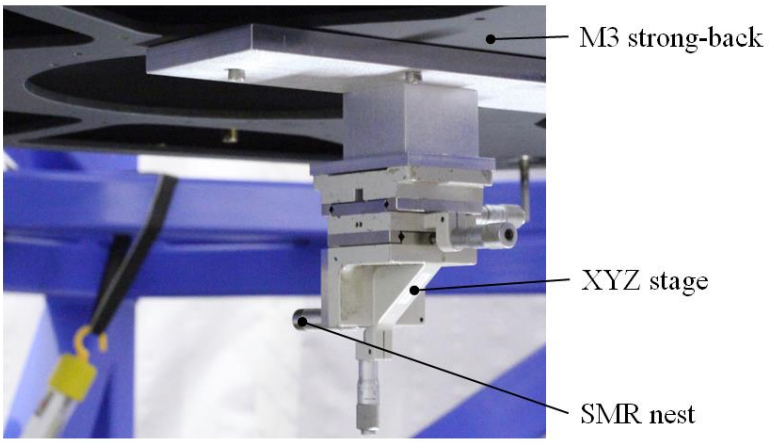

Figure 4.20: SMR mount for interferometer focus alignment in the M2-M3 test.

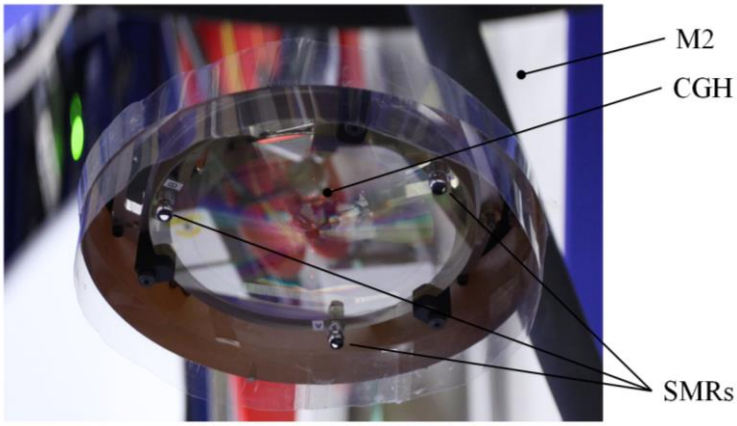

Figure 4.21: M2-M3 test CGH mounted to the M2-M5 strong-back visible within the inner bore of M2. Three SMRs are mounted in nests outside of the test pattern.

The CGH has three SMR nests which were measured relative to the center of its test pattern so that the laser tracker can measure the position of the CGH. The CGH is shown in its mount in Figure 4.21. The backplane of the CGH was also polished with minimal wedge relative to the front surface so that the alignment autocollimator could align this optic relative to the M4 tilt reference. Additionally, the CGH has an annular alignment pattern which retro-reflects light from the interferometer. Thus, it was possible to make a wavefront referencing measurement to constrain the interferometer focus along the axis of this CGH. The assembled M2-M3 test is shown fully assembled and under alignment in Figure 4.22.

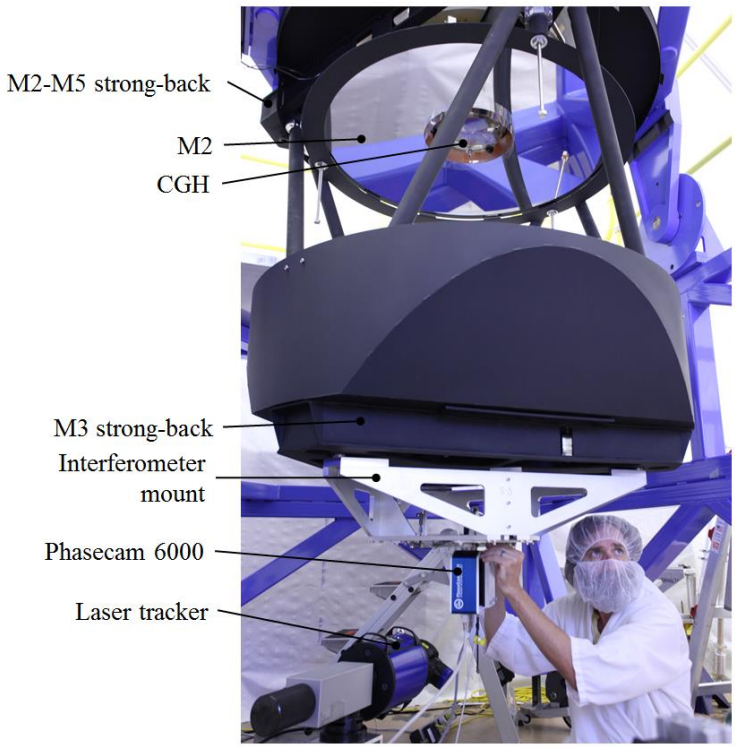

Figure 4.22: M2-M3 test under alignment by Bryan Keener Smith.

The subsystem test OPD map was fit to a Zernike standard annular polynomial basis generated as discrete terms in Matlab. Terms Z1-Z8 and Z11 from this basis are given in analytic form in Appendix B for transparency. These are consistent with the terms generated for a given obscuration ration in Zemax. The terms are orthogonal over the annular test aperture and the coefficient values represent the independent contributions of each term to the RMS wavefront OPD.

The aligned positions of the test optics for the M2-M3 test on 10/09/2014 are given in Table 4.14. The M2-M3 test response after alignment of M2 and M3 to compensate tilt and coma is shown as an OPD map and interferogram in Figure 4.23. The test parameters associated with the test for this measurement are given in Table 4.15. The obscuration ratio was used to generate the Zernike basis which was used to fit the OPD map. The Zernike standard annular term coefficients are given in Noll ordering in Table 4.16. The mirror misalignments listed in Table 4.17 and Table 4.18 were calculated from these aberration coefficients. Note that the absolute tilt values are susceptible to uncertainty due to uncertainty in the positions of optics aligned with other references. However, the relative tilts between the mirrors are based on the aberration coefficient uncertainties and these are relatively precise. The analysis to set these uncertainties was provided by Hanshin Lee of the University of Texas. The analysis was based on alignment and interferometer measurement uncertainties provided by the University of Arizona. The relative mirror tilts are more analogous to the random tilt errors addressed in the original tolerance analysis, whereas the correlated mirror tilts were addressed by a separate statistical analysis before

acceptance of the WFC. These results represent an adequate result from which we moved to a co-alignment with the M4-M5 subsystem test.

Table 4.14: M2-M3 test surface laser tracker alignments measured 10/09/2014. Coordinate system set to place CGH and focus on-axis.

Surface	X (mm)	Y (mm)	Z(mm)	δZ (mm)
M2-M3 test focus	0.000	0.000	394.763	0.081
M2 vertex	0.004	-0.011	-925.759	0.000
M3 vertex	-0.005	0.009	61.463	-0.003
M2-M3 test CGH	0.000	0.000	-937.151	0.005

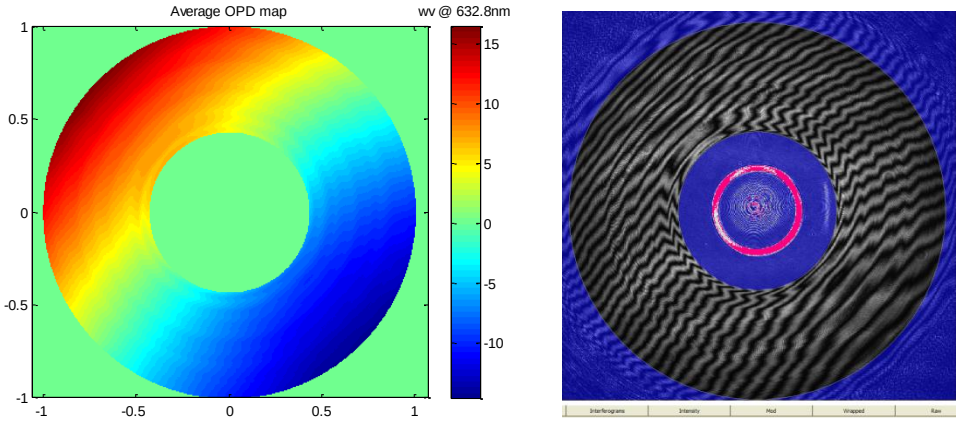

Figure 4.23: M2-M3 test response after alignment , measured on 10/09/2014

Table 4.15: Parameters of the M2-M3 test.

Test parameter	Value
Test wavelength, λ	632.8 nm
Obscuration ratio, ϵ	0.43
Outer test beam semi-diameter at M2	417.8 ± 2 mm
Inner test beam semi-diameter at M2	179.6 ± 1 mm
Numerical aperture at diverger lens	0.31
Wedge factor (OPD scaling)	1

Table 4.16: Aberration coefficients from fitting M2-M3 test data to a Zernike standard annualr term basis. Terms are numbered by Noll ordering, as in Zemax. Terms compensated with M2 and M3 tilt alignments are highlighted in blue. Data collected 10/09/2014.

Term	Aberration	Zernike standard annular coefficient value (wv)	Coefficient uncertainties (wv, 2σ)
1	Piston	-0.0349	0.0023
2	Tilt 0-deg	-6.09	0.29
3	Tilt 90-deg	5.9	0.2
4	Power	0.511	0.048
6	Astigmatism 0-deg	0.069	0.05
5	Astigmatism 45-deg	-0.022	0.045
7	Coma 90-deg	0.065	0.02
8	Coma 0-deg	0.116	0.029
11	Primary Spherical	0.1193	0.0059
16	Secondary Coma 0-deg	-0.035	0.01
17	Secondary Coma 90-deg	0.0195	0.0046
22	Secondary Spherical	-0.0925	0.0016
29	Tertiary Coma 90-deg	-0.0054	0.0023
30	Tertiary Coma 0-deg	0.0073	0.0046
37	Tertiary Spherical	0.05373	0.00059
46	Quaternary Coma 0-deg	-0.0031	0.0018
47	Quaternary Coma 90-deg	0.0047	0.0014
56	Quaternary Spherical	-0.01571	0.0005

Table 4.17: Calculated absolute tilt values for M2 and M3 relative to the testing axis defined by the interferometer and CGH. The asterisks indicate correlation between the DOF where misalignment of one mirror tends to result in compensation by misalignment of the other. Data collected 10/09/2014.

DOF	Calculated tilt (μrad)	Estimated uncertainty (μrad)
M2 Ry*	25	±115
M2 Rx**	4	±115
M3 Ry*	27	±125
M3 Rx**	-2	±125

Table 4.18: Calculated relative tilt values for M2 relative to M3. The relative tilt uncertainties are much lower and within the original tolerances. Data collected 10/09/2014.

Relative tilts	Calculated tilt (μrad)	Estimated uncertainty (μrad)
M2 Ry - M3 Ry	-2	±35
M2 Rx - M3 Rx	6	±35

After aligning the M4-M5 test to the M2-M3 test the M2-M3 test was repeated on 11/20/2014. The constraints were set identically to the limit of measurement and adjustment accuracies and the M2 and M3 tilts were calculated again. The M2 and M3 tilt alignments from this second M2-M3 test are given in Table 4.19 and Table 4.20. The difference between the values from 10/09/2014 and from 11/20/2014 are given in Table 4.21. These differences are all well within the bounds of uncertainty predicted by Hanshin Lee. This observation supports the accuracy of the estimated uncertainties for mirror alignments calculated from the interferometer test results. Furthermore, the superior repeatability of the relative tilts is consistent with Lee's prediction of lower uncertainty for tilt of M2 relative to M3.

Table 4.19: Calculated absolute tilt values for M2 and M3 relative to the testing axis defined by the interferometer and CGH. The asterisks indicate correlation between the DOF. Data collected 11/20/2014.

DOF	Calculated tilt (μrad)	Estimated uncertainty (μrad)
M2 Ry*	-5	±115
M2 Rx**	-54	±115
M3 Ry*	4	±125
M3 Rx**	-78	±125

Table 4.20: Calculated relative tilt values for M2 relative to M3. Data collected 11/20/2014.

Relative tilts	Calculated tilt (μrad)	Estimated uncertainty (μrad)
M2 Ry - M3 Ry	-9	±35
M2 Rx - M3 Rx	24	±35

Table 4.21: Calculated tilt discrepancies between two independent alignments and measurements of the M2-M3 test. The discrepancies are all well within the uncertainty intervals predicted by Hanshin Lee. The relative tilts are more repeatable than absolute tilts.

DOF	Tilt discrepancy (µrad)	Estimated uncertainty (µrad)
M2 Ry*	-30	±115
M2 Rx**	-58	±115
M3 Ry*	-23	±125
M3 Rx**	-76	±125
M2 Ry - M3 Ry	-7	±35
M2 Rx - M3 Rx	18	±35

4.3.2 M4-M5 subsystem test

The M4-M5 test is composed of 4 optical surfaces with a 4D Phasecam 6000 focusing light and measuring light from the focus surface. The axial positons of these surfaces are given relative to the paraxial focus of the HET in Table 4.22.

Table 4.22: Axial positions of the M2-M3 test surfaces. Paraxial focus of HET is used as the reference location, consistent with the WFC prescription given in Chapter 3.

Surface	Z (mm)
M4-M5 test focus	-3404.733
M5 vertex	-1168.496
M4 vertex	-1505.881
M4-M5 test CGH	-1101.045

The first alignment task was alignment of M4 to the aligned M2-M3 subsystem. M4 was being coated while the M2-M3 test was aligned, so the centration and tilt alignment scheme was actually done in an interesting way where the M4 center reference CGH was under alignment to the M2 and M3 CGH references. This is not inherently different, but in practice it was necessary to illuminate the M4 CGH at the correct angle so that the alignment axis created by the M4 reference CGH

would coincide with the already aligned M2 and M3 center reference CGHs. The relationship between the mirrors' decenters and tilts is illustrated in Figure 4.24. Ideally the autocollimator beam is aligned normal to the M2-M3 test CGH and M4 is aligned so that its CGH projects a datum alignment axis concentric to the M2 and M3 center references. This is impossible to achieve to perfection in practice and it is true that the M2 and M3 mirrors were aligned by laser tracker to the M2-M3 test CGH and interferometer. Thus, this CGH co-alignment which was used to align M4 to the M2-M3 test is inherently different and residual M2 and M3 decenter errors were expected.

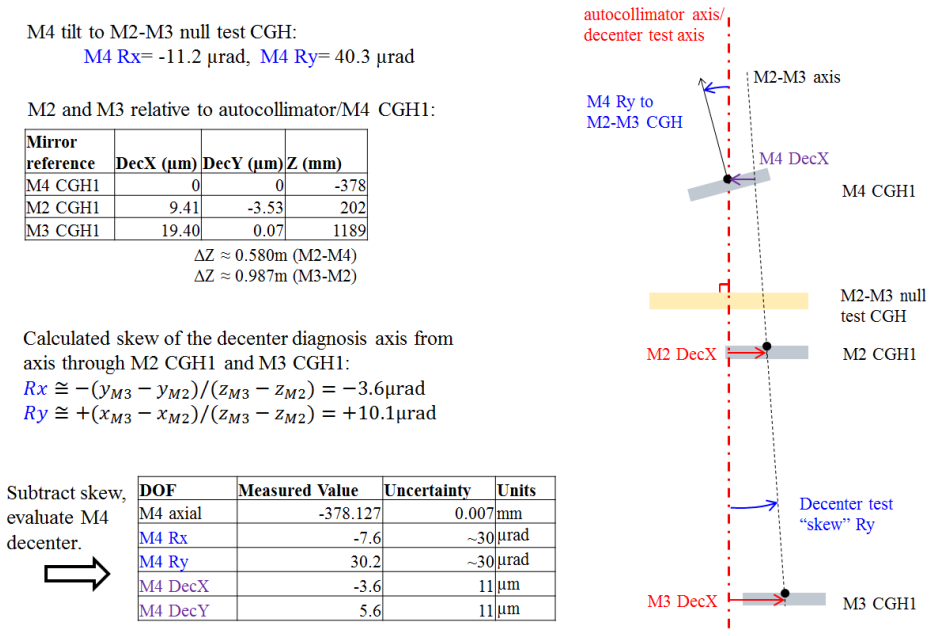

Figure 4.24: Illustration of alignment values in relation to the decenter measurement axis and a transformed reference frame for processing of alignment results for alignment diagnosis of M4 to the M2-M3 test. The transformation calculation is given and a calculation of the M4 alignment relative to M2 and M3.

In order to keep all of the misalignments within tolerance, during the adjustment of M4 the tilt and decenter alignment values for all of the mirrors were transformed in a consistent manner. The centration reference uncertainties for M2 and

M3 were already fairly large, so the alignment results were transformed to maintain a constraint where the M2 and M3 CGH reference were both along the axis of alignment. This is accomplished by changing the orientation and translating the reference frame in which the alignment data are considered. Figure 4.24 shows this nicely, where it is clear that such a transformation will influence the centration of M4 relative to an axis through the M2 and M3 references as well as the tilt of *all* the references. Therefore, it is entirely possible to make the tilt DOF suffer in the pursuit of compensating residual centration errors and this transformation is only justifiable based on a specific set of alignment results.

The data given in Figure 4.24 were actually collected *after* alignment of the M4-M5 test when the M2-M3 test was repeated and M4 position diagnosed to verify the full system alignment by repeating all of the alignment diagnoses. Thus, the tilt and decenter of M4 given in Figure 4.24 are *verification* results and subject to any instabilities and unrepeatability in aligning the M2-M3 test by laser tracker and interferometer measurements. Furthermore, all these values are well within tolerance and the more sensitive alignment of M4 to M5 is addressed by aligning M5 within the M4-M5 null test.

The alignment of the test optics was performed with a laser tracker and the alignment autocollimator. One of the M4 center references was aligned in tilt, along with M4, to match the M2-M3 test CGH before it was removed following the M2-M3 test. The M4-M5 test CGH was then aligned with the alignment autocollimator to the M4 center reference to match the angle of this test CGH with that of the aligned M2-

M3 test CGH. Again, the interferometer focus only required translation alignment and an SMR was placed on an XYZ stage and aligned to the target focus position. The XYZ stage with an SMR nest on the end of a rod is shown mounted to the interferometer testing tower in Figure 4.25. The interferometer was positioned with a separate mount to focus at the center of the SMR. This alignment of the interferometer focus was diagnosed by observing a null from the interferometer to indicate retro-reflection from the ball surface.

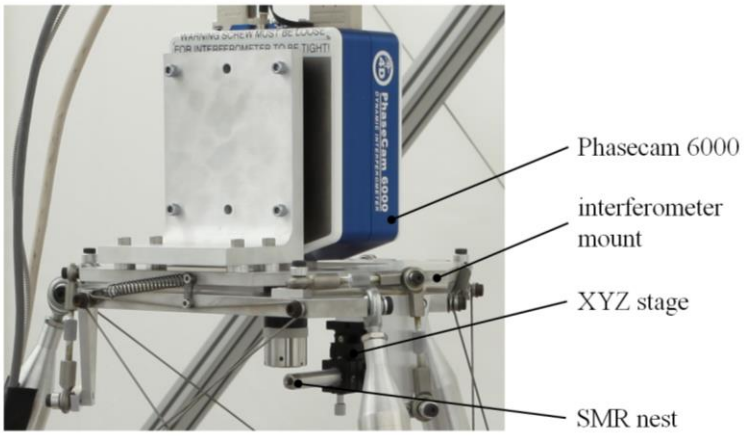

Figure 4.25: Interferometer mounted above the HET WFC with XYZ stage to position a nested SMR to locate and align the M4-M5 test focus.

The CGH has three SMR nests which were measured relative to the center of its test pattern so that the laser tracker can measure the position of the CGH. The CGH is shown in its mount in Figure 4.26. The backplane of the CGH was also polished with minimal wedge relative to the front surface so that the alignment autocollimator could align this optic relative to the M4 tilt reference. This CGH is obscured from the interferometer focus position by the M4 backplane, so there is no annular alignment pattern on this CGH. The alignment of the interferometer focus and CGH are done entirely by laser tracker guidance relative to the M2-M3 test axis.

M4 was aligned to M2 and M3 by CGH reference co-alignment. CGH and focus of the M4-M5 test were aligned to the M2-M3 test axis which had been diagnosed in its aligned state with the laser tracker. The assembled M4-M5 test is shown fully assembled in Figure 4.27.

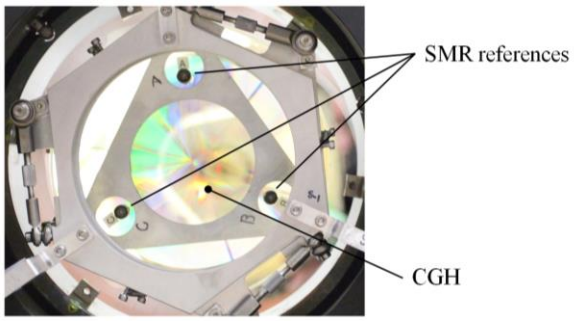

Figure 4.26: View from below the M4-M5 test of the M4-M5 test CGH in its mount with the SMR references installed at tits backplane.

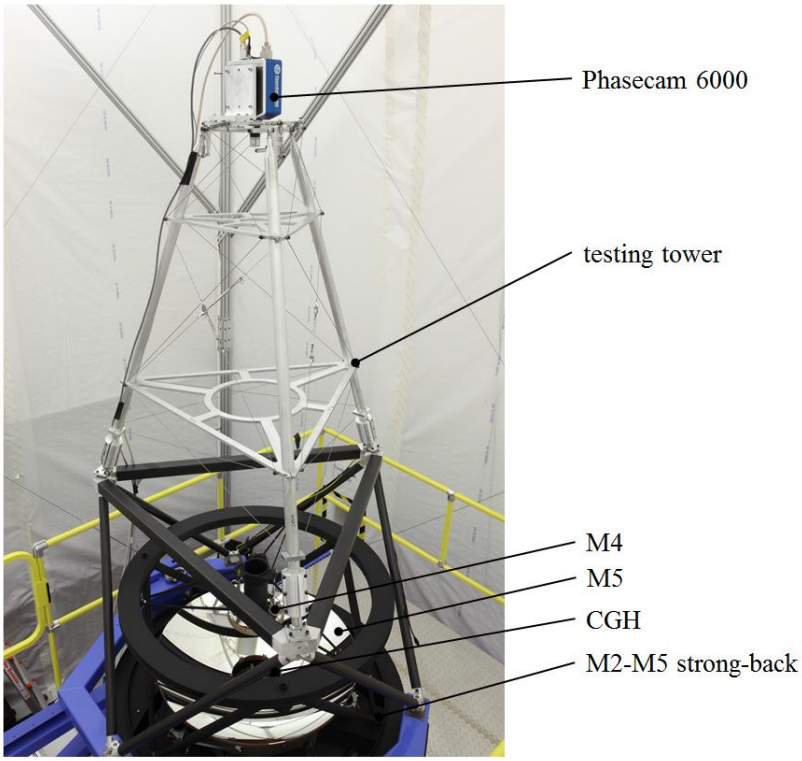

Figure 4.27: Labeled image of the M4-M5 test setup. The CGH is mounted to the M2-M5 strong-back and is positioned within the inner bore of M5.

The aligned positions of the test optics for the M4-M5 test on 11/10/2014 are given in Table 4.23. The M2-M3 test was also set-up again and the alignment of the M2-M3 test components were measured again to verify that the co-alignment of the two subsystem tests was repeatable. The results of laser tracker diagnosis of the M2-M3 test components are also given in Table 4.23 within a common coordinate reference frame. These laser tracker data show that the M4-M5 test CGH and focus position are adequately aligned to the M2-M3 subsystem test and that the measurement of the co-alignment is repeatable. M4 was aligned to M2 and M3 with the CGH alignment technique, as described above.

The M4-M5 test response after alignment of M5 to compensate tilt and coma is shown as an OPD map and interferogram in Figure 4.28. The test parameters associated with the test for this measurement are given in Table 4.24. The obscuration ratio was used to generate the Zernike basis which was used to fit the OPD map. The Zernike standard annular term coefficients are given in Noll ordering in Table 4.26.

Table 4.23: Laser tracker aligned positions of the M4-M5 test optics and re-measured M2-M3 test optics within the reference frame of the M2-M3 test. The data represent a successful co-alignment between the subsystem tests. M4 was aligned to M2 and M3 with the CGH alignment technique.

Component	X(mm)	Y(mm)	Z(mm)	δZ(mm)	Date
M4-M5 focus	-0.041	-0.019	-3404.324	0.408	20141110
M4	-	-	-1505.881	0.000	20141110
M5	-	-	-1168.492	0.003	20141110
M4-M5 CGH	-0.018	-0.026	-1101.043	0.001	20141110
M2-M3 CGH	0	0	-937.147	0.008	20141119
M2	0.001	-0.019	-925.752	0.006	20141110
M3	-0.009	-0.014	61.466	-0.001	20141119
M2-M3 focus	0	0	394.774	0.091	20141119

The mirror misalignments listed in Table 4.25 were calculated from the aberration coefficients in Table 4.26. It is very important to recognize that the uncertainties for the tilt and centration of M5 to M4 are *not* independent. Similar to the absolute tilts of M2 relative to M3, the misalignment of a tilt DOF of M5 produces first-order wavefront tilt that can be compensated by a decenter of M5. The coma terms are used to discriminate between a tilt and decenter in a given plane, but the coma terms' uncertainties and testing optics' position uncertainties create random uncertainty associated with positioning M5 based on the interferometer measurements. The analysis to set these uncertainties was provided by Hanshin Lee of the University of Texas. The analysis was based on alignment and interferometer measurement uncertainties provided by the University of Arizona.

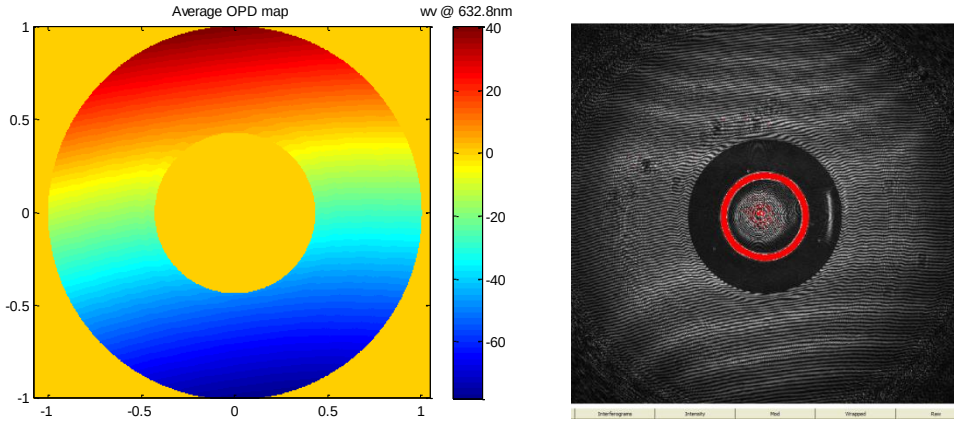

Figure 4.28: M4-M5 test response after alignment, measured on 11/10/2014

Table 4.24: Parameters of the M4-M5 test.

Test parameter	Value
Test wavelength, λ	632.8 nm
Obscuration ratio, ϵ	0.3671
Numerical aperture at diverger lens	0.31
Wedge factor (OPD scaling)	1

Table 4.25: Calculated tilt and centration values for M5 relative to the M4-M5 test alignment axis. The asterisks indicate correlation between the DOF where misalignment of one DOF tends to result in compensation by misalignment of the other.

DOF	Calculated alignment	Estimated uncertainty	Units
M5 Ry*	-19	±45	µrad
M5 Rx**	0	±45	µrad
M5 DecX*	-10	±30	µm
M5 DecY**	1	±30	µm

Table 4.26: Aberration coefficients from fitting M4-M5 test data to a Zernike standard annular term basis. Terms are numbered by Noll ordering, as in Zemax. Terms compensated with M5 tilt and centration alignments are highlighted in blue. Data collected 11/10/2014.

Term	Aberration	Zernike standard annular coefficient value (wv)	Coefficient uncertainties (wv, 2σ)
1	Piston	0.1983	0.0059
2	Tilt 0-deg	11.859	0.078
3	Tilt 90-deg	-8.986	0.084
7	Coma 90-deg	-0.018	0.0073
8	Coma 0-deg	0.0413	0.0091
11	Primary Spherical	0.3894	0.0034
16	Secondary Coma 0-deg	-0.0361	0.0037
17	Secondary Coma 90-deg	0.03	0.0029
22	Secondary Spherical	-0.1706	0.002
29	Tertiary Coma 90-deg	-0.01428	0.00091
30	Tertiary Coma 0-deg	-0.0013	0.0023
37	Tertiary Spherical	-0.04432	0.00085
46	Quaternary Coma 0-deg	0.0097	0.0011
47	Quaternary Coma 90-deg	-0.00227	0.00041
56	Quaternary Spherical	0.0392	0.0005

4.4 WFC SYSTEM ALIGNMENT RESULTS AND VERIFICATION

Following the subsystem tests and mirror alignments a final and fully self-consistent processing of the measurements from the laser tracker, alignment autocollimator, CGH centration test and interferometer test was done to find the

expected WFC alignment. These results were sufficient to move on to two independent alignment verification test. The M4-M5 conjugate test was performed by the University of Texas team with assistance provided by the U of A. This test was meant to verify the performance of the M4-M5 subsystem with a set of off-axis source points viewed through M4 and M5 with a wavefront sensor. The WFC System test was designed and performed by the U of A to test the on-axis double-pass transmitted wavefront through the full WFC system.

This section presents the final reported expectation values for all of the degrees of freedom for the HET WFC alignment. An explanation is provided for the diagnosis each alignment DOF and each expectation value is compared to the original tolerance set during the design of the WFC. The M4-M5 conjugate test is not elaborated upon, but it is noted that the results passed the University of Texas team's pass/fail criteria. The WFC System interferometer test is fully explained and results are given for this test conducted in a zenith-pointing and 35 degree orientation. This test also passed the University of Texas team's pass/fail criteria. These final results were also reviewed by an independent review board and found to be sufficient evidence to justify final delivery of the WFC.

4.4.1 System alignment results

Table 4.27 lists the expected alignments of each degree of freedom in the HET WFC against the original tolerances. Table 4.28 lists the alignment methods and alignment diagnosis uncertainty contributions related to each degree of freedom. Table 4.29 provides documentation of contributions to the net uncertainties.

Table 4.27: Final alignment expectation values and uncertainties relative to the original tolerances set for the WFC system. Expected alignment values within tolerance are given in green and those out of tolerance are shown in red. The correlated alignments are marked with a common number of '*'.

DOF	Expected Alignment	Net Uncertainty (±)	Tolerance	Unit
M2 to M3 axial	-7	11	100	µm
M2 to M5 axial	3	9	100	µm
M4 to M5 axial	3	8	20	µm
M2 Rx *	-54	115	49	µrad
M2 Ry **	-5	115	49	µrad
M2 DecX	0	38	50	µm
M2 DecY	0	38	50	µm
M3 Rx *	-78	125	49	µrad
M3 Ry **	4	125	49	µrad
M3 DecX	0	9	50	µm
M3 DecY	0	9	50	µm
M2 to M3 Rx	24	35	-	µrad
M2 to M3 Ry	-9	35	-	µrad
M5 Rx ***	0	45	49	µrad
M5 Ry****	-19	45	49	µrad
M5 DecX****	-10	30	20	µm
M5 DecY***	1	30	20	µm
M4 Rx	-7.6	~30	81	µrad
M4 Ry	30.2	~30	81	µrad
M4 DecX	-3.6	11	50	µm
M4 DecY	5.6	11	50	µm

* indicate DOF correlation

Table 4.28: List of the methods of alignment and the random uncertainties associated with the alignment measurements by degree of freedom.

DOF	Measurement Uncertainty (±)	Unit	Alignment method/comment
M2 to M3 axial	3	µm	laser tracker data
M2 to M5 axial	3	µm	laser tracker data
M4 to M5 axial	3	µm	laser tracker data
M2 Rx *	115	µrad	M2M3 test aberrations, uncertainty from constraints
M2 Ry **	115	µrad	M2M3 test aberrations, uncertainty from constraints
M2 DecX	1	µm	Datum, CGH centration test
M2 DecY	1	µm	Datum, CGH centration test
M3 Rx *	125	µrad	M2M3 test aberrations, uncertainty from constraints
M3 Ry **	125	µrad	M2M3 test aberrations, uncertainty from constraints
M3 DecX	3	µm	Datum, CGH centration test
M3 DecY	3	µm	Datum, CGH centration test
M2 to M3 Rx	35	µrad	M2M3 test aberrations, uncertainty from constraints
M2 to M3 Ry	35	µrad	M2M3 test aberrations, uncertainty from constraints
M5 Rx ***	45	µrad	M4M5 test aberrations, uncertainty from constraints
M5 Ry****	45	µrad	M4M5 test aberrations, uncertainty from constraints
M5 DecX****	30	µm	M4M5 test aberrations, uncertainty from constraints
M5 DecY***	30	µm	M4M5 test aberrations, uncertainty from constraints
M4 Rx	5	µrad	autocollimator, CGH reference to M2M3 CGH
M4 Ry	5	µrad	autocollimator, CGH reference to M2M3 CGH
M4 DecX	5	µm	CGH centration alignment to M2 and M3
M4 DecY	5	µm	CGH centration alignment to M2 and M3

*indicate DOF correlation

Table 4.29: List of the net alignment uncertainties which are the RSS of reference and measurement uncertainties.

DOF	Reference Uncertainty (±)	Measurement Uncertainty (±)	Net Uncertainty (±)	Unit
M2 to M3 axial	10.6	3	11	µm
M2 to M5 axial	8.1	3	9	µm
M4 to M5 axial	7.7	3	8	µm
M2 Rx *	-	115	115	µrad
M2 Ry **	-	115	115	µrad
M2 DecX	38	1	38	µm
M2 DecY	38	1	38	µm
M3 Rx *	-	125	125	µrad
M3 Ry **	-	125	125	µrad
M3 DecX	8	3	9	µm
M3 DecY	8	3	9	µm
M2 to M3 Rx	-	35	35	µrad
M2 to M3 Ry	-	35	35	µrad
M5 Rx ***	-	45	45	µrad
M5 Ry****	-	45	45	µrad
M5 DecX****	-	30	30	µm
M5 DecY***	-	30	30	µm
M4 Rx	~30	5	~30	µrad
M4 Ry	~30	5	~30	µrad
M4 DecX	10	5	11	µm
M4 DecY	10	5	11	µm

*indicate DOF correlation

4.4.2 System test

The HET WFC System test is a double-pass CGH-corrected null test which includes all of the optical components in the WFC. This includes an optic called the “aspheric corrector plate” (ACP) which replaced the exit window of the WFC. This was added to correct for spherical aberration that was predicted based on the as-built mirror prescriptions and WFC alignment. The ACP is located near the exit pupil of the telescope system so that it can correct for spherical aberration across the field of

view. This refractive optic also has loose centration and axial position tolerances of ±0.5mm and a tilt tolerance of ±0.25deg per axis. The alignment of this optic was done with an alignment telescope and laser tracker with relatively little difficulty. The nominal axial positions of all the optics in the System test are given relative to the paraxial focus position in Table 4.30.

Table 4.30: Nominal axial positions of the optics in the HET WFC System test relative to the ideal paraxial focus position of the telescope.

Surface	Z (mm)
SYSTEM test focus	-3413.987
ACP vertex	-2601.152
M5 vertex	-1168.496
M4 vertex	-1505.881
M3 vertex	61.466
M2 vertex	-925.759
SYSTEM test CGH	75.054

The uncertainties associated with the measurement of each test optic position in the System test are given in Table 4.31. The System test focus was aligned to the same axis as the M2-M3 test and M4-M5 test. The CGH was used as a compensator for this test. Movement of the CGH is analogous to movement of the WFC relative to the HET primary mirror and its incident wavefront from an on-axis object. The axial position of the CGH was adjusted to compensate for power in the test wavefront. The CGH was *translated* to compensate for wavefront tilt and *tilted* to compensate for primary coma in the test. No other components were purposefully adjusted away from their nominal positions to compensate test wavefront aberrations.

Table 4.31: List of alignment position uncertainties for all of the optics in the WFC System test other than the mirrors.

DOF	Position Uncertainty (2σ)	Units	Comments
focus centration (X or Y)	30	μm	statistics from 20150130 measurements, 5 avgs. Excludes possible long-term drift.
focus axial (Z)	10	μm	statistics from 20150130 measurements, 5 avgs.
ACP centration (X or Y)	29	μm	Assumed 21um registration, 20um LT measurement based on measurement statistics
ACP axial (Z)	23	μm	Assumed 21um registration, 10um LT measurement based on measurement statistics
ACP angle (Rx or Ry)	30	μrad	Davidson Optronics AT
CGH centration (X or Y)	23	μm	21um CGH registration, 10um LT measurement
CGH axial (Z)	23	μm	21um CGH registration, 10um LT measurement
CGH angle (Rx or Ry)	5	μrad	Electronic autocollimator

The WFC was tested several times in several configurations. The WFC was tested with and without the ACP to measure its influence on WFC performance. The first test configuration presented here has the ACP installed and the WFC in the vertical orientation in which it was aligned. A labeled photograph and optical layout of the WFC System test is shown in Figure 4.29. The mounted System test CGH is shown in Figure 4.30. The positions of the testing optics measured on 02/18/2015 are given in Table 4.32. The decenter and tilt of the CGH are both within the allowable range for decenter and tilt of the WFC as a whole within the Hobby Eberly Telescope. The interferogram and corresponding OPD map from the WFC System test performed on 02/18/2015 is shown in Figure 4.31. This OPD map was fit to 36 Zernike standard annular terms with the testing parameters given in Table 4.33. A selection of the most significant test aberration terms are given in Table 4.34. The aberration coefficient values from the System test on 02/18/2015 and 03/11/2015 are

compared to show that the test repeatability matches the random coefficient variation during the test *except* the CGH alignment-dependent aberrations tilt and coma. The test was also aligned without the ACP on 02/18/2015 to characterize the ACP influence on the double-pass transmitted wavefront. The change of the spherical aberration coefficient terms by the aspheric corrector plate are given in Table 4.35.

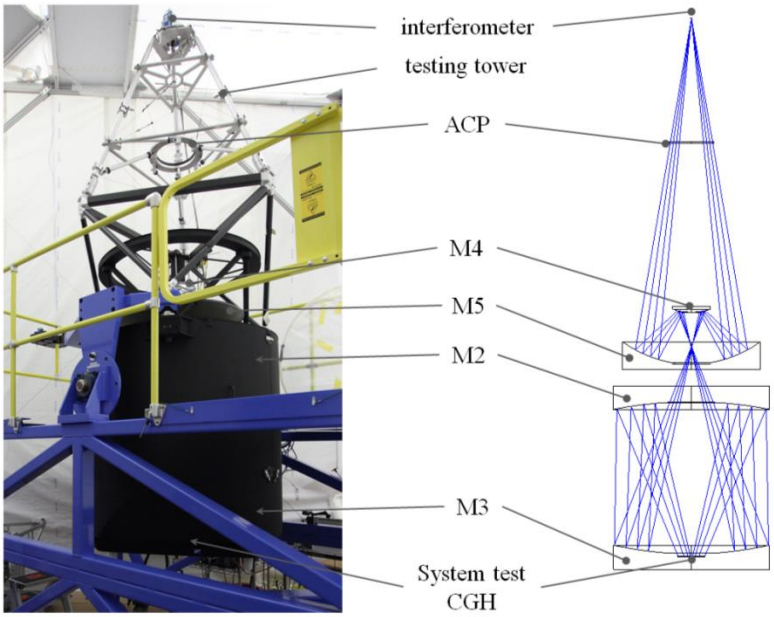

Figure 4.29: HET WFC System test picture and layout with labeled components in the vertical testing position.

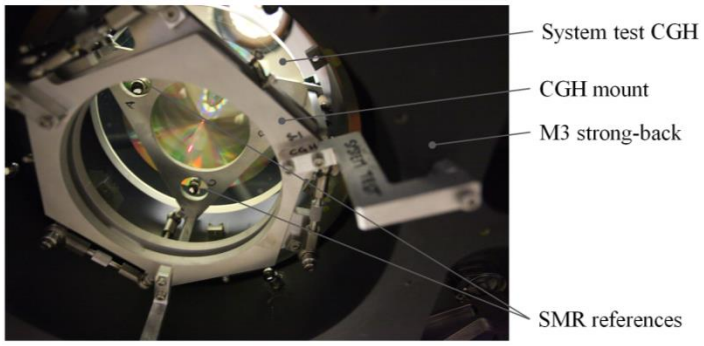

Figure 4.30: System test CGH mounted at the M3 strong-back.

Table 4.32: Measured positions of WFC System test components on 02/18/2015.

Component	X (mm)	Y (mm)	Z (mm)	Ry (μrad)	Rx (μrad)
Focus	0.001	0.003	-3413.987	-	-
ACP vertex	-0.307	-0.011	-2601.113	-	-
CGH	-0.001	-0.127	74.989	-59.2	78.1

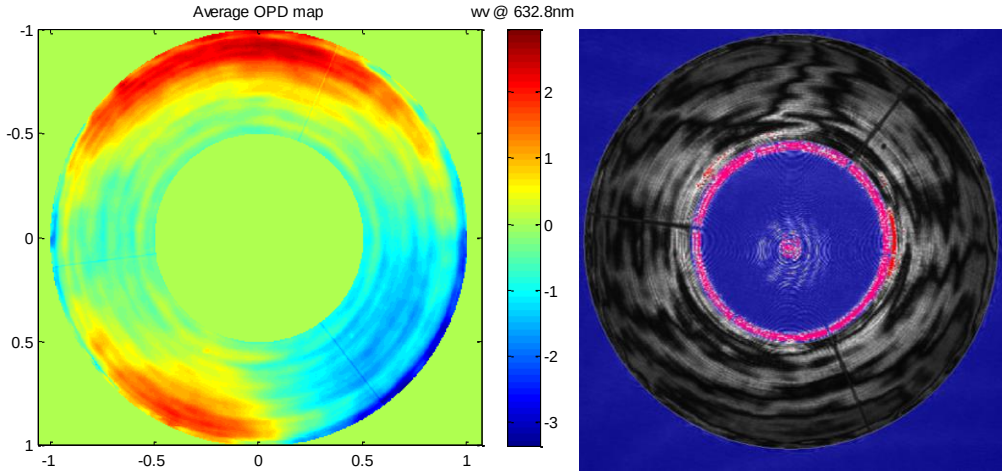

Figure 4.31: Average OPD map (left) and interferogram (right) from HET WFC System test conducted on 02/18/2015.

Table 4.33: WFC System test parameters for 02/18/2015.

Testing parameter	As-tested status
WFC orientation	0 degrees (vertical)
Aspheric Corrector Plate	Installed
Zernike fit type	Zernike Standard Annular
Obscuration ratio	0.5
OPD scaling	Actual OPD, no compensation for double-pass
Data Averaging	100 acquisitions, 9 averages/acquisition

Table 4.34: Aberration coefficients from WFC System test data measured on 02/18/2015. The coefficient variation values represent 2σ variation from the set of 100 measurements conducted in sequence. The coefficient discrepancy values compare results from identical testing configurations on 02/18/2015 and 03/11/2015

Term	Aberration	Zernike standard annular coefficient value (wv)	Coefficient variation (wv, 2σ)	Coefficient discrepancy (wv)
1	Piston	0.008	0.001	0.003
2	Tilt 0-deg	-0.386	0.253	0.190
3	Tilt 90-deg	-0.469	0.243	0.356
4	Power	0.274	0.083	-0.136
5	Astigmatism 45-deg	-0.336	0.067	0.002
6	Astigmatism 0-deg	-0.497	0.066	0.016
7	Coma 90-deg	-0.14	0.056	-0.118
8	Coma 0-deg	-0.086	0.049	-0.223
9	Trefoil 30-deg	-0.099	0.034	0.021
10	Trefoil 0-deg	0.245	0.036	-0.002
11	Primary Spherical	-0.104	0.014	0.006
12	Secondary Astigmatism 0-deg	-0.054	0.027	-0.002
13	Secondary Astigmatism 45-deg	0.047	0.027	0.003
14	Tetrafoil 0-deg	-0.001	0.023	-0.002
15	Tetrafoil 22.5-deg	0.095	0.02	-0.007
16	Secondary Coma 0-deg	-0.042	0.01	-0.008
17	Secondary Coma 90-deg	0.031	0.017	0.021
18	Secondary Trefoil 0-deg	0.021	0.017	0.002
19	Secondary Trefoil 30-deg	0.02	0.018	-0.005
22	Secondary Spherical	-0.203	0.007	0.008
23	Tertiary Astigmatism 45-deg	0.017	0.011	0.000
24	Tertiary Astigmatism 0-deg	0.026	0.012	-0.004
29	Tertiary Coma 90-deg	0.000	0.008	0.007
30	Tertiary Coma 0-deg	-0.009	0.004	-0.002
37	Tertiary Spherical	-0.129	0.005	0.008

Table 4.35: Changes to the spherical aberration coefficients in the WFC System test caused by installing the ACP.

Term	Aberration Coefficient	ACP influence (wv)
11	Primary Spherical	+1.26
22	Secondary Spherical	-0.07
37	Tertiary Spherical	0.00

This System test was also performed at a 35 degree angle relative to vertical. The 35 degree angle matches the nominal orientation of the WFC in the HET tracker. The WFC is shown in the 35 degree orientation in Figure 4.32. This testing configuration represents the most realistic prediction of WFC on-sky performance. Aside from the orientation of the structure the test was conducted in a manner identical to the vertical test. The measured positons of the test optics are given in Table 4.36. Note that the angle and centration of the CGH represents a compensation which is in very close agreement with the results from testing in a vertical orientation. Figure 4.33 shows the average OPD map from a set of measurements and a masked interferogram. Table 4.37 gives the testing parameters and Table 4.38 gives the most relevant aberration coefficients for the WFC System test at 35 deg.

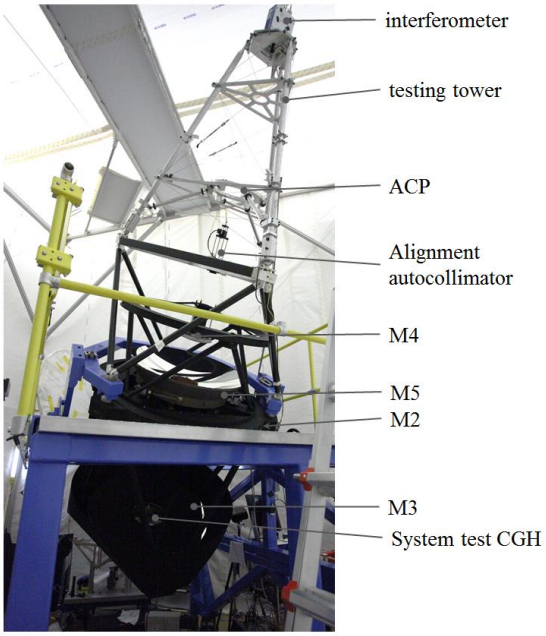

Figure 4.32: Photograph of the HET WFC in the 35 degree System test configuration. The alignment autocollimator is installed in this image, where it was being used to measure the System test CGH angle.

Table 4.36: Measured positions of WFC System test components on 02/04/2015.

Component	X (mm)	Y (mm)	Z (mm)	Ry (µrad)	Rx (µrad)
Focus	-0.004	-0.004	-3413.977	-	-
ACP vertex	-0.125	-0.458	-2601.080	-	-
CGH	0.027	-0.137	74.978	-75	90.2

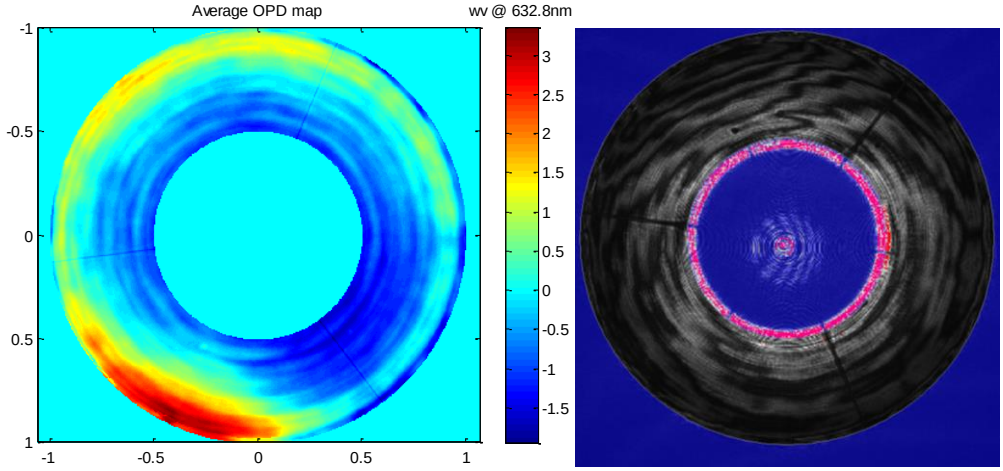

Figure 4.33: Average OPD map (left) and interferogram (right) from HET WFC System test conducted on 02/04/2015.

Table 4.37: WFC System test parameters for 02/04/2015.

Testing parameter	As-tested status
WFC orientation	35 degrees (tilted)
Aspheric Corrector Plate	Installed
Zernike fit type	Zernike Standard Annular
Obscuration ratio	0.5
OPD scaling	Actual OPD, no compensation for double-pass
Data Averaging	98 acquisitions, 9 averages/acquisition

Table 4.38: Aberration coefficients from WFC System test data measured on 02/04/2015. The coefficient variation values represent 2σ variation from the set of 98 measurements conducted in sequence. The differences compare the coefficients from 02/04/2015 with those from 02/18/2015. Astigmatism 0-deg shows a notable change.

Term	Aberration	Zernike standard annular coefficient value (wv)	Coefficient uncertainties (wv, 2σ)	Difference: 35 deg - vertical (wv)
1	Piston	-0.012	0.005	-0.020
2	Tilt 0-deg	-0.454	0.21	-0.068
3	Tilt 90-deg	0.561	0.577	1.030
4	Power	0.589	0.056	0.315
5	Astigmatism 45-deg	-0.297	0.069	0.039
6	Astigmatism 0-deg	-0.25	0.073	0.247
7	Coma 90-deg	0.103	0.036	0.243
8	Coma 0-deg	-0.104	0.034	-0.018
9	Trefoil 30-deg	-0.107	0.039	-0.008
10	Trefoil 0-deg	0.257	0.04	0.012
11	Primary Spherical	-0.078	0.011	0.026
12	Secondary Astigmatism 0-deg	-0.056	0.024	-0.002
13	Secondary Astigmatism 45-deg	0.035	0.021	-0.012
14	Tetrafoil 0-deg	-0.004	0.022	-0.003
15	Tetrafoil 22.5-deg	0.115	0.026	0.020
16	Secondary Coma 0-deg	-0.056	0.008	-0.014
17	Secondary Coma 90-deg	0.006	0.01	-0.025
18	Secondary Trefoil 0-deg	0.021	0.017	0.000
19	Secondary Trefoil 30-deg	0.02	0.017	0.000
22	Secondary Spherical	-0.186	0.005	0.017
23	Tertiary Astigmatism 45-deg	0.018	0.009	0.001
24	Tertiary Astigmatism 0-deg	0.032	0.01	0.006
29	Tertiary Coma 90-deg	-0.016	0.005	-0.016
30	Tertiary Coma 0-deg	-0.029	0.004	-0.020
37	Tertiary Spherical	-0.146	0.003	-0.017

4.5 CONCLUSION

The WFC System test results demonstrated a successfully aligned and stable WFC system. The results of a revised alignment scheme were verified by an independent system test. Although practical difficulties undermined the utility of the

original alignment plan the CGH centration and tilt alignment scheme was critical to the alignment of M4 to M2 and M3 and to the subsystem null test CGHs. These results were presented to the University of Texas team and an independent review committee. The alignment and testing results were coupled with Hanshin Lee's analysis of the expected telescope performance to show that the WFC was ready for shipment to the HET observatory site.

Furthermore, the WFC performance has been measured across the expanded field of view with successful first-light observations at HET. The wavefront sensor measurements collected by Lee *et al.* indicate that the HET with the WFC can produce a point-spread function with FWHM between 0.3 and 0.8 arcsec within the science field of view[24]. The FWHM values are comparable to the telescope specification which required 80% EE within 0.48 arcsec at the center of the field of view. The wavefront sensor measurements have also practically eliminated the worst-case predictions as possibilities for the WFC alignment[24]. With the risk of any large misalignment substantially ruled-out, it is clear that the methods followed in this implementation were successful for aligning the HET Wide Field Corrector.

CHAPTER 5

PHASE FIDUCIAL DEMONSTRATION

This chapter will present the fabrication and testing of phase fiducials on a glass surface and demonstrate their utility in a set of interferometer experiments. As a matter of convenience these phase fiducial fabrication demonstrations were performed on optical flats. The interferometer demonstrations are all flat tests with a CGH to accommodate the phase fiducial alignment reference features.

The fabrication experiments demonstrate the procedures and results from making phase fiducials of two distinct curvatures. There is also a demonstration of a sample with two fiducials separated by a specified distance across the flat. The interferometer alignment demonstrations show experimentally what sensitivities the fiducials provide for alignment of the CGH projection to the test optic. The two-fiducial sample experiments demonstrate the application of phase fiducials for aligning the clocking and magnification of the CGH projection. A number of practical design and implementation considerations are addressed to enforce the best practices for implementation of phase fiducials. It is shown that the parametric design calculations are accurate and that the phase fiducial alignments perform as expected.

5.1 PHASE FIDUCIAL FABRICATION

All of the phase fiducials are nominally spherical features polished into an otherwise flat polished surface. The fiducials are made individually with a special guide ring fixture and spherical pitch lap. The curvature of the fiducials is

approximately matched to the complimentary curvature of the guide ring and pitch lap surfaces. The position of the guide ring over the flat sets the location of each fiducial. An appropriately shaped guide ring and pitch lap applied at a specified position on the flat produces the desired phase fiducial curvature departure in an isolated area of the flat.

This section documents the procedures and test results from producing and characterizing phase fiducials. The production of samples with one phase fiducial as well as a two-fiducial sample that features a pair of phase fiducials is described. This section provides insight on how to make these alignment features on a glass substrate and also demonstrates the performance of the fabrication methods.

5.1.1 Single phase fiducial fabrication

The fabrication of a single phase fiducial follows a procedure which is very similar to traditional spherical surface fabrication. Fundamentally this *is* spherical surface fabrication, but the phase fiducials are meant to be sub-aperture features which leave the surrounding parent optic surface unaffected. Additionally, these phase fiducials have extremely shallow feature depths on the order of microns. The location of the phase fiducial within the test aperture may also be important. These three aspects to phase fiducial fabrication present some challenges and motivate the use of a particular set of fixtures, guides and tools.

5.1.1.1 Concept overview

The concept is to create tooling that matches the desired curvature of the fiducial, align the tooling to the area where the fiducial should be and then polish the feature into the desired sub-aperture. The tooling consists of a steel conditioning plate, aluminum guide ring, steel grinding tool and steel & pitch polishing lap. Figure 5.1 illustrates the polishing process where the guide ring in waxed to the optic at a suitable height such that the steel & pitch tool removes glass from the calibration optic to a desired depth. The height of the guide ring and corresponding depth of the polishing determines the diameter of the fiducial. The curvature of the tooling determines the curvature of the fiducial. The location, diameter and curvature of the fiducial are its relevant parameters. It is also valuable to have a large diameter clear aperture with accurate surface figure compared to the full diameter of the affected region. This method was designed to achieve a small rolled-edge region to preserve the rest of the parent optic's surface for use in calibration.

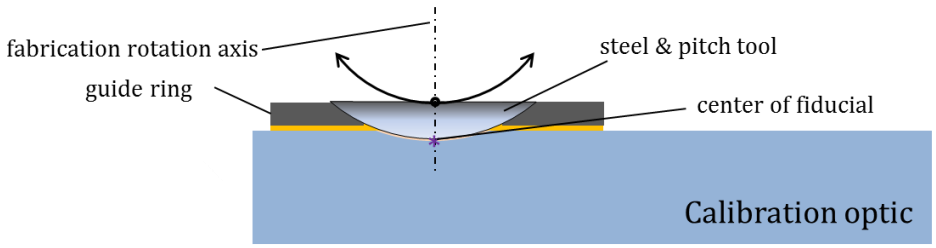

Figure 5.1: Conceptual illustration of the phase fiducial fabrication process in cross-section.

5.1.1.2 Tooling

The basic procedural outline for tool preparation is given below:

Tooling preparation

1. Machine the grinding and polishing tools and the conditioning plate.
2. Grind the grinding lap and conditioning plate with progressively finer grits to remove machined surface finish.
3. Polish the conditioning plate with a felt pad applied to the grinding tool and Simichrome metal polish
4. Pour hot pitch onto the polishing tool and press out the pitch on the conditioning plate to create a spherical polishing lap.
5. Cut at least two channels in the polishing lap surface.
6. Run the polishing lap on the condition plate surface with 0.3 μm alumina to break it in.
7. Machine the guide ring (two options)
    a. Machine all features via CNC milling/lathe. This will require grinding and polishing the spherical guide surface similarly as done with the conditioning plate.
    b. Machine the guide ring by conventional machining including a conical (or spherical) cut across the spherical surface. Finish cutting the spherical surface with a diamond turning machine.
8. Measure the sag of the finished guide surface with a spherometer

This section will discuss this process in more detail and provide photographs and diagrams to better explain the procedure.

As outlined in the concept overview and there is a conditioning plate, guide ring, grinding tool and a polishing tool. There is also a mount for the substrate and fine-thread adjusters on the guide ring which are used to control the guide ring height. The materials used for these parts are listed in Table 5.1. A set of mechanical drawings of for the tooling parts used to create a 252mm radius phase fiducial are given in Appendix C. The radius of the spherical tool surfaces are not 252 mm because of an empirical tendency of this process to produce slightly flatter fiducial surfaces. A similar set of parts were made for fabricating an 80mm radius phase fiducial and these are shown in two assembled configurations in Figure 5.2 and

Figure 5.3. The radius of the guide ring is shorter for this shorter radius phase fiducial and the guide ring is small diameter and thicker.

Table 5.1: Tooling parts and material specifications.

Part name	*Material Specification*
Conditioning plate	4340 steel alloy
Guide ring	6061-T6 aluminum alloy
Grinding tool	4340 steel alloy
Polishing tool	4340 steel alloy
Guide ring adjuster bushings	Phosphor bronze, 3/16”-100TPI
Guide ring adjuster screws	Stainless steel, 3/16”-100TPI
Substrate mount	6061-T6 aluminum alloy

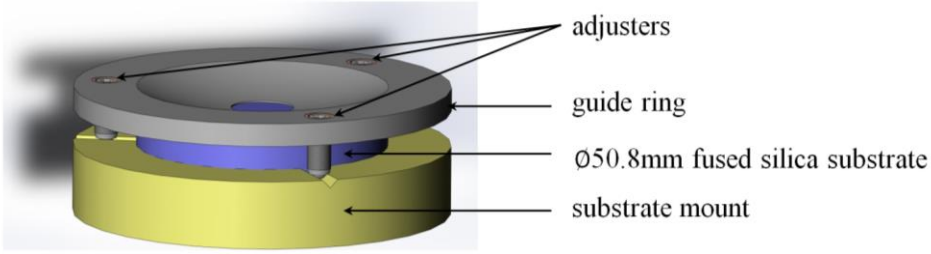

Figure 5.2: Solid model assembly of the guide ring tooling for 80mm radius phase fiducial fabrication on a 50.8mm optical flat.

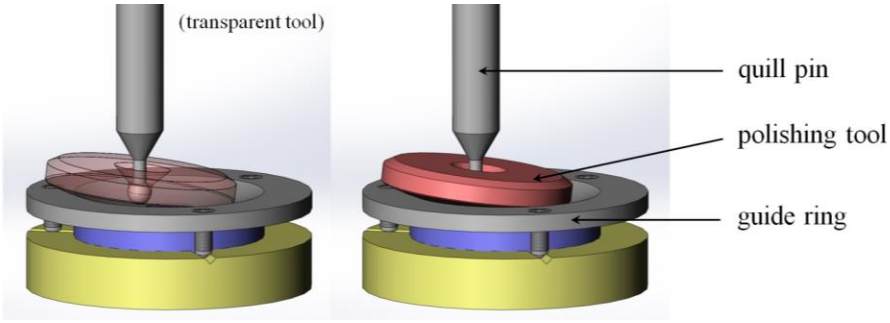

Figure 5.3: Solid model assembly of 80mm radius phase fiducial tooling with the polishing machine quill pin installed. The quill pin translated left to right from this viewpoint while the substrate is driven about a spindle axis near the centerline of the guide ring.

As the fiducial radius gets longer the guide ring must get thinner at a given off-axis distance for the polishing tool to contact the substrate through the center of the guide ring. To avoid having a very thin, fragile and flexible guide ring it is

possible to make the outer diameter of this part larger as the radius gets longer. This is what motivated the larger diameter guide ring for the 252 mm radius fiducial fabrication.

The surfaces of the conditioning plate and the guide ring must be polished. If these surfaces are not polished the pitch lap polishing tool fragments as it slides across these reference surfaces. There are two approaches which were pursued for making the conditioning plate and guide ring spherical surfaces: machine (CNC or manual), loose-abrasive grind and polish *or* CNC single-point diamond turning. Images of the surfaces generated by these two approaches are shown in Figure 5.4. It is highly advantageous to diamond-turn the guide ring to achieve a superior surface figure and immediately specular surface which requires less processing.

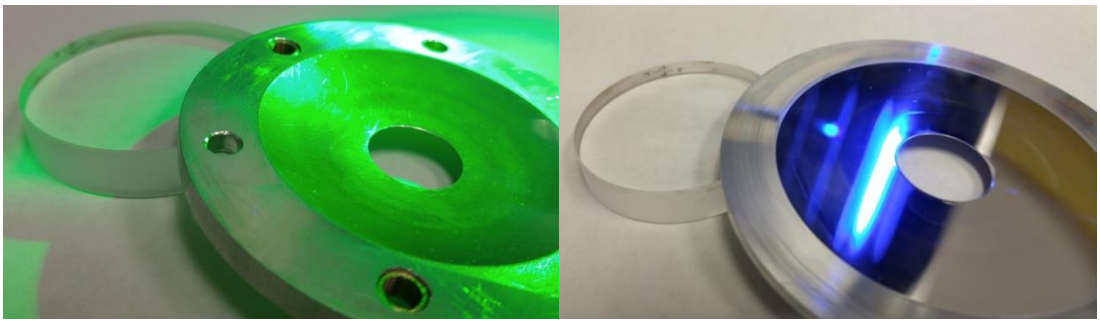

Figure 5.4: Pictures of the 80mm radius (left) and 252mm (right) phase fiducial guide rings after spherical surface figuring by machining and polishing vs. diamond-turning, respectively.

In these fabrication experiments both of the conditioning plates were steel and both were brought to a polished surface by grinding and polishing after CNC machining. Figure 5.5 shows the initial machined surfaces of the steel grinding tool, steel conditioning plate, and aluminum guide ring used to make 80mm radius phase

fiducials. A Strausbaugh polishing machine was used to perform all of the loose abrasive grinding and polishing. This machine and a close up of the loose abrasive grinding setup are shown in Figure 5.6. The grinding tool was driven by a quill pin with the conditioning plate or guide ring waxed to a flat steel mount on the spindle. The parts were ground to a very smooth surface by gradually reducing the grit size through a series of grinding runs. Table 5.2 provides a list of all the grinding and polishing materials used to condition the tooling.

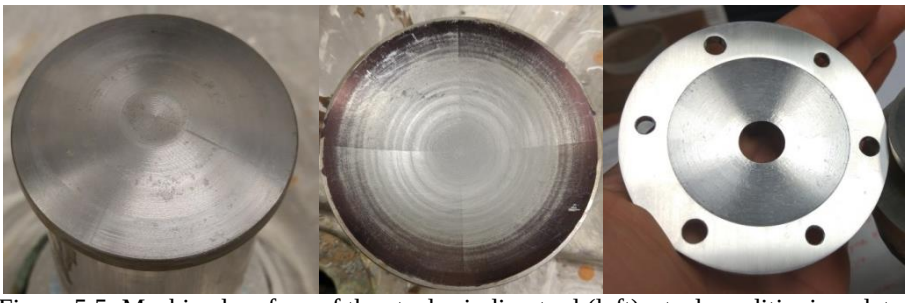

Figure 5.5: Machined surface of the steel grinding tool (left), steel conditioning plate after some coarse grinding (center), and aluminum guide ring after machining (right).

Figure 5.6: Close up view of a guide ring and grinding tool in the coarse grinding phase (left) and a broader view of the grinding and polishing Strausbaugh machine grinding on a conditioning plate.

Table 5.2: Grinding and polishing materials and specifications in the order in which they were used to condition the tooling.

Material name	*Specification*
Coarse grinding slurries	80 grit, SiC and water
	120 grit, SiC and water
	220 grit, SiC and water
Fine grinding slurries	40 μm, Al-oxide, water and detergent
	25 μm, Al-oxide, water and detergent
	15 μm, Al-oxide, water and detergent
	7 μm, Al-oxide, water and detergent
Metal polish	Simichrome and felt pad
Polishing slurry	0.3 μm, alumina, water and detergent
Polishing pitch	Gugolz 64/73 (mix, unknown ratio)

Once the conditioning plate and guide ring were polished the pitch lap polishing tool was prepared. A layer of pitch was poured onto the face of this spherical tool and the pitch was pressed against the conditioning plate with an arbor press at a temperature of approximately 160 degrees F. A soapy polishing slurry was applied to the condition plate while pressing to avoid adhesion between the lap and the conditioning plate. The result of this process is shown with a photograph in Figure 5.7 at left. Two channels were cut into the face of each polishing lap to allow slurry to easily migrate across the parts as shown in the center of Figure 5.7.

Figure 5.7: Polishing tool pressed out on conditioning plate (left), polishing tool with channels cut and broken in (center), and ball socket machine interface (right).

The polishing laps were broken in on the conditioning plates before polishing on the guide rings. Although it is possible to jump from 7 μm Al-oxide grinding to

0.3 μm Alumina polishing with the pitch lap, it was found that polishing with Simichrome is helpful. Simichrome metal polish works nicely on a felt pad applied to the steel grinding tool as in Figure 5.8. This tool and Simichrome polish are also effective for polishing the aluminum guide rings if conditioning is needed following grinding or to knock off small burrs after diamond-turning.

Figure 5.8: Polishing tool and polish for polishing conditioning plate and guide ring.

It has already been mentioned that the radius of curvature of the guide ring and the polishing tool must be set appropriately to generate a fiducial of a certain radius. It is very important to measure the sag of the guide ring and the conditioning plate with a spherometer to compare these curvatures. This is done to verify the value of the curvatures and to check whether the conditioned polishing tool will fit the guide ring. The spherometer is also used later to measure the height of the guide ring above the flat substrate, as in Figure 5.9. This height is calculated from the difference between the base sag of the guide ring surface and the sag to the glass through the guide ring. The measured sag and calculated radius from each spherometer measurement is given in Table 5.3. There was a particularly large discrepancy between the conditioning plate and guide ring for the 252mm fiducial. Interestingly this did not cause a significant issue during polishing. This process is apparently not

particularly sensitive to a curvature discrepancy between the conditioning plate and the guide ring.

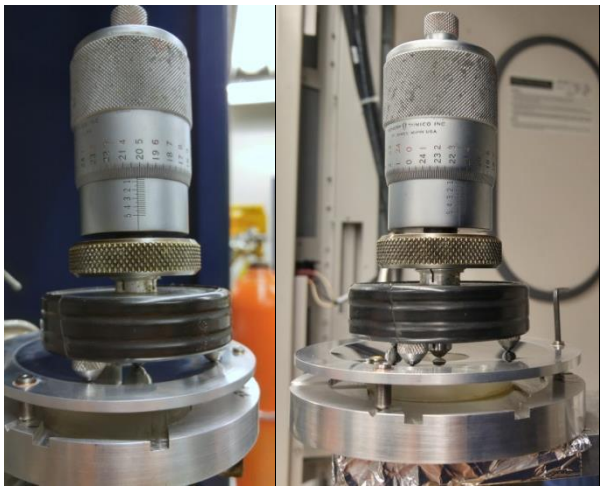

Figure 5.9: Spherometer measuring the base sag of the guide ring (left) and sag to the glass substrate surface at the center of the guide ring (right).

Table 5.3: Spherometer measurements of the conditioning plates and guide rings.

Part name	Spherometer baseline (radius, in)	Sag (mm)	Radius of curvature (mm)
Conditioning plate (80mm)	0.5	-1.1989 ±0.0025	71.0 ±0.3
Guide ring (80mm)	0.5	-1.1913 ±0.0025	71.5 ±0.3
Conditioning plate (252 mm)	1	-1.3665 ±0.0025	240.0 ±0.6
Guide ring (252 mm)	1	-1.4122 ±0.0025	232.3 ±0.6

5.1.1.3 Polishing process

The basic procedural outline for polishing phase fiducials is given below:

Polishing fixture preparation

1. Install three threaded bushings in the guide ring for precision height/tilt adjustment.
2. Install fine adjustment screws in the guide ring assembly.
3. Machine a fixture for the substrate with kinematic interfaces for the fine adjustment screws on the guide ring.
4. Wax the back side of the polished substrate to the fixture.
5. Set the height of the guide ring.

   a. Put the guide ring in direct contact with the substrate, then lift each side uniformly with the fine adjustment screws (avoid tilting)
   b. Measure the sag from the guide ring to the glass. The spherometer must have its three outer contact points on the guide ring and the center contact at the center of the guide ring. This sag should be *less than* the sag measured for the guide surface by an amount equal to the desired feature depth.
6. Apply wax to the substrate top surface, place the ring on top of the wax, then heat the assembly until the guide ring is on its fine adjustment supports again.
7. Measure the height of the guide again, as in step 5b. Reheat the assembly and move all the fine adjustment screws by the same amount to adjust the height to the target value.
8. Verify the guide ring height at room temperature with the adjustment screws removed.

Polishing

1. Attach the polishing fixture assembly to a Stausbaugh polishing machine spindle.
2. Run the polishing lap on the guide ring and glass with 0.3μm alumina polishing slurry until the feature is polished-out (10 - 30 minutes)

This subsection describes the process of applying the tooling to create a phase fiducial of a desired depth at a given tool radius. The process will be described in detail with photographs to demonstrate how the procedure was followed.

The most important part of the process is applying the guide ring to the substrate at the appropriate height. This is done by using the adjusters to control the height of the guide ring, the spherometer to measure the height, and opticians' blocking wax to create a stable bonded interface between the ring and the glass. The assembly is shown under alignment in Figure 5.10. It is also important that the back of the guide ring matches the shape of the glass well so that it may be set against the glass and raised uniformly at each adjuster. This avoids tilting the guide ring during height adjustment. The result is shown in Figure 5.11 where the diamond-turned guide ring for a 252 mm fiducial is mounted to the flat and ready to polish a fiducial.

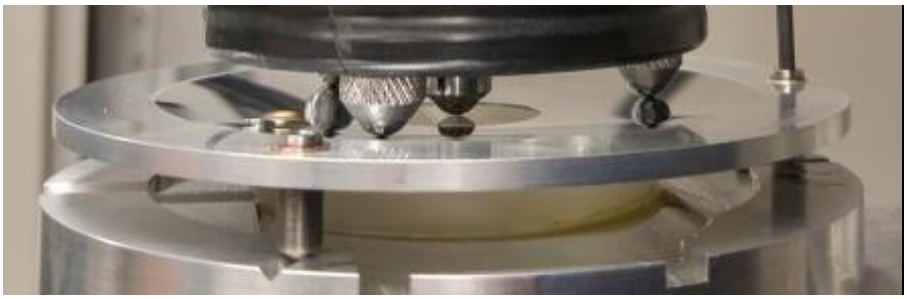

Figure 5.10: Close up of the guide ring for 252 mm fiducials waxed to the substrate and supported by the fine adjuster screws for height adjustment. The spherometer is in contact with the flat to measure the height of the ring.

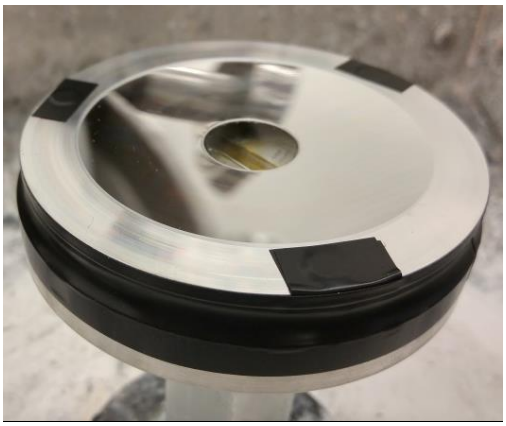

Figure 5.11: Guide ring for 252mm fiducials mounted to an optical flat in the substrate mount on the Strasbaugh spindle.

Mounting the guide ring in this manner presents several notable challenges. The wax bonding requires the addition of heat to the glass and metal. This was relatively easy with a small optic, but it would be more risky to locally heat a much larger mirror substrate. Care must be taken not to break the glass with the heat and it was found that a heat gun was most effective. The metal parts were heated with a blow torch sometimes for expediency. The wax flows very easily when it is warm, so the guide ring has no stability relative to the glass substrate other than that provided

by the guide ring supports. On a larger optic a fixture would be necessary to constrain the transverse location of the guide ring, but the height constraint is still possible with the same ball-end adjuster supports in contact with the glass. Interestingly, the wax does tend to hold the guide ring backplane at least 0.001" away from the substrate. Having the guide ring slightly thinner than nominal is necessary to avoid interference. Also, a dry-fit at the target guide ring height before applying the wax did *not* allow an immediate alignment. The wax likely influences how the ring bends under the weight of the spherometer, where adding the wax supports and bends the center of the ring upward. This observation motivated the repeated heating and adjustment of the screws to attain the target guide ring height.

The relationship between guide ring height and fiducial diameter depends on the fiducial curvature. This relationship is easily represented accurately with the first-order expressions,

$$h \cong \frac{\emptyset_f^2}{8R_f} \quad \text{and} \quad \emptyset_f \cong \sqrt{8Rh}\,, \tag{5.1}$$

where these geometric parameters are illustrated in Figure 5.12. Notice that the diameter of the fiducial, $\emptyset_f$, changes most rapidly as a function of the guide ring height, h, when h is small. Table 5.4 lists the nominal designs for the phase fiducial surfaces that were attempted with this fabrication process. In addition, Table 5.4 gives the values for the aligned height of the guide rings, the expected feature diameter, and the measured diameter of the as-built fiducial. The measured diameter, $\emptyset_{measured}$, is considered the area which is measurable by the interferometer. These results identify

that it is not necessarily as simple as was initially assumed to make a feature of a given size based on the guide ring height. As with many optical fabrication techniques some practice may be needed to achieve a desired feature size. It is also notable that the height measurement is very sensitive and local errors on the guide ring may add uncertainty in addition to the finite precision of the micrometer.

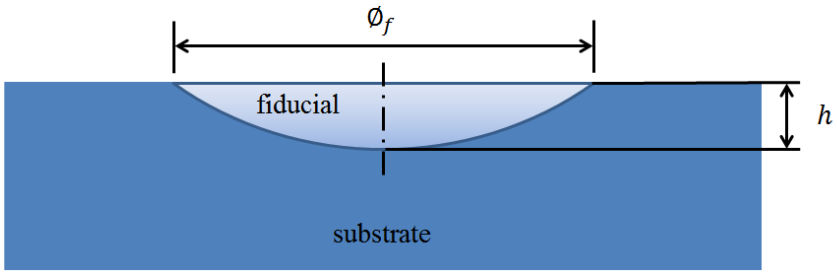

Figure 5.12: Illustration of the parameters for phase fiducial diameter and guide ring height from a cross-sectional view.

Table 5.4: Nominal, expected and measured values for fiducial height and resulting feature diameter in Sample 2 and Sample 5.

Sample name	$R_{nominal}$ (mm)	$h_{nominal}$ (mm)	$\emptyset_{nominal}$ (mm)	h_{meas} (mm)	$\emptyset_{expected}$ (mm)	$\emptyset_{measured}$ (mm)
Sample 2	80	0.0011	0.84	0.01524	3.12	1.7
Sample 5	252	0.0029	2.4	0.00635	3.58	3.9

Once the guide ring is applied to the substrate at an acceptable height the adjusters are removed and the substrate mount is attached to the Strasbaugh polisher spindle. The polishing process was run at ~90-120 RPM at the spindle and the stroker arm. Some care was taken so that these ran at a noticeably different rate to avoid a bias for removal in a given direction on the part. The stroke was off-axis by about one quarter of the polishing lap diameter and the lap was stroked across the center instead of reversing direction on-center. A 1933g lead weight was set on the polishing arm as

shown in Figure 5.13. The polishing slurry was a mixture of 0.3 μm Alumina, water and a drop of Dawn detergent. Some slurry was added every minute or so to maintain a smooth polishing lap stroke. These choices were made for the sake of avoiding chatter and fragmentation of the polishing lap while seeking a high enough pressure at the tool to remove glass quickly. The exact choice for speed, stroke and pressure should be made by the optician based on the particular lap, polisher and guide ring.

Figure 5.13: Polishing lap (left) and polishing process on Strasbaugh (right) with 1933g lead weight on the polishing arm.

The best samples from these single fiducial fabrication experiments were Sample 2 and Sample 5. A photograph of each of these samples is shown in Figure 5.14. Quantitative testing results for these samples are given in the next subsection.

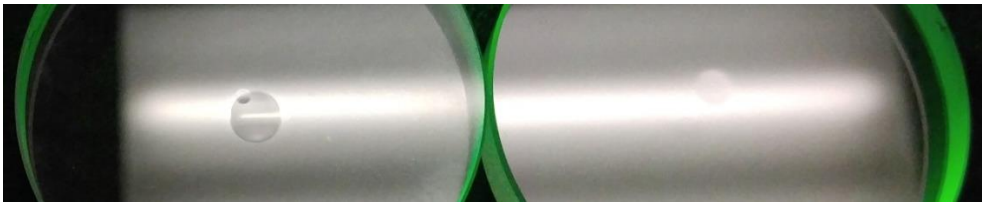

Figure 5.14: Pictures of Sample 2 (left) and Sample 5 (right) on 50.8 mm diameter fused silica flats. Sample 2 is the smaller sub-aperture feature at left, there is another feature on the back of that same substrate.

5.1.1.4 Testing results

The samples were tested with a Fizeau interferometer and F/3.3 transmission sphere. The samples were held in a tip/tilt, X/Y mount on a rail system with an encoder. This arrangement is shown in Figure 5.15. The test was aligned such that the sample could be translated from the cat's eye reflection position back to where the focus was at the center of curvature of the fiducial. The encoder was used to measure the offset between these two positions to find the best-fit radius of each sample. The testing parameters, best-fit radii and aberrations are given below. Note that this equation used to calculate the best-fit radius accounted for residual power:

$$R = \left[\frac{16\sqrt{3}Z_4}{\emptyset^2} + \frac{1}{R_{encoder}}\right]^{-1} \tag{5.2}$$

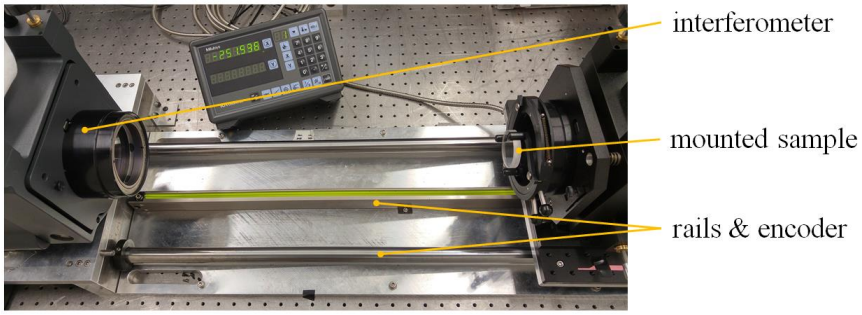

Figure 5.15: Fizeau interferometer and encoder rail system for testing the samples.

The testing results for Sample 2 and Sample 5 are given through two series of figures and tables below:

Sample 2

Table 5.5: Testing parameters and results for the surface test of Sample 2.

Test Date	2/26/2016
Test Instrument	Zygo verifier ATZ, 632.8nm, 4" f/3.3 ref sphere
Averaging	10x acquisitions
Part Name	Sample 2 (phase fiducial)
Part Size	1.8 mm fiducial OD, 50.8 mm diameter flat substrate
Affected diameter	2.3 mm
$R_{encoder}$	72.11 mm
R_f	80.2 ± 1 mm
$\emptyset_f$	0.9 mm (CA OD for processing)

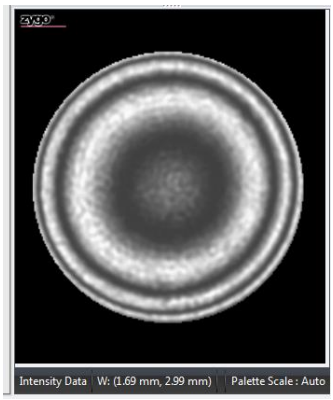

Figure 5.16: Interferogram from measurement of Sample 5 with edge of circle at 1.7mm diameter.

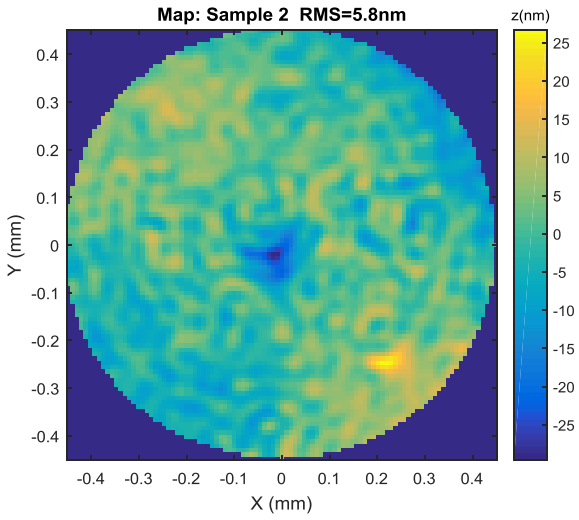

Figure 5.17: Sample 2 surface error map, Z1-Z4 terms subtracted

Table 5.6: Zernike standard surface error coefficients from surface test of Sample 2 at a 72.11 mm encoder offset across a 0.9mm diameter clear aperture.

Noll index (j)	**n**	**m**	**Zernike Standard term name**	**Coefficient (nm)**
1	0	0	Piston	857.26
2	1	1	Tilt (0)	3.11
3	1	-1	Tilt (90)	0.93
4	2	0	Power	-40.81
5	2	-2	Astigmatism (45)	-3.61
6	2	2	Astigmatism (0)	-0.03
7	3	-1	Coma (90)	-1.18
8	3	1	Coma (0)	-0.61
9	3	-3	Trefoil (30)	-0.13
10	3	3	Trefoil (0)	-0.63
11	4	0	Primary Spherical	-1.16
12	4	2	2nd Astigmatism (0)	-0.01
13	4	-2	2nd Astigmatism (45)	-0.04
14	4	4	Tetrafoil (0)	-0.48
15	4	-4	Tetrafoil (22.5)	-0.03
16	5	1	2nd Coma (0)	-0.23
17	5	-1	2nd Coma (90)	-0.13
18	5	3	2nd Trefoil (0)	0.29
19	5	-3	2nd Trefoil (30)	0.06
20	5	5	Pentafoil (0)	0.07
21	5	-5	Pentafoil (18)	0.23
22	6	0	Secondary Spherical	0.81

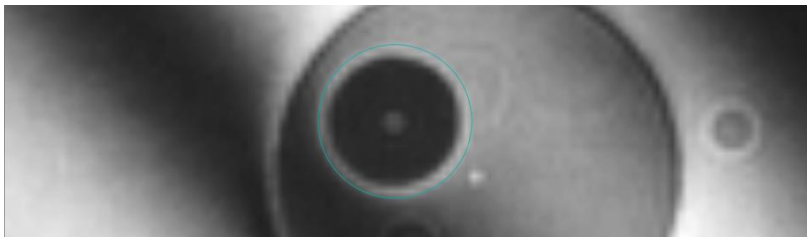

Figure 5.18: Close up of interferogram from measuring flat parent optic with a circle drawn for reference with 2.3 mm diameter around sample 2 surface.

Sample 5

Table 5.7: Testing parameters and results for the surface test of Sample 5.

Test Date	4/25/2016
Test Instrument	Zygo verifier ATZ, 632.8nm, 4" f/3.3 ref sphere
Averaging	10x acquisitions
Part Name	Sample 5 (phase fiducial)
Part Size	3.9 mm fiducial OD, 50.8 mm diameter flat substrate
Affected diameter	8.3 mm
$R_{encoder}$	252.05 mm
R_f	258.6 ± 1 mm
$\emptyset_f$	3.4 mm (CA OD for processing)

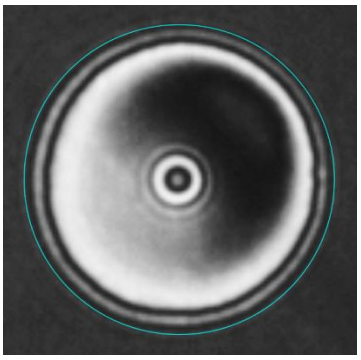

Figure 5.19: Interferogram from measurement of Sample 5 with a circle drawn for reference with 3.9mm diameter.

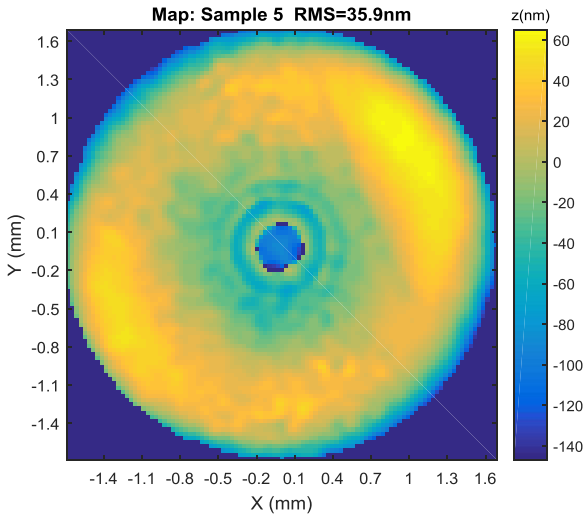

Figure 5.20: Sample 5 surface error map, Z1-Z4 terms subtracted.

Table 5.8: Zernike standard surface error coefficients from surface test of Sample 5 at a 252.05 mm encoder offset across a 3.4mm diameter clear aperture.

Noll index (j)	n	m	Zernike Standard term name	Coefficient (nm)
1	0	0	Piston	412.49
2	1	1	Tilt (0)	-5.35
3	1	-1	Tilt (90)	13.31
4	2	0	Power	-41.60
5	2	-2	Astigmatism (45)	13.41
6	2	2	Astigmatism (0)	3.37
7	3	-1	Coma (90)	-3.76
8	3	1	Coma (0)	-5.32
9	3	-3	Trefoil (30)	0.00
10	3	3	Trefoil (0)	-2.24
11	4	0	Primary Spherical	-30.42
12	4	2	2nd Astigmatism (0)	0.52
13	4	-2	2nd Astigmatism (45)	1.98
14	4	4	Tetrafoil (0)	0.75
15	4	-4	Tetrafoil (22.5)	2.61
16	5	1	2nd Coma (0)	-2.30
17	5	-1	2nd Coma (90)	0.03
18	5	3	2nd Trefoil (0)	-0.12
19	5	-3	2nd Trefoil (30)	-0.32
20	5	5	Pentafoil (0)	-0.16
21	5	-5	Pentafoil (18)	0.09
22	6	0	Secondary Spherical	-5.51

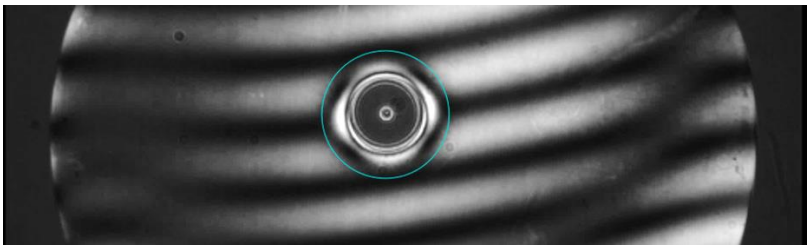

Figure 5.21: Interferogram from measuring flat parent optic with a circle drawn for reference with 8.3 mm diameter around the Sample 5 surface.

5.1.2 Two-fiducial fabrication

Making two fiducials is nothing more than following the single-fiducial fabrication process with the guide ring positioned in two places. A fixture was made to accomplish this where the substrate was translated under the guide ring for making a 252 mm fiducial. This fixture is shown with the substrate installed in Figure 5.22. The original substrate holder was cut to make a slot for the substrate to slide along and a flat interface at the end to use as a stop. A puck was made for the edge of the substrate and glued to the glass with 2216 B/A gray adhesive. This adhesive was chosen for its heat resistance and dependability bonding aluminum to glass. The edge puck was used as a datum for translating the substrate with minimal rotation. The translation was applied between fabrication runs by melting the wax and adding a 40mm aluminum spacer. The spacer has the same thickness as the substrate to support the part of the guide ring which hangs over the edge of the glass.

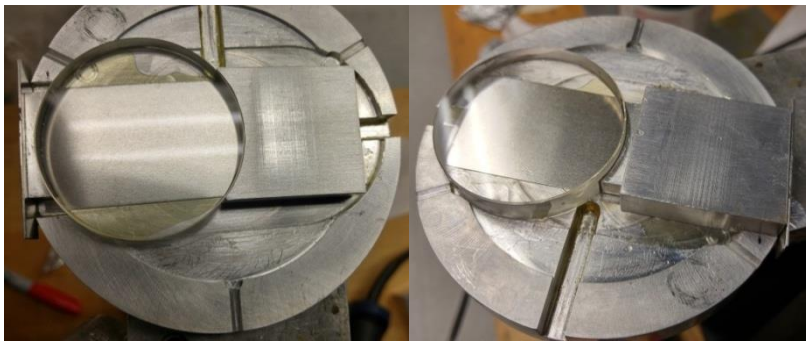

Figure 5.22: Substrate fixture for making two fiducials: from left to right a 40mm block is added to translate the substrate relative to the point where the polishing tool contacts.

A view of the fixture with the guide ring installed is shown in Figure 5.23. In this image the edge of the substrate is visible through the guide ring. The presence of the block which rests against the edge of the substrate was useful to contain the

polishing slurry within the guide ring and on the substrate and also to support the guide ring during polishing. A finished fiducial is visible near the edge. Two features were made using the 40 mm spacer to separate the features by approximately 40 mm. The finished part is shown in Figure 5.24. The main point to be made here is that the fixture must be *very* accurate with good surface finish to make the separation of the features accurate. The substrate should not tilt during translation and the adjusters should also not allow the guide ring to wiggle. The spacer edge puck, and stop must all be accurate geometric shapes with minimal angular errors where the faces are expected to be perpendicular or parallel. Machining inaccuracies are suspected to be the cause of the error reported from testing the separation distance between the fiducials.

Figure 5.23: Guide ring over the two-fiducial fixture with a finished fiducial visible on the glass.

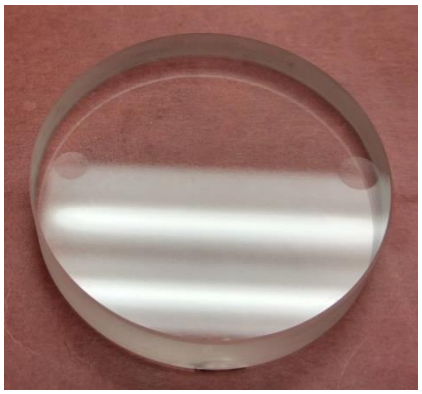

Figure 5.24: Sample 6 with two phase fiducials.

The individual features on Sample 6 were tested with the same setup as Sample 2 and Sample 5. The separation between the fiducials was diagnosed by measuring the translation of the substrate between two null responses from the interferometer test. The fiducial features were also measured relative to mechanical data with a PSM probe on a CMM. The data and results from test and measurements on Sample 6 are given in the series of figures and tables below:

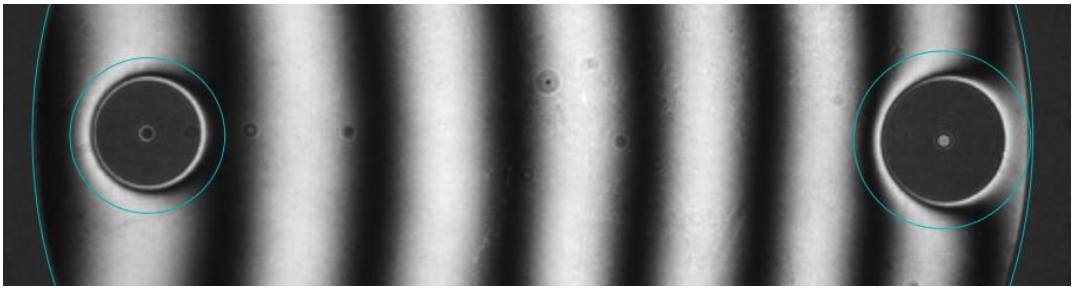

Figure 5.25: Interferogram from measuring the Sample 6 flat parent optic with circles drawn for reference with 7.9 mm (left) and 9.0 mm (right) diameters around the affeted regions.

Sample 6, Feature 1

Table 5.9: Testing parameters and results for the surface test of Sample 6, Feature 1

Test Date	4/27/2016
Test Instrument	Zygo verifier ATZ, 632.8nm, 4" f/3.3 ref sphere
Averaging	10x acquisitions
Part Name	Sample 6, Feature 1 (phase fiducial)
Part Size	4.8 mm fiducial OD, 50.8 mm diameter flat substrate
Affected diameter	7.9 mm
$R_{encoder}$	252.02 mm
R_f	247.2 ± 1 mm
$\emptyset_f$	4.8 mm (CA OD for processing)

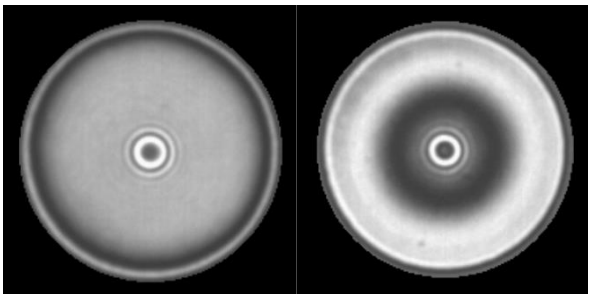

Figure 5.26: Fringes from measuring Sample 6, Feature 1 with an encoder offset of 241.18 mm (left) and 252.02 mm (right). The bull's eye at the center is a hotspot from the back surface of the substrate, not surface error.

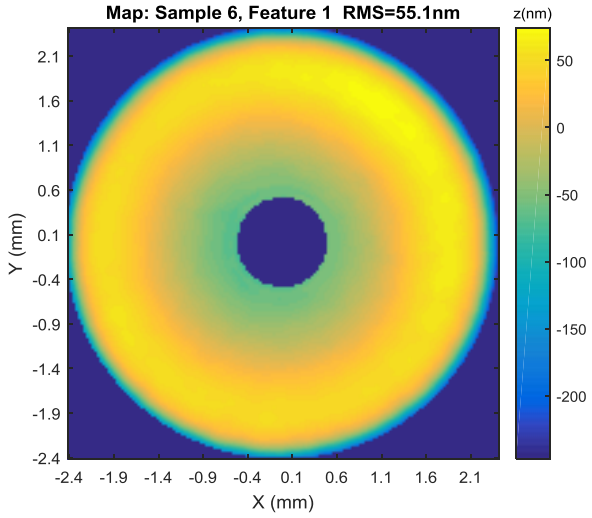

Figure 5.27: Sample 6, Feature 1 surface data map, terms 1-4 subtracted

Table 5.10: Sample 6, Feature 1 Zernike standard term fit coefficients (no aberration subtraction)

Noll index (j)	n	m	Zernike Standard term name	Coefficient (nm)
1	0	0	Piston	11.81
2	1	1	Tilt (0)	-9.68
3	1	-1	Tilt (90)	-6.33
4	2	0	Power	64.16
5	2	-2	Astigmatism (45)	3.25
6	2	2	Astigmatism (0)	0.32
7	3	-1	Coma (90)	-5.34
8	3	1	Coma (0)	-8.21
9	3	-3	Trefoil (30)	-1.52
10	3	3	Trefoil (0)	-0.77
11	4	0	Primary Spherical	-47.84
12	4	2	2nd Astigmatism (0)	0.23
13	4	-2	2nd Astigmatism (45)	0.13
14	4	4	Tetrafoil (0)	-0.13
15	4	-4	Tetrafoil (22.5)	-0.54
16	5	1	2nd Coma (0)	-2.40
17	5	-1	2nd Coma (90)	-3.20
18	5	3	2nd Trefoil (0)	-0.01
19	5	-3	2nd Trefoil (30)	-1.00
20	5	5	Pentafoil (0)	-0.65
21	5	-5	Pentafoil (18)	-0.36
22	6	0	Secondary Spherical	-22.87

Sample 6, Feature 2

Table 5.11: Testing parameters and results for the surface test of Sample 6, Feature 2

Test Date	4/29/2016
Test Instrument	Zygo verifier ATZ, 632.8nm, 4" f/3.3 ref sphere
Averaging	10x acquisitions
Part Name	Sample 6, Feature 2 (phase fiducial)
Part Size	5.3 mm fiducial OD, 50.8 mm diameter flat substrate
Affected diameter	9.0 mm
$R_{encoder}$	252.15 mm
R_f	243.5 ± 1 mm
$\emptyset_f$	5.3 mm (CA OD for processing)

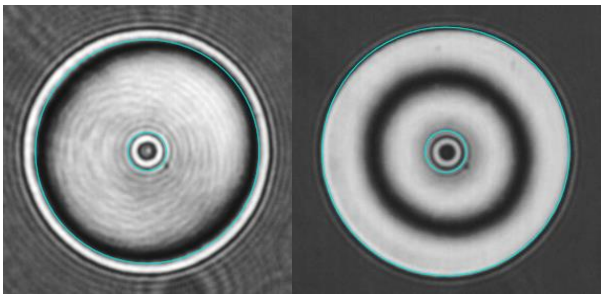

Figure 5.28: Fringes from measuring Sample 6, Feature 2 with an encoder offset of 240.62 mm (left) and 252.15 mm (right). The bull's eye at the center is a hotspot from the back surface of the substrate, not surface error.

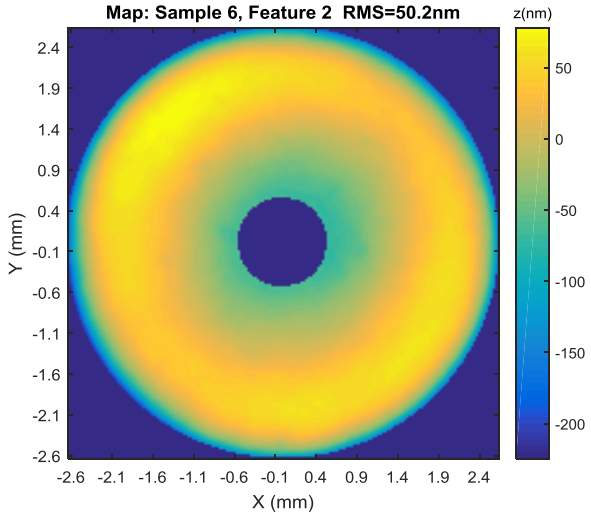

Figure 5.29: Sample 6, Feature 2 surface data map, terms 1-4 subtracted

Table 5.12: Sample 6, Feature 2 Zernike standard term fit coefficients (no aberration subtraction)

Noll index (j)	n	m	Zernike Standard term name	Coefficient (nm)
1	0	0	Piston	270.88
2	1	1	Tilt (0)	3.47
3	1	-1	Tilt (90)	-4.52
4	2	0	Power	125.06
5	2	-2	Astigmatism (45)	-9.62
6	2	2	Astigmatism (0)	-2.11
7	3	-1	Coma (90)	0.76
8	3	1	Coma (0)	6.49
9	3	-3	Trefoil (30)	2.55
10	3	3	Trefoil (0)	2.82
11	4	0	Primary Spherical	-47.16
12	4	2	2nd Astigmatism (0)	-1.67
13	4	-2	2nd Astigmatism (45)	1.81
14	4	4	Tetrafoil (0)	1.09
15	4	-4	Tetrafoil (22.5)	-0.78
16	5	1	2nd Coma (0)	0.61
17	5	-1	2nd Coma (90)	-1.90
18	5	3	2nd Trefoil (0)	0.38
19	5	-3	2nd Trefoil (30)	1.26
20	5	5	Pentafoil (0)	0.42
21	5	-5	Pentafoil (18)	-1.05
22	6	0	Secondary Spherical	-14.44

Fiducial location measurement

The separation between the fiducials is nominally 40 mm and this was measured both on the interferometer test bed and with a CMM. The interferometer measurement of the separation had good optical sensitivity to the fiducials, but the diagnosis of the translation was done with a long-stroke dial indicator with 0.001" resolution. The actuator on the stage used to move the substrate was also used to check the displacement between null measurements of the features. The separation measurements are given with estimated 2σ uncertainties in Table 5.13.

Table 5.13: Measurements of the feature separation on the interferometer test bed.

Diagnosis	Separation (mm)	Est. 2σ
Dial indicator	40.34	0.06
Actuator reading	40.40	0.06

A PSM was attached to a CMM to measure the separation between the centers of curvature of the two features. This constituted a similar optical diagnosis of the features at center of curvature, but this method relied on locating the centroid of a rather large retro-reflected focus. The foci from the two features are shown just as they were viewed during the measurements in Figure 5.30. Locating centroids afforded very high repeatability in these measurements, where the 2σ variation was $\sim 1\mu m$. The measurement results from the CMM diagnoses are given in Table 5.14.

Table 5.14: Measurements of the feature separation on the CMM with PSM and 4X NA 0.1 objective used as non-contact probe at center of curvature.

Measurement	Separation (mm)
1	40.3320
2	40.3321
3	40.3330
2σ	0.0011

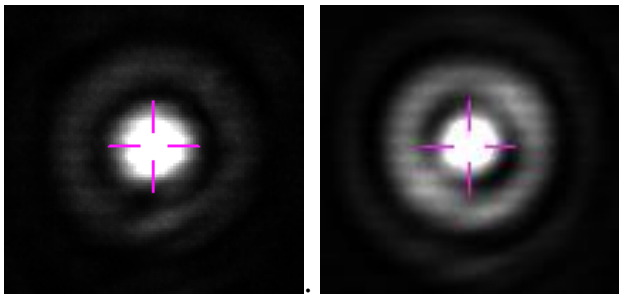

Figure 5.30: Images of the return focus from PSM diagnosis of Sample 6 Feature 1 (left) and Feature 2 (right) at center of curvature.

In order to align the fiducials with other objects in the optical test a registration must be made between the locations of the fiducials *at the surface* and a set of mechanical data. A fixture was prepared with three chrome balls to serve as the mechanical data to establish a coordinate reference frame, as shown in Figure 5.31. The PSM and CMM measured the centers of these balls, the surface of the flat at three widely-separated points, and the centers of curvature of the fiducial features. A coordinate system was established for each measurement with the origin at the center of a circle described by the ball centers and the center of ball A along the X-axis with the Z-axis pointing away from Sample 6. The fiducial vertices were diagnosed for three independent measurements. A projection normal to the flat from the center of

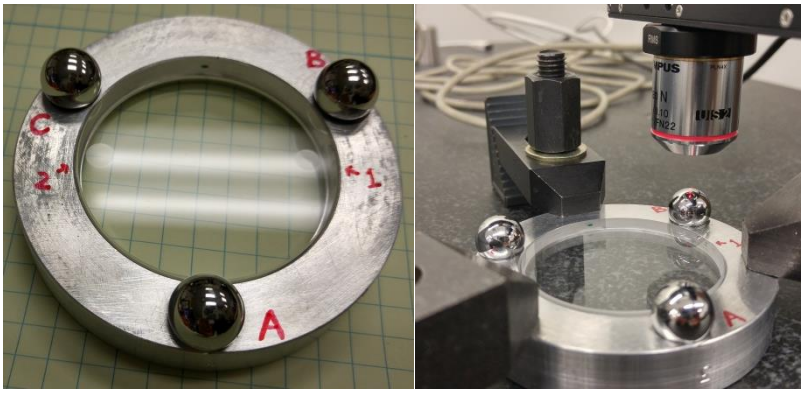

Figure 5.31: Mechanical reference fixture with Sample 6 (left) and CMM measurement with PSM measuring a ball datum (right).

curvature of each feature was evaluated at the surface of the flat to find the location of each feature's vertex. These vertices represent the locations of maximum depth relative to the flat parent optic. The results are given in Table 5.15. Note that it is the limitation in evaluating the *orientation of the flat* which has caused the large ~55μm random errors in the vertex locations and not the precision in detecting the center of curvature locations. All of the results are presented in the same reference frame.

Table 5.15: Measurements of the feature vertex locations on the CMM with PSM. Vertex locations depend on normal projection onto flat from centers of curvature.

Object	Measurement	X (mm)	Y (mm)	Z (mm)
Feature 1 vertex	1	-0.524	19.449	-2.774
	2	-0.530	19.428	-2.782
	3	-0.573	19.463	-2.779
	Average	-0.542	19.447	-2.778
	2σ	0.054	0.035	0.008
Feature 2 vertex	1	0.870	-20.859	-2.698
	2	0.877	-20.802	-2.691
	3	0.823	-20.846	-2.694
	Average	0.857	-20.836	-2.694
	2σ	0.059	0.060	0.007

5.2 INTERFEROMETER DEMONSTRATIONS

The samples made and presented in Section 5.1 were made for specific demonstration experiments. This section presents the experimental setup and the application of the phase fiducial samples in a set of alignment demonstrations. For each demonstration it is found that the sensitivity of the phase fiducials to misalignment matches expectations. The demonstrations provide valuable insight into the practicality of this approach for alignment. It is demonstrated that the limited

dynamic range of the fiducials does not pose a problem for rough alignment and that the feedback the interference response provides gives the technician very subtle control and instantaneous observation of the optical test alignment and stability.

5.2.1 Experimental setup

A CGH-corrected Fizeau interferometer was designed and built to test a flat test optic with phase fiducials. The experiment was carried out to demonstrate:

1. The principle of operation is valid; phase fiducials are readily and effectively implemented
2. The parametric design formulae accurately predict the alignment sensitivity and dynamic range performance of phase fiducials
3. A set of phase fiducials may be used to detect projection magnification and clocking misalignment.

The experiment is also critical to explore any practical issues that may arise in an implementation of this alignment technique. This subsection presents the design and performance of the interferometer before a set of experiments and results are shown in subsequent subsections.

The optical layout of the reference branch of the interferometer is superimposed on the assembled instrument in Figure 5.32. This interferometer substantially follows the design form of the TAO secondary mirror test interferometer. However, there are several notable differences. The source is a single unpolarized on-axis single mode fiber. In its nominal state this interferometer exhibits

symmetry across the Y-Z plane, defined in Figure 5.33. Temporal phase-shifting is used with a PZT scanner providing 5 x $\pi/2$ – phase shifts per acquisition. The CGH is *not* multiplexed to create a common pattern for sharp focus in the reference branch. The CGH is binary amplitude modulated instead of binary phase modulated. There is no AR coating on the CGH backplane which creates some benign artifacts in the interferograms.

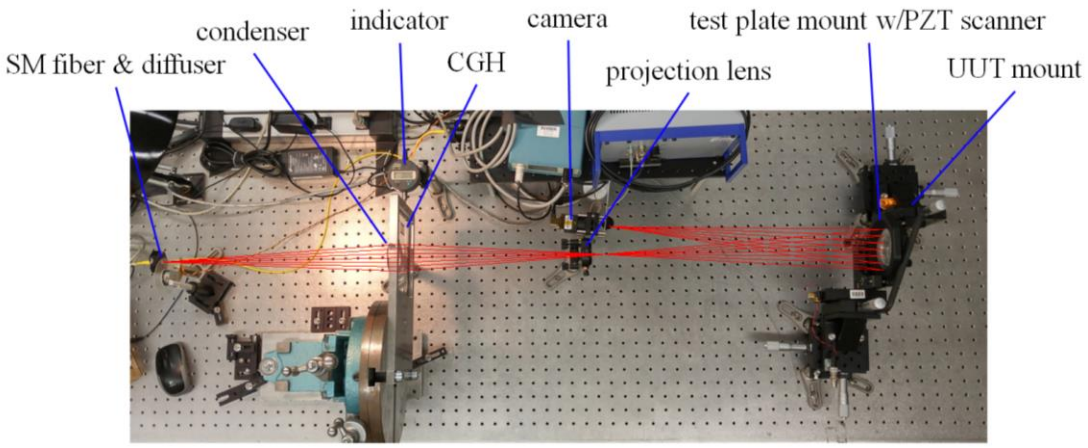

Figure 5.32: Optical layout of the bench test interferometer superimposed on the assembled instrument.

The design of the flat testing configuration is substantially described by the optical layout and tables below. Table 5.16 describes the optical elements of the bench test interferometer. Table 5.17 lists the manufacturers and part numbers of all the stock optics used in the interferometer. Table 5.18 provides a list of all the air gap distances in sequential order. All of these were measured to some degree, but the most crucial distances for the magnification experiments were those related to the CGH projection conjugates. The distance from the back of the PL to the TP was measured with an inside micrometer, as was the distance from the CL to the front of

the TP. The CGH was positioned relative to the PL within ±2mm which corresponds to a system projection magnification of 1.61 ± 0.01. Table 5.19 lists other important parameters which document the design, and hardware for a thorough description of this apparatus.

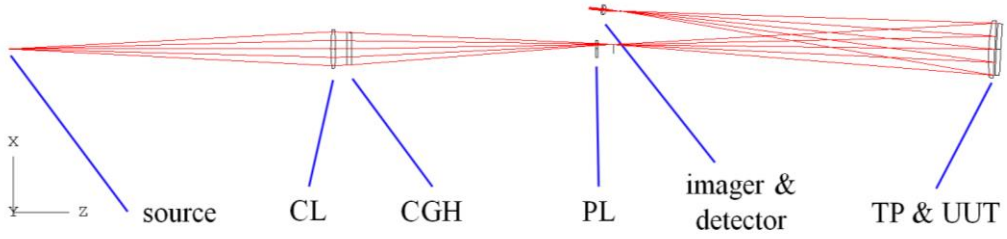

Figure 5.33: Optical layout of the bench test interferometer with labels for each optical element.

Table 5.16: Bench test interferometer optical element nominal design parameters.

Interferometer element	Material	CA OD (mm)	ct (mm)	R_1 (mm)	R_2 (mm)	R_3 (mm)
source fiber	-	~0.005	-	-	-	-
diffuser	Polycarbonate	~ 2	0.78	∞	∞	-
condenser lens (CL)	N-BK7	48.3	6.2	205	-205	-
CGH	Fused Silica	23	6.35	∞	∞	-
projection lens (PL)	N-BK7	22.9	2.8	205.6	-205.6	-
test plate (TP)	N-BK7	73.5	8	258.4	∞	-
spatial filter	black shim	2 - 3	0.3	-	-	-
Imager lens (doublet)	N-BAF10, N-SF6HT	11	4.5, 1.5	12.94	-11.04	-59.26

Table 5.17: Manufacturers and part numbers of stock optics used in the bench test interferometer.

Stock optic	Manufacturer	Part number
source fiber	THOR LABS	P1-630A-FC-1
diffuser	EDMUND OPTICS	#47-677
condenser lens (CL)	THOR LABS	LB1199
projection lens (PL)	THOR LABS	LB1945
test plate (TP)	EDMUND OPTICS	#63-483
Imager lens	THOR LABS	AC127-019-A

Table 5.18: Air gaps between optical elements in the bench test interferometer. The back of the CGH has the diffractive pattern, as indicated in the table. Design excludes the thin diffuser; this optic s near the source and only serves to slightly alter spatial coherence.

Surfaces	*Nominal air gap (mm)*	*Measured air gap (mm)*	*Measurement tool*
source-CL front	425.19	(nominal) ± 2	tape measure
CL back - CGH front	15	(nominal) ± 2	tape measure
CGH back/pattern - PL front	322	(nominal) ± 2	tape measure
(CL back - PL front)	(343.35)	341.10 ± 0.1	inside micrometer
PL back - TP front	515.8	514.43 ± 0.1	inside micrometer
TP back - UUT	2	(nominal) ± 1	tape measure
TP front - spatial filter	485.8	compensator: focus @ filter	(compensator)
spatial filter – imager front	24.34	(nominal) ± 0.5	caliper
imager back – detector	16.35	compensator: sharp image	(compensator)

Table 5.19: Definition of various parameters and surface locations and tilts in the bench test interferometer.

Design Parameter	*Value*
test wavelength	632.8 nm
source coordinates (test, reference)	(on-axis)
spatial filter off-axis distance	+50 mm (X)
CCD detector	Flea 2, FL2G-13S2M-C
object-space sampling frequency	10.2145 samples/mm
image-space sampling frequency	266.667 samples/mm
PS algorithm	5-step, (Schwider-Hariharan)[21]
stop surface	TP back (second pass)
stop diameter	67.94 mm (695 samples)
TP & UUT , tilt about front of TP	-2.9378 deg (Ry), 0 deg(Rx)
UUT, tilt about UUT center	-0.3300 deg(Ry), 0 deg(Rx)

5.2.2 Single phase fiducial demonstrations

Sample 2 and Sample 5 were used to demonstrate alignment between a test CGH projection and a phase fiducial on the test optic. These samples were made with this demonstration in mind where the target diameters and curvatures were driven by

the interferometer design. Sample 2 was made *before* the CGH, so the CGH was designed to compensate the as-built surface figure. Sample 5 was made *after* the CGH, but early attempts making a fiducial with the same curvature had a radius of ~252mm. The design of the CGH pattern for Sample 5 assumed $R_f = 252\text{mm}$ based on an empirically derived expectation.

The optical layouts of the Sample 2 and Sample 5 demonstrations are shown in Figure 5.34. These layouts show the beam off-axis at the PL due to the tilt term in the CGH which separates the diffracted orders. The Sample 2 and Sample 5 configurations have the maximum beam footprint to avoid a vignette from the PL aperture. This represents the condition consistent with maximum alignment sensitivity from each fiducial feature. The parametric design parameters from each of these demonstration configurations are given in Table 5.20. The first-order expected performance of each sample configuration for alignment is also given in Table 5.20.

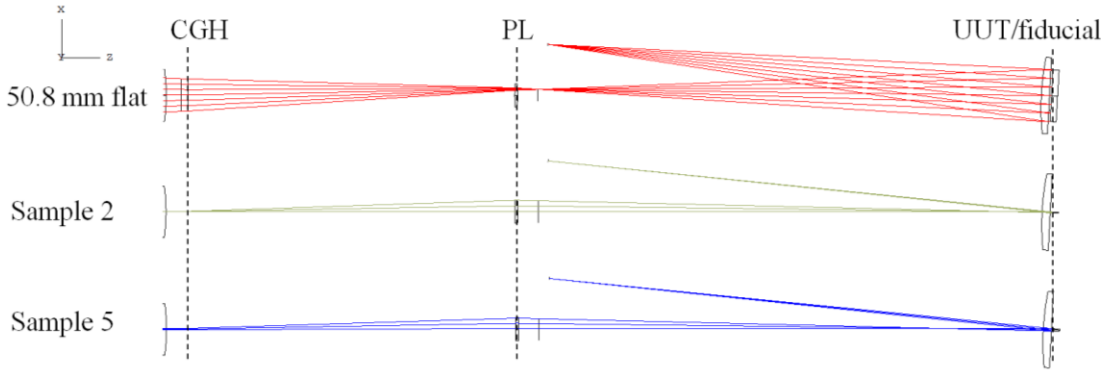

Figure 5.34: Optical layouts of the test branch configurations for the single fiducial experiments. These layouts exclude the source to condenser lens path which is common to all three and already presented above.

Each fiducial has a complimentary phase function at the CGH which shapes the incident wavefront such that it reflects from the fiducial to a focus at the spatial filter. Surrounding this local fiducial pattern there is a large area which primarily tilts the transmitted wavefront so that light reflected from the surrounding flat also focuses at the spatial filter. Note that the clear apertures and affected areas of the phase fiducial samples are larger than the $\emptyset_f$ design values. This creates an uncompensated dark region around each fiducial in the interferogram. Expanding the CGH pattern will not alleviate this unless the projection lens aperture can be expanded to pass the light.

Table 5.20: Parametric design values and expected performance of the phase fiducials for alignment.

Design parameter	*Sample 2*	*Sample 5*
λ (nm)	632.8	632.8
$\emptyset_f$ (mm)	0.84	2.4
C_f (mm)	0.0125	0.00397
f_{samp} (samples/mm)	10.2145	10.2145
Sensitivity (mm/wave)	0.030	0.033
Dynamic range (±mm)	0.065	0.204

5.2.2.1 Sample 2 demonstration

Sample 2 was mounted behind the test plate with a narrow gap of 2 ± 1mm separating the flat interfaces. The mounted phase fiducial sample is shown, visible through the TP, in Figure 5.35. The CGH was translated so that the spatially multiplexed pattern compensating both the flat test surface and the curved fiducial surface at center were projected near the center of the test plate aperture. The mounted CGH is shown with one of several patterns aligned near the CL in Figure

5.36. Sample 2 was tilted to align the test beam focus in the +1-order at the center of the spatial filter. Sample 2 was then translated to get an interference signal from the phase fiducial. The resulting interferogram is given in Figure 5.37. Both the flat and the phase fiducial interference are measured simultaneously with both reflections in the +1-order of the CGH. The unwrapped OPD map for the full measurement is shown in Figure 5.38. It is difficult to see the very small phase fiducial interference pattern, so Figure 5.39 shows a set of close-up views of the phase fiducials in the presence of varying amounts of CGH shear. Note that the dark region around the fiducial is a beam stop imposed by the CGH. The CGH was produced with this obscuration in chrome blocking the beams out to a 2.4mm diameter on the UUT.

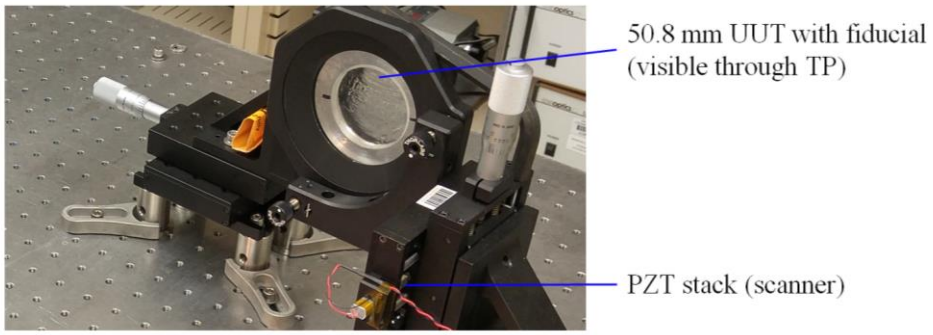

Figure 5.35: Phase fiducial sample mounted in aluminum cell visible through TP.

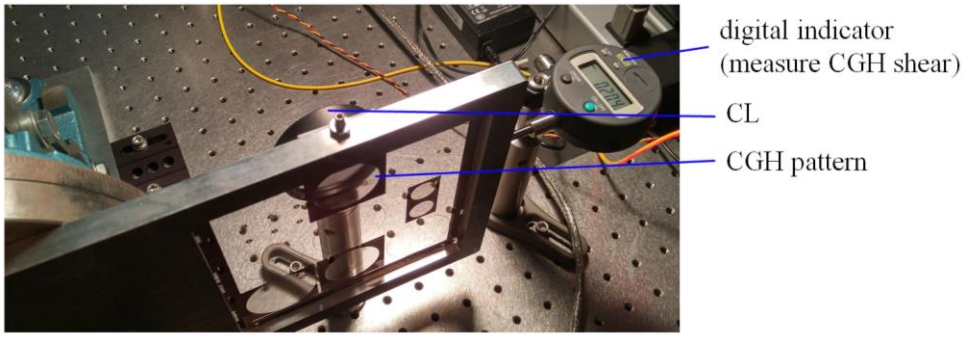

Figure 5.36: CGH pattern aligned to the condenser lens with an indicator to measure movement of the CGH along one axis.

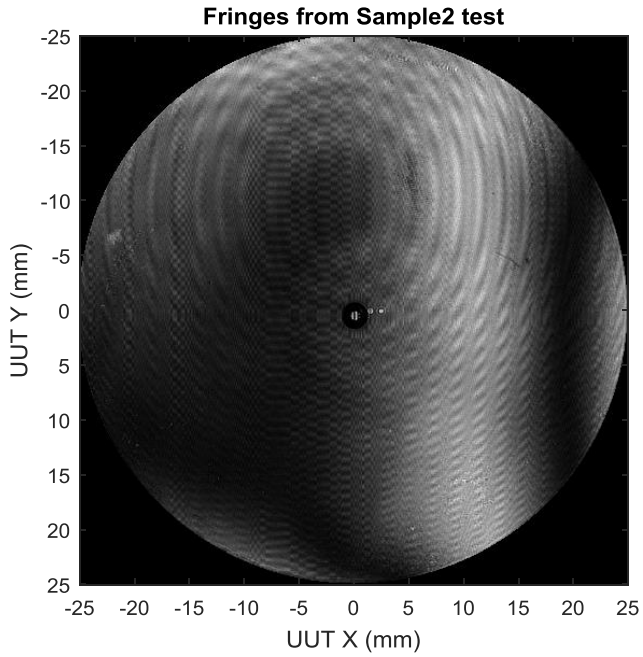

Figure 5.37: Interferogram from the Sample 2 test with some of tilt in the phase fiducial interference and a near-null from the surrounding flat.

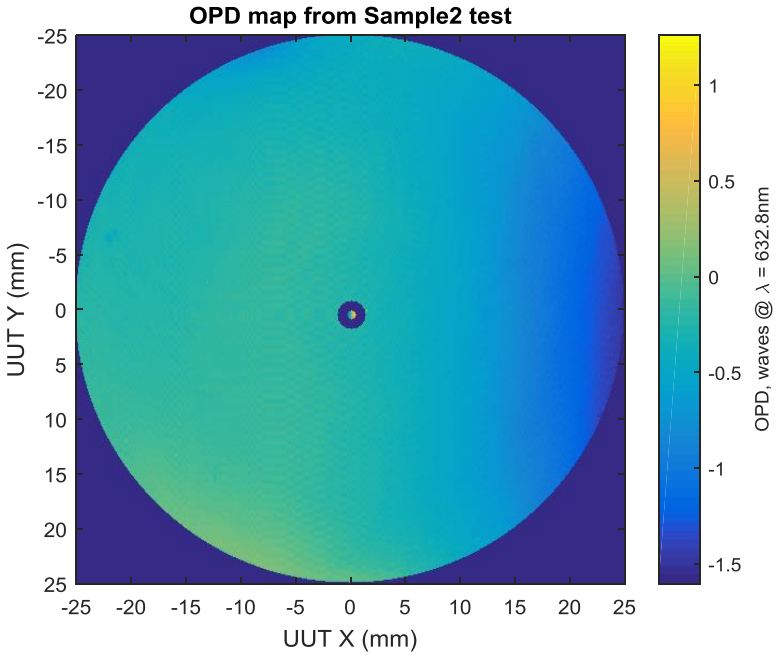

Figure 5.38: Unwrapped phase map from measuring Sample 2 and processing 5 interferograms similar to that shown above. Data with no modulation are masked in this plot.

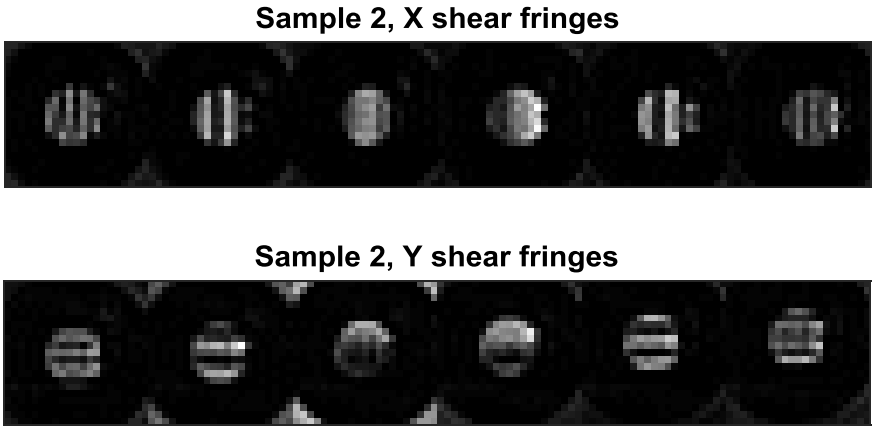

Figure 5.39: Interferograms from the Sample 2 phase fiducial as a function of X and Y shear of the CGH relative to the rest of the interferometer.

A series of measurements were made with the CGH translated to create a transverse shear between its projection and the phase fiducial on Sample 2. The CGH was translated in the X and Y directions separately in two distinct series of measurements. In each case a digital indicator was set up parallel to the axis of CGH translation to measure its displacement. This indicator is Mitutoyo model ID-S112E with a specified accuracy of ±0.003mm and 0.001mm resolution. Note that the CGH was translated instead of Sample 2 because small tilts of the CGH do not influence the measured OPD tilt. The phase fiducial reflects the light, so a tilt of Sample 2 during translation of this optic would tilt the test beam and cause errors in the measurements of shear sensitivity.

The peak-to-valley OPD (PV-OPD) is plotted against CGH displacement for both horizontal (X) and vertical (Y) CGH shear in Figure 5.40. For every data point 5 independent OPD maps were fit to Zernike tilt terms. The Zernike tilt varied between each set acquisition and the average was evaluated to generate the data. The error bars

represent the 2σ estimated random uncertainty for each acquisition based on variance in the Zernike tilt coefficients for each set of OPD measurements. Figure 5.41 highlights the deviations of the results from a linear fit. There is a clear linear regime within ±60μm and the dynamic range extends to ~76μm, exceeding the estimated 65μm range. Table 5.21 gives the expected and measured sensitivities of peak-to-valley OPD tilt as a function of shear, where the measured values are parameters of the linear fits shown in Figure 5.40. It has been found that the simple parametric expressions are in quite close agreement with the experiment. The median uncertainty of peak-to-valley tilt in the OPD has been related to shear uncertainty in Table 5.22. These uncertainties are based on the measurement statistics and calculated sensitivities.

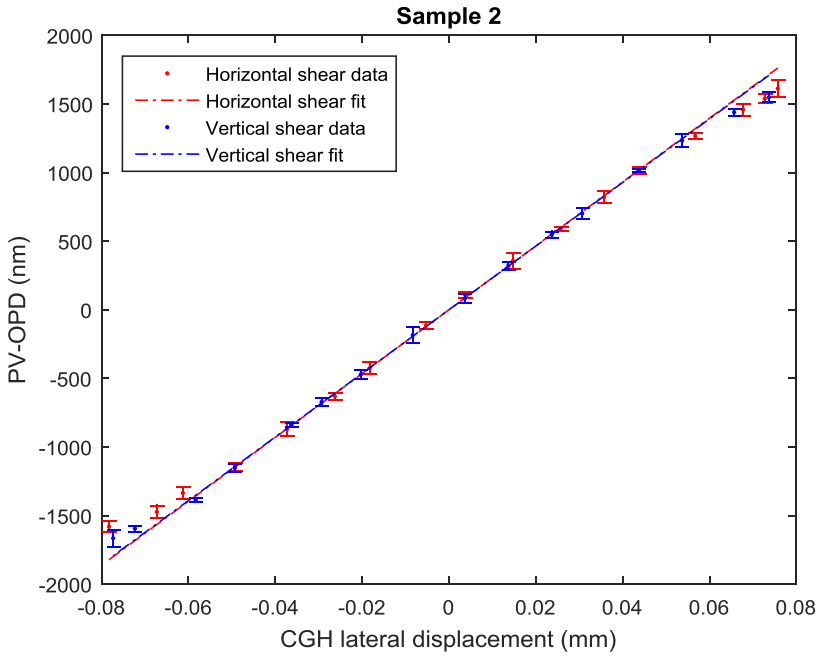

Figure 5.40: PV-OPD plotted against CGH displacement for both horizontal (X) and vertical (Y) CGH shear with Sample 2.

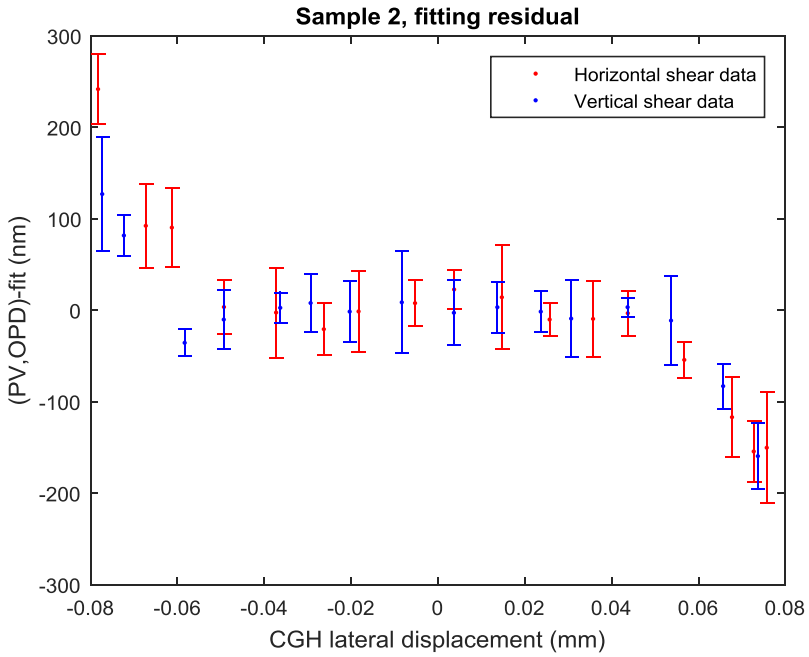

Figure 5.41: Deviations of the Sample 2 PV-OPD results from a linear fit.

Table 5.21: Diameter of regions evaluated for tilt aberration on Sample 2, expected sensitivity from parametric model, and measured sensitivity. Sensitivities have been scaled by 1.61 to represent sensitivity to projection shear at the sample.

Shear direction	Measurement diameter (mm)	Expected sensitivity (PV-OPD/mm)	Measured sensitivity (PV-OPD/mm)	Calculation Error
X	0.587	23627	23270	-1.5%
Y	0.587	23627	23185	-1.9%

Table 5.22: Median uncertainties from PV-OPD tilt diagnoses in the Sample 2 shear experiments. The corresponding projection shear uncertainties are also given.

Shear direction	PV-OPD uncertainty (nm, 2σ)	Projection shear uncertainty (μm, 2σ)
X	±32	±1.4
Y	±29	±1.3

Following the structure of Table 3.11 in Chapter 3, the contributions of error for an alignment made with Sample 2 are given in Table 5.23. All of the values are

estimated from measurements of phase fiducial samples and converted to alignment errors in microns of shear. The fiducial CoC and vertex location values have been estimated based on the Sample 6 CMM measurement data.

Table 5.23: Error contributions and estimated values for projection alignment with Sample 2.

		Alignment error (μm)	
Error contribution (Sample 2)	Error Sources	Relative	Absolute
OPD acquisition	Measurement	1.4	1.4
Power	Fabrication & Measurement	0.6	0.6
Coma	Fabrication & Test	1.5	1.5
Fiducial CoC relative locations (est.)	Fabrication & Test	1.0	1.0
Fiducial vertex absolute location (est.)	Fabrication & Test	-	17.0
	RSS	2.3	17.2

5.2.2.2 Sample 5 demonstration

Sample 5 was mounted, aligned and tested with the same procedure as Sample 2. An interferogram showing a null across the flat and a small amount of tilt in the phase fiducial is given in Figure 5.42. Both the flat and the phase fiducial interference are measured simultaneously with both reflections in the +1-order of the CGH. The unwrapped OPD map for the full measurement is shown in Figure 5.43. It is difficult to see the very small phase fiducial interference pattern, so Figure 5.44 shows a set of close-up views of the phase fiducials in the presence of varying amounts of CGH shear. There is a visible region of zero modulation outside of the tilt fringes which is within the fiducial affected diameter but not compensated by the CGH.

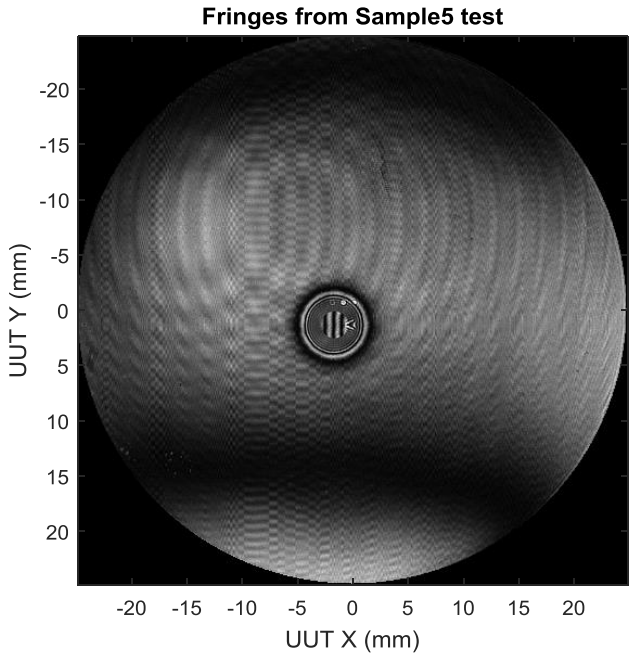

Figure 5.42: Interferogram from the Sample 5 test with some of tilt in the phase fiducial interference and a near-null from the surrounding flat.

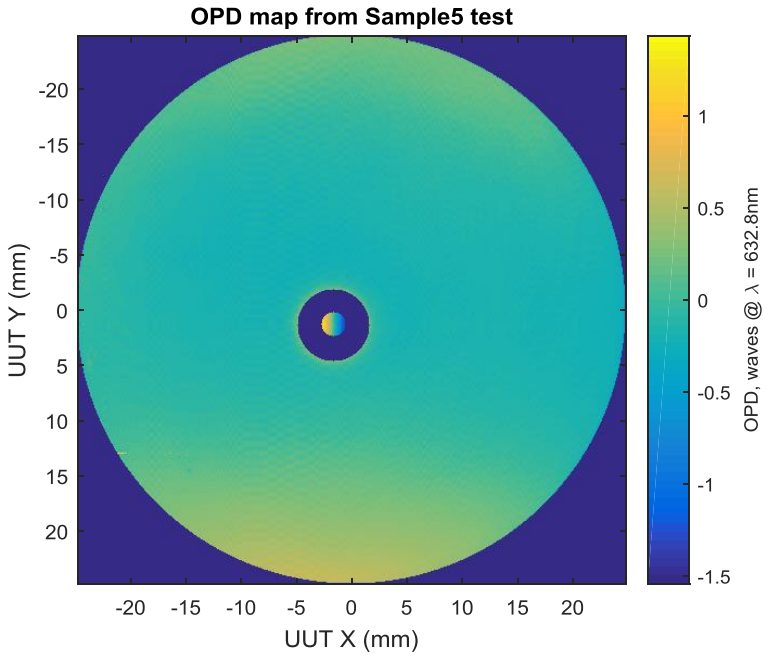

Figure 5.43: Unwrapped phase map from measuring Sample 5 and processing 5 interferograms similar to that shown above. Data with no modulation are masked in this plot.

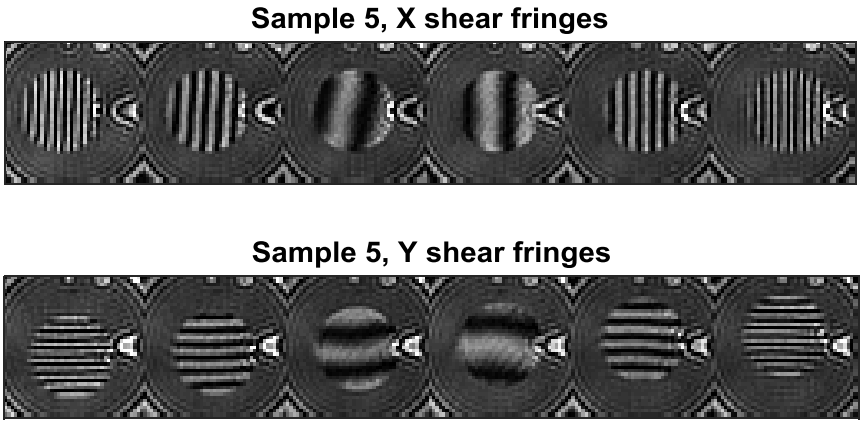

Figure 5.44: Interferograms from the Sample 5 phase fiducial as a function of X and Y shear of the CGH relative to the rest of the interferometer.

A series of measurements were made with the CGH translated to create a transverse shear between its projection and the phase fiducial on Sample 2. The CGH was translated in the X and Y directions with translation measured by the indicator. The peak-to-valley OPD (PV-OPD) is plotted against CGH displacement for both horizontal (X) and vertical (Y) CGH shear in Figure 5.45. Figure 5.46 highlights the deviations of the results from a linear fit. The entire dynamic range shows good linearity. The measured dynamic range extends to ~203μm in close agreement with the estimated 204μm range. Table 5.24 gives the expected and measured sensitivities of peak-to-valley tilt in the OPD as a function of shear, where the measured values are parameters of the linear fits shown in Figure 5.45. It has been found that the simple parametric expressions are in quite close agreement with the experiment. The median uncertainty of peak-to-valley tilt in the OPD has been related to shear uncertainty in Table 5.25. These uncertainties are based on the measurement statistics and calculated sensitivities.

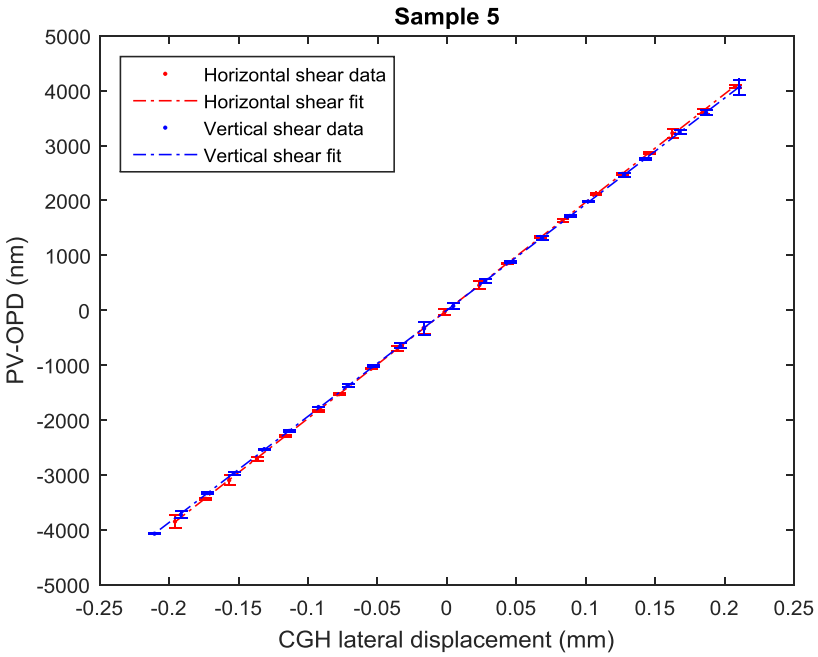

Figure 5.45: PV-OPD plotted against CGH displacement for both horizontal (X) and vertical (Y) CGH shear with Sample 5.

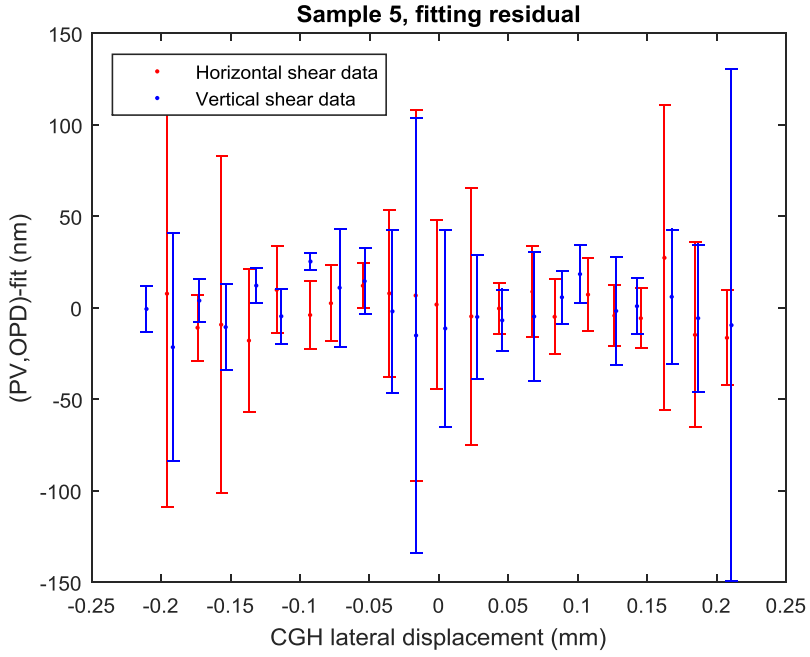

Figure 5.46: Deviations of the Sample 5 PV-OPD results from a linear fit.

Table 5.24: Diameter of regions evaluated for tilt aberration on Sample 5, expected sensitivity from parametric model, and measured sensitivity. Sensitivities have been scaled by 1.61 to represent sensitivity to projection shear at the sample.

Shear direction	Measurement diameter (mm)	Expected sensitivity (PV-OPD/mm)	Measured sensitivity (PV-OPD/mm)	Calculation Error
X	1.566	19499	19713	1.1%
Y	1.566	19499	19341	-0.8%

Table 5.25: Median uncertainties from PV-OPD tilt diagnoses in the Sample 5 shear experiments. The corresponding projection shear uncertainties are also given.

Shear direction	PV-OPD uncertainty (nm, 2σ)	Projection shear uncertainty (μm, 2σ)
X	±32	±1.6
Y	±29	±1.5

Following the structure of Table 3.11 in Chapter 3, the contributions of error for an alignment made with Sample 5 are given in Table 5.26. All of the values are estimated from measurements of phase fiducial samples and converted to alignment errors in microns of shear. The fiducial CoC and vertex location values have been estimated based on the Sample 6 CMM measurement data.

Table 5.26: Error contributions and estimated values for projection alignment with Sample 5.

Error contribution (Sample 5)	Error Sources	Alignment error (μm)	
		Relative	Absolute
OPD acquisition	Measurement	1.6	1.6
Power	Fabrication & Measurement	0.9	0.9
Coma	Fabrication & Test	2.0	2.0
Fiducial CoC relative locations (est.)	Fabrication & Test	1.0	1.0
Fiducial vertex absolute location (est.)	Fabrication & Test	-	55.0
	RSS	2.9	55.1

5.2.3 Two-fiducial demonstrations

The two-fiducial Sample 6 can be used to align the CGH projection to the fiducial pattern in X and Y (shear), Rz (clocking) and Z (magnification). Experiments were conducted to demonstrate each of these applications. The optical layouts of the test branch at the flat and test branch through the fiducials are shown in Figure 5.47. The CGH was actuated and measured in X, Y, Rz and Z and the OPD from the two phase fiducials was recorded. The shear sensitivity experiments were performed in a manner which is nearly identical to the single-fiducial shear experiments. The only difference was that the CGH was moved to a different position between the CL and PL to alter the projection magnification and compensate for the +0.33 mm error in the as-built fiducial separation. The two-fiducial shear experiments were conducted at an estimated magnification of,

$$m = -\frac{\text{fiducial separation}}{\text{CGH pattern separation}} = -\frac{40.33}{24.95} = -1.616. \tag{5.3}$$

This was accounted for in the analysis of the expected projection alignment sensitivities at each feature. The sensitivities measured in the shear experiments were

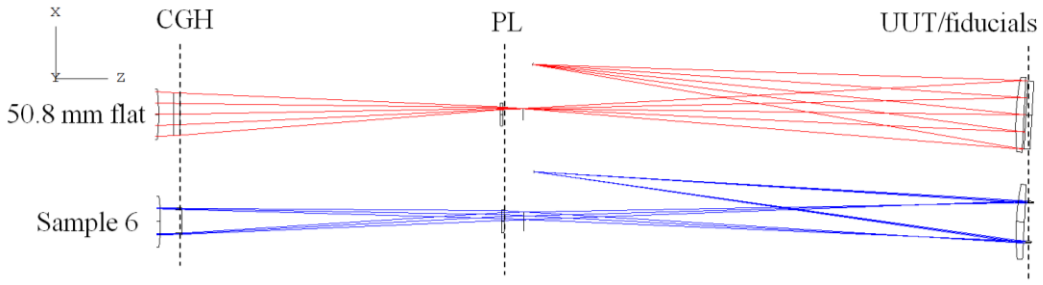

Figure 5.47: Optical layouts of the test branch configurations for the two-fiducial experiments. These layouts exclude the source to condenser lens path which is common to all three and already presented above.

used to calibrate the test to measure clocking and magnification change.

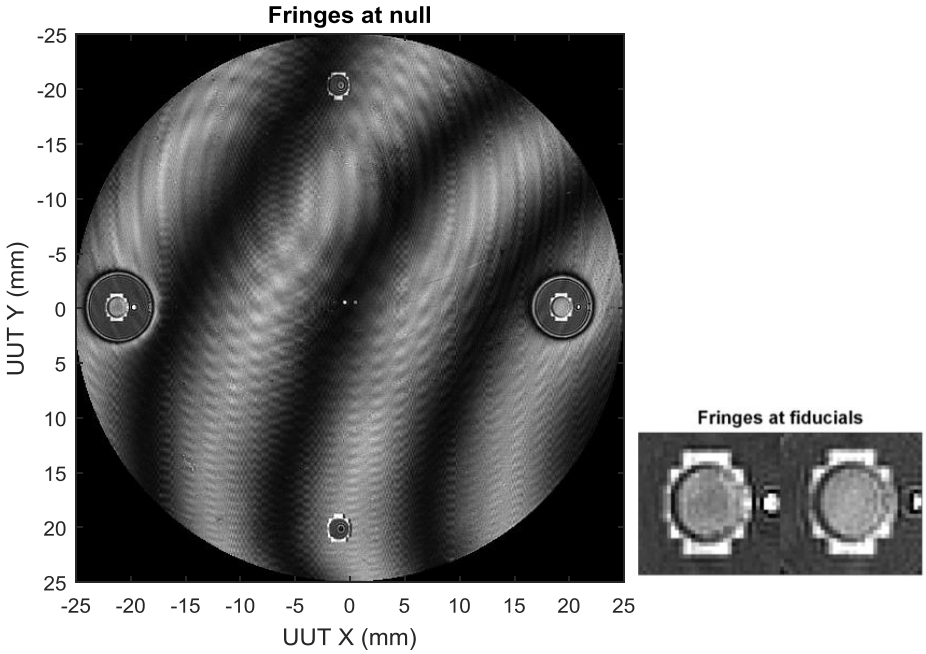

Figure 5.48: Interferogram from the Sample 6 test with some of tilt across the flat and null response from the phase fiducials. Feature 2 (left) and Feature 1 (right) are also shown close-up.

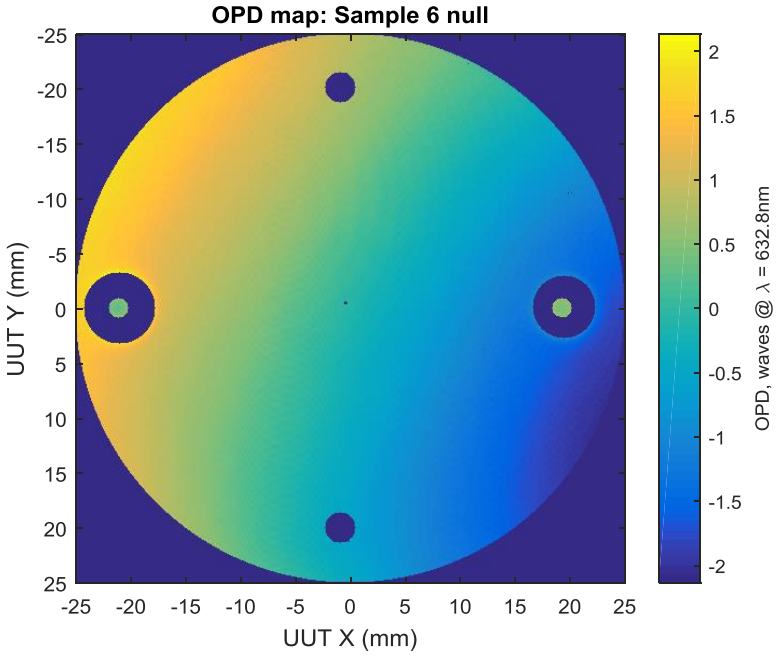

Figure 5.49: Unwrapped phase map from measuring Sample 6 and processing 5 interferograms similar to that shown above. Data with no modulation are masked in this plot.

The interferograms from the pair of fiducials are shown in Figure 5.48. Figure 5.49 provides an OPD plot of the measureable area on the flat surface and at the fiducials. In the shear experiments the CGH was actuated in X and Y to create changes in the fiducial interference similar to that shown in Figure 5.50.

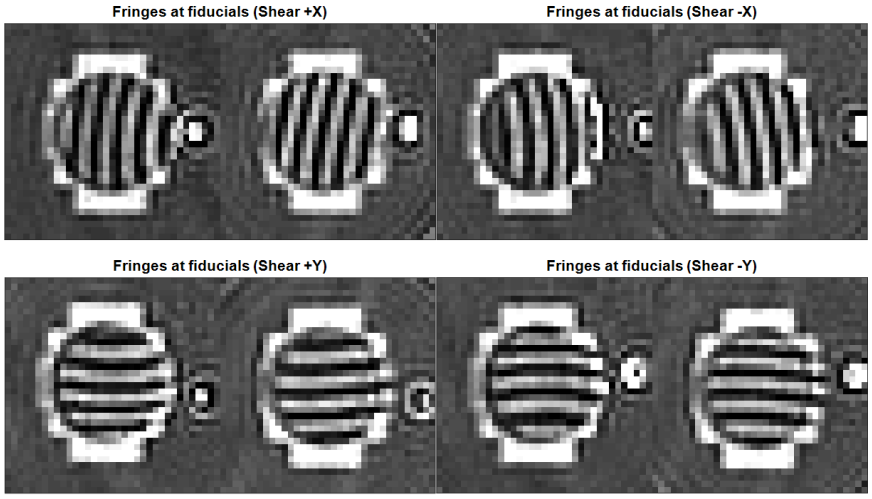

Figure 5.50: Fringes at Feature 2 (left) and Feature 1 (right) for +X, -X, +Y, and –Y shear of the CGH.

A series of measurements were made with the CGH translated to create a transverse shear between its projection and the phase fiducials on Sample 6. The CGH was translated in the X and Y directions with translation measured by the indicator. The peak-to-valley OPD (PV-OPD) is plotted against CGH displacement for both horizontal (X) and vertical (Y) CGH shear in Figure 5.51 and Figure 5.53. Figure 5.52 and Figure 5.54 highlight deviations of the results from the linear fits. The entire dynamic range shows good linearity. The measured dynamic range extends to ~190 μm in Y and ~170 μm in X. It is expected that this degradation of the dynamic range results from interference of the tilted wave with a more aberrated off-axis portion of the reference beam. The degradation is not severe and could be

improved with a common CGH pattern to correct aberration in the reference branch. Table 5.27 gives the expected and measured sensitivities of peak-to-valley tilt in the OPD as a function of projection shear, where the measured values are parameters of the linear fits shown in Figure 5.51 and Figure 5.53. It has been found that the simple parametric expressions are in reasonably agreement with the experiment. The median uncertainty of peak-to-valley tilt in the OPD has been related to shear uncertainty in Table 5.28. These uncertainties are based on the measurement statistics and calculated sensitivities.

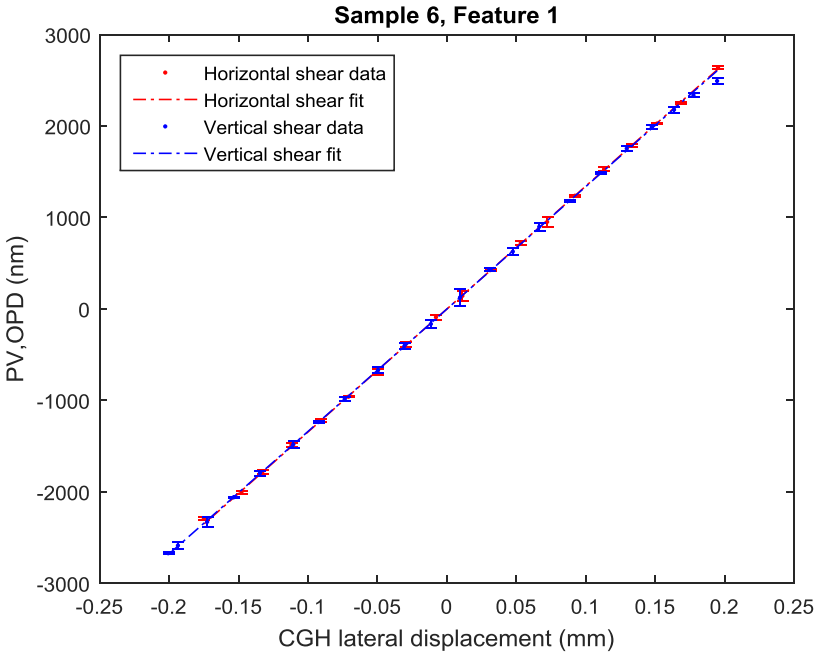

Figure 5.51: PV-OPD plotted against CGH displacement for both horizontal (X) and vertical (Y) CGH shear with Sample 6, Feature 1.

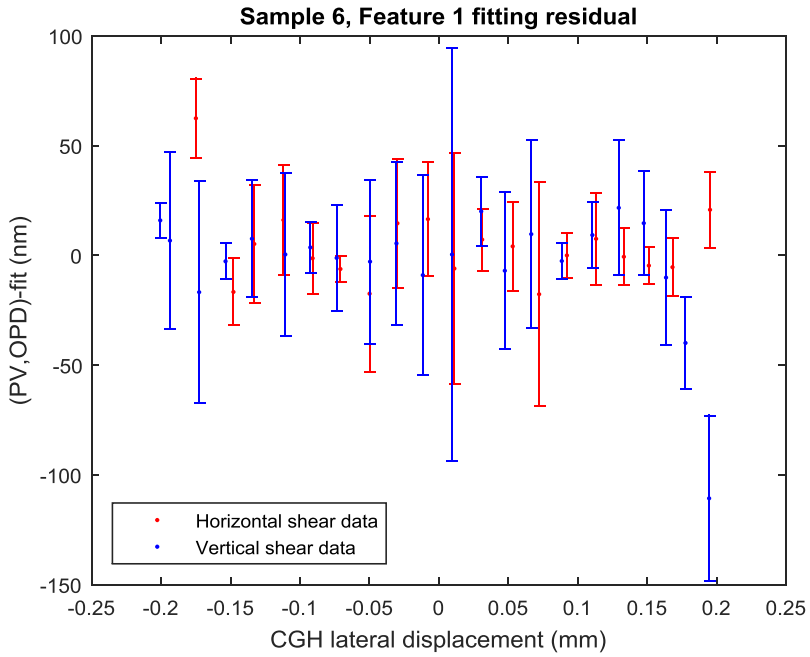

Figure 5.52: Deviations of the Sample 6, Feature 1 PV-OPD results from a linear fit.

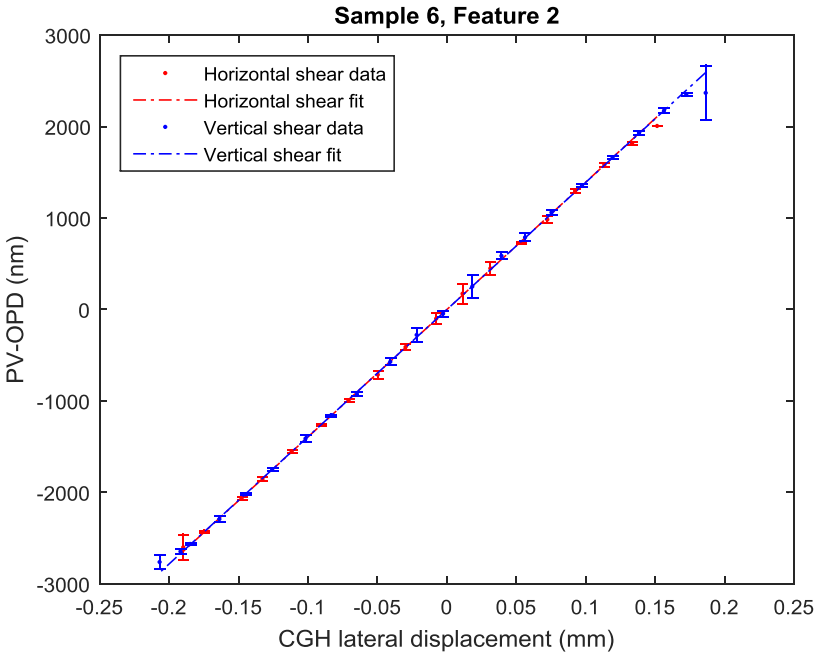

Figure 5.53: PV-OPD plotted against CGH displacement for both horizontal (X) and vertical (Y) CGH shear with Sample 6, Feature 2.

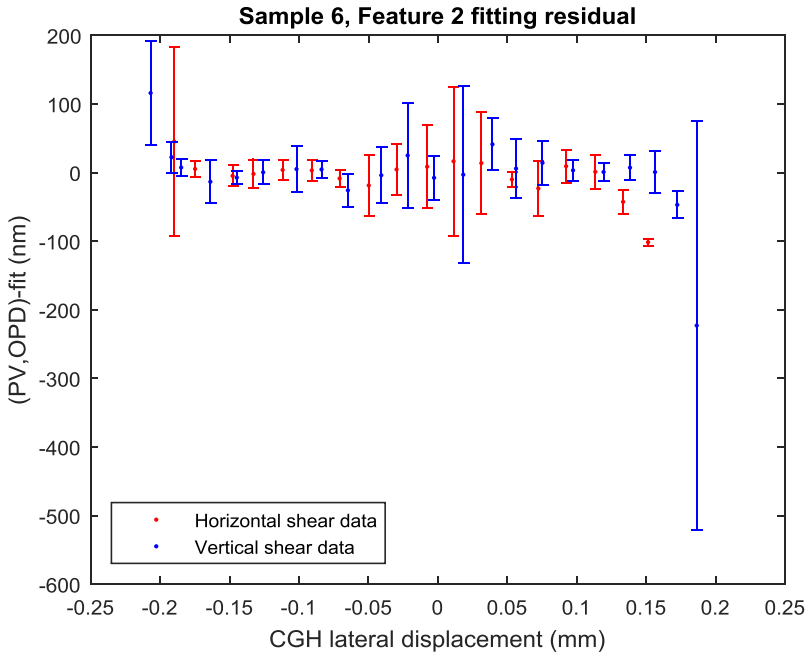

Figure 5.54: Deviations of the Sample 6, Feature 2 PV-OPD results from a linear fit.

Table 5.27: Diameter of regions evaluated for tilt aberration on Sample 6, expected sensitivity from parametric model, and measured sensitivity. Sensitivities have been scaled by 1.616 to represent sensitivity to projection shear at the sample.

Shear	Measurement diameter (mm)	Expected sensitivity (PV-OPD/mm)	Measured sensitivity (PV-OPD/mm)	Calculation Error
Feature 1, X	0.979	12800	13446	4.8%
Feature 1, Y	0.979	12800	13390	4.4%
Feature 2, X	0.979	12994	13938	6.8%
Feature 2, Y	0.979	12994	13913	6.6%

Table 5.28: Median uncertainties from PV-OPD tilt diagnoses in the Sample 6 shear experiments. The corresponding projection shear uncertainties are also given.

Shear	PV-OPD uncertainty (nm, 2σ)	Projection shear uncertainty (μm, 2σ)
Feature 1, X	21	1.6
Feature 1, Y	31	2.3
Feature 2, X	31	2.2
Feature 2, Y	31	2.2

Following the structure of Table 3.11 in Chapter 3, the contributions of error for an alignment made with Sample 6 are given in Table 5.29 and Table 5.30. All of the values are estimated from measurements made on Sample 6.

Table 5.29: Error contributions and estimated values for projection alignment with Sample 6, Feature 1.

Error contribution (Sample 6, Feature 1)	Error Sources	Alignment error (μm)	
		Relative	Absolute
OPD acquisition	Measurement	2.3	2.3
Power	Fabrication & Measurement	4.1	4.1
Coma	Fabrication & Test	1.6	1.6
Fiducial CoC relative locations (meas.)	Fabrication & Test	1.0	1.0
Fiducial vertex absolute location (meas.)	Fabrication & Test	-	55.0
	RSS	5.1	55.2

Table 5.30: Error contributions and estimated values for projection alignment with Sample 6, Feature 2.

Error contribution (Sample 6, Feature 2)	Error Sources	Alignment error (μm)	
		Relative	Absolute
OPD acquisition	Measurement	2.3	2.3
Power	Fabrication & Measurement	8.0	8.0
Coma	Fabrication & Test	1.6	1.6
Fiducial CoC relative locations (meas.)	Fabrication & Test	1.0	1.0
Fiducial vertex absolute location (meas.)	Fabrication & Test	-	55.0
	RSS	8.5	55.7

With Sample 6 under test, the CGH was actuated in Rz (clocking) and measurements were made at various orientations. The measured sensitivities given in Table 5.27 were used to convert the tilt measurements into shear misalignments at each fiducial. The difference in Y shear was converted to a clocking angle of the projection alignment. The clocking angle was also evaluated with two Mitutoyo digital indicators in the configuration shown in Figure 5.55. The interference from the

fiducials with a CW and CCW clocking of the CGH are shown in Figure 5.56. The difference in angular misalignment diagnosed by the phase fiducial interference vs. the indicators is plotted against the clocking angle in Figure 5.57. The dotted line at zero represents a perfect agreement between the diagnoses. The error bars represent the 2σ random error from aberration uncertainties in each set of data acquisitions. The dynamic range is ~0.7 degrees with a median 2σ error of ±0.005 degrees.

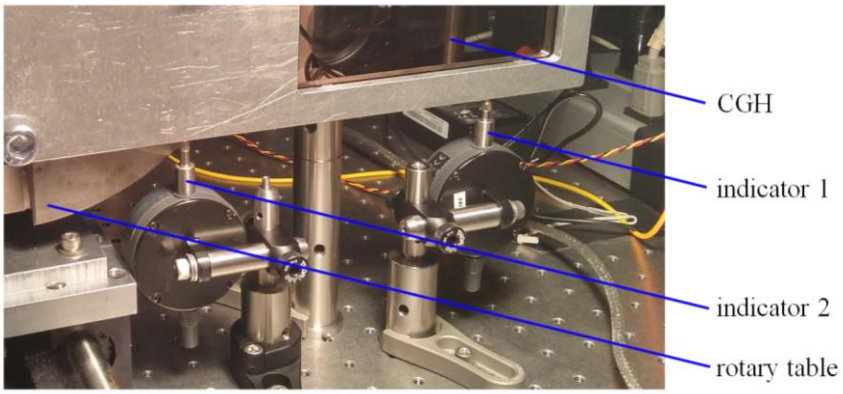

Figure 5.55: Photograph of the indicator configuration to measure clocking of the CGH. Indicators separated by 161.58 mm

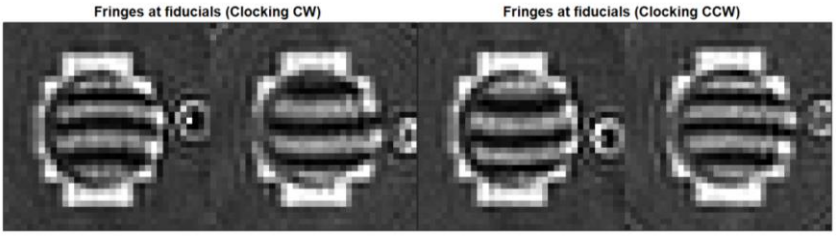

Figure 5.56: Fringes at Feature 2 (left) and Feature 1 (right) for CW and CCW clocking of the CGH.

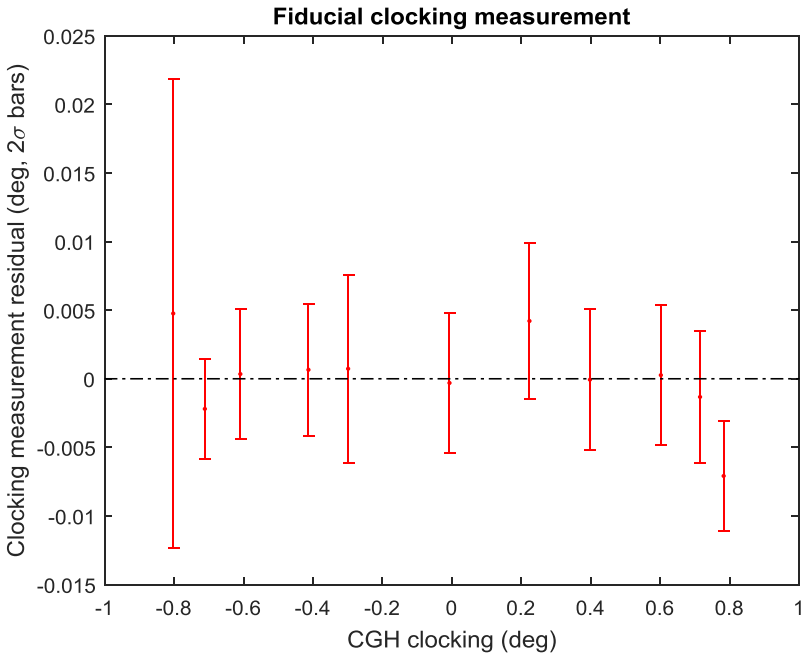

Figure 5.57: Discrepancies between clocking measured by fiducials and by indicators. Error bars represent random errors from aberration measurements at each angle.

The magnification of the CGH projection to the phase fiducials was varied by translating the CGH in Z with all other optics fixed. An indicator was set up to measure the Z translation, as shown in Figure 5.58. The projection shear was derived from measurements of the fiducial interference at various CGH positions. Examples of the interference observed at the fiducials for + and – magnification deviations are given in Figure 5.59. The difference in X shear at the fiducials was processed as projection height deviations to derive what the magnification of the system was for each measurement. The median random uncertainty for magnification measurement was ±0.0003 (2σ). To match this precision by measurement of conjugate distances from the projection lens a ±0.050 mm (2σ) distance measuring precision is required.

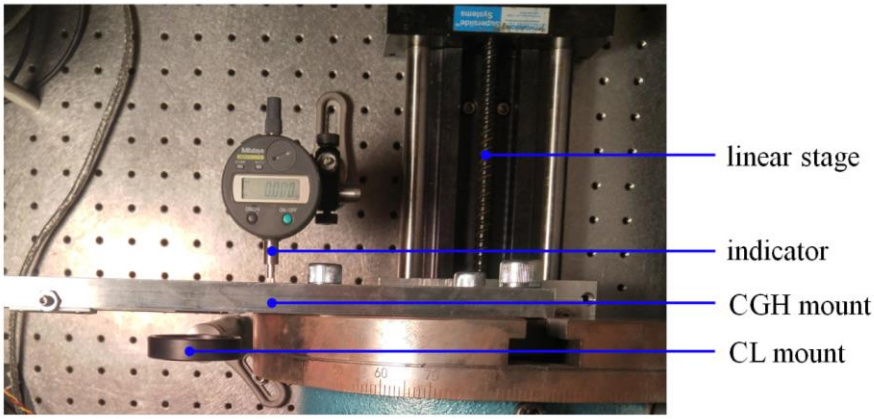

Figure 5.58: Photograph of the indicator configuration to measure magnification deviations in the CGH projection.

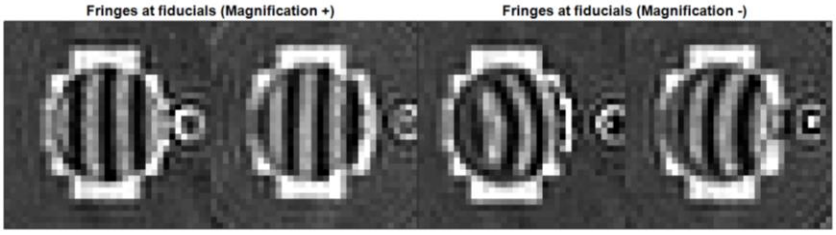

Figure 5.59: Fringes at Feature 2 (left) and Feature 1 (right) for + and – magnification deviations in the CGH projection.

The expected values for magnification were gotten from perturbing a raytrace model calibrated to match the measured dimensions and sensitivities of the interferometer and fiducials. The measured and simulated magnification values are plotted against CGH Z-translation in Figure 5.60. In general the measurement is in close agreement with the model, but for large magnification deviations there is an unknown source of inaccuracy. Ideally the CGH is designed to match the as-built fiducial separation and alignment of the instrument would not involve working at the edges of the dynamic range.

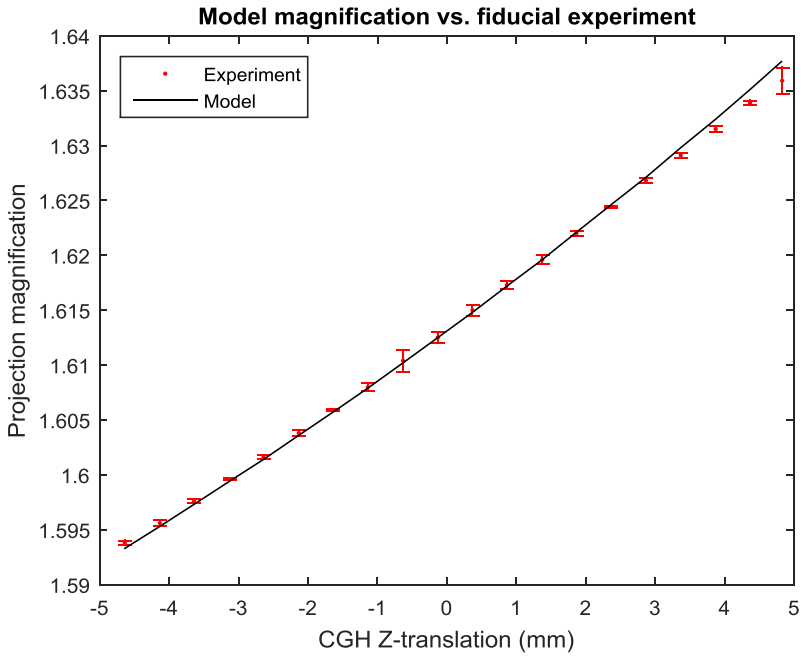

Figure 5.60: Plot showing the measurement-derived magnification values against those predicted by the raytrace model configured with as-aligned dimensions of the interferometer.

CHAPTER 6

CONCLUSIONS

This dissertation has provided a set of analyses, demonstrations and implementations of alignment schema to expose the strength of CGH phase references for optical alignment. The implementation of CGH co-alignment for the HET Wide Field Corrector alignment was combined with wavefront referencing methods within two subsystem tests. Despite the challenges with the HET WFC alignment, the use of CGHs as phase references provided a well-bounded solution and a successful system alignment. Currently, our shop is aligning a CGH-corrected Fizeau interferometer by incoherent amplitude-referencing. This dissertation has presented an alternative for aligning phase projections for this type and other types of CGH-corrected interferometer with sub-aperture phase references called "phase fiducials."

Phase fiducials are effective references for aligning a CGH-produced wavefront to an optical or mechanical datum within an interferometer test. It has been shown that the phase fiducial features offer very high alignment sensitivity and that the features may also serve directly as mechanical data in the case of ball references or may be registered to a set of mechanical data. The demonstrations show that the parametric design and performance predictions for this alignment scheme are valid. There is a fundamental trade-off in this method between dynamic range and sensitivity which the designer must consider. The analysis and case studies provide the means to determine which fiducial designs will perform as required.

APPENDIX A:

Acronym definitions

CGH: Computer-Generated Hologram

HET WFC: Hobby-Eberly Telescope Wide Field Corrector

TAO: Tokyo Atacama Observatory

TAO SM: Tokyo Atacama Observatory Secondary Mirror

PSD: Position Sensitive Detector

OAP: Off-Axis Parabola

UUT: Unit Under Test

PSM: Point-Source Microscope

EE: Encircled Energy

FFOV: Full Field of View

CC: ConCave

CX: ConveX

CoC: Center of Curvature

FZP: Fresnel Zone Plate

SMR: Sphere Mounted Retroreflector

DOF: Degree(s) Of Freedom

RSS: Root Sum Square

APPENDIX B:

Zernike Standard Annular basis terms

Table B.1 Zernike annular basis terms defined in terms of a normalized radial pupil coordinate system bounded at $\rho = 1$ and the central obscuration ratio, ϵ.

Term	Aberration	Formula
Z1	Piston	1
Z2	Tilt 0-deg	$2[\rho/(1+\epsilon^2)^{1/2}]\cos\theta$
Z3	Tilt 90-deg	$2[\rho/(1+\epsilon^2)^{1/2}]\sin\theta$
Z4	Power	$\sqrt{3}(2\rho^2-1-\epsilon^2)/(1-\epsilon^2)$
Z5	Astigmatism 45-deg	$\sqrt{6}[\rho^2/(1+\epsilon^2+\epsilon^4)^{1/2}]\sin 2\theta$
Z6	Astigmatism 0-deg	$\sqrt{6}[\rho^2/(1+\epsilon^2+\epsilon^4)^{1/2}]\cos 2\theta$
Z7	Coma 90-deg	$\sqrt{8}\dfrac{3(1+\epsilon^2)\rho^3-2(1+\epsilon^2+\epsilon^4)\rho}{(1-\epsilon^2)[(1+\epsilon^2)(1+4\epsilon^2+\epsilon^4)]^{1/2}}\sin\theta$
Z8	Coma 0-deg	$\sqrt{8}\dfrac{3(1+\epsilon^2)\rho^3-2(1+\epsilon^2+\epsilon^4)\rho}{(1-\epsilon^2)[(1+\epsilon^2)(1+4\epsilon^2+\epsilon^4)]^{1/2}}\cos\theta$
Z11	Primary Spherical	$\sqrt{5}[6\rho^4-6(1+\epsilon^2)\rho^2+1+4\epsilon^2+\epsilon^4]/(1-\epsilon^2)^2$

APPENDIX C:

252mm phase fiducial tooling drawings

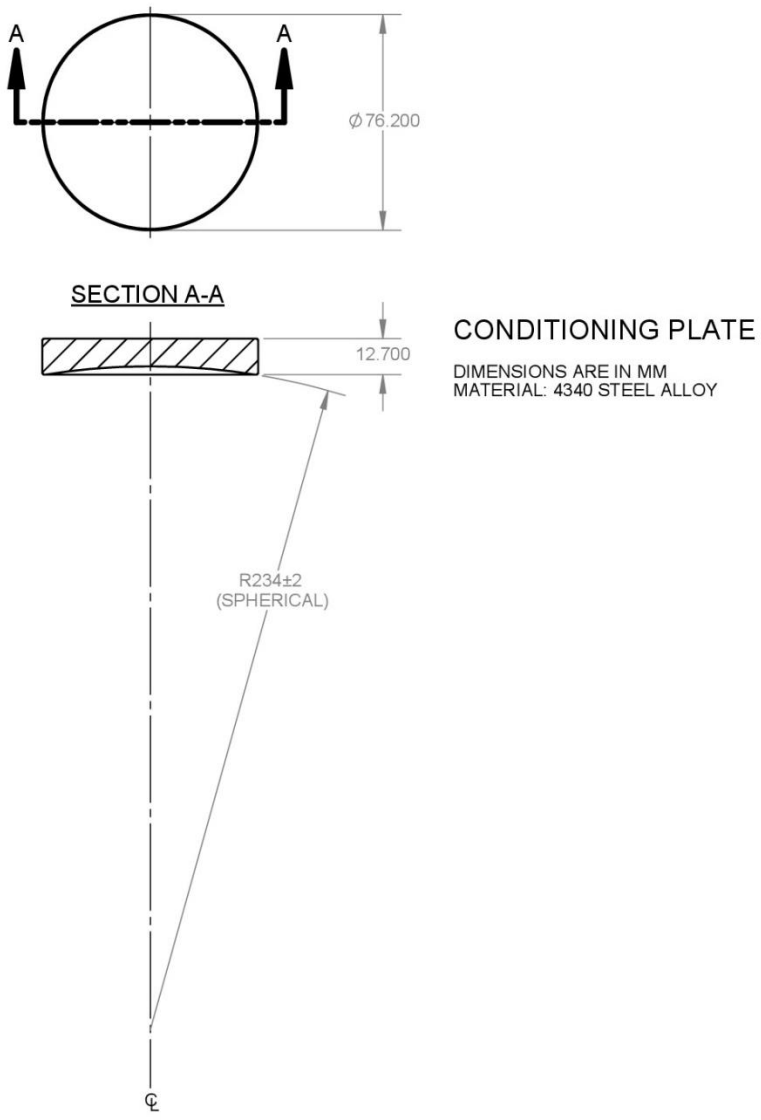

Figure C.1: Mechanical drawing of the conditioning plate for making Sample 5 and Sample 6.

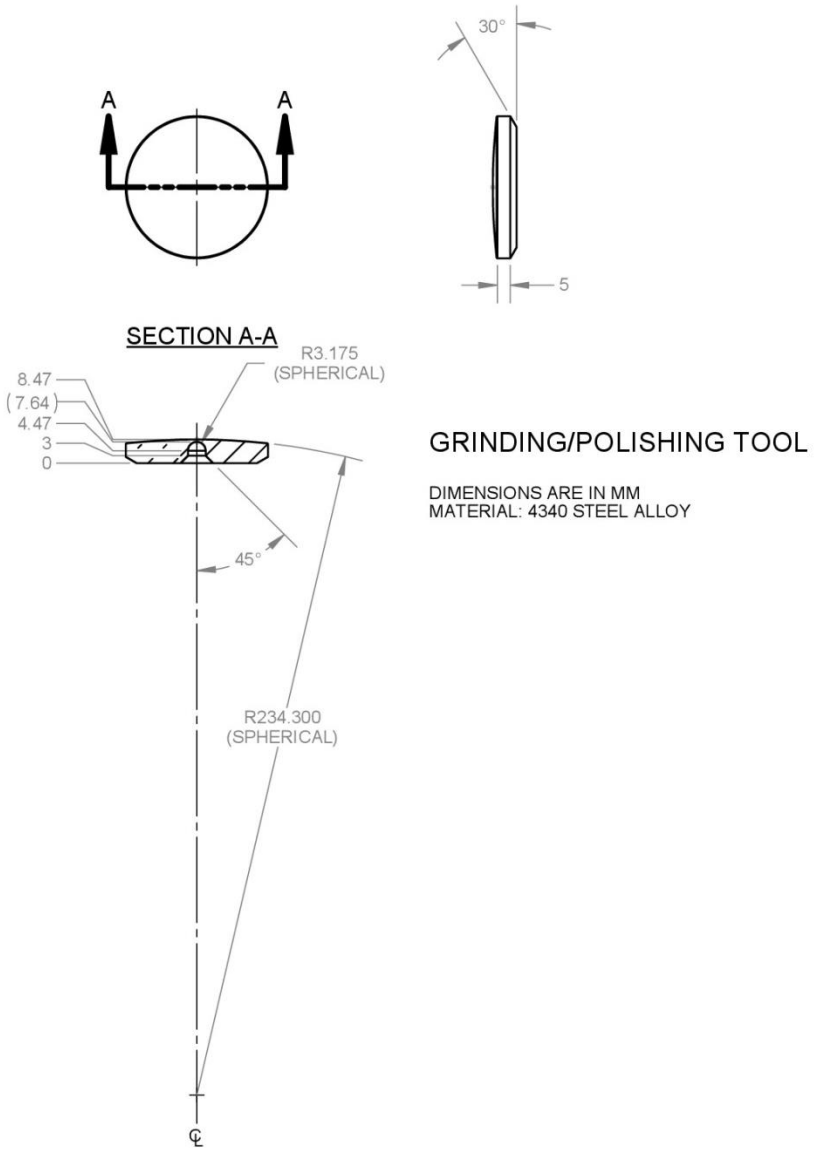

Figure C.2: Mechanical drawing of the tools for making Sample 5 and Sample 6.

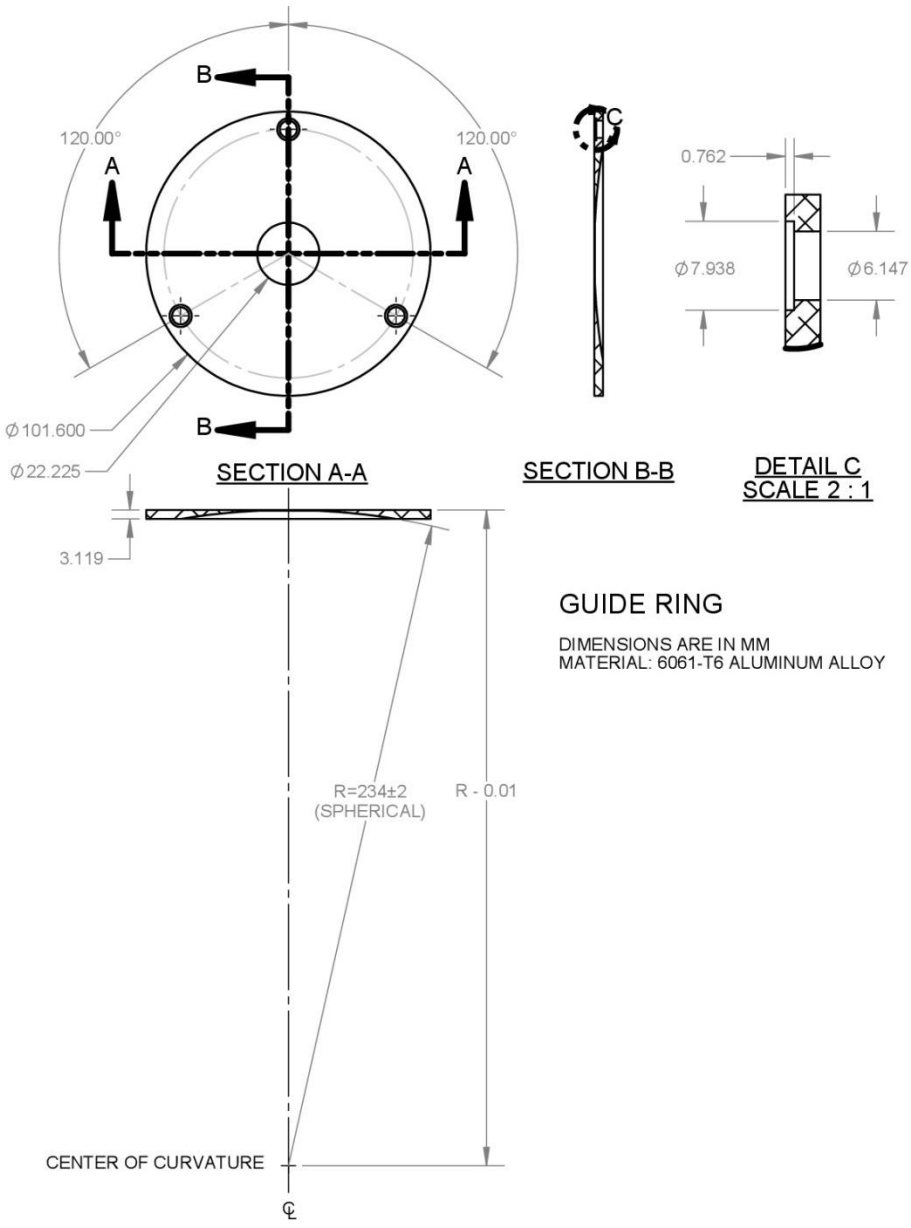

Figure C.3: Mechanical drawing of the guide ring for making Sample 5 and Sample 6.

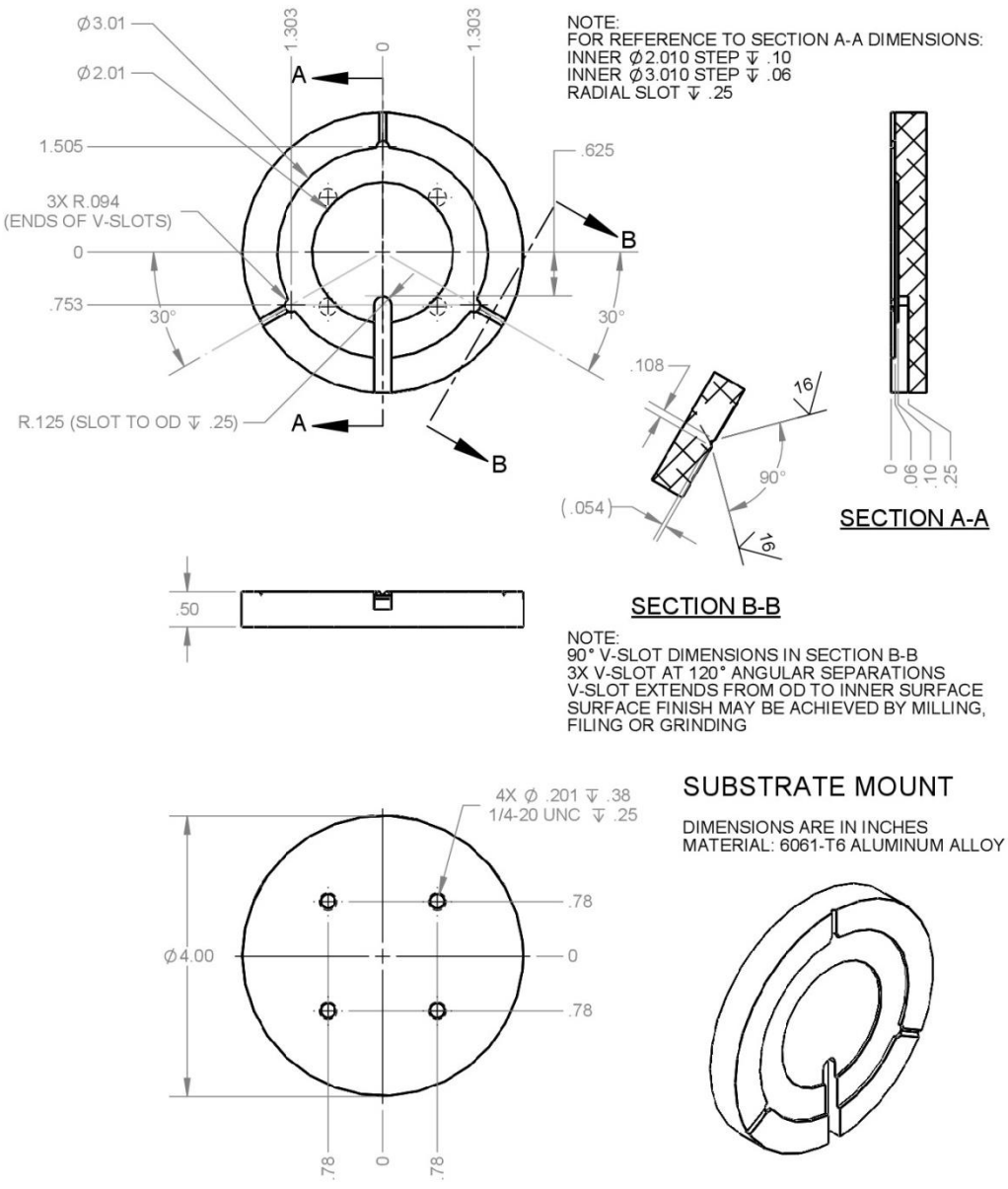

Figure C.4: Mechanical drawing of the substrate mount for making Sample 5. The ø 2.01 inch recession was machined into a slot for holding Sample 6 at two locations.

REFERENCES

[1] Dagnall, R. H., and Pearn, B. S. *Optical Alignment.* Hutchinson & CO LTD: London, England (1967). Print.

[2] "Autocollimating Alignment Telescope D-275". <http://davidsonoptronics.com/pdfs/D-275.pdf> Retrieved July 11, 2016

[3] Manuel, Anastacia. 2009. *Field-dependent Aberrations for Misaligned Reflective Optical Systems.* Ph.D. dissertation, University of Arizona, Tucson, Arizona.

[4] Burge, James H., *et al.* "Development of a wide field spherical aberration corrector for the Hobby Eberly Telescope," Proc. SPIE 7733, (2010)

[5] Coyle, L. E., M. B. Dubin, and J. H. Burge, "Design and analysis of an alignment procedure using computer-generated holograms," Optical Engineering 52(8), 084104 (August 2013).

[6] Burge, J. H., Rene Zehnder, and Chunyu Zhao, "Optical alignment with computer generated holograms," Proc. SPIE 6676, (2007)

[7] Burge, J. H., Chunyu Zhao, and Matt Dubin, "Measurement of aspheric mirror segments using Fizeau interferometry with CGH correction," Proc. SPIE 7739, (2010)

[8] Zehnder, R., J. H. Burge, and C. Zhao, "Use of computer generated holograms for alignment of complex null correctors" Optical System Alignment and Tolerancing 6676, (2006).

[9] Coyle, L. E., M. B. Dubin, and J. H. Burge, "Locating computer generated holograms in 3D using precision aligned SMRs," Classical Optics (2014)

[10] Scheiding, Sebastian, *et al.* "Freeform mirror fabrication and metrology using a high performance test CGH and advanced alignment features," Proc. SPIE 8613, (2013)

[11] Parks, Robert E., and William P. Kuhn. "Optical alignment using the Point Source Microscope," Proc. SPIE 5877, 58770B (2005).

[12] Martin, H. M., J. H. Burge, S. D. Miller, B. K. Smith, R. Zehnder and C. Zhao, "Manufacture of a 1.7-m prototype of the GMT primary mirror segments", in *Optomechanical Technologies for Astronomy*, ed. E. Atad-Ettedgui, J. Antebi and D. Lemke, Proc. SPIE **6273,** 62730G (2006).

[13] Burge, J. H., L. B. Kot, H. M. Martin, C. Zhao and R. Zehnder, "Design and analysis for interferometric testing of the GMT primary mirror segments", in *Optomechanical Technologies for Astronomy*, ed. E. Atad-Ettedgui, J.Antebi and D. Lemke, Proc. SPIE **6273,** 6273GM (2006).

[14] Domenicali, Peter L., and George C. Hunter. Optical Interferometer System with CCTV Camera for Measuring a Wide Range of Aperture Sizes. Zygo Corporation, assignee. Patent US4201473 A. 6 May 1980. Print.

[15] Oh, Chang Jin, Eric H. Frater, Laura E. Coyle, *et al.*, "Alignment of four-mirror wide field corrector for the Hobby-Eberly Telescope", Proceedings of SPIE Vol. 8844, 884403 (2013) SPIE Digital Library

[16] Morokuma, Tomoki, *et al.* "Design and development status of the University of Tokyo Atacama Observatory 6.5m telescope," Proc. SPIE 9145, (2014)

[17] Coyle, L. E., M. B. Dubin, J. H. Burge, "Low uncertainty alignment procedure using computer generated holograms," Proc. SPIE 8131, (2011).

[18] Millerd, James, Neal Brock, John Hayes, Brad Kimbrough, Matt Novak, Michael North-Morris and James C. Wyant. "Modern Approaches in Phase Measuring Metrology", Proc. SPIE 5856 (2004)

[19] Morel, Sophie, Matthew Dubin, Joe Shiefman, and James Burge, "Application of a synthetic extended source for interferometry", Applied Optics, Vol.53 No. 33, (2014)

[20] Burge, James H. "Applications of computer-generated holograms for interferometric measurement of large aspheric optics", Proc. SPIE 2576 (1995)

[21] Hariharan, P., B. F. Oreb, and T. Eiju, "Digital Phase-Shifting Interferometry: A Simple Error-Compensating Phase Calculation Algorithm," *Appl. Opt.*, **26**, 2504 (1987).

[22] Greivenkamp, J. E. and Bruning, J. H. (1992) Phase Shifting Interferometers. In D. Malacara (Ed.), *Optical Shop Testing* (pp. 501-598). New York: John Wiley & Sons, Inc. Print.

[23] Siegman, Anthony E. *Lasers*. Mill Valley, CA: University Science Books, 1986. Print.

[24] Lee, H., *et al*., "Delivery, installation, on-sky verification of Hobby Eberly Telescope wide-field corrector," Proc. SPIE 9906-156 (2016)